Development of a multimodal nanoprobe for the comprehension of post-stroke inflammation

Szilvia Karpati

N°d'ordre NNT : 2019LYSE1211

THÈSE de DOCTORAT DE L'UNIVERSITÉ DE LYON
opérée au sein de
l'Université Claude Bernard Lyon 1

Ecole Doctorale N° 206
Ecole Doctorale de Chimie de Lyon

Spécialité de doctorat : Chimie Procédés Environnement
Discipline : Chimie des matériaux

Soutenue publiquement le 18/10/2019, par :
Szilvia Karpati

Development of a multimodal nanoprobe for the comprehension of post-stroke inflammation

Devant le jury composé de :

Président du jury	
Prof. Jean-Marie DEVOISSELLE	Professeur des Universités – Université de Montpellier
Rapporteurs	
Dr. Bruno BUJOLI	Directeur de recherche – CNRS / Université de Nantes
Dr. Éva JAKAB-TOTH	Directrice de recherche – CNRS
Examinateurs	
Dr. Fabienne ARCHER	Directrice de recherche – INRA / Université Lyon 1
Prof. Jean-Marie DEVOISSELLE	Professeur des Universités – Université de Montpellier
Directeur de thèse	
Prof. Stéphane PAROLA	Professeur des Universités – Université Lyon 1
Co-encadrant	
Dr. Frédéric LEROUGE	Maître de Conférences – Université Lyon 1
Membres invités	
Dr. Olivier PASCUAL	Chargé de recherche – INSERM
Dr. Marlène WIART	Directrice de recherche – CNRS / Université Lyon 1

“The human brain has 100 billion neurons, each neuron connected to 10,000 other neurons. Sitting on your shoulders is the most complicated object in the known universe.”

Michio Kaku

Acknowledgments

First and foremost, I express my sincere thanks to my supervisor, Prof. **Stéphane Parola**, for his valuable advice, support, confidence, and consideration towards me during the three years of my thesis work. He allowed me to realize this Ph.D. project in extremely good conditions and a friendly and welcoming atmosphere. His door was always open when I needed any guidance or assistance.

I am extremely grateful to **Frédéric Lerouge**, my co-supervisor, who introduced me to the field of nanotechnology. He taught me with patience and pedagogy, in particular at the early stages of my learning and progressively gave me more and more autonomy, without abandoning me. He was always extremely helpful and willing to discuss any of my ideas. He always gave me advice or assistance when I faced any difficulties.

I express my thank to **Chantal Andraud**, head of the Chemistry Laboratory, for allowing me to join this laboratory and for her genuine caring attitude during my presence there.

I want to thank **Yann Bretonnière** for his precious help and advice in the organic chemistry part of my work, what he followed with interest. He also contributed to the project by synthesizing an essential compound of the developed contrast agent, the fluorescent label.

I also acknowledge all our collaborators in the project NanoBrain. Special thanks to **Violaine Hubert** and **Inès Hristovska**, and their respective supervisors, **Marlène Wiart** and **Olivier Pascual**, who taught me a lot about the biological and imaging aspects of the work. It was a real pleasure to join them for the *in vivo* experiments. Thanks to **Marc Lecouvey** and **Maëlle Monteil** for proving the precious PEG-ligands for the nanoparticle. I acknowledge **Patrice Marche** and his colleagues for the toxicology assessment of the nanoparticles and **Jean-Marc Lancelin** and colleagues for NMR measurements.

I would also like to extend my thanks to **Frédéric Chaput**, who was always available with his real ingenuity when I needed special jigs and set-ups.

Thanks to **Mikael Lindgren** for the two-photon measurements. I also want to thank **Olivier Maury** for fluorescence training and discussions, **Laure Guy** for LC-MS training and discussions and **Sandrine Denis-Quanquin** and **Jean-Christophe Mulatier** for NMR training and measurements.

Thanks to **Christian Melkonian** for his IT support and **Marie-Françoise Guiot**, **Edwige Royboz** and **Damien Séon** for their help in administrative questions.

I also want to acknowledge my other colleagues and friends from the laboratory, who contributed to the good atmosphere.

I also express my thank to **Sylvie Tencé-Girault**, **Ilias Iliopoulos**, **Marie-France Boucher, Alba Marcellan**, and **Guylaine Ducouret** who were much more than colleagues at ESPCI and who always believed in me and encouraged me in my initiatives.

And last, but not least, I am profoundly grateful to my husband, **Akos,** and my daughters, **Emma,** and **Anna** for their infinite patience, support, sacrifice, and encouragements during my thesis.

Summary

Ischemic stroke, as one of the most common causes of death, represents an important health issue. The pathology consists of the occlusion of an artery in the brain leading to an acute inflammatory process. Post-stroke inflammation usually results in irreversible secondary brain tissue damage. To date, the clinical application of anti-inflammatory treatments has been either negative or inconclusive. For a better understanding of this complex pathophysiological process and development of efficient treatment, there is an urgent need to develop performant *in-vivo* diagnostic tools.

In that context, we proposed to design a multimodal hybrid nanoprobe for enhancing the contrast in three different clinical and pre-clinical imaging modalities. The ability of this probe to enhance contrast in MRI (Magnetic Resonance Imaging) and a recently developed spectral photon counting scanner computed tomography (SPCCT) is intrinsic to the inorganic GdF_3 core. The inorganic nanoparticle size and morphology was optimized for the biological application. The third modality, intravital two-photon imaging, provides high spatial resolution, high sensitivity, and allows real-time imaging. To make GdF_3 nanoparticles visible by two-photon microscopy, a specially designed organic moiety is added to the nanoplatform.

The inorganic nanoparticles are synthesized by the original solvothermal method developed in our group. Surface modifications with different PEG derivatives confer to the GdF_3 nanoparticles high stability in physiological media (such as blood), biocompatibility, and stealth. The two-photon active chromophore synthesized in our laboratory is grafted to the particle surface *via* a thermally activated (catalyst-free) alkyne-azide click reaction.

Toxicity of the nanoobjects has been assessed by using two different tests on four human-derived cells, and no cytotoxic effect of the particles was found.

After the demonstration of the multimodality of the particles, pre-clinical *in vivo* experiments were performed. We evidenced that the particles successfully enhance SPCCT, MRI contrast in the brain of the small animal *via* a T2-effect and provide a high-intensity two-photon signal for in-vivo microscopy. Besides, the nanoparticles revealed to be stable and long-circulating in the blood, which favored their extravasation through the altered blood-brain barrier. Their uptake by activated immune cells offered the possibility to follow cell-trafficking.

Résumé

L'accident vasculaire cérébrale (AVC) ischémique est une des premières causes de mortalité dans le monde, par conséquent il constitue un véritable enjeu de santé publique. Cette pathologie résulte de l'obstruction d'une artère cérébrale par un caillot et déclenche une inflammation, pouvant majorer les lésions tissulaires du cerveau. À ce jour les traitements anti-inflammatoires appliqués en clinique se sont révélés inefficaces. Il est donc indispensable de développer de nouvelles approches diagnostiques pour une meilleure compréhension des mécanismes biologiques impliqués dans cette pathologie.

Dans ce contexte, nous avons proposé la conception d'une nanoplateforme hybride multimodale comme agent de contraste adapté à trois techniques d'imagerie médicale et pré-clinique. Ces nanoparticules au cœur inorganique, composé de GdF_3 augmentent sensiblement le contraste en IRM et leur opacité procure un rehaussement de contraste pour le Scanner Spectral à Comptage Photonique (SPCCT), une technique de développement récent. La troisième modalité, la microscopie biphotonique procure une haute résolution et une très grande sensibilité, tout en permettant d'obtenir des images en temps réel. Grâce à un chromophore adapté, greffé à la surface de la particule, cette modalité devient également accessible.

Ces particules inorganiques sont synthétisées par une méthode solvothermale originale, développée par notre équipe. La surface des nanoparticules est ensuite modifiée par différents ligands polyéthylène glycol (PEG) fonctionnalisés, qui rendent les particules de GdF_3 stables en milieu physiologique (comme le sang), biocompatibles et furtives. Enfin, un chromophore spécialement développé au sein de notre laboratoire, pour des applications d'absorption biphotonique, a été greffé à la surface de la particule. Le couplage du chromophore a été effectué *via* une réaction click azoture-alcyne, activée thermiquement (sans catalyse par Cu(I)).

La toxicité des particules a été évaluée par deux techniques différentes, appliquées sur des cellules d'origine humaine. À l'issue de ces tests aucun effet cytotoxique n'a été observé.

Après avoir démontré les propriétés multimodales de ces nanoobjets, des expériences précliniques *in vivo* ont été menées. Nous avons montré que lors de l'observation du cerveau de souris la nanosonde augmente efficacement le contraste en SPCCT, IRM et produit un signal intense en microscopie intravitale à deux photons. Les particules se sont révélées particulièrement stables dans le sang : grâce à leur furtivité elles restent dans la circulation longtemps, ce qui favorise leur passage à travers la barrière hémato-enchéphalique lésée. Elles sont également phagocytées par les cellules immunitaires activées. La dynamique spatio-temporelle de ces cellules marquées par les nanoparticules a pu être imagée.

List of Recurrent Acronyms

AA	Alendronic Acid
ACF	Autocorrelation function
ACN	Acetonitrile
ATR-FTIR	Attenuated Total Reflection Fourier-Transform Infrared spectroscopy
BBB	Blood-Brain Barrier
BP	Bisphosphonate
BPPEG	Bisphosphonate Polyethylene Glycol
BPPEGCOOH	Acid carboxylic-functionalized Bisphosphonate Polyethylene Glycol
CA	Contrast Agent
CMC	Critical Micelle Concentration
CNS	Central Nervous System
CNT	Classical Nucleation Theory
CSF	Cerebrospinal Fluid
CT	Computerized Tomography
DCC	N,N'-Dicyclohexylcarbodiimide
DCM	Dichloromethane
DCR	Derived Count Rate
DHU	Dicyclohexylurea
DLMCA	Diffusion-Limited Monomer-Cluster Aggregation
DLS	Dynamic Light Scattering
DLVO	Derjaguin-Landau-Verwey-Overbeek Theory
DMAP	4-Dimethylaminopyridine
DMF	Dimethylformamide
DMSO	Dimethyl sulfoxide
DOTA	1,4,7,10-Tetraazacyclododecane-1,4,7,10-tetraacetic acid *or* tetraxetan
EDTA	Ethylenediaminetetraacetic acid
EG	Ethylene Glycol
FDA	Food and Drug Administration
FID	Free Induction Decay

FTIR	Fourier-Transform Infrared spectroscopy
GBCA	Gadolinium-based Contrast Agent
GFP	Green Fluorescent Protein
HF	Hydrofluoric acid
HMG	Hydroxymethyl Glutaryl
ICP-AES	Inductively Coupled Plasma Atomic Emission Spectroscopy
IO	Iron oxide
IR	Infrared
IS	Inner Sphere
KF	Potassium Fluoride
LC-MS	Liquid-chromatography Mass spectrometry
LDH	Lactate Dehydrogenase
LEM-A	Lemke-type chromophore with alkyne group, synthesized in LC ENS
LSW	Lifshitz-Slyozov-Wagner theory
MCA	Middle cerebral artery
MD	Molecular Dynamics
MPS	Mononuclear Phagocyte System
MRI	Magnetic Resonance Imaging
MS	Mass spectrometry
MW	Microwave
NIR	Near Infrared
NMP	N-methyl-2-pyrrolidone
NMR	Nuclear Magnetic Resonance
NP	Nanoparticle
NSF	Nephrogenic Systemic Fibrosis
OD	Optical Density
OS	Outer Sphere
PDI	Polydispersity Index
PEG	Polyethylene Glycol
PEI	Polyethylene Imine

PET	Positron-Emission Tomography
PPEG	Phosphonate Polyethylene Glycol
QY	Quantum Yield
RCF	Relative Centrifugal Field
RES	Reticuloendothelial System
RF	Radio frequency
ROS	Reactive Oxygen Species
RT	Room Temperature
SEM	Scanning Electron Microscopy
SPAAC	Strain-Promoted Azide-Alkyne Cycloaddition
SPCCT	Spectral Photon Counting Computed Tomography
SPECT	Single Photon Emission Tomography
SPIO	Superparamagnetic Iron Oxide nanoparticles
SS	Second Sphere
TE	Echo Time (MRI)
TEM	Transmission Electron Microscopy
TGA	Thermogravimetric Ananlysis
TLC	Thin Layer Chromatography
TPA	Two-photon Absorption
TPE	Two-photon Excitation
TPLSM	Two-photon Laser Scanning Microscopy
TPM	Two-photon Microscopy
TR	Repetition Time (MRI)
USPIO	Ultrasmall Superparamagnetic Iron Oxide nanoparticle
UV	Ultra-violet
XPS	X-ray Photoelectron Spectroscopy
XRD	X-ray Diffraction
XRPD	X-ray Powder Diffraction
ZP	Zeta-potential

Table of Contents

CHAPTER 1

Introduction

Content

It's what you thought was a typical Friday evening… You are sitting in a restaurant, having a good time with your friends. Suddenly one side of your face droops, when you're smiling. You are trying to catch your glass, but your arm doesn't obey. One of your friends is telling a story, which according to the reaction of the others, sounds funny, but you are not sure why… Your friend sitting in front of you is asking something, but you don't understand, so you ask him to repeat, but instead, some slurred sounds come out. At that moment, you lost feeling on the whole right side of your body and the surrounding became blurry… What's happening?

EMERGENCY! You are probably having a STROKE!

I – Ischemic stroke and neuroinflammation

According to the World Health Organization statistics, every 2 seconds someone in the world suffers a stroke. This severe brain injury claims a life every 6 seconds in the world and, due to the lack of effective treatment, it is one of the leading causes of acquired permanent disability worldwide.[1,2] But what exactly is a stroke?

Stroke is an acute central nervous system injury, caused by a sudden occlusion of a cerebral artery (ischemic stroke) or by rupture of an artery in the brain (hemorrhagic stroke). It is estimated, that approximately 87 % of strokes are ischemic.[3] As opposed to muscles, brain tissue doesn't have any energy store, therefore cells which are deprived of blood flow due to the obstruction (usually due to the rupture of an atherosclerotic plaque), can maintain their viability only within 2-3 minutes.[4] After that time lapse, approximately 1.9 million neurons are lost each minute (in case of a large vessel occlusion),[5] which was highlighted by the well-known mantra "Time is brain" of C. R. Gomez in 1993.[6]

During the first hours (< 24h) of the injury three regions may be distinguished in brain tissue: (1) the ischemic core, where the brain tissue is irreversibly damaged, (2) the ischemic penumbra, which is a region at risk in which infarction evolves and (3) a region of oligemia, where blood flow is reduced, but still enough to maintain cell activity.[7] If the blood circulation is not restored rapidly, the ischemic core grows and progressively gains the whole penumbra leading to a higher volume of lost tissue.

In some very limited cases, eligible patients (2 – 7 % of cases in developed countries[8]) who present within 4.5 hours[9] of the onset of symptoms may receive an intravenous thrombolytic treatment, using recombinant tissue plasminogen activator (r-tPA), which restores blood flow by dissolving the clot. After that therapeutic time window, this treatment is not administrated, because it represents a risk of hemorrhage causing serious complications. Very often people do not get to the hospital within 4.5 hours of the start of a stroke and miss the time window, beyond which, depending on their condition, some strictly selected patients can be treated by mechanical embolectomy for recanalization, but no treatment is available for the majority of the stroke victims.[10] Only the blood pressure is lowered by medication, if necessary and a treatment composed of anticoagulant and antiplatelet is prescribed in the subacute and chronic phases, in order to prevent new clots forming. Lack of universal treatment and high occurrence of this pathology in the population make of stroke an important health issue. There is an urgent

need to identify and better define determinants of stroke prognosis and develop efficient treatment in the acute and subacute phases.

The diagnosis starts with a detailed medical interview of the patient to determine symptoms and risk factors, which is completed by a neurological exam and lab tests. To decide about the choice of treatment, *i.e.* to exclude intracerebral hemorrhage and visualize precise infarcted area location and size, quick neuroimaging tests, such as Computerized Tomography (CT) scan and Magnetic Resonance Imaging (MRI) are of key importance. However, acute stroke imaging protocol usually depends on the availability of imaging tools and the expertise of medical team.

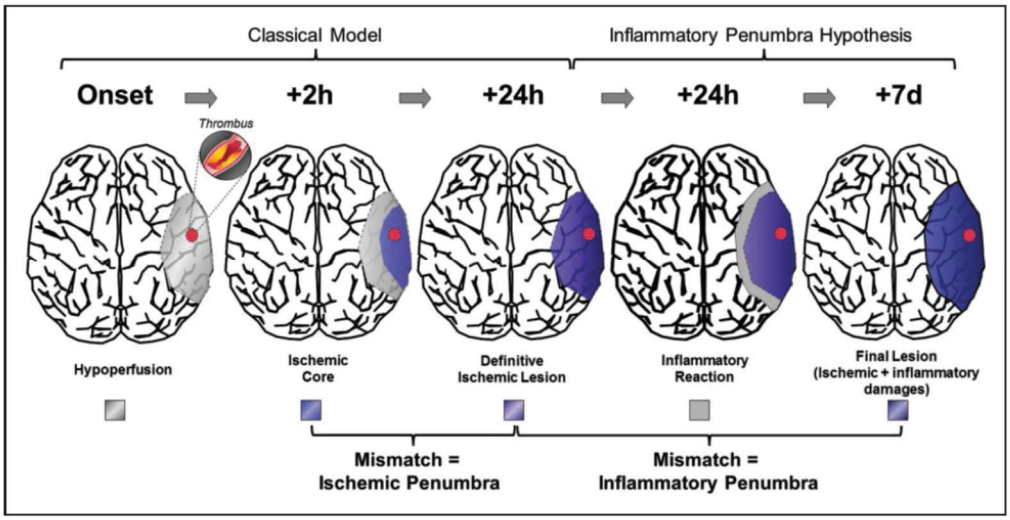

Figure 1 Evolution of damaged tissue volume after ischemic stroke. Adapted from ref [7].

Stroke is a complex multiphasic process, presenting in addition, heterogeneities within individuals.[11] Within minutes to a few hours following obstruction of the artery, in the *acute phase* of ischemic stroke, due to hypoperfusion, ionic homeostasis of cells deprived of oxygen and glucose is perturbed, which induces an osmotic pressure, leading to the swelling of cells. At that time, the patient may experience a severe headache, due to the increased intracranial pressure (malignant edema). The *subacute phase* extends over a period of a few days. Necrotic cells, death cell debris and increased concentration of reactive oxygen species (ROS) trigger a sterile (without microbes) neuroinflammatory response in brain tissue, which can induce secondary damages. During the chronic phase (up to several months after the onset of stroke), reorganization and repair of the damaged brain occurs progressively. Neuroinflammation and regeneration phase determine the extent of damage and the final functional outcome of the patient.

The infarcted volume extends progressively over these phases. Ischemic core area increases progressively over time and finally gains the whole penumbra, constituting the final ischemic lesion. However, in the surrounding tissue, ongoing neuroinflammation may extend damaged area. This inflammatory area has been suggested to represent the inflammatory penumbra (***Figure 1***).[7] Damage in the core is inevitable, therefore it is of reduced therapeutic interest. As mentioned before, ischemic penumbra is, on the contrary, salvageable by rapid reperfusion (in a limited number of eligible patients). Most of the scientific efforts are focused on the inflammatory area, because damaged tissue volume would be significantly confined if inflammation could be efficiently managed.

First clinical trials of anti-inflammatory drugs were reported in the 1980s, but to date all of the promising preclinical agents failed, when translated into human studies.[8,12] Several reasons (such as timing of drug administration, low drug concentration due to poor penetration into brain tissue etc.) have been evoked for this failure, however, it seems evident, that for the development of effective immunomodulatory agents for the brain, this complex biochemical process must be properly characterized at the cellular level.

In 2009, Gelderblom and co-workers, published a study of the temporal and spatial dynamics of immune cells, that are the major actors of neuroinflammation. By quantifying resident cell accumulation and infiltrating immune cells into the ischemic hemisphere in rodent stroke model, they showed, that the concentration of the different subsets of immune cells varies over time. In normal, homeostatic conditions, except for the resident immune cells (microglia), the presence of other immune cells in brain tissues is negligible. After a stroke injury, neuronal cell death activates microglia, which secret chemical messages (cytokines and chemokines), inducing migration of neutrophils and monocytes/macrophages into the ischemic parenchyma. In normal conditions, cross-talk between brain tissue cells and blood components is limited by the blood-brain barrier (BBB), composed of tightly joined endothelial cells on blood vessel wall. However, in neuroinflammatory conditions, activated microglia induce permeability of BBB, which favors infiltration of immune cells from blood. Each type of participating immune cell (microglia and infiltrating cells) may have positive or negative effects in the inflammatory process and their role changes upon time. This dual role of the inflammatory cascade following injury is a very complex interplay of all participating cells. For example, activated microglia may either behave as pro-inflammatory cell, inducing further neuronal death in the acute phase, and later switch to an anti-inflammatory and neuroprotective role, contributing to recovery.[13,14]

Deep understanding of the complex pathophysiological cascade of ischemia, would allow to develop treatments, that reduce injury-exacerbating characteristics of these cells and/or amplifying their repair functions in the appropriate time interval. This leads to an urgent need to find more performant imaging tools to investigate *in vivo* stroke evolution.

II – Brain imaging techniques

Medical imaging techniques are non-invasive tools to visualize *in vivo* systems and assist diagnosis of different pathologies by providing anatomical, physiological or even molecular information. During the past 40 years these methods have been undergoing a revolution owing to fast technological developments and improvement of digital image processing techniques. Imaging the brain has been of a particular challenge for these non-invasive techniques, because this organ is the most unapproachable due to skull protection. To date, many types of bioimaging methods, also called imaging modalities, are available spanning from whole-body anatomical visualization techniques to subcellular imaging. In neuroimaging currently three basic modalities are clinically used, including Magnetic Resonance Imaging (MRI), X-rays Computed Tomography (CT) and Positron Emission Tomography (PET). Neuronal tissue imaging with intravital microscopy is for the moment limited to small animal models, however its clinical use in cancer research (essentially skin) is under development. In the following paragraphs these modalities are briefly presented and ***Table 1*** summarizes their main advantages and limitations.

Table 1 Characteristics of main brain imaging techniques

Modality	*Resolution*[a]	*Depth*	*Acquisition time*	*Advantages*	*Limitations*	*Clinical use*
MRI	100 µm-1 mm	No limit	min – h	Non-invasive, high resolution, non-ionizing radiation	Low sensitivity, high cost, time consuming, patient needs to be motionless	Yes
CT	200 µm-1 mm	No limit	min	Non-invasive, high resolution	Radiation, low sensitivity, poor soft tissue contrast	Yes
PET	1-2 mm	No limit	min – h	Quantitative, high sensitivity, specificity, real-time scans	Radiation, low resolution, cyclotron is needed	Yes
Optical imaging	1-3 µm	< 1mm	s – min	High sensitivity, real-time imaging, fast	Low penetration depth	In development

[a] Typical resolution values are from refs. Key *et al.*[15] and Zhang *et al.*[16]

Magnetic Resonance Imaging (MRI) uses a strong magnetic field and radio waves to create detailed anatomical and physiological images of a living body. This non-invasive clinical

diagnosis technique is characterized by a high spatial resolution without any penetration depth limit. Good contrast is obtained for soft tissues, but the technique suffers from limitations in terms of sensitivity, therefore a relatively long data collection is required for image construction. In order to increase sensitivity and contrast in MR images, a paramagnetic contrast agent (Gd-, Mn-, Fe-compounds) may be introduced into the body. These agents are described more in details in paragraph ***II.1.2 MRI contrast agents***.

Another clinically used, non-invasive brain imaging technique is X-rays Computed Tomography (CT). During acquisition of a CT scan, patients are exposed to ionizing radiation (X-rays) for a brief time laps, and in first approximation, the collected signals scale with the electron density of the tissues, making this technique particularly suitable for evaluation of skeleton abnormalities. High spatial resolution of CT imaging and rapidity of scans make it the modality of choice in cases of trauma and other acute neurological emergencies. However, its low sensitivity, especially in soft tissues is the main limitation of CT. Specific, high atomic number (Z) elements, such as iodine, barium or bismuth-based compounds, can be administered to the patient to overcome low sensitivity.

Conversely, Nuclear imaging modalities (Positron Emission Tomography or PET and Single Photon Emission Tomography or SPECT) do not allow for such a high spatial resolution, as MRI or CT, but provide the highest sensitivity of all imaging techniques. A positron/γ-ray emitter radioisotope source (*e.g.* ^{18}F, ^{15}O, ^{13}N for PET and ^{99m}Tc, ^{131}I, ^{111}In for SPECT) injection is a prerequisite for imaging. This special class of contrast agents is produced in cyclotron sources, which limits availability of PET and SPECT in clinical diagnosis.

Very high sensitivity is achieved by two photon excitation microscopy, which is based on the detection of fluorescence coming from labeled tissues. Endogenous (*e.g.* fluorescent proteins) or exogenous (synthetic) fluorophores are both used for labeling cells of interest. Such as PET, this technique also provides a real-time imaging of cellular activities in living systems, but unlike PET, subcellular level resolution is accessible. However, main limitations of optical imaging rely on light attenuation by absorption and scattering by tissue components, which reduces exponentially the signal with depth.

In this work, MRI, CT and intravital microscopy play a key role, hence we propose to describe these three techniques briefly.

II.1 – Magnetic Resonance Imaging

II.1.1 Basic principles of MR-imaging

During an MR-imaging procedure, the subject is placed in a strong magnetic field, B_0 (approximately 100 000 times more than Earth's magnetic field), resulting in the temporary magnetization of tissues. This translates into the creation of a bulk magnetic moment (M) arising from the orientation along the axis defined by B_0 of the individual magnetic moments of protons inside the tissues (essentially water and fat protons, which are most abundant in human body). Then a radiofrequency (RF) pulse is applied, which perturbs the protons and their magnetic moment flips into the perpendicular plane to B_0. When the RF pulse is turned off, the protons exponentially relax into their initial equilibrium state and their overall magnetic moment gradually comes back into B_0 direction. (For more details, please refer to Appendix 3.)

This relaxation process has two components: spin-spin and spin-lattice relaxations, corresponding to the decay of the transverse component of M and the regrowth of its longitudinal component, respectively. Relaxation of these two components are characterized by two time constants, transversal or T_2 and longitudinal or T_1 relaxation times. Evolution of these two components are monitored to create images. Different tissues may have slightly different relaxation times. For example, microenvironment of the protons in the cerebrospinal fluid (CSF) is different from fat containing tissues (such as white matter in brain) leading to different T_1 and T_2 times. Relaxation is also different in a lesion, as compared to healthy tissues. Differences in T1 an T2 relaxations give rise to different signal intensities in the MR image, depending on the image weighting.

The contrast, *i.e.* the relative difference of intensities in two observed areas is determined by T_1- T_2 times and proton density in this area, which are three intrinsic tissue parameters. Contrast can be enhanced by appropriate selection of measuring conditions, such as the repetition time (TR) and flip angle of the RF pulses, or the data acquisition time referred to as echo time (TE).[17] TR, flip angle and TE are the operator-selectable parameters influencing the contrast. For a flip angle of 90°, the relation governing the signal intensity for a spin-echo sequence, is given by the following equation:[18]

Equation 1

$$Signal \propto \rho\left(1 - e^{-TR/T_1}\right)e^{-TE/T_2}$$

Spin density | T1 weighting | T2 weighting

From that equation it is easily understood, that by selecting a low TE and low TR values, the term containing T_1 is maximized, compared to T_2-term. In that case the differences in T_1 times are enhanced, which means that the contrast is improved in T_1 relaxation. We are talking about a T_1-weighted image. Conversely, by de-emphasizing T_1-term (high TE and high TR values), and exaggerate T_2-term, a T_2-weighted image is obtained.

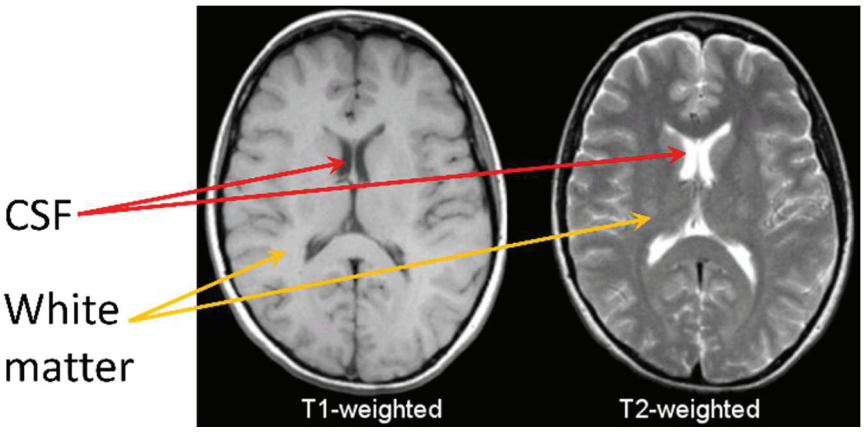

Figure 2 Illustration of T_1- and T_2-weighted images of brain tissues. Figure adapted from ref.[19]

In practice, this means that when observing brain in a T_1-weighted image (***Figure 2***), CSF, which has a longer T_1 relaxation time appears in dark, while fatty tissues (shorter T_1), such as white matter give a bright signal (white). Oppositely, in T_2-weighted images, CSF gives a brighter signal, while white matter appears in dark.

For a deeper understanding, several detailed and comprehensive reviews[17,20] introduce the reader to the theoretical background of MR-imaging.

II.1.2 MRI contrast agents

In the previous paragraph we introduced the concept of contrast and enumerated the parameters determining the signal intensity. Contrast can be enhanced by appropriately adjusting the operator-selectable parameters; however, this may not be enough to be able to visualize pathologies with certainty because of the very similar microenvironments of healthy and diseased tissues. In order to further increase contrast and obtain more detailed images, the intrinsic properties, T_1 and T_2 times also must be modulated, by introducing an exogenous

compound into the observed area, which is able to modify relaxation of tissue protons. This prompted the need for developing a new class of pharmaceutical compounds, called contrast agents (CA).

In 1978, Lauterbur and his coworkers showed the ability of paramagnetic Mn(II) ions to differentially change the relaxation of tissues *in vivo*. They evidenced the feasibility to distinguish infarcted regions from normal myocardium, by injecting manganese salt solution to dogs. They observed that the longitudinal relaxation correlated with Mn^{2+}-concentration.[21,22] The first human application of contrast enhanced MRI has been published in 1981, by Young *et al.*, who administered ferric chloride to increase contrast in the gastrointestinal tract of patients.[23] In 1984, Weinman *et al.* used for the first time Gd(III)-DTPA (diethylenetriamine-pentaacetate) complex in humans.[24] By showing the potentialities of this paramagnetic agent in contrast enhancement, they initiated the clinical use of this compound, which was marketed in 1988, known as Magnevist® (***Figure 1***). Thanks to the contrast agents, low sensitivity of MRI is compensated, therefore this imaging technique became a routine modality, in particular in brain imaging.

MRI contrast agents are complexes of paramagnetic ions, such as Gd^{3+}, Mn^{2+} and Fe^{3+}. Gadolinium has seven unpaired 4f electrons and a long electronic relaxation time; therefore, this element is the most efficient in enhancing the longitudinal proton relaxation. Today, gadolinium-chelates are clinically used as MRI contrast agents for human patients. However, some toxic issues of free gadolinium have been reported. Free Gadolinium ion is toxic for several reasons: it is a heavy metal and because its radius is very close to the radius of Ca^{2+} ions, gadolinium interferes in physiological processes dependent on Ca^{2+} influx.[25] The median lethal dose (LD50) in rats has been reported to be about 0.4 mmol/kg.[21] In addition, in renal failure patients gadolinium(III) replaces endogenous metals by transmetallation reactions, provoking the development of nephrogenic systemic fibrosis (NSF), a generalized fibrotic disorder. This phenomenon was reported in 1997, and the correlation with Gd CA was first demonstrated in 2006, by Grobner.[26] Since then, a huge effort has been done to develop high stability gadolinium based contrast agents by macrocyclic chelates, such as Dotarem® (Gd-DOTA), ProHance® (Gd-HP-DO3A) and Gadovist® (Gd-DO3A-butrol) (the structure of these examples is shown in ***Figure 3***.). Restriction of linear chelator-based CAs has been recommended by the European Medicines Agency.[25] Gadolinium based CAs have been used for *in vitro* MRI cell tracking, by Cabella *et al.*, who demonstrated in 2006,[27] that if the Gd-chelate is not stable enough, free gadolinium ions are released and cells can act as sponges of

Gd^{3+}, leading to an overestimation of the amount of CA uptake by the targeted cells. Therefore, in addition to health issues, free gadolinium ions possibly induce artefacts in MRI signal.

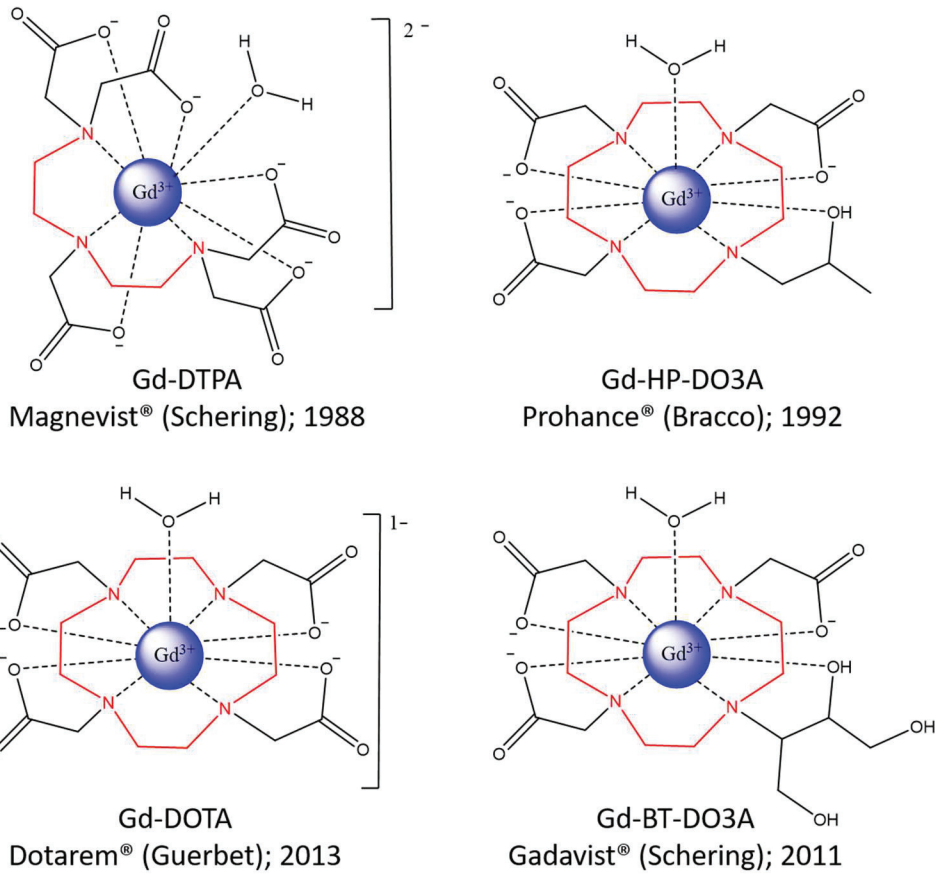

Figure 3 Examples of clinically used Gd-based contrast agents. Molecular structure of the complexes is represented, with the corresponding overall charges for ionic CAs. Red parts of the structures enhance the difference between linear and macrocyclic CAs.

Brain is one of the most sensitive organs physically protected by the skull and from inside, the so-called blood brain barrier (BBB) isolates brain tissues from blood flow. Therefore, it was thought that Gd-complexes cannot cross this barrier. However, in 2014, Kanda *et al.* reported areas of abnormally increased MR signal on unenhanced T_1-weighted images of patients' brain, previously subjected to repeated gadolinium-based contrast material administrations. This observation evidenced, that gadolinium ion (with acyclic or to a lesser extent macrocyclic ligands) can also deposit in brain tissues.[28,29]

Therefore, the actual challenge in gadolinium-based contrast agent (GBCA) development is to increase both complex stability and contrast enhancement efficiency of the gadolinium compound, in order to prevent free-gadolinium release and to lower the dose necessary for high contrast. This initiated several strategies reviewed by Botta *et al.*,[30] such as ligand development for more stable complexes, encapsulation of Gd-complexes in organic nanoparticles

(dendrimers or liposomes), attachment of the complex to an inorganic nanoparticle, such as silica nanoparticles or incorporation into inorganic nanoparticles (Gd-oxide), or even Gd-complex encapsulation in fullerene.[31]

Manganese complexes has recently attracted new interest and are proposed as an alternative to gadolinium.[32] However, Mn(II) has slightly less strong paramagnetic effect and its aqua complexes are less stable.[33]

Another class of clinically used MRI contrast agents is iron-oxide (IO) nanoparticles. As opposed to Gd- and Mn-complexes, superparamagnetic iron ion reduces the intensity of T_2 signals, causing negative enhancement in T_2-images. Clinically, two commercially available IO nanoparticle-based contrast suspensions have been applied: Feraheme® (Ferumoxytol) and Resovist® (Ferucarbotran).[34] (To date, the last one, Resovist is not used anymore.) Iron compounds are non-toxic, however IO nanoparticles present a drawback related to contrast: as a T_2-agent it contributes to a signal decrease and not increase like T_1-agents.[35] In addition, iron has a high magnetic susceptibility, therefore it distorts locally the magnetic field (this is the so-called blooming effect), resulting in possible artifacts in MR images.

II.1.3 Efficiency of paramagnetic contrast agents

II.1.3.1 T1 relaxation mechanism

Relaxation of protons in the close vicinity of a paramagnetic ion is accelerated, *i.e.* the relaxation rate ($1/T_i$; i=1,2) increases. The observed relaxation rate is therefore composed of two contributions, diamagnetic and paramagnetic. Diamagnetic contribution is similar to the relaxation rate in the absence of contrast agent (usually water relaxation), measured in the same conditions as $1/T_{obs}$, while the paramagnetic term is proportional to the paramagnetic ion concentration.[17,21]

Equation 2

$$\left(\frac{1}{T_i}\right)_{obs} = \left(\frac{1}{T_i}\right)_{dia} + \left(\frac{1}{T_i}\right)_{para} \text{ ; with } i = 1,2$$

Equation 3

$$\left(\frac{1}{T_i}\right)_{para} = r_i[CA]; \quad or \quad r_i = \frac{1/T_i}{[CA]}$$

The proportionality constant r_i is termed as the relaxivity of the contrast agent and is expressed in $mM^{-1}\ s^{-1}$. Relaxivity is a fundamental property of a contrast agent, quantifying its efficiency. Therefore, when designing a contrast agent, its relaxivity must be optimized.

Relaxation process is the result of different types of proton-CA interactions, which are governed by several external factors, such as temperature and field strength, but intrinsic parameters are also very important. Water protons are interacting with Gd^{3+} ions through a complex dipolar interaction, therefore the interaction strength strongly depends on the H-Gd distance ($1/d^6$). The closest hydrogen nuclei, which are directly bound to the paramagnetic ion, are more effectively relaxed, than protons which are more distant. Based on this assumption, three different solvation spheres can be distinguished. The inner sphere (IS) contains water molecules bound to Gd^{3+} ions. Weakly interacting water molecules, which participate in hydrogen-bonding with the metal or which are coordinated to the ligands in the complex, are more distant and constitute the second sphere (SS). Water molecules of the bulk phase are in the outer sphere (OS), and this contribution depends on bulk water diffusion to the inner sphere. However, induced proton relaxation enhancement is negligible for protons in this sphere.

Inner sphere term is the determining part in the paramagnetic ion relaxivity and is theoretically described by the Solomon-Bloembergen-Morgan model.[36,37] According to this theory, inner sphere relaxivity of a CA is linearly proportional to the hydration number of the metal ion (q), and also depends on the exchange rate of relaxed, coordinated water molecule with a bulk water molecule ($\tau_m = 1/T_m$, where T_m is water residence time in the IS), the inverse of the correlation time of the unpaired electron spin relaxation (*i.e.* $1/T_e \sim T_1$ of the electron) and the molecular tumbling rate (τ_R), related to the rotational dynamics of the CA molecule.

Relatively long electron spin relaxation time of Gd^{3+} ion[21] is one of the reasons, why gadolinium based CAs are so efficient as T_1 CA, hence this parameter is inherently optimized. Therefore, efficient CA design strategies are focused on increase of the three other parameters, q, τ_m and τ_R. Increasing steric crowding of the coordination sphere of gadolinium favors water release, *i.e.* water exchange rate increases, however the complex stability suffers greatly.[38–40] Increasing the number of coordinated water molecule also has been investigated and was found efficient in relaxivity enhancement. However, insertion of supplementary water molecules is only possible by decreasing denticity of the other ligands, which again leads to the collapse of thermodynamic stability.[41] To date, all FDA-approved CAs contain only one water molecule. The third parameter, which can be influenced by design is the molecular tumbling rate. By

lengthening τ_R of the CA, the coupling between unpaired electrons of Gd^{3+} and water proton spin is more efficient, which increases relaxivity. Rotational dynamics of a molecule in solution is highly dependent on its hydrodynamic volume. Therefore, increasing the size of the CA slows down its motion, leading to enhanced relaxivity. This latter strategy was largely explored by two main ideas: the gadolinium-complex can be covalently or non-covalently linked to a larger structure, such as a protein (*e.g.* human serum albumin, HAS) or an inorganic nanoparticle (*e.g.* silica), and another approach may be to increase size of the ligands in gadolinium-complex.[41,42]

For an efficient CA design all these relevant parameters must be optimized in the same time, by preserving stability and water solubility of the CA. Gadolinium-based nanoparticles seems to be promising candidates, since they concentrate in a small space a huge number of paramagnetic ions leading to high local concentration, with a huge size compared to molecular complexes, decreasing the tumbling rate. Moreover, the surface can be appropriately modified for optimizing water exchange rate and solubility properties.

II.1.3.2 T2 relaxation mechanism

All contrast agents shorten both T1 and T2 relaxation, but their relative contribution to each process determines which relaxation enhancement is dominant. Superparamagnetic iron oxide nanoparticles form the majority of T2 CAs. Local magnetic field gradients induced by the large anisotropic magnetic susceptibility of these particles reduce efficiently T2 relaxation of water protons, through fast dephasing of the transverse magnetization.

As described by the outer-sphere theory, relaxivity r_2 is dependent on the saturation magnetization, particle radius, diffusivity of water molecules and thickness of an impermeable surface coating.[42] Saturation magnetization or the ability to easily be magnetized by external magnetic field, can be improved by increasing the crystallinity of the particles or by making them anisotropic (such as rod shaped particles). Surface coating has a crucial role in the interaction of the aqueous surroundings with the particle. For example, hydrophilic and highly hydrated ligands are favorable to the water residency in the second sphere, which increases relaxivity. In addition, water has to access easily to the particle surface; therefore, a not fully covered surface is required (low grafting density). Furthermore, a thick coating layer elongates water (from second sphere and outer sphere) - NP distance, which reduces r_2 relaxivity of the CA.[43]

As a summary, it was shown that improvement of relaxivities r_1 and r_2 is a complex physicochemical problem involving many parameters. Therefore, design of efficient MRI CAs represents a challenging field.

II.2 – Two-photon microscopy

Predicted in 1931 by Maria Göppert-Mayer, two-photon excitation (TPE) phenomenon was first observed in 1961 by Kaiser and Garrett. However, it was only in 1990, that Denk *et al.* described the conception of the first microscope based on this principle, which is called two-photon laser scanning microscopy (TPLSM) or shortly, two-photon microscopy (TPM).[44]

In two-photon absorption (TPA), two low-energy photons, whose overall energy corresponds to the energy needed for one photon absorption (OPA) are almost simultaneously absorbed by a chemical species. As TPA occurs very rapidly (within femtoseconds) with the participation of two photons, its probability is very low in excitation conditions required for OPA induced microscopy. However, due to its quadratic intensity dependence, at very high photon densities, which can be achieved by pulsed lasers, TPA becomes very efficient. Owing to its multiple advantages compared to classical OPA induced fluorescence, TPA is largely applied in fluorescence microscopy.

Endogenous components of biological tissues, such as hemoglobin, cytochromes, etc. absorb and scatter UV and visible light, making use of OPA induced fluorescence imaging very limited. In contrast, TPA shifts the excitation to the near-infrared region (NIR) which is highly beneficial in several aspects. On one hand, the NIR excitation is less absorbed by biological tissues, thus it gives rise to reduced phototoxicity and autofluorescence compared to the corresponding OPA, which occurs at half the wavelength. On the other hand, NIR excitation increases the penetration depth of TPM, because scattering decreases with the increasing excitation wavelength. This part of the spectral region is the so-called biological or optical transparency window (***Figure 4***).[45,46] Two-photon excitation with such low-energy photons increases the penetration depth from ~ 50 µm (OPA) to ~ 400 to 1000 µm, depending on the examined tissue.

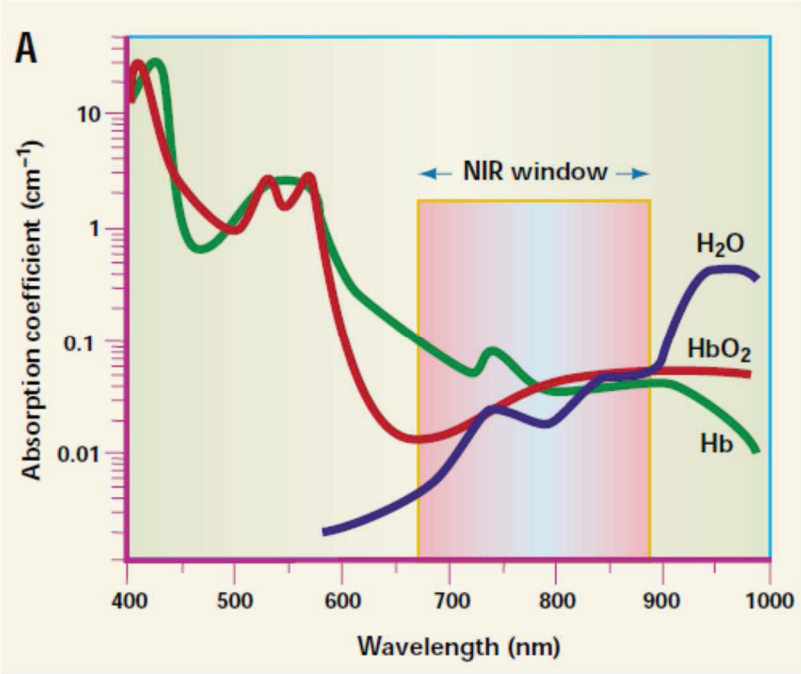

Figure 4 Illustration of the biological transparency window. Adapted from ref. [46]

Furthermore, in two-photon microscopy, TPA occurs only in the high intensity region of a tightly focused laser beam (typically, the focal volume is less than $1 \cdot 10^{-15}$ L)[44], which eliminates inherently all out-of-focus fluorescence and significantly increases the spatial resolution. Due to the same reason, the strongly confined TPA also removes the out-of-focus photodamage, allowing long-term imaging of biological tissues without altering their function.

TPM is one of the most powerful intravital microscopic techniques, however due to its low penetration depth compared to other imaging techniques (such as MRI, CT), for human patients actually, it is limited to clinical skin biopsy analysis essentially in cancer research and also the recently developed, minimally invasive microendoscopy, also used in dermatological applications. In addition, it has been demonstrated that it represents a promising tool for image-guided surgery.[47]

In pre-clinical research, however, TPM is widely used for *in vivo* small animal imaging. In this case, when it is necessary, the observed tissue is exposed by performing a surgical preparation. For example, the brain tissues are completely hidden by the skull, therefore imaging in this area is only possible by creating a window through the skull. This is routinely done by two methods. Craniotomy may be performed, which consists in removing a portion of the skull, but this technique may induce meningeal inflammation. Skull thinning technique is recommended in brain imaging studies, which requires significant surgical practice,[48] but the final thickness of 20 – 30 µm of skull is enough to protect the brain and avoid any infection.[49]

In order to generate a fluorescent signal for imaging, a broad range of fluorescent labels are currently available. Depending on the application, endogenous (*e.g.* NADH, FAD etc.) or exogenous (*e.g.* fluorescent proteins) biomolecules can be used. Organic dyes, quantum dots, lanthanide-doped upconversion nanoparticles are also widespread applied. To date the only FDA-approved NIRF dye for clinical use is indocyanine green (ICG).[50] Genetically modified (transgenic) animals, expressing anatomical markers, such as green fluorescent proteins (GFPs)[51] are often used to image tissue resident cells.[52]

II.3 – Spectral Photon Counting Computed Tomography (SPCCT)

X-ray Computed Tomography is a well-established tissue imaging modality, employed in the clinics, as well as for research purposes. The signal obtained in this technique depends on the atomic number ($\propto Z^4$) of the elements composing the observed tissue and the local electron densities ($\propto \rho$). High X-ray attenuation contrast media are frequently used for soft tissue imaging.[53] However, the clinically used iodine based contrast agents are not tissue-type specific (different tissue composition may result in the same attenuation value) and are not efficient in the detection of pathologic processes and limits diagnostic performance. This motivated numerous technical advances, such as exploiting spectral information of the signal.[54]

For a CT scan acquisition, the X-ray source energy is adjusted to closely match the K absorption edge (binding energy of a K-shell electron in atoms) of the contrast agent element (*e.g.* 50.2 keV for gadolinium-based compounds). Conventional CT devices integrate all transmitted (and scattered) X-ray photons into a single attenuation value, without any spectral information. Recently, accurate recording and analyzing of the spectra became available, thanks to advances in detection technologies and software development. This technological breakthrough gave rise to the development of a new generation CT, called Spectral Photon Counting or multicolor CT (SPCCT).[55] The energy-sensitive photon-counting detector enables the energy discrimination of photons, leading to an element-specific imaging. SPCCT allows precise detection and also quantification of contrast agents, with the possibility to simultaneously detect two or more contrast agents based on their K-edge energy.

In the frame of the European Project Spectral Photon Counting CT - H2020, Philips Medical systems developed a pre-clinical spectral CT scanner, which has been installed at CERMEP, Lyon. After the first successful *in vitro* and *in vivo* experiments,[55] a human sized clinical

SPCCT device has also been developed for translating the results on large animals and on humans.

For technical reasons, the energy range available in SPCCT is 40 to 100 keV, which rules out use of the low K-edge value iodine (33.2 keV) as contrast agent.[56] In addition, currently used iodine CAs are not specific and as molecular agents, are rapidly eliminated. This leads to the necessity to develop new contrast media, suitable for SPCCT.

Within the collaborative European project, in collaboration with Philips, Professor Stéphane Parola's team (Laboratoire de Chimie - ENS Lyon) are developing such contrast agents. They showed, that gadolinium, with a K-edge of 50.2 keV enhances efficiently contrast in K-edge imaging.[57]

III – Multimodal imaging

III.1 – Basic idea of multimodality

In the previous paragraph, advantages and drawbacks of the different imaging techniques were briefly pointed out. In clinical diagnosis, imaging techniques became standard practice and because the need to get as precise images as possible, technological improvements push the limits of each modality. However, one modality imaging is a potential source of artefacts and diagnostic errors. Such as a chemist needs to characterize a new molecule by several techniques to get information on composition, structure and different physico-chemical properties of the synthesized compound, combining different imaging techniques provides a more detailed vision, leading to more accurate diagnosis and it allows to rule out false negative (often due to a limited sensitivity) and/or false positive (due for example to extravasation through leaky BBB, endogenous contrast, like microhemorrhages, *etc*.) signals.

Multimodality may be achieved either by combining two techniques within the same device or combining results obtained from imaging with two or more devices. For example, recently, Cui *et al.* published the proof-of-concept for using two-photon microscope integrated in magnetic resonance imaging system,[58] and MRI is very often combined with CT or PET for brain imaging.[15]

Combination of different imaging techniques simultaneously or sequentially require contrast agents that are efficiently detectable with all the involved modalities. Considering that each modality is characterized by a different sensitivity and is based on different source-tissue

interactions, development of a single contrast agent eligible for the combined techniques is a challenging task.

III.2 – Nanoparticles for imaging

Nanoparticles (NPs) of appropriate composition used as contrast agents, are of particular interest for multimodality and are increasingly employed as innovative tools in preclinical studies,[8] in particular for stroke research. Their size of 1 – 100 nm is much smaller than cellular dimensions and is comparable with proteins or viruses,[59] therefore NPs can efficiently interact with biological systems at the subcellular level, in a very specific and localized manner.

The choice of NPs composition is oriented by its application as a contrast agent: for MRI, paramagnetic or superparamagnetic (Gd, Fe, Mn) elements are included, for CT imaging, high radioopacity is achieved with electron-rich elements (I, Au, Ba, Gd, etc.) and for optical imaging, suitable organic dye NPs, quantum dots or upconversion rare-earth nanoparticles are used.[15] One of the major advantages of using NPs, is that a huge number of contrast elements (several thousands) are concentrated in a small volume, which increases considerably the resolution of the imaging technique. Another interesting aspect of NP-based CAs is the infinite possibility to adapt their surface properties, that can be obtained by adding various functionalities to the particle. Due to their high specific surface, a typical NP of ~ 10 nm may accommodate ~ 1500 reactive sites.[60] This offers the possibility to specifically target a tissue of interest, such as tumors,[61] by conjugation of targeting moieties to the particle. In spite of the versatility of NP-based CAs, their application in bioimaging is not yet translated to routine clinical use. Only a few NP agents are approved by the Food and Drug Administration (FDA) in the United States.[62] The main reason for this restriction is the limited knowledge base concerning health issues, that may arise from the particulate nature of these agents.

Indeed, once introduced into a living body, the particles immediately interact with the defense system of the organism. As a foreign entity, they are considered as enemies and must face a hostile environment.

The most common way of administration of contrast agents is intravenous injection. Upon renal filtration, CA molecules and small particles (~ 5 nm) are rapidly cleared (~ 1.5 h) from the blood by urine, while due to the limited physiologic pore size in kidney, larger particles are not filtered, which increases their blood half-life. These particles may have three possible fates. (1) They are metabolized to clearable components. However, this route is usually extremely slow, due to the high physiological stability of particles. (2) They may be excreted by the liver

into bile. Hepatic uptake may also take place through Kupfer cells (liver resident macrophages). (3) They are taken up by the mononuclear phagocyte system (MPS), also known as reticuloendothelial system (RES). In the blood, plasma proteins adsorb on the surface of particles, and form the so-called protein corona. Some of these proteins, called opsonins are biological markers, initiating recognition and endo/phagocytosis of the particles by circulating monocytes and macrophages. This increases significantly their circulation half-life in blood and finally are accumulated in liver, spleen and bone marrow or lymph nodes.[63]

The fate of particles is not only dependent on their size, but other physicochemical properties, such as shape (surface curvature), surface charge and their hydrophobicity/hydrophilicity are also of key importance, in particular for their recognition.[59] If nanoparticles are expected to target specific tissues, they must avoid RES. This can be achieved by optimizing particle parameters and make them stealth (*i.e.* "invisible") for immune cells. Macrophage-evading, long circulating particles have more time to efficiently accumulate in the targeted tissue.

Surface modification strategies have been developed to obtain stealth particles, for example coating with hydrophilic polymers, such as poly(ethylene-glycol) (PEG) or dextran.[59] The polymer shell around the inorganic (or organic) core suppresses effectively protein adsorption and increases stability of the particles in physiological conditions.

IV – Imaging neuroinflammation in stroke

Ischemic stroke studies with neuroimaging methods have four main targets: (1) activation of central nervous system (CNS) immunocompetent cells, such as microglia, (2) BBB permeability, (3) hematogenous immune cell infiltration into the CNS, and (4) pathological consequences, such as edema, cellular and axonal damage, etc.[64]

Glial cell (microglia and astrocytes) activation has been observed both in pre-clinical animal models of ischemic stroke and in human disorders, by PET imaging. Specially developed radiotracers (*e.g.* [^{11}C]PBR28, [^{18}F]DPA-714) target translocator protein (TSPO), which is upregulated in activated glial cells during neuroinflammation. The first multimodal imaging of microglia activity has been reported by Zinnhardt et al, in 2015.[65] They used µCT for anatomic information, µMRI for identify stroke location and volume and they combined these images with µPET, and µSPECT images to evaluate the temporal and spatial evolution of activated microglia in mouse models of transient cerebral ischemia.

In clinical practice or in pre-clinical research, gadolinium-enhanced MRI is routinely used for BBB integrity imaging. Gadolinium chelates do not cross the intact BBB, while, these contrast agents are small enough to cross a leaky (compromised) BBB by passive diffusion (extravasation) into the parenchyma, which is detected in T1-weighted MRI observations.[66]

Studying infiltration of immune cells into the ischemic area with PET or SPECT is limited, because the difficulty to distinguish intraparenchymal and intravascular cellular locations. Similarly, Gd-chelates do not allow to discriminate inflamed from non-inflamed lesional areas with MRI. In 1990, Weissleder and co-workers demonstrated, that ultrasmall superparamagnetic iron oxide nanoparticles (USPIO) are taken up by macrophages and suggested their use as cell-specific MRI contrast agents.[67] More than a decade later, Rausch *et al.* first applied USPIO particles in experimental ischemic stroke animal models to study infiltration of circulating monocytes in the ischemic lesion.[68] Due to their efficiency in MRI contrast enhancement and their biocompatibility, several superparamagnetic iron oxide nanoparticles have been developed and first approved by FDA (*e.g.* Resovist, Lumirem, and Feridex), but later, their clinical use has been disrupted, because of the observed side effects, in particular impaired mitochondrial function, generation of ROS and DNA damage were observed. Therefore, currently ferumoxytol (Feraheme), a carboxymethyl dextran coated iron oxide nanoparticle, is the only FDA-approved USPIO, for the treatment of iron deficiency anemia.[69] Another limitation of iron-based MRI contrast agents is that stroke-related endogenous MRI signal sources (*e.g.* edema or microbleeds), may lead to erroneous detection of CA-labeled cells.[70] Furthermore, the strong magnetic susceptibility of iron ions extends the local magnetic field of these nanoparticles, well beyond the actual cell radius (blooming effect).[71]

Besides MRI studies, two-photon imaging of spatiotemporal dynamics of circulating and resident immune cells have also been reported.[72–75] In these studies microglia are labeled with endogenous (eGFP,[74] tdTomato[73]) or intravenously injected fluorescent dyes (CD68[72]).

Inspite of the already acquired knowledge in stroke research, the complex mechanism of brain immune response still remains unclear. Development of more efficient and specific contrast agents and multimodal imaging techniques are necessary for further accumulation of valuable experimental data, which are necessary to improve our understanding in this field.

V – Objectives and outline of the study

The present work is part of a multidisciplinary research project, *Nanobrain* (supported by ANR, the French National Agency for Research), involving scientific expertise in stroke neuroscience, nanotechnology, imaging techniques, organic and biochemistry, seeking to contribute to the understanding of neuroinflammation processes after stroke injury, by multimodal imaging of immune cells and open new routes for the development of stroke therapies.

Probably the most effective way to selectively label immune cells, is binding the imaging probe to the cell surface. The cell surface receptor Mac-1 (also called complement receptor CR3, CD11b/CD18) is a pattern recognition receptor, which is expressed on infiltrating neutrophils, mononuclear phagocytic cells (macrophages) as well as on activated microglia. [76] This receptor is therefore widely used by neuropathologists for inflammation assessment with immunohistology and confocal microscopy. In addition, as Mac-1 binds a broad range of ligand types (in the order of 50), this receptor appears as a good target for labeling the immune cells of interest.

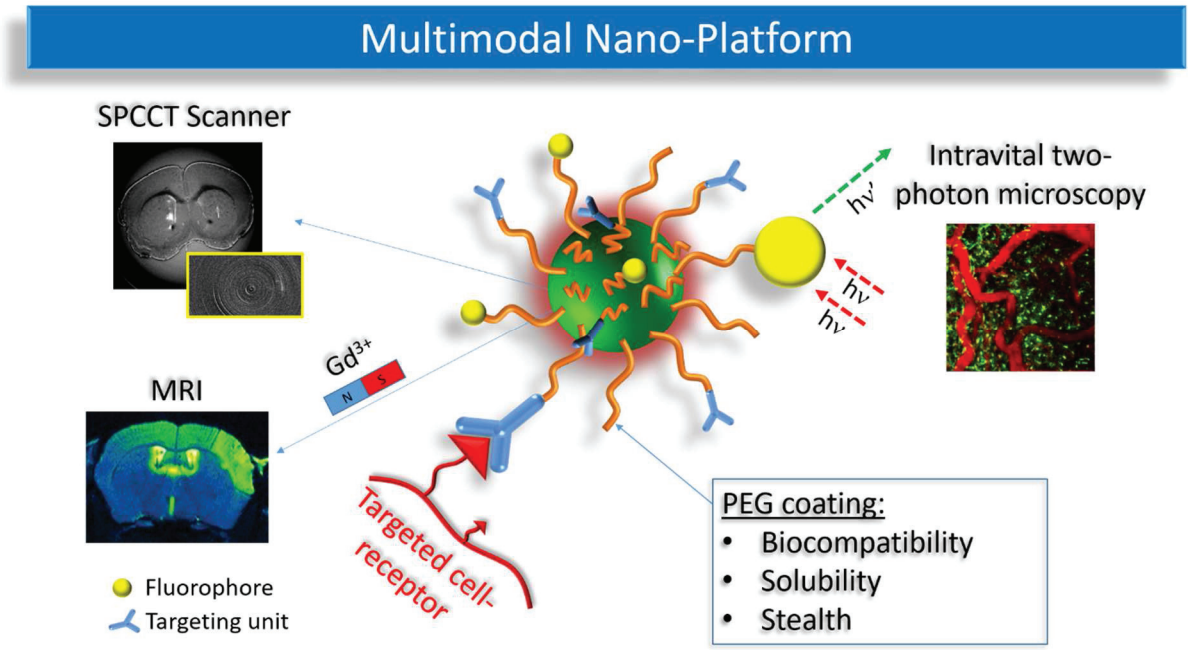

Figure 5 Multimodal GdF_3 nanoparticle-based contrast agent

This thesis work aims at providing an innovative nanoprobe to visualize immune cells in neuroinflammation by three imaging techniques, namely MRI, CT and intravital (two photon) microscopy. The first challenge in the design of such a multimodal nanoparticle for brain

imaging is the accumulation of the contrast agent in the brain parenchyma. BBB limited path and clearance through distribution, metabolism and excretion processes reduce significantly the available particles for cell labeling in the brain. This can be overcome by increasing the injected CA dose; however, it also increases the risk to induce undesirable side effects. Instead, the probe itself has to be optimized to be less recognizable by the reticuloendothelial system and more easily delivered to the brain. By modifying the surface with PEG, stealth particles are obtained, which circulate longer in blood, increasing the probability for their accumulation in the brain. Size also has to be optimized: brain uptake is inversely proportional to particle radius,[77] therefore smaller nanoparticles are preferred, but too small particles, as it was previously mentioned, are rapidly eliminated from the blood. The particles should be stable, non-aggregating in physiological media and has to be non-toxic. In addition to its optimized physico-chemical properties, the nanoparticle, as a multimodal probe, should enhance contrast in MRI, CT and two-photon microscopy.

In this thesis an efficient brain imaging probe fulfilling previously enumerated requirements was designed, fully characterized and applied for pilot *in vivo* biological experiments. Following this first chapter of introduction, Chapter 2, describes the synthesis and physico-chemical characterization of the optimized inorganic core (GdF_3) of the nanoprobe. Radiopaque and highly paramagnetic core containing a multitude of gadolinium ions, is expected to induce significant contrast enhancement in MRI and CT.

In Chapter 3 surface modifications of the nanoobject are presented. PEG coating with strong anchoring and optimized ligand density provide stealth, solubility and colloidal stability to the probe. The nanoparticle is also equipped with a fluorescent molecule, specially elaborated for two-photon imaging. Jensen *et al.* demonstrated the ability of simvastatin to target the receptor CR3 (Mac-1) in the pro-inflammatory conformation.[78] On the basis of this study, the parent compound of simvastatin (lovastatin) has been selected and tentatively coupled to the particle for the specific targeting of Mac-1 receptor.

Finally, Chapter 4 covers biological evaluations, such as cytotoxicity or biodistribution and preclinical *in vivo* imaging results of the multimodal hybrid nanoparticle.

CHAPTER 2

LnF_3 Nanoparticles: Synthesis and Characterization

Content

I – Introduction to nanoparticle synthesis and characterization

The noted physicist Richard Feynman delivered a very famous lecture at the annual American Physical Society meeting at Caltech (December 29, 1959), which is often considered as the genesis of the modern field of nanotechnology.[79] In his visionary lecture entitled "There's plenty of room at the bottom", he predicted that conception of nanosized objects would open the route for many technological developments and launch new fields of research. He imagined that in the future, we will be able to manipulate matter atom by atom to construct an object. However, this brilliant physicist was also aware of the difficulties of fabricating at such a small scale. Today, based on a huge number of trial-and-error experiments, scientists elaborate different nanoparticles with controlled size and morphology, but to date, no theoretical model exists, which would provide a deep understanding of the mechanism of nanoparticle (NP) formation.[80]

I.1 – Inorganic nanoparticle nucleation and growth

Based on the classical nucleation theory (CNT) developed by Becker and Döring[81] in the 1930s, LaMer and Dinegar[82,83] proposed a model in the 1950s, for the mechanism of formation of colloidal particles, which is to date still considered as the basic model in most nanoparticle synthesis. The fundamental idea of this theory is the separation of nucleation and growth processes in two distinct stages. ***Figure 6*** shows the precursor (or monomer) concentration variation in time. In stage I the precursor (*e.g.* $GdCl_3 \cdot H_2O$ in the case of GdF_3 nanoparticles, which will be discussed later on) is solubilized and its concentration increases in the solution, until a threshold concentration is reached. At this concentration the solution is in the supersaturated state (unstable zone in ***Figure 7***), which induces a spontaneous nucleation in stage II. Upon nuclei formation, the concentration of monomer decreases and when it falls under the critical concentration (C_{min}), nucleation stops. Stable nuclei start to grow (stage III) by chemical attachment of monomers on the surface of the particles. Growing process continues until the concentration lowers to the solubility of the constituents, where the solid particles precipitate. It is evident, that nucleation and growth kinetics depends on the supersaturation of the solution and determines size and crystal phase of each crystalline region. Upon rapid evaporation of the solvent, supersaturation is reached rapidly and at a higher temperature, which

results in small crystallites. However, if evaporation and/or cooling is slow, larger particles can grow.

Figure 7 shows the evolution of the concentration during these processes for two different polymorphs of the clusters. When the solution is cooled down to induce supersaturation (unstable zone, the concentration is between C_{max}, the maximum supersaturation and C_{min}), nucleation occurs. Nucleation decreases the concentration rapidly to the point A for the crystal form **1** and to point C for the form **2**.

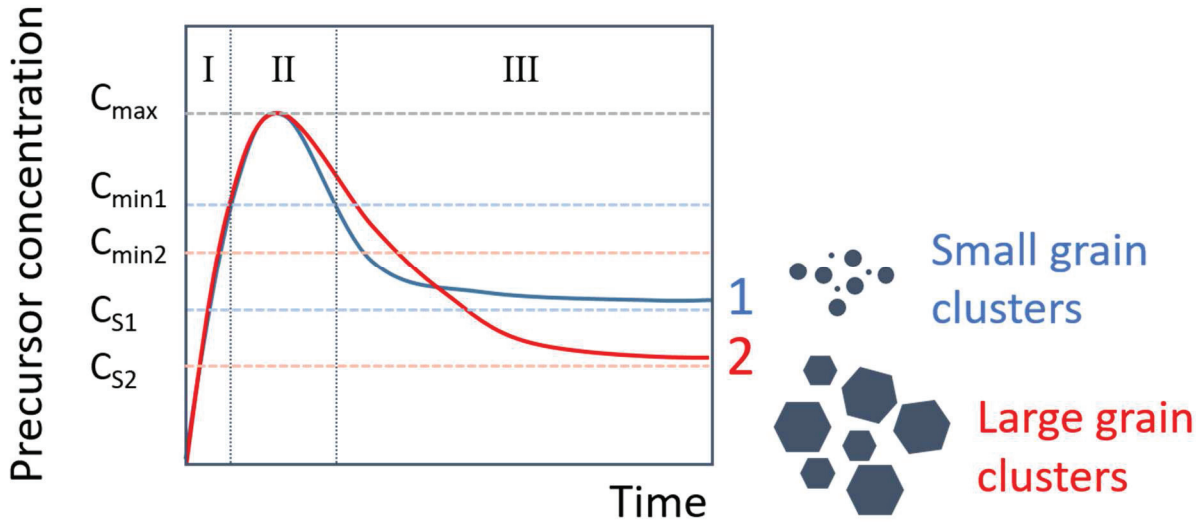

Figure 6 LaMer diagram of nanoparticle formation, showing the concentration of precursor in the reaction medium as a function of time. Stage I: precursor solubilization or injection. Stage II: Burst nucleation. Stage III: growth. C_{max} is the supersaturation limit; $C_{S\,i}$ and $C_{min\,i}$ are solubility and critical supersaturation values for compound i. Figure adapted from ref. [84]

The concentration crosses the supersaturation curve, and the system becomes metastable, inducing growth of particles. The concentration of monomers in the solution continues to decrease, until points B and D for form **1** and **2**, respectively, which are on the solubility curve. Solubility curve is the limit where solid crystalline particles precipitate out from the solution. As form **1** has higher solubility value (C_{S1}), than form **2**, form **1** is less stable (*i.e.,* more soluble). In the LaMer diagram (***Figure 6***), nucleation and growth of form **1** are qualitatively described by the blue curve, which leads to small grain size clusters and form **2** (red curve) corresponds to the formation of large grain clusters, with a lower growth rate.

Nucleation is the localized formation of a new thermodynamic phase (*e.g.,* solid in liquid phase) which may be homogeneous or heterogeneous. Homogeneous nucleation is a stepwise sequence of bimolecular additions of monomers until a critical size is reached. It happens spontaneously

and homogeneously throughout the supersaturated solution. Conversely, heterogeneous nucleation occurs at structural heterogeneities (impurities, bubbles, the surface of the container, etc.). Phase boundaries of these heterogeneities decrease the activation energy barrier of nucleation; therefore, heterogeneous nucleation happens with more probability in the case of solid formation in the liquid phase.

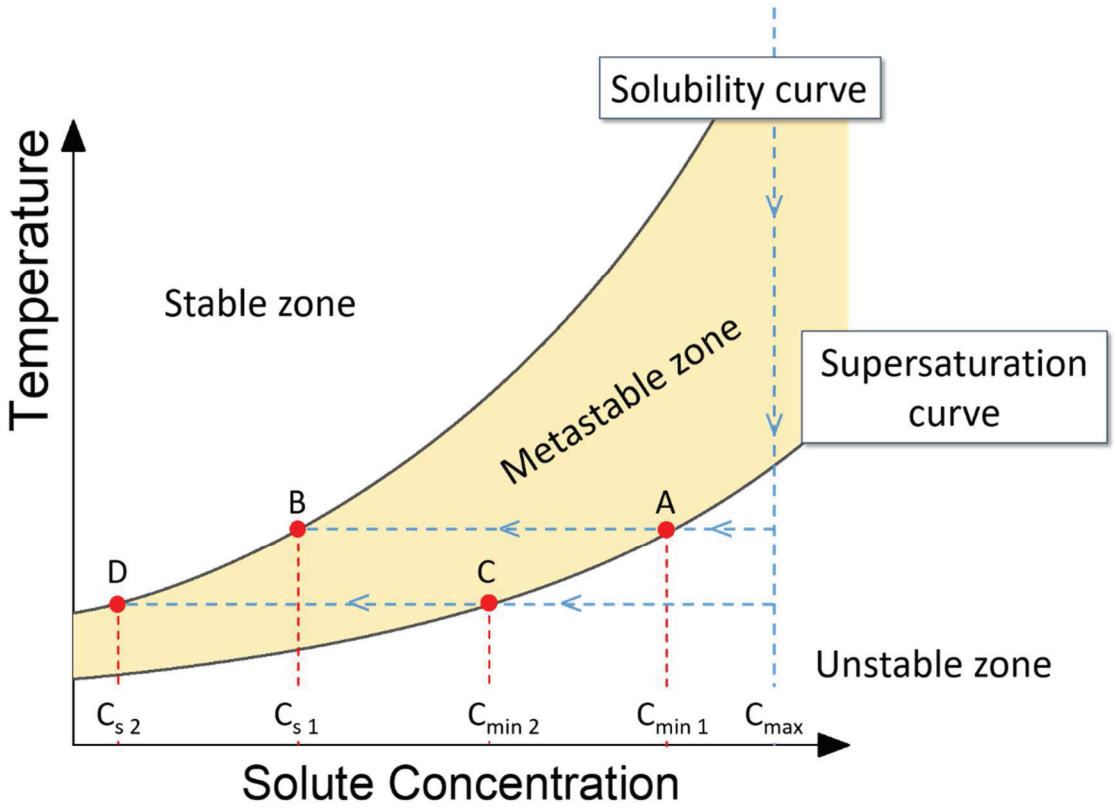

Figure 7 Schematic temperature-concentration phase diagram of solid phase formation in a liquid. In the stable zone, no nucleation or growth can occur. Crystals can nucleate in the unstable zone and growth occurs in the metastable zone, delimited by solubility and supersaturation curves. Figure adapted from ref. [85]

The existence of a critical size for nuclei to survive and to start to grow is easily understood by the thermodynamic description of nucleation. Formation of a particle depends on its total free energy (ΔG). This energy is composed of a term related to surface energy, γ(*i.e.,* the amount of energy that is required to produce an interface per unit area of the interface) and the bulk free energy, ΔG_{bulk} (the energy of stabilization due to crystal formation). For a spherical particle of radius r, ΔG is given by the following expression:

Equation 4

$$\Delta G = 4\pi r^2 \gamma + \frac{4}{3}\pi r^3 \Delta G_{bulk}$$

where ΔG_{bulk} depends on the temperature (T), Boltzmann constant (k_B), supersaturation (S) of the solution, and its molar volume (v):

Equation 5

$$\Delta G_{bulk} = -\frac{k_B T}{v}\mathrm{Ln}(S)$$

The surface energy is always positive, and bulk free energy is always negative; therefore, their sum, ΔG, passes through a maximum, where its derivative is zero:

Equation 6

$$\frac{d\Delta G(r)}{dr} = 0$$

If *Equation 4* and *Equation 6* are combined, the radius at this maximum can be calculated and is given by the following expression:

Equation 7

$$r_c = -\frac{2\gamma}{\Delta G_{bulk}(r_c)} = -\frac{2\gamma}{\Delta G^*(r_c)}$$

The value of ΔG at the critical radius r_c, represents the activation barrier of nucleus formation. ***Figure 8*** shows the evolution of γ, ΔG_{bulk} and ΔG functions with the particle radius. Let us consider the two crystal forms (**1** and **2**) as previously. The free energy required for form **1** to nucleate is lower than for form **2**; therefore, it forms more easily, and its critical radius is also smaller. That means that the form with a higher initial supersaturation (*i.e.,* a large number of nucleation sites) will favor the formation of a large number of small-sized nuclei (see also blue and red curves in ***Figure 6***).

Besides, the evolution of ΔG tells us that the higher is the temperature, the higher is the energy barrier and the critical radius. Consequently, at high temperatures, the energy barrier is so important (dominated by the surface energy), that no stable nuclei are formed. This corresponds to a non-saturated state (see also ***Figure 7***). Further details of mathematical description are given in the comprehensive review of Thanh *et al.*[86]

According to LaMer theory, once the critical radius is achieved, the nucleus can start to grow, which will strongly determine the shape of the final nanoparticle. Classically, growth may be governed by two mechanisms: surface reactions and precursor diffusion to the surface.

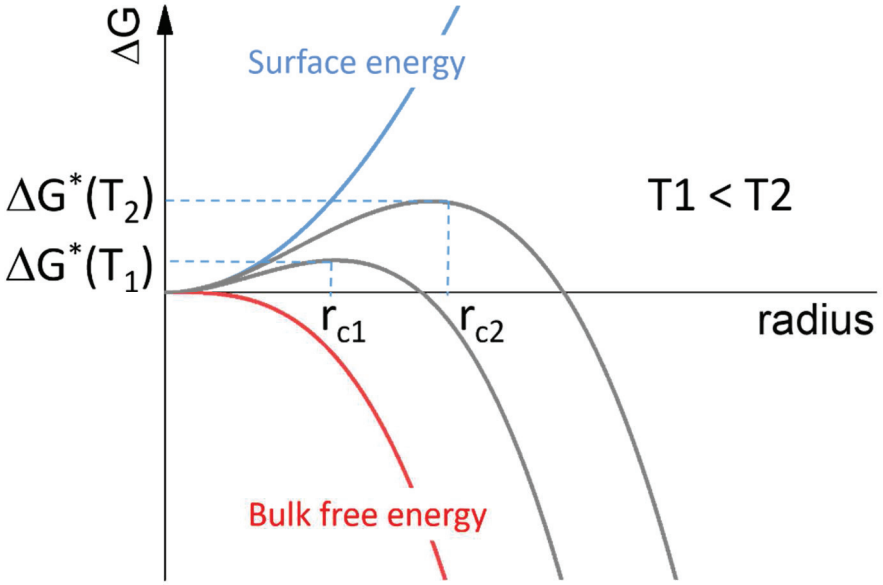

Figure 8 Total free energy change versus cluster size is a combination of solid-liquid interfacial energy (surface energy, destabilizes the nuclei) and bulk free energy. $\Delta G^*(T_i)$ is the total free energy corresponding to the critical radius, r_{ci}. For $r < r_{ci}$.nuclei dissolve and for $r > r_{ci}$.nuclei are stable. Figure adapted from ref. [86].

When diffusion is the slowest step (diffusion limited growth), growth is essentially controlled by the probability of the monomers to reach the cluster. In such growth, the collision of small particles (or nuclei) due to Brownian motion, is a rare event, so that the structure grows one particle by one particle, rather than by chunks of particles. This phenomenon called diffusion-limited monomer-cluster aggregation (DLMCA) was theoretically described by Witten and Sander (1983).[87] Furthermore, on probabilistic bases, one can easily understand, that a monomer approaching cluster surface will stick preferentially to a particle which has only one neighbor (***Figure 9***). This results in loosely aggregated dendritic clusters, without crystallographic symmetry.[88] Diffusion-controlled growth is induced under a low degree of supersaturation, for example, at low monomer concentration or high viscosity.

In the other limiting case, the rate determining step is the monomer reaction at the particle surface, which is referred to as reaction limited or kinetic-limited growth. In this case, the monomer diffuses very fast to the particle surface, and then it has time to find the energetically favorable position before attachment. This mechanism results in flat surfaces (***Figure 9***).

Grown particles undergo subsequent coarsening phase. Ostwald[89] described in 1900 ripening of colloidal particles, which was later theoretically described by Lifshitz and Slyozov[90] and Wagner (LSW theory).[91] The driving force for this process is the decrease in surface energy of the solid phase. The solubility of the particles is size-dependent, and due to a higher surface to volume ratio, small particles are less stable and dissolve, while larger ones grow. Another ripening process has been described by Lee *et al.*[92]. In this model, the larger particles dissolve, and smaller particles grow. This phenomenon is the so-called digestive ripening. Both mechanisms predict a narrowing of size distribution in colloidal solution.

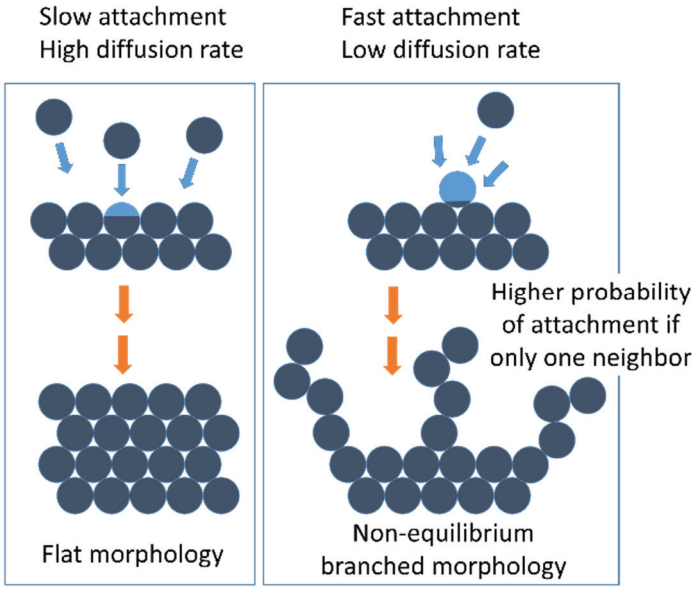

Figure 9 Schematic representation of kinetically and diffusion-controlled growth. In kinetically controlled growth, the attachment (surface reaction) is slow compared to diffusion, *i.e.,* the incoming particle has time to diffuse on the surface, before its attachment. In diffusion-controlled situation, the slowly diffusing particle attachment is instantaneous, as soon as it comes into contact with the surface. Branching structure forms as particles are more likely to hit or attach to outer portions of the structure.

As prepared particles may also coalesce, *i.e.,* two particles merge during contact to give one single particle. Oriented attachment is a very similar process, but the two particles are preferentially oriented along a common crystallographic alignment and are converted to single crystals by interface fusion.[93–95]

I.2 – Synthesis methods

In the previous section, the mechanism of formation of nanoparticles were briefly reviewed. In the following part, common synthesis methods are introduced. Two basic approaches exist for NP synthesis. One consists of dividing the bulk matter into smaller and smaller parts with physical methods until NP size is obtained. This is the so-called top-down approach. Some

commonly used physical methods are high energy ball milling, ion or plasma etching, and electron-beam lithography. Oppositely, in the bottom-up approach, atoms, molecules or ions are assembled to give clusters, which grow to nanoparticles. This approach is characterizing chemical and biological methods. Solvothermal or hydrothermal, sol-gel, co-precipitation, microemulsion, and polyol techniques are some of the most commonly used chemical routes. Microorganism assisted biogenesis, bio-templating, and plant extracts assisted biogenesis are some examples of biological bottom-up NP synthesis. These methods are described in more details, for example, in the comprehensive overview of Dhand *et al.*[96]

In this work, the particles are elaborated by solvothermal or hydrothermal methods. The general principle of all solvothermal techniques is growing crystalline particles from a non-aqueous solution, under moderate to high pressure (1 to 10^4 atm) and temperature (100 to 1000°C). This is achieved by using an autoclave, a thick-walled steel vessel, equipped with an inner Teflon-lined reactor chamber, specially designed for resisting high temperature and pressure. The reactants are dissolved in the appropriate solvent, which often plays the role of capping agent and stabilizes the particle surface. The solution is transferred to the Teflon liner inside the autoclave and after a careful sealing, the whole apparatus is placed in a laboratory drying oven. Usually magnetic stirring is used during the heating process. Hydrothermal synthetic process is based on the same principle, but water is used as the solvent.

In solvo/hydrothermal synthesis temperature, heating rate, pressure and reaction time are important parameters, which have to be optimized. The temperature is set higher than the boiling temperature of the solvent, creating superheated conditions, which enhances chemical reactivity and kinetics. The final product obtained in that conditions are highly crystalline.

I.3 – Characterization techniques

After the synthetic process, the prepared nanoparticles need to be characterized. Size, morphology, and surface state are fundamental characteristics of NPs, which are determined by the combination of several analytic techniques. Average hydrodynamic size is determined by dynamic light scattering (DLS) measurements. Transmission electron microscopy (TEM) or in case of large nanoparticles, scanning electron microscopy (SEM) observations show size and morphology of particles. For hybrid nanoparticles (*e.g.,* inorganic core and organic shell), the overall organic and inorganic content is determined by thermogravimetric analysis (TGA). The inorganic core crystallinity is characterized by X-ray diffraction (XRD) techniques. Nature and

coordination mode of organic ligands on the surface are being studied by Attenuated Total Reflectance Fourier Transformed Infrared spectroscopy (ATR-FTIR) and X-ray photoelectron spectroscopy (XPS). If the organic layer has some optical properties, NPs are also characterized by absorption and fluorescence spectroscopy. In the present section, these techniques will be briefly overviewed.

I.3.1 Techniques based on light-matter interactions

When light propagates and interacts with matter, different phenomena may occur depending on the optical properties of the material and characteristics of the light source. Wave description of light (classic electromagnetic theory) can explain different *scattering* phenomena, while its particle nature explains *absorption* and *emission*. When light passes through a medium without interacting, we are talking about *transmission*. Each interaction discloses some specific properties of the matter, therefore, by applying different light sources (different energy, *i.e.,* wavelength range) on the matter, different types of information can be obtained on the chemical composition or the electronic structure of the material under investigation. The techniques based on the study of light-matter interactions are called *spectroscopies*.

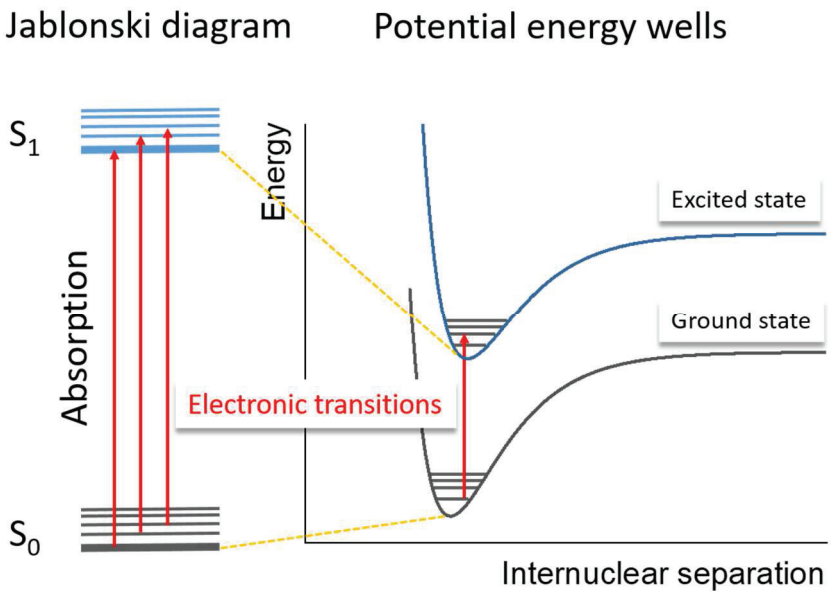

Figure 10 Correlation between diatomic potential energy surface and Jablonski diagram. Electronic ground state, S0 is represented by the yellow potential energy curve. Upon absorption, an electronic transition brings the system in the first excited state, S1. Vibrational energy levels at each electronic state are represented by thinner lines.

Through light-matter interactions, it is possible to probe the energy levels of a given molecule. The mathematical relationship between these energy states of a molecule and its geometry

defines a surface called the adiabatic potential energy surface of an electronic state. The idea behind that is that each structure (geometry) is associated with a unique energy. A Polish physicist, Alexander Jablonski proposed in 1933[97] a schematic representation of the electronic levels of molecules and transitions between these levels.

Figure 10 shows the correlation between potential energy surfaces and their representation in Jablonski diagram for a diatomic molecule. S_0 denotes the lowest electronic energy level, called the ground state and S_1 is the first excited state of the molecule.

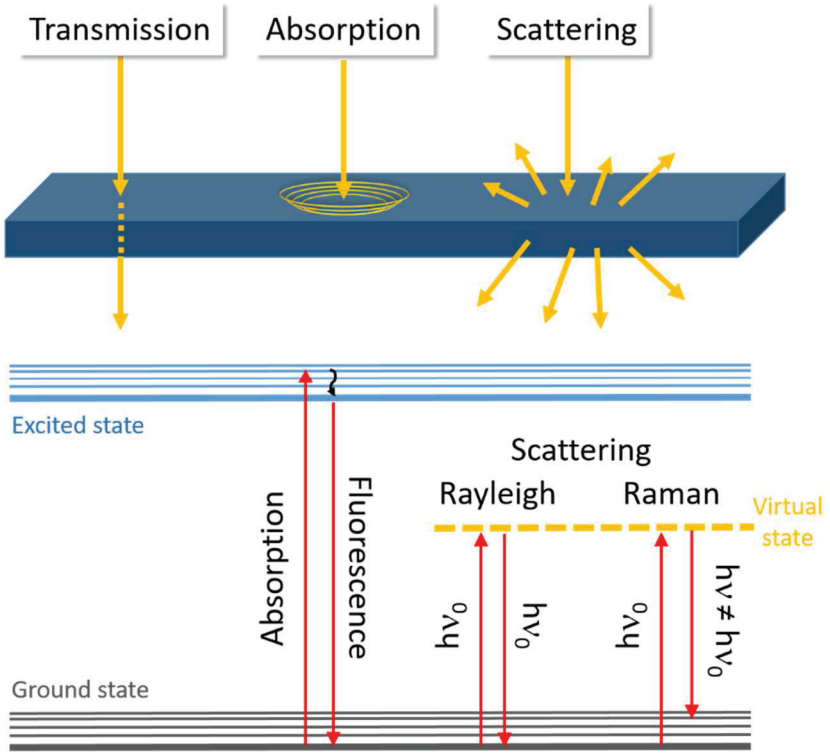

Figure 11 Principal interactions of light with matter.

The sub-levels represent the different vibrational states of the molecule. Absorption and fluorescence spectroscopy techniques probe transitions between the electronic levels and infrared (IR) spectroscopy gives information on vibrational states of a molecule. The energy gap between S_0 and S_1 is approximately two orders of magnitude higher than the gap between vibrational levels. In the following paragraphs, the possible light-matter interactions (***Figure 11***) are briefly reviewed in the aim of introducing some useful concepts for later discussion of results.

Transmission. If a light beam passes through a matter without any interaction, then incident and transmitted radiations are identical. When measuring the transmittance T of a sample, it gives the ratio of transmitted (I) to incident light intensity (I_0).

Equation 8

$$T = \frac{I}{I_0}$$

Scattering. When electromagnetic wave (light) propagating through matter, interacts with molecules, it locally perturbs their spatial charge distribution, causing small geometrical changes in their structure. The energy absorbed from light excites electrons of the absorbing species to a short-lived, high energy state (called "virtual state", see ***Figure 11***), which is in between the electric ground state and excited states. The disturbed charge distribution creates an induced electric dipole moment, which oscillates following the time-modulation of the incident electric wave vector. In a homogeneous medium, the dipoles cancel each other, except in the forward direction, but it is not the case when inhomogeneities (nanoparticles in our case) are present.

According to the laws of electromagnetism, an induced oscillating dipole acts as an emitter of electromagnetic wave, the scattered wave. In terms of particulate nature of light, when the kinetic energy of the reradiated photon is the same as the incident one, the scattering is called *elastic* (*e.g.,* Rayleigh scattering) and if the kinetic energy is not conserved, the scattering is *inelastic* (*e.g.,* Raman scattering).

Nanoparticles in suspension are constantly experiencing a random motion due to thermal density fluctuations of the solvent (Brownian motion). This movement modulates through Doppler effect, the scattered photon energy by a small difference. Therefore, in a colloidal solution, the light that strikes moving particles is experiencing a *quasi-elastic scattering*. Dynamic Light Scattering technique, also known as *Quasi-Elastic Light Scattering* (or *Photon Correlation spectroscopy*) uses this Doppler effect to extract information about particle size.

When considering a set of particles at fixed positions, the light scattered on one particle will interfere with scattered light coming from the other particles. This induces an interference pattern. When the particles are subjected to Brownian motion, the observed interference pattern at a given angle results in intensity changes over time (***Figure 12***). Meanwhile, velocity of particles depends on their size: smaller particles are moving rapidly, while bigger ones are

slower. Therefore, the scattered light intensity fluctuates accordingly to the size of the particles. This ability to move more or less rapidly is characterized by the translational diffusion coefficient, D_t.

To quantify intensity fluctuations in DLS experiments, the measured intensity at a time t is compared by itself, at a time $t+\Delta t$. Mathematically this is translated into the so-called autocorrelation function (ACF), which consists in the multiplication of the time-dependent intensity ($I(t)$) by itself after a small time shift of Δt and these products are averaged over the total measurement time: ACF = $< I(t)\ I(t+\Delta t)>/< I(t)^2>$. The time lapse Δt is called the correlation time, $\tau = \Delta t$. The ACF is related to the probability to find a particle at time $t+\Delta t$ in the same position than at time t. Therefore, if the time lapse is small, the particles do not have time to change their relative positions, the correlation is high, and by increasing Δt, this correlation decreases. After Fourier transformation, the correlogram is plotted against τ, results in a decay function, as shown in ***Figure 12***. The correlogram is then fitted to a mathematical model, resulting in a distribution of translational diffusion coefficients.

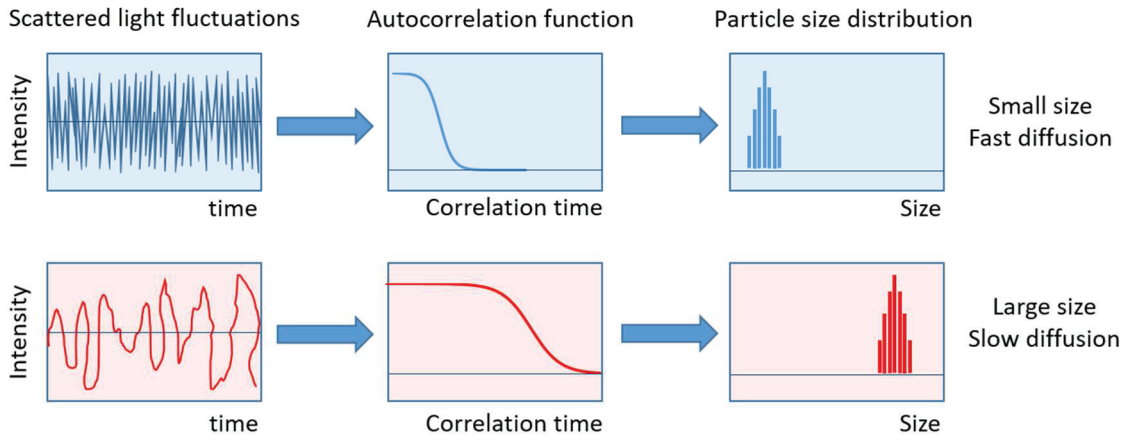

Figure 12. Dynamic Light Scattering principle. The measured light intensity is transformed into a so-called autocorrelation function (ACF), and the particle size distribution is derived. Larger particles move slower, resulting in a longer correlation time. Figure adapted from Otsuka Electronics website.[98]

For monodisperse samples, the correlation function is fitted to a single exponential decay and a single value, the mean value of translational diffusion coefficient D_t is derived, which is proportional to the lifetime of the exponential decay. This can be converted to a mean intensity value, *i.e.,* a mean size called *z-average* size. This fitting algorithm is the so-called cumulant analysis, developed by Koppel in 1972.[99]

For polydisperse (large distribution) or multi-modal (two or more distributions) particles, multi-exponential fitting algorithms (*e.g.,* CONTIN developed by Provencher in 1982[100]) are employed.

The size of perfectly spherical particles can be described with a single number, the radius or diameter. However, most of real particles are not perfectly spherical; therefore, an accurate description of their size would be a very complex problem. Hence, many size determination techniques, like DLS, are based on the convenient assumption that the particles are spherical. Thus, the reported size value is the radius or diameter of an equivalent sphere. (Usually, this assumption results in a good approximation of the size, except for particles with a very large aspect ratio, such as fibers.) In DLS experiments, this hypothetical sphere is a hard sphere that diffuses with the same speed as the particle under examination. The Stokes-Einstein equation (*Equation 9*) gives the relationship between D_t and the hydrodynamic radius (R_H) of the scattering particle, provided, that the temperature T and solvent viscosity η are known (k_B=1.38064852 × 10^{-23} J/K is the Boltzmann constant).

Equation 9

$$D_t = \frac{k_B T}{6\pi\eta R_H}$$

Translational diffusion of the particle depends on its surface structure, which means that any surface modification affects its diffusion speed and its apparent size. For example, if a polymer is lying flat on the surface of the particle, the apparent size will not change significantly compared to the case, when the same polymer chain anchored to the particle floats in the solvent and slows down the particle diffusion, correspondingly increasing the apparent size of the whole object.[101]

As mentioned before, the mathematical analysis of the correlogram results in a distribution of translational diffusion coefficient values, which, combined with the Stokes-Einstein equation (*Equation 9*) leads to a distribution of sizes. As intensities are measured, the first order information on sizes is a plot of relative intensity scattered by particles in different size bins. This plot is called the *intensity weighted size distribution*. If the distribution is a single (monomodal) and relatively sharp peak, the particles are monodispersed, and the mean size is given by the z-average size (cumulants fit), and the size distribution width defines the polydispersity index (PDI). A sample with PDI ≤ 0.1 is considered highly monodisperse, PDI values of 0.1-0.4 and > 0.4 correspond to moderately and highly polydisperse samples, respectively. For multimodal

or polydisperse samples CONTIN algorithm is adapted: the fit of the correlation function gives size distribution with the average size for every peak, as well as their width.

In the Rayleigh approximation, the scattering intensity is proportional to the 6^{th} power of the particle radius. Therefore, intensity distribution emphasizes larger particles. For this reason, a more realistic view of size distribution is provided if the intensity weighted size distribution is also converted (using Mie theory) into volume and number weighted size distributions. In a *volume-weighted distribution*, the contribution of each particle relates to its volume, *i.e.,* the relative contribution is proportional to the 3^{rd} power of the radius. In other words, the higher peak value in a volume distribution gives the size of particles, which represent the higher volume of the totality of the scattering particles. *Number weighted distribution* is very often compared to the size distribution obtained by image analysis (*e.g.,* transmission electron microscopy). A peak in this representation shows the size of the particles, which are present in the majority.

Absorption. Let us consider light as a particle. When a photon passes through matter if its energy is higher or equal to the available energy states of the molecules, it is absorbed, and the photon disappears. The energy gain promotes an electron of the absorbing species from the ground state orbital to a higher state orbital. In this case, the absorbing molecule is in a "real" electronic excited state. Electronic transitions are characteristic for a molecule and are routinely used for analytical purposes in the ultraviolet (UV)–visible absorption spectroscopy. The *absorbance* (A) of a sample defined as the ratio of absorbed radiant power to incident radiant power measures the *light attenuation* by the sample. Absorbance is obtained from the measured transmittance (absorption spectroscopy). In a reasonable concentration range (typical validity range in absorbance: 0.1<A<1.0) valid Beer-Lambert law (***Equation 10***) describes the linear relationship that exists between absorbance and concentration of the absorbing species.

Equation 10

$$A = -log\frac{I}{I_0} = -\log T = \varepsilon \cdot c \cdot x$$

I_0, I: the intensity of the beam before and after passing through the sample;
ε: molar extinction coefficient (SI unit: $m^2\ mol^{-1}$, unit in practice: $M^{-1}\ cm^{-1}$);
c: concentration (mol L^{-1});
x: path length of the measuring beam in the sample (cm)

By making a dilution series of a molecule and measuring absorbance values for each concentration, one can determine its molar extinction coefficient (ε), which is simply the slope

of the *A* vs. *c* plot. Molar extinction coefficient indicates how strongly this species absorbs light at a given wavelength. It depends on chemical composition, the chemical structure of a chemical species and can vary with solution conditions, like ionic strength, pH, temperature, *etc*. Alternatively, the concentration of the known extinction coefficient molecule can be determined by simply measuring its absorbance.

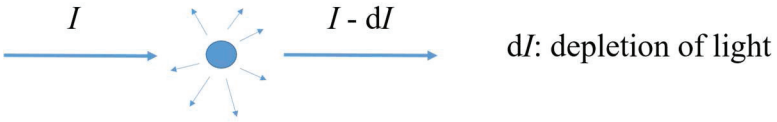

Figure 13 Light attenuation in the matter. The incident light of intensity I is attenuated by dI after interaction with matter.

For colloidal systems, like nanoparticle suspensions, absorption and scattering may occur at the same time. In that case, the measured light attenuation (absorbance) is the combination of these two contributions and is known as *total extinction*. The beam attenuation described by ***Equation 11*** depends on the number of entities scattering (N_s) and absorbing (N_a) the light, and the probability of a photon being scattered (scattering cross-section: σ_s) or absorbed (absorption cross-section: σ_a):

Equation 11

$$\begin{aligned} \mathrm{d}I &= (I \cdot N_s \cdot \sigma_s)\mathrm{d}x + (I \cdot N_a \cdot \sigma_a)\mathrm{d}x \\ &= I(N_s \cdot \sigma_s + N_a \cdot \sigma_a)\mathrm{d}x \end{aligned}$$

Symbolically dividing by *I*, gives:

Equation 12

$$\frac{\mathrm{d}I}{I} = (N_s \cdot \sigma_s + N_a \cdot \sigma_a)\mathrm{d}x$$

Integration of ***Equation 12*** gives the following expression:

Equation 13

$$I = I_0 \cdot \mathrm{e}^{-(N_s \cdot \sigma_s + N_a \cdot \sigma_a) \cdot x}$$

Transmittance is then expressed as:

Equation 14

$$T = \frac{I}{I_0} = \mathrm{e}^{-(N_s \cdot \sigma_s + N_a \cdot \sigma_a) \cdot x}$$

By taking the natural logarithm of the expression and dividing it by Ln 10 (≈2.30) the following expression is obtained for absorbance:

Equation 15

$$A = -\log T = -\frac{\ln T}{\ln 10} = \left(\frac{N_s \cdot \sigma_s}{\ln 10} + \frac{N_a \cdot \sigma_a}{\ln 10}\right) x$$

The terms ($N_s \cdot \sigma_s$) and ($N_a \cdot \sigma_a$) are called scattering (μ_s) and absorption (μ_a) coefficients respectively, which can be expressed with the more common units of the molar attenuation coefficients (ε). Assuming that the same species absorb and scatter light (C=C_a=C_s), this transformation leads to an expression for the absorbance, similar to the well-known Beer-Lambert law:

Equation 16

$$A = (\varepsilon_s + \varepsilon_a) \cdot C \cdot x$$

N_s, the number density has an inverse volume dimension (cm^{-3}). It is, therefore, possible to replace it by the mass concentration ($\mu g/cm^3$) C_w of the individual particles divided by m_p, the mass of one particle (µg). Then, by considering only the scattering term, *Equation 15* becomes:

Equation 17

$$A = (\ln 10)^{-1} \cdot \sigma_s \cdot C_w \cdot m_p^{-1} \cdot x$$

This relation shows that by measuring the absorbance of a scattering solution, it is possible to obtain an estimation of the size of one scattering particle. Based on this relation, a tentative calculation of the average mass of one nanoparticle is proposed in section ***II.3 – Scattering of GdF3*** .

When scattering particles have dimensions lower than one-tenth of the wavelength (typically when size < 50 nm for irradiation with light of 500 nm), the scattering cross section σ_s, is described by the Rayleigh approximation. Rayleigh scattering of particles considered as hard spheres of radius R, the scattering cross section is related to their geometry, wavelength (λ) and refractive index n of the matter:

Equation 18

$$\sigma_s = \frac{128\pi^5}{3} \frac{R^6}{\lambda^4} \left(\frac{n^2 - 1}{n^2 + 2}\right)^2$$

This relation shows strong wavelength dependence (λ^{-4}) and even stronger size dependence (R^6) of scattered light.

Fluorescence. Absorption of ultraviolet or visible light (wavelength range from 200 to 800 nm) leads to electronic excitation of the absorbing molecule. Following absorption, the molecule returns to its ground state by a de-excitation process. The energy restitution may happen through *radiative* (transition leading to the emission of a photon) or *non-radiative* (no photon emission) pathways. An example of a non-radiative process is vibrational relaxation, which happens the excess energy is transferred from the excited molecule to its environment by collision with other molecules (typically solvent molecules). This relaxation may occur when the molecule is in its electrical ground state and only vibrationally excited, but it also occurs in the electronic excited states. Radiative relaxations are usually preceded and/or followed by vibrational relaxation and as stated by Kasha,[102] photon emission occurs from the lowest energy vibrational state of S_1. The emission itself is as fast as the absorption ($\approx 10^{-15}$ s), but the molecule stays in the S_1 excited state for a certain time. Here we consider only fluorescence (relaxation of the molecule from the singlet excited state to the singlet ground state with the emission of light) as radiative decay. Therefore, when measuring the fluorescence of a compound, the detected light comes with a time delay after the absorption.

Let us consider a molecular species M in solution, whose concentration is [M]. By absorbing light, a certain number of these molecules are excited to the state S_1, then these molecules return to the ground state, S_0, either by radiative or by non-radiative mechanisms. The rate of disappearance of the excited molecules may be described by the same kinetic approach as radioactive decay.

Equation 19

$$-\frac{d[M^*]}{dt} = (k_r + k_{nr}) \cdot [M^*]$$

The overall decay rate (k) is composed of two terms; one is relative to the radiative process (k_r) and another relative to non-radiative processes (k_{nr}). By integrating this equation, the time evolution of excited molecules is obtained as an exponential decay, with an initial concentration of the excited molecules denoted as $[M^*]_0$.

Equation 20

$$[M^*] = [M^*]_0 exp\left(-\frac{t}{\tau}\right)$$

The constant τ=1/(k_r+k_{nr}), called *excited state lifetime* is the average time the molecule spends in the excited state before return to the ground state. The efficiency of fluorescence emission compared to absorption is given by the fluorescence quantum yield, Φ_f. The precise definition of Φ_f is the number of emitted photons relative to the number of absorbed photons. For fluorophores with a quantum yield close to unity, fluorescence emission dominates all other de-excitation processes, and if a molecule has low quantum yield, the most absorbed energy is lost by thermal effects. *The intensity of fluorescence emission* defined as the number of photons emitted per unit time and per unit volume of solution is proportional to the instantaneous concentration of molecules still excited. However, the *measured fluorescence intensity* is modulated by a proportionality factor depending on instrumental conditions. Consequently, fluorescence intensity is obtained on an arbitrary scale (*i.e.,* in arbitrary units). The plot of measured fluorescence intensity *vs.* emission wavelength is called the fluorescence emission spectrum of the fluorophore.

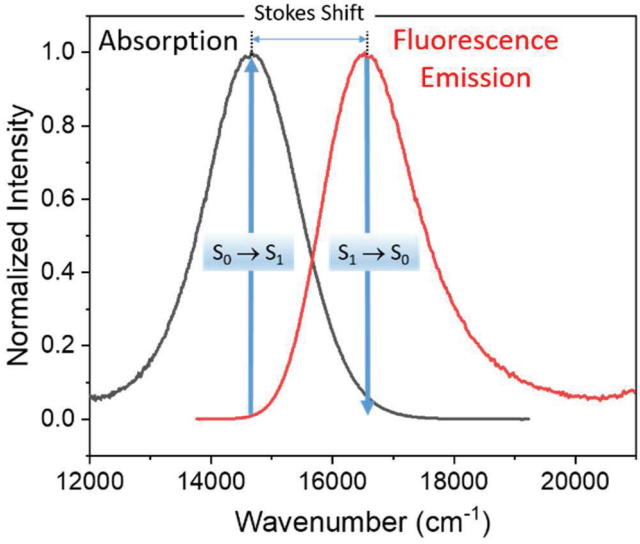

Figure 14 Absorption and Fluorescence Emission spectra: Mirror Image rule; Stokes shift is the difference of their maxima.

According to Kasha's rule mentioned previously, the emission spectrum is independent of the excitation wavelength and is the mirror image of the absorption corresponding to the $S_0 \rightarrow S_1$ transition (***Figure 14***). Upon absorption, the molecule is usually excited to a higher energy excitation level of the electronic excited state S_1. The excess vibrational energy is transferred

to the environment (by heat transfer or solvent reorganization processes). This implies that the fluorescence emission occurs at higher photon energies (longer wavelengths or shorter wavenumbers) than absorption. The distance between the absorption maximum and fluorescence emission maximum corresponding to the same transition the *Stokes shift.* In Chapter 3, we will see that large Stokes shift is of key importance in the detection of the emitted fluorescence in biological applications.

Emission maximum of a molecule is usually dependent on the environment. The reason is related to the fact that the excited state dipole moment of the molecule interacts with solvent molecules by reorienting their dipoles. In the same time, reorientation or relaxation of surrounding solvent dipoles implies lowering of the excited state of the fluorophore. This effect called solvatochromism is increased with solvent polarity and is also observed in absorption spectra, but fluorescence emission is much more sensitive to the environment of the excited molecule because the emitting molecule is in the already relaxed environment.

For recording the emission spectrum, the excitation wavelength is fixed, and the detection wavelength is changing. However, it is possible to proceed inversely: fix the detection at a specific wavelength (generally the emission maximum) and record fluorescence intensity by scanning the excitation wavelengths. The spectrum obtained by this method is the so-called *excitation spectrum*. In common fluorescent spectroscopy instruments, the light source is a xenon arc lamp that emits radiation in the ultra-violet, visible and near-infrared regions. The emitted intensity of this source is wavelength dependent; therefore, it is necessary to correct excitation spectra for the variation of emission intensity of the lamp by multiplying the spectrum with a correction curve.

Provided that the excitation spectrum is properly corrected, and a single fluorescent species is present in solution, the shape of the excitation spectrum is identical to the shape of the absorption spectrum.[103–105] From an analytical viewpoint this assumption is interesting because it means that by recording the excitation spectrum, it is possible to obtain the absorption spectrum even if the sample is too diluted to acquire a normal absorption spectrum.

I.3.2 Characterization of nanoparticle morphology: TEM

Transmission electron microscopy is a technique using high-velocity electrons as “light” source (typically a tungsten filament or a field emission gun). The electrons are accelerated under vacuum with a high voltage. Typically, an accelerating voltage of 80 kV produces electrons

with a velocity of 150 000 km/second ($1.5 \cdot 10^8$ m/s), which is half the speed of light. The electron beam is focused on the specimen by electromagnetic lenses and metal apertures. When the electrons hit the sample, they interact with the atomic constituents of the observed matter, and transmitted electrons are collected with an electronic imaging device, usually a CCD (charge-coupled device) camera. Primary effect causing contrast in the obtained image is related to the local electron density (atomic number) and sample thickness. However, in crystalline specimens' contrast is also generated by intensity variations due to the interaction of diffracted and transmitted electrons.

I.3.3 Characterization of the composition: XRPD and TGA

X-ray powder diffraction (XRPD) is a rapid analytical method for phase identification of crystalline materials. The X-ray beam interacts with matter, and the periodic array in crystalline samples produces constructive interferences at specific angles. These interferences are related to the interplanar spacing in the crystalline powder according to Bragg's law. Each crystalline phase produces a unique diffraction pattern, which allows identification of the crystal structure. Furthermore, in a mixture of different crystalline compounds, each crystalline phase generates its pattern independently from the other one. The identification of each phase is made by comparing the peaks with a standard pattern, provided by the International Center for Diffraction Data (ICDD).

For hybrid nanoparticles, the proportion of organic and inorganic content is an important information. Thermogravimetric analysis can provide that information, by a precise measure of weight losses (due to dehydration, or decomposition) as a function of temperature. This technique also provides information on the thermal stability of materials. Dehydration, evaporation, desorption, and decomposition are typical weight loss producing processes, that can be monitored.

I.3.4 Surface characterization techniques: ATR and XPS

Attenuated total reflectance Fourier transformed infrared spectroscopy (ATR-FTIR) enables solid or liquid samples to be examined. ATR is an accessory to measure FTIR spectrum at the surface of the material. The typical penetration depth is typical of the order of a few microns (0.5-3 µm). In FTIR spectroscopy, the molecules are excited to a higher vibrational level by absorbing IR light, and this absorption provides a molecular fingerprint of the sample with information about the chemical bonds present in the molecules. With the ATR accessory, IR

light doesn't pass through the sample, but instead an evanescent wave is generated in the ATR crystal (IR transparent material), which penetrates the first layer of the sample surface. The major benefit of this technique is that it doesn't require complex sample preparation.

X-ray photoelectron spectroscopy (XPS) is a very sensitive technique for analysis of surface atoms. Upon irradiation by X-rays, electrons are ejected from the inner shells of atoms (photoelectric effect). The ejected electrons have a kinetic energy characteristic of this atom, therefore by detecting these electrons, the chemical composition at the surface of the sample (analyzed depth is < 10nm, typically 5 nm) can be quantitatively determined (except for H and He atoms, which are not detected). As the kinetic energy of ejected electrons is proportional to the binding energy of the atom to its neighbors, the electronic structure and ionization energies are also determined. XPS measurements in this work were performed by Science et surface, a private and independent laboratory, specialized in surface characterization of materials.

II – Results and discussion

II.1 – Synthesis, and characterization of LnF_3 nanoparticles

II.1.1 - Parameters affecting crystal phase and morphology of LnF_3 NPs

Various wet chemical routes have been described in the literature for the synthesis of binary rare earth fluorides with controlled morphology, phase, and size distribution.[106,107] In a large number of reported works, the authors tried to elucidate the fundamental parameters that determine the final morphology of LnF_3 particles. Some examples of general trends emerged from these works are introduced here in a nutshell.

II.1.1.1. The ionic radius of Ln^{3+} and F^-:Gd^{3+} molar ratio

Mansmann pointed out first, that the crystal phase of LnF_3 compounds depends on the ionic radius of the Ln^{3+} ion and estimated the critical radius ratio, r_{Ln}/r_F for the change from hexagonal (LaF_3) to orthorhombic (YF_3) phase to 0.94.[108] This ratio is between Sm and Eu. Later, Li group performed a systematic study of LnF_3 (Ln = La to Yb, Y) nanoparticles phase, synthesized by the hydrothermal route and distinguished three regions of Ln according to their preferential phase: La-Nd (hexagonal), Sm-Gd (mixed phase) and Tb-Yb (orthorhombic).

Xie *et al.* used thermal co-precipitation method to prepare hexagonal and orthorhombic nanocrystals of LnF_3 and investigated their growth mechanism.[109] They observed the same crystal phase tendency of LnF_3 compounds. Light rare earth elements (La-Eu) form hexagonal phase crystals with spheroidal morphology, while heavier ones grow in an orthorhombic phase, with rhombic nanoplates. For GdF_3 nanoparticles, they also study the effects of the F^-:Gd^{3+} molar ratio on the growth mechanism. Gadolinium is in the middle of the rare earth series and presents both characteristics: with a molar ratio of F^-:Gd^{3+} equals to 3:1, GdF_3 gives a mixture of the two crystal structures (orthorhombic and hexagonal). As the ratio was changed to 1:1, a pure orthorhombic phase was observed, while with a large excess of fluoride ions (9:1), the pure hexagonal phase was detected. As no further phase change occurred during the growth process, Xie *et al.* concluded, that the crystal phase of the final product must be determined during the nucleation stage, and the molar ratio of F^-:Gd^{3+} is one of the parameters, that directs crystalline phase. However, other important parameters are also affecting the phase and morphology of the nanoparticles.

II.1.1.2. Fluoride source

The nature of the fluoride precursor was also observed to be a key factor in the phase and morphology. Zhang and coworkers investigated this effect on europium doped GdF_3 nanoparticles (GdF_3:Eu^{3+}). They performed the synthesis in simple soft chemical conditions (in water and at room temperature) with three different fluoride sources: NaF, NH_4F, and $NaBF_4$. They observed, that NaF and NH_4F resulted in the same orthorhombic phase but with different morphologies, while $NaBF_4$ gave the hexagonal form of GdF_3:Eu^{3+}. They interpreted this phase difference by the fact, that F^- ions are immediately available in the solution for NaF, NH_4F, while slow hydrolysis is necessary for $NaBF_4$. They concluded that the low production of fluoride ions might help the formation of the hexagonal phase. One must notice, however, that both three fluoride precursors were added at the same concentration of 0.015 mol, even if $NaBF_4$ contains more fluoride ions, than the two other ones. Therefore, their molar ratio of F^-:Gd^{3+} was set to 3:1 for NaF, NH_4F, but 12:1 for $NaBF_4$, and as it was previously mentioned, a high molar ratio usually gives hexagonal phase. The morphology difference between the two orthorhombic phases was not discussed.

Ocaña and coworkers[110] synthesized GdF_3:Eu^{3+} NPs and ionic liquid ($BMIMBF_4$) as fluoride reservoir. By heating the reaction mixture at 120°C for 15h, they obtained homogeneous, quasi-

spheroidal morphology nanoparticles, with the hexagonal crystal structure. They also attributed the formation of the less stable crystalline form to the slow release of F^- ions.

Our group developed an original solvothermal synthetic approach to elaborate small size, highly crystalline, water dispersible LnF_3 nanoparticles [Patent FR 0954263 (2009)].[111,112] In this process, an amide-hydrofluoric acid charge-transfer complex is used as F^- precursor. This complex decreases F^- ion release, which allows controlling the growth rate of the particles. This process was transferred to industry, and large scale production is running today by the company MATHYM. (More detailed description is given in the next section.)

II.1.1.3. Viscosity and Temperature

Samanta *et al.*[113] tried to correlate polymorphs of GdF_3 nanocrystals to the reaction temperature and viscosity of reaction medium. They suggested that by tuning the viscosity, the reaction rate can be tuned. They used KF as fluoride source, different water/EG or water/DMSO or water/glycerol mixtures as solvent and reaction temperature varied as well. They obtained a pure orthorhombic phase in water, at 150°C, while by changing the viscosity with the addition of EG (H_2O:EG was 1:1), the hexagonal phase is formed. In the meantime, if the reaction temperature is increased to 200°C, the same reaction mixture with water/EG gives the orthorhombic phase. Further increasing the viscosity by using pure EG as the solvent, the hexagonal phase appears again, even at 200°C. In a mixture of water/DMSO lower reaction temperature (150°C) results in the hexagonal phase, but at 180°C, the orthorhombic crystal is obtained. The water/glycerol mixture and pure DMSO induced the hexagonal phase. The authors concluded, that with increasing the viscosity, the temperature of formation of the thermodynamically more stable form (orthorhombic) increases. They also suggested, that viscosity (and inherently the temperature) controls the rate of release of F^- ions, which explains the observed morphology and phase differences.

Veggel's group[114] operated in mild hydrothermal conditions (75°C), with a F^-:Ln^{3+} molar ratio of 2.25 and observed for lighter rare earth elements (La, Ce, Nd) the formation of the less stable crystalline form, the trigonal structure, and in the case of the heavier salts (Dy, Ho, Er, Yb the cubic form was obtained, but, in this latter case nonstoichiometric compounds ($Na_xLn_yF_z$) appear and no LnF_3 compound was formed. For gadolinium and europium, a mixture of hexagonal and orthorhombic phases is obtained in a percentage ratio of 40:60, respectively. Upon heating to 300°C, this mixture is transformed into a pure orthorhombic phase. The

conclusion of this work was that the growth rate was high, because of the high solubility of the fluoride precursor (NaF) at this temperature (75°C), therefore the kinetically stable product could crystallize.

Passuello *et al.*[115] obtained rod-like orthorhombic phase GdF_3, in the presence of polyethylene glycol, through hydrothermal route. They examined the morphology of the particles prepared in the same conditions, but at different temperatures. They did not observe any morphology change, but the size increased slightly with temperature.

II.1.1.4. Organic additives

Organic additives are often introduced to the reaction mixture containing Ln^{3+} and F^- precursors to stabilize nanoparticles. However, it was largely demonstrated, that their presence is not innocuous for morphology and size of the obtained particles. During the growth step, the organic moieties are adsorbed on the inorganic material, and usually, the different crystallographic facets have not the same surface energy; therefore, the organic molecules adsorb selectively. If one facet is less covered by organics, its growth will be faster than others, which will modulate the shape of the final object, resulting in anisotropic morphologies.

As an example, Li group[116] examined the effect of citrate anions, on the morphology of different LnF_3 (Ln = La-Lu) nanoparticles prepared by simple hydrothermal route, in the presence or without trisodium citrate. They observed, that citrate had no effect on the crystallographic phase, but morphology and size changes were induced. In particular, LnF_3 particles of the group Eu-Er, in the presence of citrate, form spindle-like aggregates, composed of self-assembled prolate spheroidal nanoparticles, aligned along the spindle's long axis, with an aspect ratio of approximately 2. In the absence of citrate, large scale irregularly shaped morphologies are obtained. For the other Ln-compounds (La-Sm and Yb, Lu) only the size decreases without significant modification of the shape. The authors emphasize, that citrate ions form complexes with Ln^{3+} ions, which further lowers the reaction rate, along with the slow release of F^- from $NaBF_4$ precursor.

Recently, the same group used tartaric acid, a hydroxy dicarboxylic acid, with six coordination sites, which can form a stable complex with lanthanide ions and gradually release them during the reaction process.[117] The morphology of the as-prepared GdF_3 NPs with tartaric acid was oblate spheroidal with smaller dots in their centers, while without tartaric acid, doughnut-like

particles are obtained. Again, the crystalline phase was not affected by the organic molecule: the orthorhombic phase was observed in both cases.

II.1.1.5. Reaction time

In the same paper[117], Li group studied the evolution of GdF_3 nanoparticles in time, during the hydrothermal synthetic process in the presence of tartaric acid. In the first 15 minutes, the XRD pattern showed an amorphous material, but after 20 minutes, a hexagonal phase appears, which is gradually transformed to the orthorhombic structure. The observed morphology at the beginning was donut-like, which turned to peanut-like and finally oblate spheroid with a dot in the center when reaction time increased. The authors explained this gradual phase transformation by the variation in the release rate of both fluoride and Gd^{3+} ions. In the beginning, the fluoride ion is the rate-limiting process: the slow hydrolysis of $NaBF_4$ causes F^- ions deficiency, which is known to promote the hexagonal phase formation of GdF_3. Then, the reaction time increases, and the hydrolysis reaction progresses, *i.e.,* F^- ions are no longer deficient and gradually replace tartarate ligands in Gd-complexes. At this stage, Gd^{3+} ion release is the determinant factor in the NP formation.

II.1.2 Solvothermal synthesis of LnF_3 nanoparticles (Autoclave)

In this work, a previously described synthetic process was adapted to produce GdF_3 nanoparticles. Chaput *et al.* reported that using an amide with hydrofluoric acid (HF) as fluoride ion source in the reaction with rare earth trichlorides leads to the formation of highly monodispersed rare-earth trifluoride NPs, with well-defined morphology and crystallinity, in exceptionally mild (170°C) solvothermal conditions.[111]

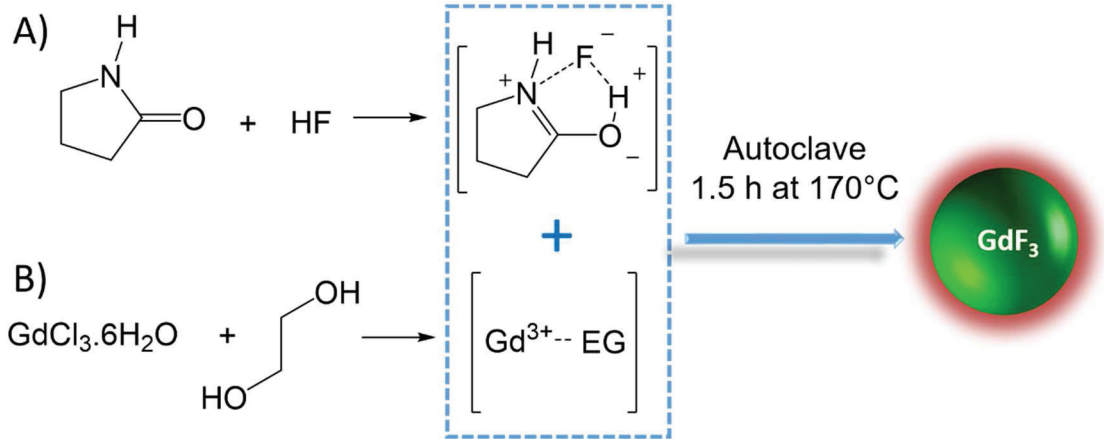

Figure 15 Principle of the synthetic procedure of GdF_3 nanoparticles.

They showed that the amide forms a charge transfer complex with HF (see ***Figure 15***), resulting in amidium cation, and this complex can react at low temperature with rare earth salts. The amide compound in a large excess also has the role of solvent. Besides, at the end of the synthetic process, it also stabilizes the prepared nanoparticles as a capping agent.

In the typical synthetic process of GdF_3 nanoparticles, 4.83 g (0.013 mol) of $GdCl_3 \cdot 6H_2O$ (Alfa Aesar 99.9%) was stirred at room temperature in 2 mL of ethylene glycol (EG) until complete dissolution and was further diluted with 3 mL of 2-pyrrolidinone. This solution was added to a solution of 24 mL 2-pyrrolidinone containing 1.1 mL (0.0316 mol) 50 % HF. The mixture was then heated up to 170°C for 1.5 h in a 50 mL stainless steel Teflon lined digestion pressure vessel. The resultant suspension was let to cool down to room temperature and precipitated in acetone (approximately 60 mL). The colloidal nanoparticles were purified by three centrifugation-redispersion cycles using methanol as solvent. After purification, the nanoparticle-pellets were resuspended in approximately 10 mL of purified water and used directly or freeze-dried for further use.

II.1.3 Characterization of LnF_3 nanoparticles

In the adapted process reported here, the rare earth salt is also complexed before its mixture with the complexed fluoride source, which is evidenced by ATR measurements, shown in ***Figure 16***. According to the analysis of the conformational changes of EG, provided by Guo *et al.*,[118] the ν(O-C-C-O) vibration band at 1084 cm^{-1} corresponds to the *gauche* conformation and the one at 1035 cm^{-1} to *trans* conformation of EG. As the *gauche* form is energetically more favorable, it is the predominant form at RT. Conversely, in the presence of $GdCl_3$ salt, the *trans* form is in higher proportion, showing that EG complexes Gd^{3+} through both oxygen atoms. A reorganization in vibration bands of C-H bond is also observed.

In this work, the complexing amide solvent was 2-pyrrolidinone, which is a high boiling temperature solvent (T_b = 245°C), suitable for the heat treatment in an autoclave. After purification, the obtained nanoparticles were characterized by ATR (***Figure 17***), which revealed, that pyrrolidinone is present on the particles, and it is coordinating to Gd^{3+} ions on the surface. Upon coordination through the carbonyl oxygen, the ν(C=O) stretching vibration frequency shifts from 1679 to 1648 cm^{-1}.

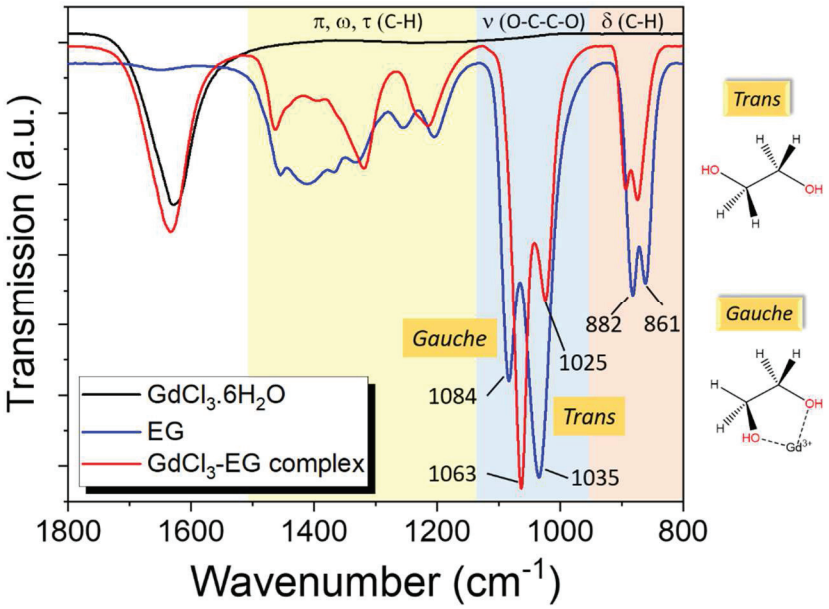

Figure 16 ATR-FTIR spectra of the precursor $GdCl_3 \cdot 6H_2O$ (black line), free EG (blue line) and their complex (red line). *Trans* and *gauche* structures of EG are illustrated beside the spectra.

The bands in the range 1463-1424 cm^{-1} are assigned to C-H deformations, and they shift to 1448 cm^{-1}. For tertiary amides, such as 2-pyrrolidinone, the band around 1284 cm^{-1} is attributed to the (C-)C-N stretching, which disappears in the spectrum of the complex, while a new band appears at 1550 cm^{-1}. This new band is characteristic of N-C=O vibrations in secondary amides, which suggests that nitrogen atom also participates in the complex formation with gadolinium ions.

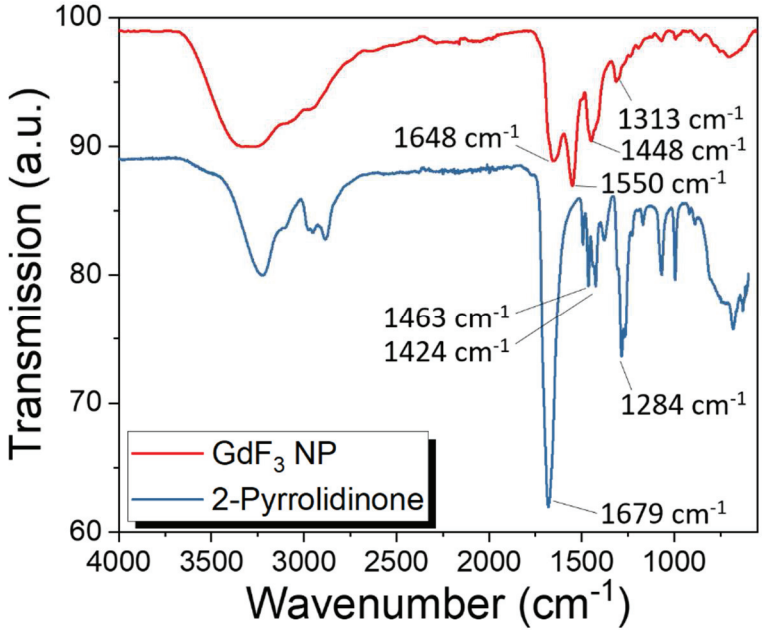

Figure 17 ATR-FTIR spectra of free 2-pyrrolidinone and as-synthesized nanoparticles.

The morphology of particles obtained by this original solvothermal method is slightly elongated rod-shaped, with a narrow size distribution centered at 16±5 nm of diameter, as shown in ***Figure 18 A*** and ***B***. Their high crystallinity is confirmed by XRPD measurements (***Figure 18 C***): the obtained diffraction pattern corresponds to the pure orthorhombic phase GdF_3.

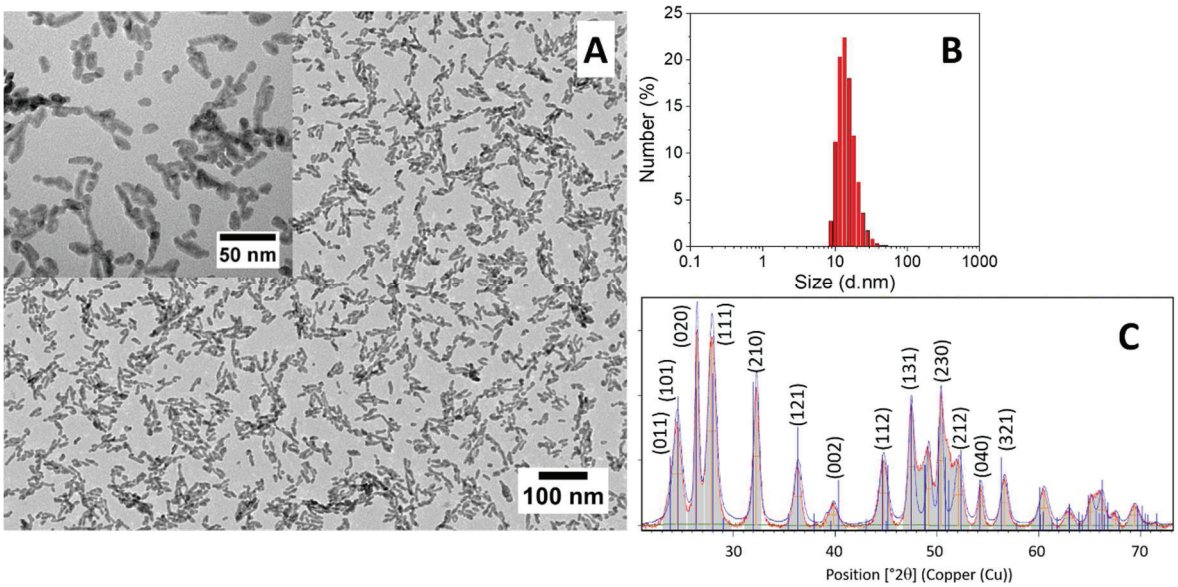

Figure 18 Characterization of GdF_3 NPs: A) TEM images. B) Mean number size distribution measured by DLS. C) XRPD pattern of GdF_3 NPs and the reference pattern (JCPDS 12-0788) for orthorhombic GdF_3. The numbers attributed to the peaks are the crystallographic planes.

TGA measurement (***Figure 19***) showed a mass loss of 8.5 wt%, which corresponds to water and organic molecules content of the nanopowder, further supporting that the nanoparticle surface is covered by solvent molecules.

The particles were then subjected to a pyrolytic treatment (700°C for 5 h in a muffle furnace) to remove all organic content and water, but the temperature was not as high that the inorganic GdF_3 could be altered. This pure GdF_3 nanopowder was analyzed by XPS (***Figure 20***). High-resolution spectra in the ranges corresponding to the 3d core level and valence bands of 4p and 4d of gadolinium were in perfect agreement with the standard values of GdF_3.[119] Slight oxidation was observed with 6 at% of oxygen. Interestingly, at the surface, the Gd:F ratio was found to be 2.6, which is very different from the theoretical 0.3 ratio. This excess gadolinium ion on the surface was also confirmed by zeta potential measurements, which showed a positive value of + 45±10 mV.

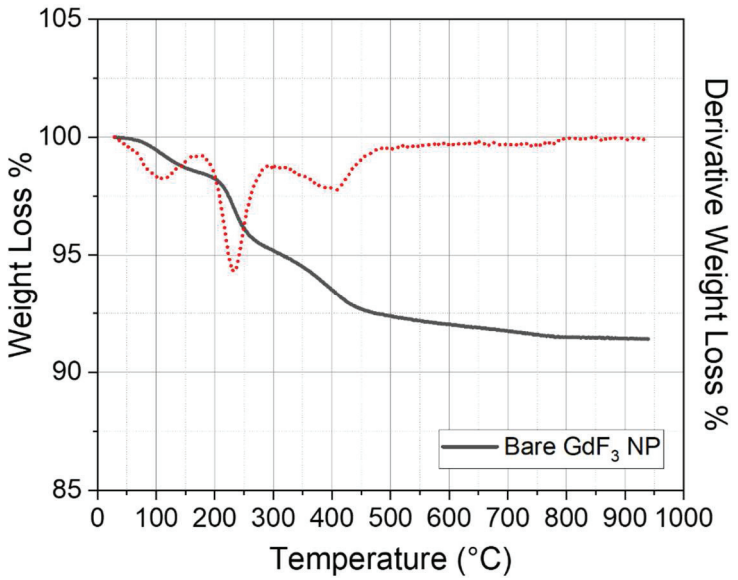

Figure 19 Thermogravimetric analysis of GdF_3 NPs.

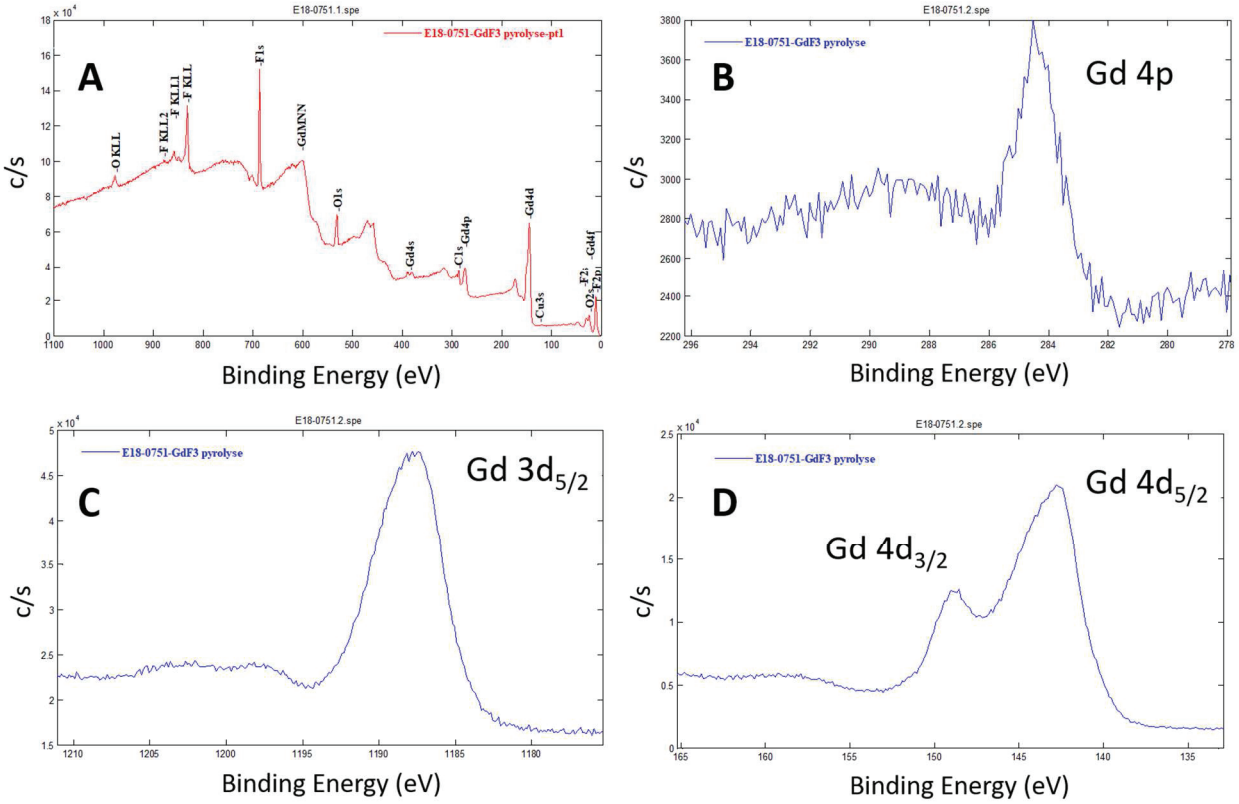

Figure 20 XPS analysis of GdF_3 NPs after pyrolysis. A) Survey spectrum B) C) D) High-resolution spectra corresponding to the binding energy regions of 4p, $3d_{5/2}$, and 4d for gadolinium. (Spectra provided by *Science et Surface*)

LnF_3 nanoparticles elaborated by solvothermal synthesis.
Pure orthorhombic phase is obtained. Slightly elongated rod-shaped particles, with narrow size-distribution centered at 16 nm of diameter are observed. NP surface: excess of Gd^{3+} ions, resulting in a positively charged particle, with 8.5 wt% of organics (solvent) and water content.

II.2 – Synthesis of GdF_3 nanoparticles with microwave technique

II.2.1 Introduction to Microwave-assisted nanoparticle synthesis

Microwave (MW) radiation is electromagnetic radiation in the frequency range 0.3–300 GHz, which corresponds to the wavelength range of 1 mm–1 m. However, in commercially available devices, usually the frequency of 2.45 GHz (wavelength of 12.25 cm), which corresponds to an energy of $1 \cdot 10^{-5}$ eV (1 J/mol).[120] This energy is much lower than the energy needed for bond cleavage (several hundreds of kJ) and even lower than the energy corresponding to the Brownian motion. Therefore, microwave irradiation affects only molecular rotations.

Microwave irradiation creates an oscillating field in the sample and polar species (molecules or ions), as dipoles try to realign to this field. During the oscillation of dipoles, resistive heating is produced in the medium, causing an energy loss, called dielectric loss. Solvents with high loss factor (> 0.5) are solvents that efficiently absorb MW radiation energy and convert it efficiently into heat, producing rapid and homogeneous heating. One of the highest loss factors is attributed to EG (1.350). Water is considered to be a medium absorber, with a loss factor of 0.123.

The penetration depth of MW radiation in the sample is inversely proportional to the dielectric loss, therefore, in a high loss factor solvent, MWs penetrate only the outer layer (typically a few centimeters) of the sample. This limits the size of reactors that can be used efficiently for MW-assisted synthesis (*i.e.,* this technique is difficult to scale up). Loss (or MW absorption) decreases with increasing temperature, while penetration depth increases.[120]

From the first reported experiments of microwave-assisted synthesis (in 1986 for organic compounds) it has been observed, that dielectric heating significantly accelerates reaction rates as compared to traditional heating methods (*e.g.,* oil bath). Besides high heating rates, this technique offers selectivity due to different MW absorption properties of compounds and reduces side reactions. Advantages of MW heating attracted more and more attention in

materials sciences, in particular in nanoparticle synthesis this technique was promising to obtain better control of nucleation and growth.

MW-assisted synthesis of rare earth fluorides has also been described — for example, Ma *et al.*[121] proposed a microwave-assisted hydrothermal synthesis of highly crystalline pure hexagonal phase PrF_3 with hollow morphology. The same group published later the microwave-assisted synthesis of flower-like CeF_3 particles, with EDTA capping agent.[122] Wang *et al.*[123] reported Yb^{3+}/Er^{3+} doped GdF_3 nanoparticles synthesized under MW irradiation, using EG as the solvent. These particles crystallized in the regular orthorhombic phase; however, their morphology was unusual: rhombic-shaped slices were obtained, which presented a high tendency to stacking. No morphological changes have been observed, when the concentration of the reactants varied (25 % of the initial concentration or five times more concentrated).

In the present work, microwave assisted GdF_3 nanoparticles were elaborated, based on the previously described solvothermal route. The effect of a few synthetic parameters has been evaluated, such as reaction time, the viscosity of the medium, the concentration of the reactants, and different capping ligands.

II.2.2 – Morphology evolution of GdF_3 NPs with time

In the first attempt, an evolution of particle morphology was observed at 1, 4- and 30 min of MW-treatment (applied power was 25 W and solution composition was the same as in the previously described protocol for LnF_3 NP synthesis). ***Figure 21*** shows the TEM images of the obtained morphologies.

After one minute of irradiation, a large number of nuclei (7-8 nm in average) are formed from the initial nanogel composed of elongated amorphous particles (***Figure 21 A***, ***B***). These amorphous phase-entities dissolve and disappear upon further heating. After 4 minutes, only small and highly monodispersed (***Figure 21 D***) nuclei are observed, but in a few areas on the TEM grid, larger particles also appear (***Figure 21 C***).

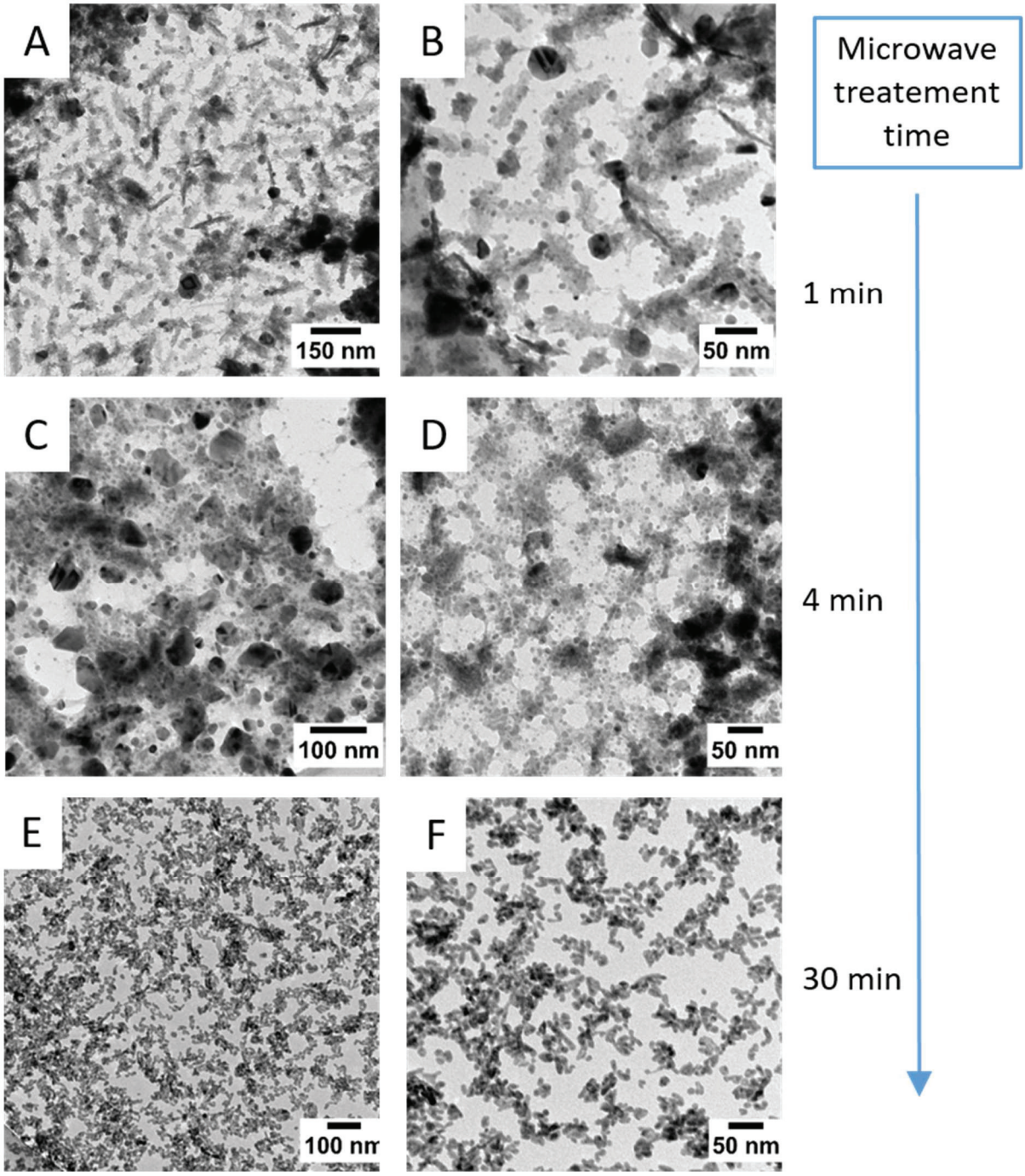

Figure 21 TEM images of GdF_3 NPs synthesized by microwave treatment, at different treatment times. A,B) 1 min, C,D) 4 min, E,F) 30 min.

After 30 minutes, crystalline and monodispersed particles are obtained (***Figure 21 E, F***), with the nearly the same characteristics as the particles obtained by conventional heating (***Figure 18 A***), but slightly less elongated morphology. As it is shown in ***Figure 22***, the measured XRPD patterns of particles produced by different heating techniques are similar.

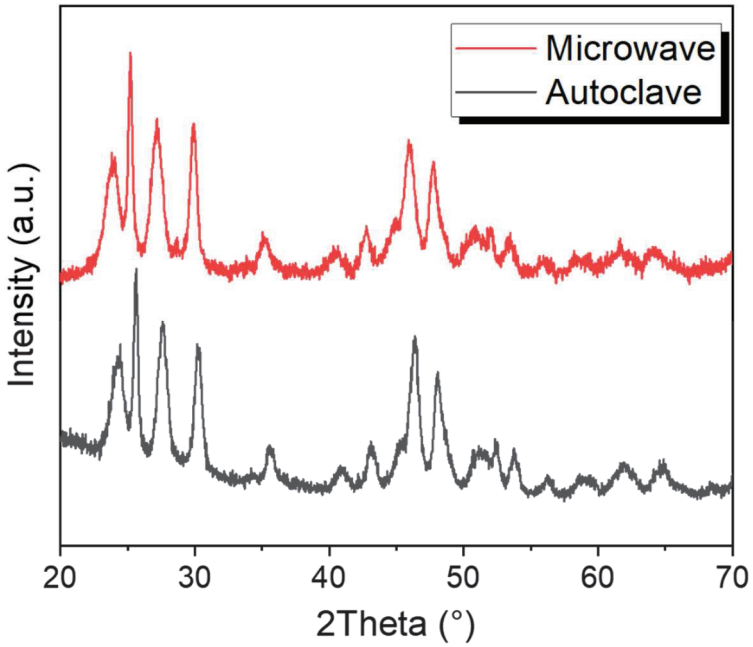

Figure 22 XRPD patterns of GdF_3 NPs synthesized by microwave treatment (red curve) and by heating in an autoclave (black curve).

No size differences were detected by DLS measurements either. Polydispersity index of the amorphous nanogel was 0.4, which decreased to 0.1 after 30 min of MW heating, showing slightly less polydisperse distribution, than for conventional heating. The measured hydrodynamic diameter was 27 nm (Z-average: 41 nm), which corresponds to the value obtained after conventional heating. Therefore, we concluded that in our experimental procedure, time-saving is the main advantage of microwave heating, besides slightly less polydispersity and elongated morphology.

MW *vs.* conventional heating
Same crystallinity, same size distribution and same morphology are obtained in both cases
Advantage of MW-heating: time-saving, better control of polydispersity and morphology
Limitation of MW-heating: small reactor size, no possibility to scale up

II.2.3 – Viscosity effect

In the next experiment, the viscosity effect of the medium was tested by increasing the relative volume of EG. The initial volume ratio of pyrrolidinone to EG was 13.5:1, here EG content was increased to have a 1:1 ratio. Concentration and ratio of the precursors ($GdCl_3$ and HF) were unchanged.

TEM observation of the colloidal solution at the early stage (***Figure 23*** A, B, C) of reaction showed a similar environment as previously: amorphous elongated particles (aspect ratio of 2) with a large number of small nuclei (7-8 nm in average).

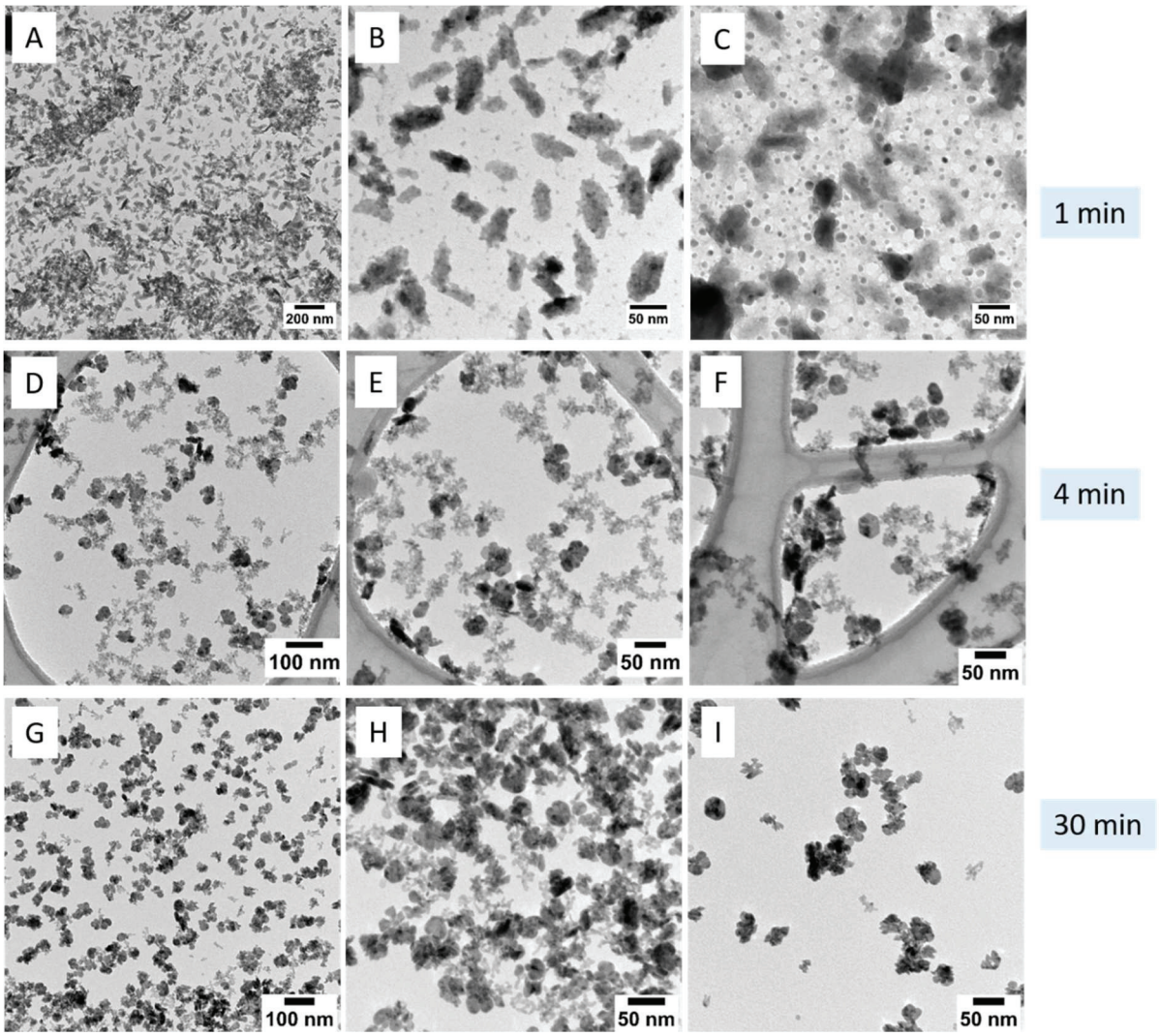

Figure 23 TEM images of GdF_3 NPs synthesized in viscous medium (EG) by microwave treatment, at different treatment times. A,B) 1 min, C,D) 4 min, E,F) 30 min.

After 4 minutes, small and irregularly aggregated particles are observed, besides some larger particles with an irregular shape. After 30 minutes, the same objects are present, but larger particles seem to be more prominent. In accordance with TEM observations, DLS measurements presented in ***Figure 24*** shows the sudden increase in size after 1 minute of MW heating (mean number size increases from 37 to 159 nm) and the size decreases after 4 minutes (32 nm) to keep the same value even after 30 minutes of heating. Measured PDI values are as follows: 0.34, 0.09, 0.10 and 0.11 for 0, 1, 4 and 30 minutes of heating, respectively.

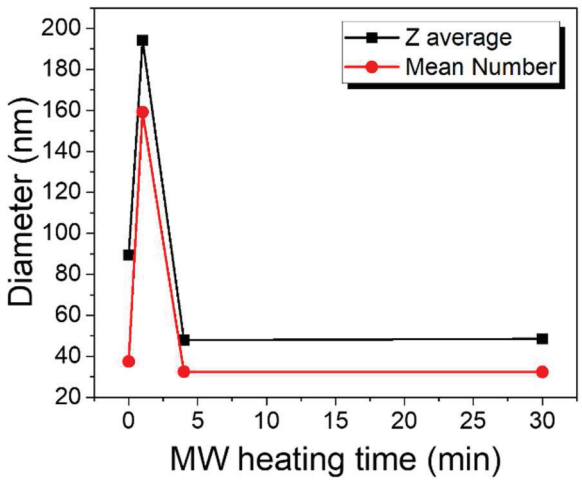

Figure 24 Size evolution of particles as a function of microwave heating time.

During MW-heating, nucleation is more homogeneous and faster, which induces a high number of nuclei. In the growth stage, however, as the solution is cooling down, the viscosity of EG increases, which in turn decreases the dissolution rate of GdF_3 clusters. This means that the critical cluster size should decrease with increasing viscosity. In the introduction, it was mentioned, that decrease of the critical nucleus size leads to less stable crystallites (see ***Figure 8***). Therefore, with increasing viscosity, precipitation of solid particles starts (*i.e.,* growth stops) at higher temperatures, leading to less stable and irregular shaped nanocrystals, as compared to the synthesis product in the non-viscous medium. Samanta *et al.*[113] observed similar viscosity effect on $GdF_3:Eu^{3+}$ nanoparticles synthesized in different conditions (see ***II.1.1.3. Viscosity and Temperature***).

Viscosity effect
High viscosity of reaction medium decreases the critical nucleus size, resulting in less stable and irregularly shaped nanoparticles.

II.2.4 – Concentration effect

II.2.4.1. Dilute medium

At low concentration of one or both reactants, growth is the limiting step in particle formation. This case was examined, by decreasing Gd^{3+} concentration from 0.4 M to 6.10^{-3} M. Molar ratio of $Gd^{3+}:F^-$ was kept identical to the usual ratio of 2.4, and heating time was 30 min. The as prepared, isolated solid presented an interesting, dendrite-like plate morphology (***Figure 25*** A).

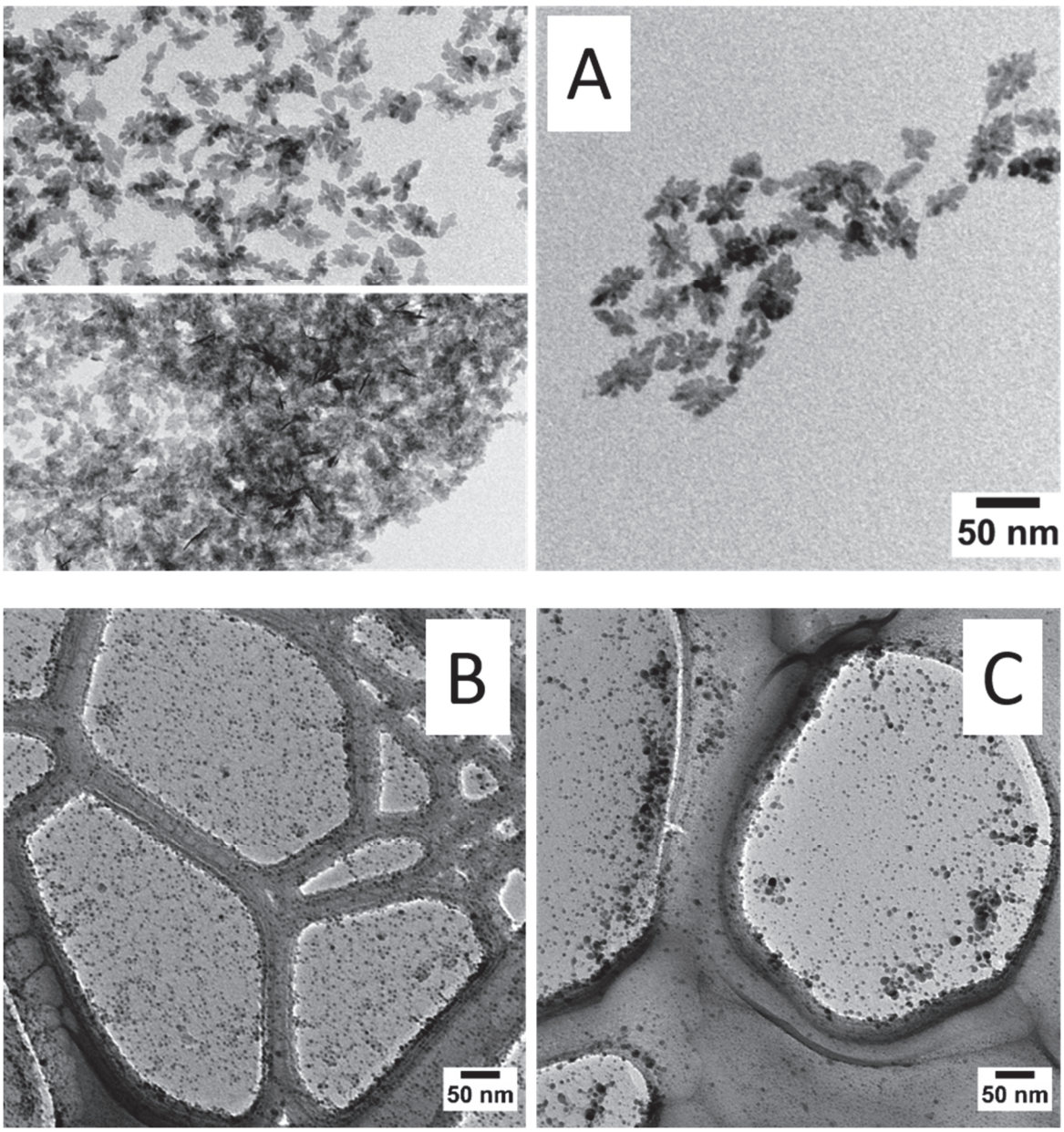

Figure 25 TEM images of GdF_3 NPs synthesized in diluted conditions. A) observation of freshly prepared suspension, C, D) suspension one week after.

After one week, the same solution was redeposited on a new TEM grid, but dendritic structures were no more observable. Instead, very small (< 5 nm) particles were observed. Eiden-Assmann *et al.*[124] obtained the same small particle morphology of CeF_3, from a similarly diluted solution (***Figure 26***). They started from $[CeCl_3] = 7.4 \cdot 10^{-3}$ M, in diethylene glycol and the F^- precursor was HF. Their particles were crystalline, and the expected hexagonal form was confirmed by XRD.

Growth and dissolution of dendritic lanthanide-based nanoparticles have already been observed in a few cases. Sturm and co-workers[125] followed dendritic yttria precursor nanostructure

evolutions by *in situ* liquid TEM. They observed the formation and rapid growth of dendritic particles, which underwent rapid fragmentation and formation of small spherical particles occurred. Further observation revealed coarsening of the small particles by coalescence or Ostwald ripening, and finally, faceted NPs formed. The authors hypothesized, that the dendrites grew under diffusion limited conditions, and when depletion of solid components occurred around the dendrites, they stop to grow and due to the increased surface energy of particles they underwent coarsening.

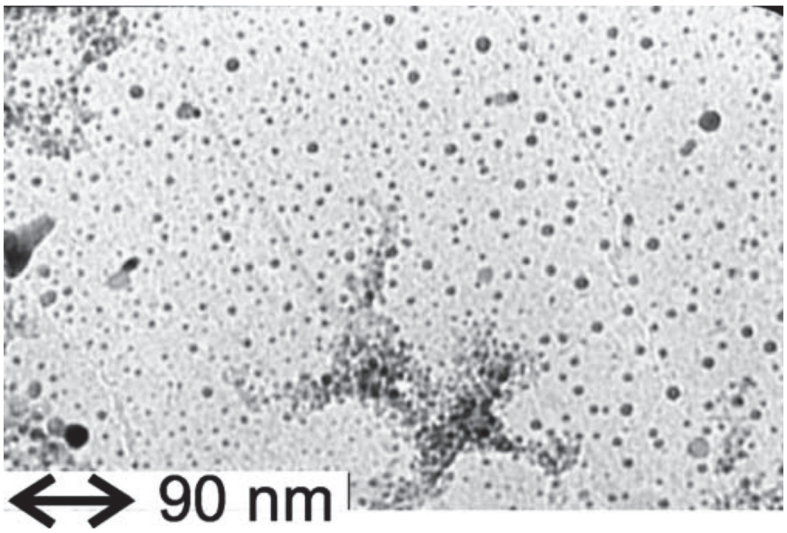

Figure 26 TEM image of CeF_3 particles obtained in a diluted medium. From ref. Eiden-Assmann and co-workers[124]

Noculak *et al.*[126] prepared $NaGdF_4:Yb^{3+},Er^{3+}$ nanocrystals via co-precipitation method with NH_4F fluoride source, and obtained different morphologies upon varying $F^-:Ln^{3+}$ molar ratio. They observed considerable influence on the size and shape evolution with varying reactant concentrations. With the highest $F^-:Ln^{3+}$ molar ratio spherical, pure hexagonal phase particles formed. By decreasing the ratio, particles were more irregular, and limb shaped. Further reducing the ratio, induced flower-like dendritic nanoparticles. In all these cases, the crystal phase of the obtained solid was hexagonal. Finally, with the smallest amount of NH_4F, a mixture of dendrites and very small particles was obtained.

In our case, the low concentration of reactants induced diffusion limited conditions, which led to the formation of dendritic particles. Dendritic structures have high surface energy and tend to decrease it; therefore, it is not surprising that they undergo high coarsening effects and even dissolution, to give small spherical particles.

II.2.4.2. High concentration

When the concentration was increased to 0.7 M, the reaction mixture was first observed by TEM, before any heat treatment (***Figure 27***). This observation revealed that the solid content in this concentrated solution was composed of small entities, self-assembled into large (approximately 160 x 40 nm elongated objects), highly monodispersed particles.

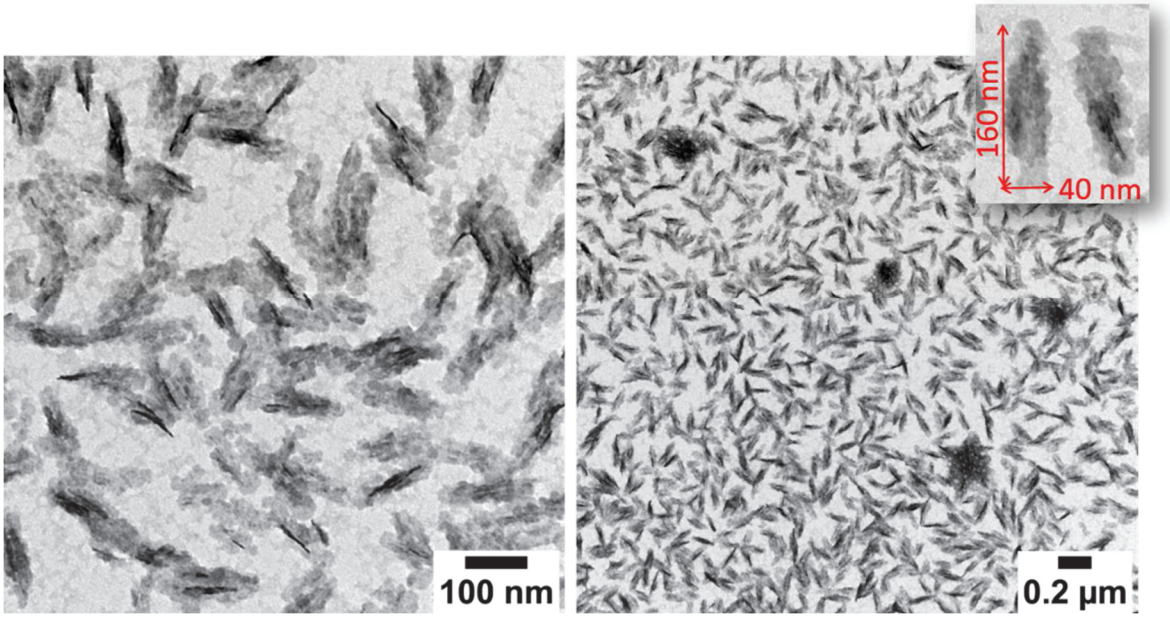

Figure 27 TEM images of the reaction mixture before any heat treatment. (GdF_3 NP synthesis)

After microwave irradiation of 30 minutes, the obtained particles were purified and observed by TEM. A mixture of faceted nanoplates and assemblies of small particles were born from this suspension (***Figure 28***).

The plate-like morphology is well illustrated in ***Figure 28***A, by the face-to-face stacked particles seen from the lateral side. In the areas of ***Figure 28*** B and C surrounded by red circles, the two different morphologies are highlighted. Interestingly, a high number of homogeneously dispersed very small (< 5 nm) spots are also visible in ***Figure 28*** A and B. As the observed suspension was obtained from purified particles, the spots cannot be originated from some impurities or unreacted compounds. Indeed, the spots correspond to very small particles, which grew from the suspension.

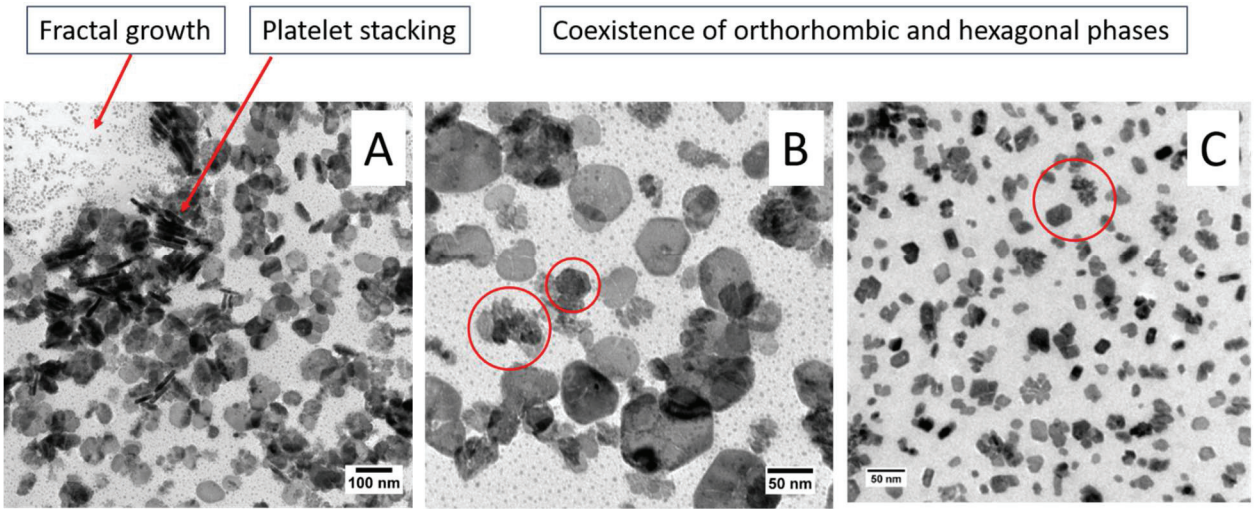

Figure 28 TEM observation of GdF_3 NPs obtained by the synthesis in a concentrated medium. Red circle marked area highlights the coexistence of hexagonal and orthorhombic crystals.

One possible explanation is that these spots are issued from the dissolution of unstable particles and the dissolved solid renucleated and grew in the suspension. For TEM, usually, the highly diluted suspension is prepared, which may explain the observed fractal-like assembly of small particles (***Figure 28***A). This assembly is a typical example illustrating diffusion-controlled growth mechanism, shown in ***Figure 9***.

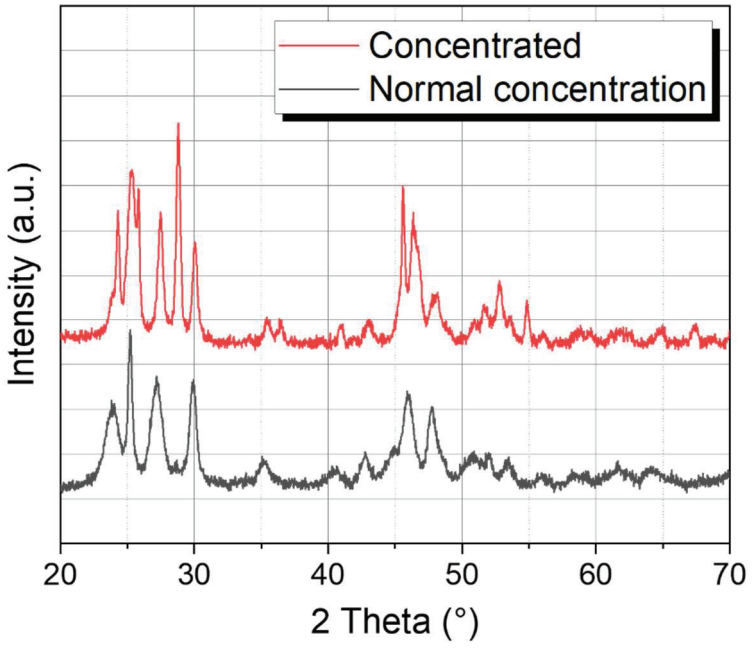

Figure 29 XRPD patterns of GdF_3 NPs obtained from concentrated solution (red curve) and in normal conditions (black curves).

After freeze-drying, the solid was characterized by XRD measurement. The observed pattern showed a highly crystalline material, and a mixture of hexagonal and orthorhombic crystalline

phases was confirmed. For comparison, the measured pattern of pure orthorhombic phase GdF_3 is also reported in ***Figure 29*** (black line).

Coexistence of the two phases is very often observed for GdF_3 nanoparticles, which is explained by the intermediate size of Gd^{3+} ions in the lanthanide series.[127] However, it is worth noting that pure orthorhombic phase can be obtained with properly adjusted, optimized conditions.

Concentration effect
- Diluted medium: the diffusion-limited conditions induced dendrite-like nanoparticles, which were dissolved and transformed to very small (<5nm) particles upon coarsening.
- High concentration: a mixture of hexagonal and orthorhombic crystal phases were obtained and the morphology of the particles was also a mixture of small, spherical and bigger, faceted particles.

II.2.5 – Effect of organic additives

Presence of organic additives in the reaction mixture is known to influence morphology of particles. Here the effect of two different ligands has been investigated. One was ethylenediaminetetraacetic acid (EDTA), a well-known chelating agent and the other one was a copolymer (referred here as copo-P), with poly (ethylene glycol) (PEG) pendant chains and phosphonic acid functional groups. This latter ligand is presented in detail in Chapter 3. It is a large, multidentate ligand, coordinating *via* its phosphonic acid groups.

To test their effect on morphology, a usual mixture of $GdCl_3.6H_2O$ with HF in pyrrolidinone was prepared (F^-:Gd^{3+} molar ratio of 2.4), but to avoid a competitive binding with EG, only water and pyrrolidinone were used as solvents. The obtained mixture was divided in two vials. EDTA was added to one vial and copo-P to the other one. In order to take into account multidenticity of the polymeric ligand, the molar ratio of EDTA to Gd^{3+} was the same (1 ligand for 24 Gd^{3+} ion) as the molar ratio of phosphonic acid functions on copo-P to Gd^{3+}.

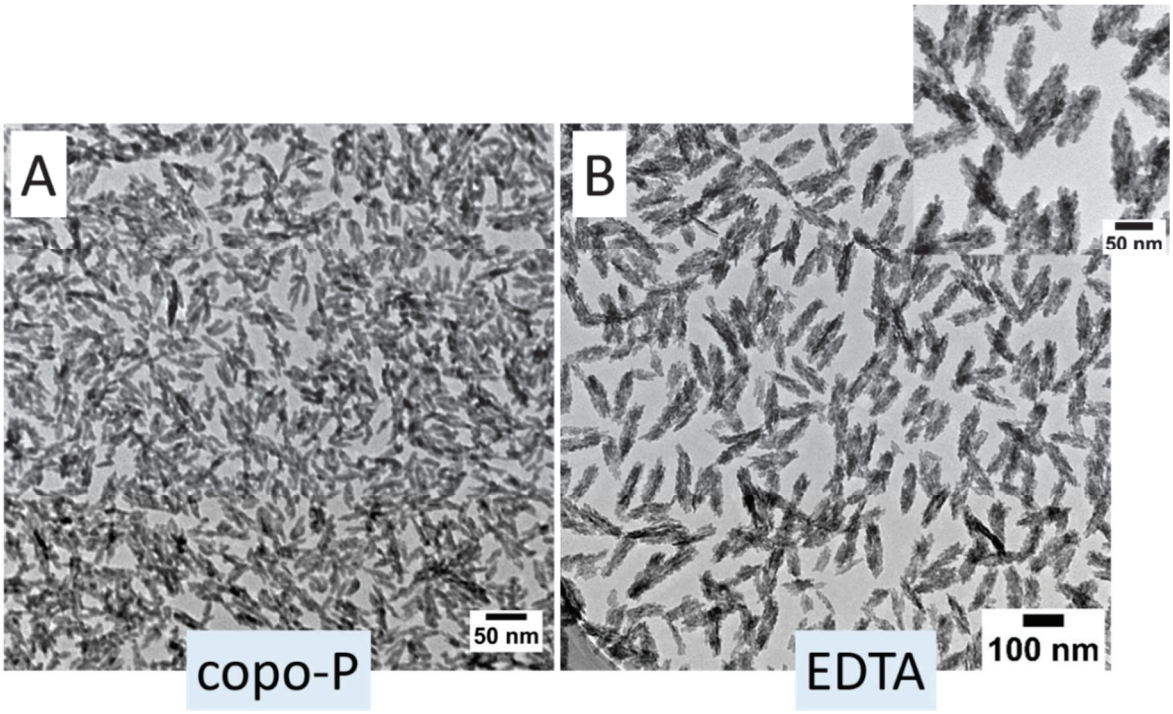

Figure 30 TEM images of GdF_3 NPs obtained by MW treatment, in the presence of A) copo-P and B) EDTA.

After the identical microwave treatment of these two solutions, the particles were collected by centrifugation and washed with ethanol. TEM observation showed in ***Figure 30*** revealed two significantly different morphologies upon addition of organic additives. In the presence of the first capping agent, copo-P, individual particles are obtained. When compared to bare particles morphology (***Figure 21***F), particles prepared in the presence of the polymer are more elongated, quasi-needle shaped. Typical size of a particle according to TEM, is 47x16 nm, corresponding to an aspect ratio of approximatively 3, while it was less than 2 for the bare particles. This observation was also confirmed by DLS measurements, which showed a measured hydrodynamic size of 45 nm, which is significantly higher than in the case of bare NPs (16 nm). The same PDI value of 0.14 was determined, corresponding to monodispersity.

Interestingly, the addition of EDTA resulted in highly monodispersed spindles of approximately 100 nm in length and 30 nm in with, characterized by an aspect ratio of 3-4. These large spindles are composed of small particles, aggregated uniquely. Exceptionally low PDI was measured to be 0.06, confirming the observed monodispersity, and the mean number size distribution was 50 nm. It must be noticed, that the same objects (same morphology and size) have been observed before any heat treatment, on the sample presented in ***Figure 27***, but with a less crystalline aspect. This suggests that EDTA has no noticeable effect on particle nucleation or growing. Oppositely, the multidentate and polymeric ligand prevents particles

from aggregation, *via* electrosteric repulsion. In Chapter 3, the origins of this efficient particle separation will be discussed in detail.

Coordination mode of EDTA was tentatively elucidated by ATR. Comparison of ATR spectra of free EDTA and NP-EDTA system is shown in ***Figure 31***, and the presence of this ligand on particles surface could be confirmed.

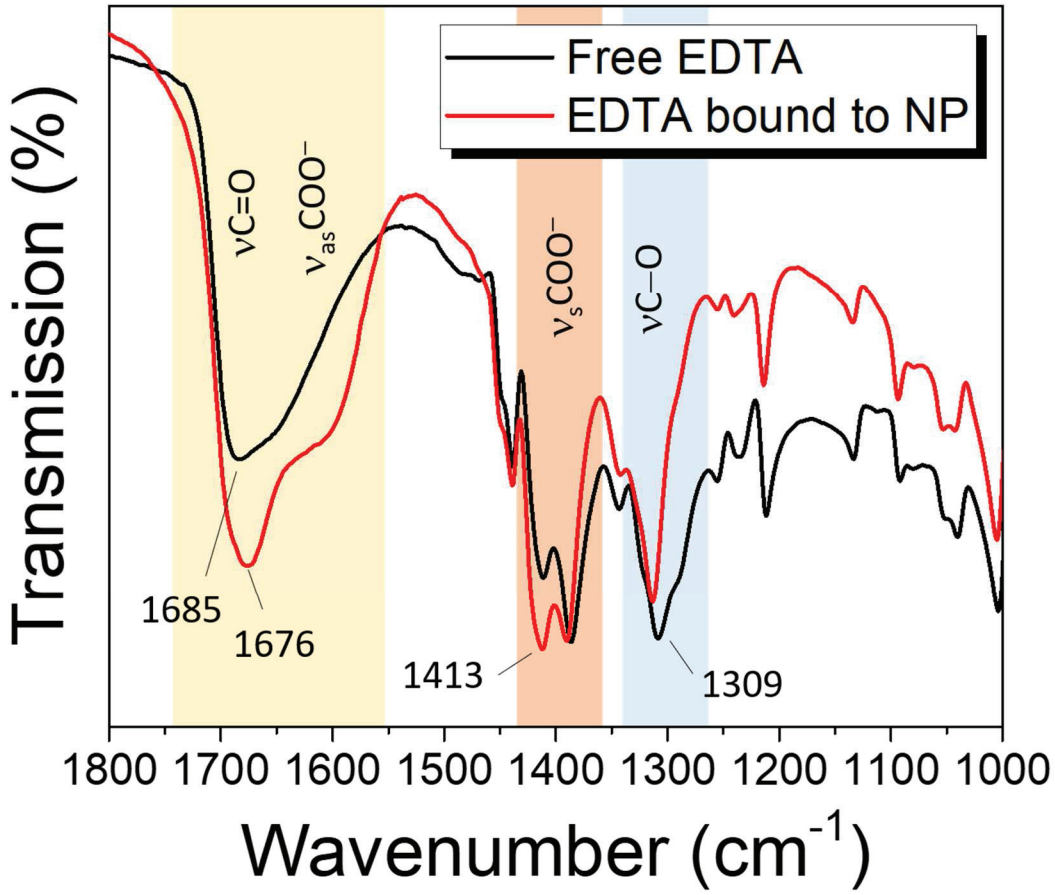

Figure 31 FTIR-ATR spectrum of GdF_3 NPs prepared in the presence of EDTA (red line) compared to the spectrum of free EDTA (black line).

Upon coordination, the vibration band corresponding to the asymmetric stretching of carboxylate group appears as a shoulder of the C=O band (1676 cm^{-1}) in the acidic form. The symmetric stretching vibration [$\nu_s(COO^-)$ = 1413 cm^{-1}] intensity increases and ν(C–O) of coordinated carboxylate is also shifted to lower wavelengths compared to the free molecule (1309 cm^{-1}) and appears as a shoulder of the later band. These observations bring the evidence that EDTA is coordinated to the surface; indeed, free acidic moieties are also present, which suggests that not all carboxylates of EDTA participate in bonding with surface gadolinium ions.

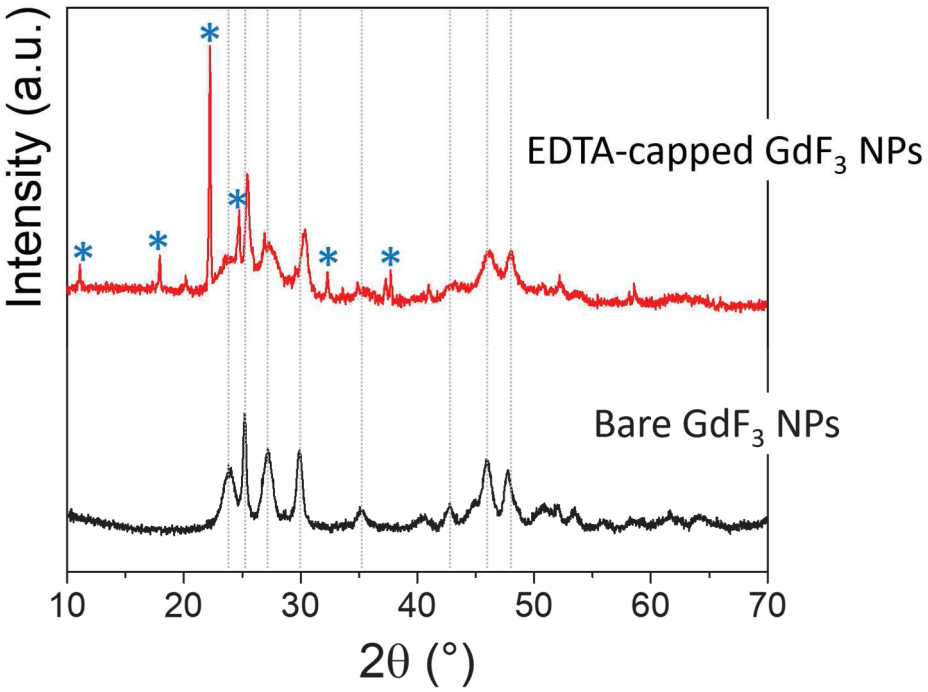

Figure 32 XRPD pattern of GdF_3 NPs prepared in the presence of EDTA (red line) compared to the pattern of bare NPs (black line). Peaks marked by an asterisk belong to an unidentified phase.

Powder XRD analysis revealed a mixture of two phases (***Figure 32***). One phase corresponds to the pure orthorhombic phase GdF_3 pattern, but additional peaks couldn't be attributed to any reference pattern of Gd-compounds.

Nanospindles obtained here with EDTA addition, has been observed for lanthanide-based nanoparticles in a few cases. Li *et al.*[116] for example obtained orthorhombic phase, submicrometer (500-600 nm) LnF_3 spindles (Ln=Gd-Er) by hydrothermal method (fluoride source: $NaBF_4$), with addition of citrate ions as capping agent. They described these objects as an assembly of ordered chains of small, slightly elongated particles, along the longer axis of the spindle. Samanta *et al.* elaborated $GdF_3:Eu^{3+}$ nanoparticles by hydrothermal route (fluoride source: KF), with addition of PVP and observed hexagonal phase spindles at low temperature synthesis, which transformed into orthorhombic phase plates at 150°C.[113] Wang *et al.* described orthorhombic rice-like nanocrystals of YF_3.[127] They have developed a hydrothermal route, using linoleate as additive and NH_4HF_2 as fluoride source. Again, the observed spindle-like particles are composed of smaller nanorods, and the authors identified the <111> direction as the faster growing direction. They hypothesized, that linoleate molecules are selectively coordinated and can cover only certain plans in the initial state of crystal formation, resulting in planes which are more reactive (in this case (111) plane) than others. Oppositely, Zhang *et al.* reported orthorhombic $GdF_3:Eu^{3+}$ with spindle-like morphology, without any organic

additives.[128] They simply added an aqueous solution of NH_4F to the Gd-precursor solution and stirred 12h at room temperature. They also noticed, that the spindles are composed of almost aligned single crystals. Lin group observed spindle formation, when they prepared Gd-doped YF_3 nanoparticles, with classical hydrothermal method: NH_4F fluoride source and water as solvent.[129]

The same morphology was not only reported for rare-earth fluorides, but also for other lanthanide-based compounds. Xu and coworkers synthesized $Ln(OH)_3$ particles by wet chemical route and obtained the same morphology.[130] They dissolved $LnCl_3$ salt in water and added NaOH, without using any surfactant or other additives. Li *et al.* obtained the same $Ln(OH)_3$ particles by a hydrothermal method, adding diethylene glycol and citrate.[131] They also examined if the addition of PEI has an effect and found that this polymeric additive doesn't influence morphology.

After a careful examination of all these synthetic protocols used for rare-earth based nanospindles, one can conclude, that only one parameter was common: the presence of water. As a reminder, in our work, spindles were also obtained from water-based synthesis, suggesting that this aggregation is somehow promoted by water.

In all cited works (except for Zhang's work), the oriented attachment mechanism is claimed for the self-assembly of small nanoparticles to spindle-like mesocrystals (*i.e.,* ordered assembly of small identical crystalline particles). The thermodynamic driving force of oriented attachment is the decrease of surface free energy of particles. Organic additives may preferentially bind to certain facets of nanocrystals at the initial stage, hence modulating the anisotropic growth and acting as morphology modifier agent. This effect was hypothesized in these articles, to be at the origin of spindles formed by oriented attachment.

Recently, Martinez-Esain and co-workers studied 15 LnF_3 nanoparticles synthesized by co-precipitation method, in water, with citrate as a stabilizing agent.[132] They obtained spindle-like supraparticles only for the orthorhombic phase EuF_3 and GdF_3 particles. As opposed, hexagonal and cubic phase LnF_3 assembled into spherical supraparticles. The authors explained this different behavior by the difference in the exposed facets during the growth process: in the orthorhombic phase, the (010) crystallographic plane is more reactive; therefore, the small rod-like particles assemble in the preferential [010] direction, giving rise to the elongated structure. In the case of the spherically assembled YF_3 particles, the same group studied in detail the

mechanism of supraparticle formation.[133] They reacted in aqueous medium $Y(CH_3COO)_3$ with NH_4F, in the presence of citrate and based on ^1H NMR, IR, and XPS analysis, supported by molecular dynamics (MD) simulations, they concluded, that electrostatic interactions are responsible for the affinity of these particles to assemble, but the adsorbed water layer is also important. Experimental results brought the evidence for the coordination of citrate and acetate anions, as well as NH_4^+ cations on the surface. Upon varying Y-precursor, the same behavior was observed; therefore, they concluded, that acetate anion has no specific role in the assembly, while switching from NH_4F to Bu_4NF resulted in the increase of supraparticle size, demonstrating, that the cation plays a key role. According to MD simulations, the authors suggest, that the multidentate citrate anion form bridges between the particles by coordination to surface Gd^{3+} or by electrostatic interactions with NH_4^+ cations.

Based on our observations combined to their results, it can be assumed, that EDTA molecules have the same effect than citrate anions and therefore, EDTA promotes spindle-like assembly of the orthorhombic nanoparticles. The polymeric ligand, copo-P prevents particles from being in close contact via steric repulsion, hence no assembly is observed. In our classical synthetic procedure, there is no multivalent ion present in the medium. The particles surface is therefore passivated by pyrrolidinone and EG, which also inhibits aggregation. The assemblies observed before MW or heat treatment (***Figure 27***) may be explained by H_3O^+ mediated aggregation,[132] in the presence of water provided by the precursor $GdCl_3 \cdot 6H_2O$ and aqueous HF-solution.

Effect of organic additives
- Multidentate polymeric ligand (copo-P) prevents aggregation of the particles through steric effects: individual elongated NPs are obtained.
- In presence of EDTA, spindle-like NP assemblies are observed. According to literature review, the assembly may be explained by the oriented attachment, through the formation of EDTA bridges between the small particles to give nanospindles.

II.3 – Scattering of GdF_3 nanoparticles: estimation of the mass of one NP and the number of GdF_3 molecules per particle.

Inorganic GdF_3 NP described in this chapter constitutes the core of the hybrid nanoplatform, that is applied as a contrast agent in biological applications (Chapter 4). Surface modification of the NPs will be described in the next chapter (Chapter 3), and one functionalization step consists of adding fluorescent labels on the particles. The reaction yield of fluorophore coupling

is quite low. Therefore, the effective concentration of labels in the contrast agent suspension must be determined. Usually, chromophore (or fluorophore) concentration determination is easily performed by using Beer-Lambert's law (***Equation 10***), which gives the relation between measured absorbance and concentration for a given chromophore. However, as it will be discussed in Chapter 4, for nanoparticle suspensions, particle scattering alters the absorption spectrum, leading to an apparent chromophore concentration, which is different from the real value. To be able to evaluate the real concentration of fluorescent label in functionalized NP suspension (contrast agent solution) scattering must be subtracted from the absorption spectrum. For that reason, scattering due to the particles is discussed in this section. Moreover, estimation of the mass of one single nanoparticle can be used to estimate the number of ligands on one particle (see section II.2.4 in Chapter 3), as well as the number of GdF_3 molecules per particle. Determination of these average numbers by using a scattering-mass relationship is proposed here.

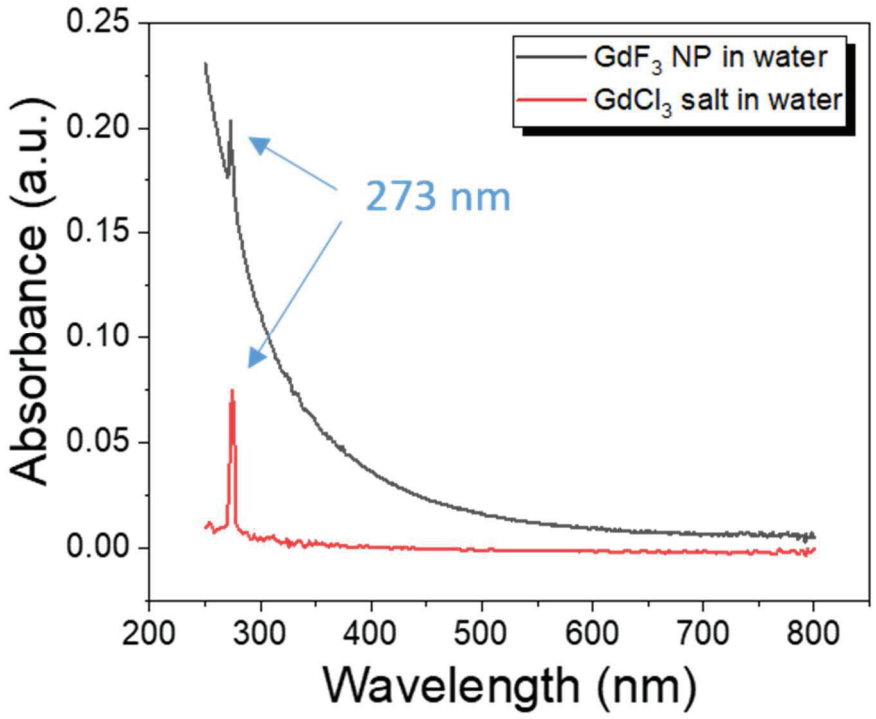

Figure 33 Absorption spectra of the aqueous suspension of GdF_3 NPs (black curve) and $GdCl_3$ solution. The sharp peak at 273 nm corresponds to the electronic transition $^8S_{7/2} \rightarrow {}^6I_J$ of gadolinium.

Figure 33 shows the absorption spectrum measured for an aqueous suspension of GdF_3 NPs. One sharp absorption band is observed at 273 nm, which is characteristic of the $^8S_{7/2} \rightarrow {}^6I_J$ transition of gadolinium (III) ions. The spectrum measured for a simple $GdCl_3$ solution (the

Gd^{3+} precursor), this sharp peak is the only signal, that appears on the background (zero absorption value), while in the case of particle suspension, a continuously decaying power-law shape signal is observed as a function of wavelength. This signal is due to the scattering of particles.

As previously mentioned in section ***I.3.1 Techniques based on light-matter interactions***, when particles are small compared to the irradiating wavelength ($R < \frac{1}{10}\lambda$), according to the Rayleigh approximation, their scattering is proportional to λ^{-4} (see *Equation 18*). This was checked for our GdF_3 nanoparticles: ***Figure 34*** shows measured absorbance of GdF_3 NP suspensions, as a function of λ^{-4}. For the as-synthesized particles, the linear relation between absorbance and λ^{-4} Shows, that the Rayleigh approximation is verified and is true for reasonable concentrations. However, when particles are aggregated, *i.e.,* typically when measured PDI > 0.2, this approximation doesn't fit anymore, in that case, the relation between absorbance and λ^{-4} is not linear (***Figure 34***).

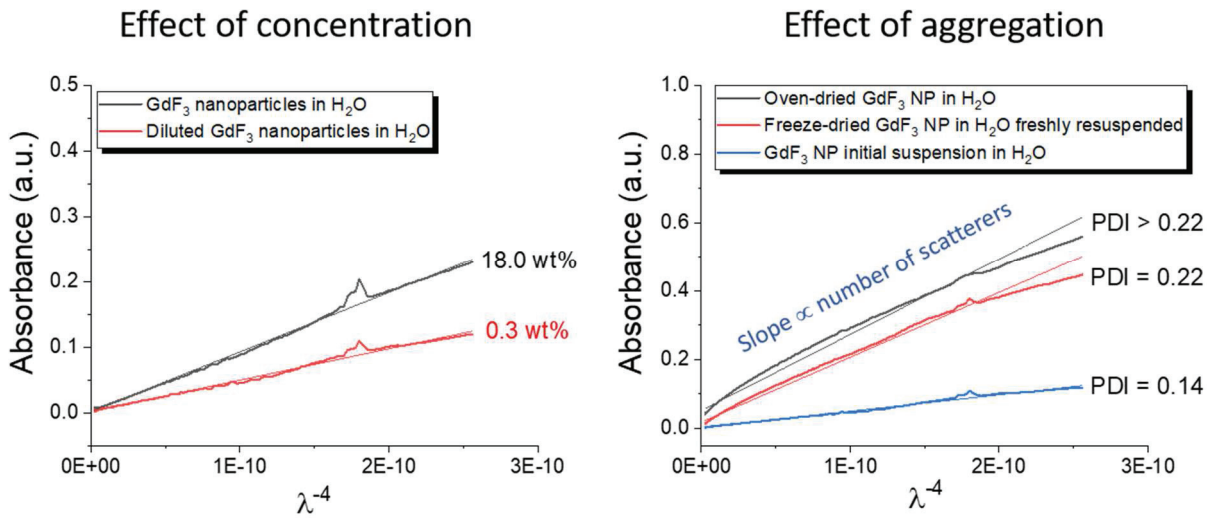

Figure 34 Measured absorption as a function of (-4)th power of wavelength. Effect of concentration: absorption spectra obtained for two different concentrations of particles (0.3 and 18.0 wt%); Effect of aggregation: absorbances measured for different aggregation state of particles (PDI = 0.14, 0.22 and > 0.22).

Consequently, for this system, the mass of one scatterer (*i.e.,* one particle) can be calculated from *Equation 17* combined with *Equation 18*. This idea was exploited by Evdokimov *et al.*, who determined size/mass parameters R^6/m_p of typical scattering entities in asphaltene solution using this method.[134] As refractive indices of solvent (n_s) and solid particles (n_p) are not the same, a slight modification of the expression for σ_s is needed, and this transformation leads to the following expression:

Equation 21

$$\sigma_s = \frac{128\pi^5 n_s^4}{3}\left[\frac{(n_p/n_s)^2 - 1}{(n_p/n_s)^2 + 2}\right]^2 \frac{R^6}{\lambda^4} = \mathrm{K} \cdot \frac{R^6}{\lambda^4}$$

Upon replacing σ_s in *Equation 17*, the expression of absorbance becomes:

Equation 22

$$A(\lambda) = \left[\mathrm{K}\frac{C_w\, x}{ln(10)}\frac{R^6}{m_p}\right] \cdot \frac{1}{\lambda^4}$$

Therefore, a linear regression of plot $A(\lambda) = \mathrm{f}(1/\lambda^4)$ results in a slope value, which is proportional to R^6/m_p, hence, can be calculated, provided, that R, the particle radius is known.

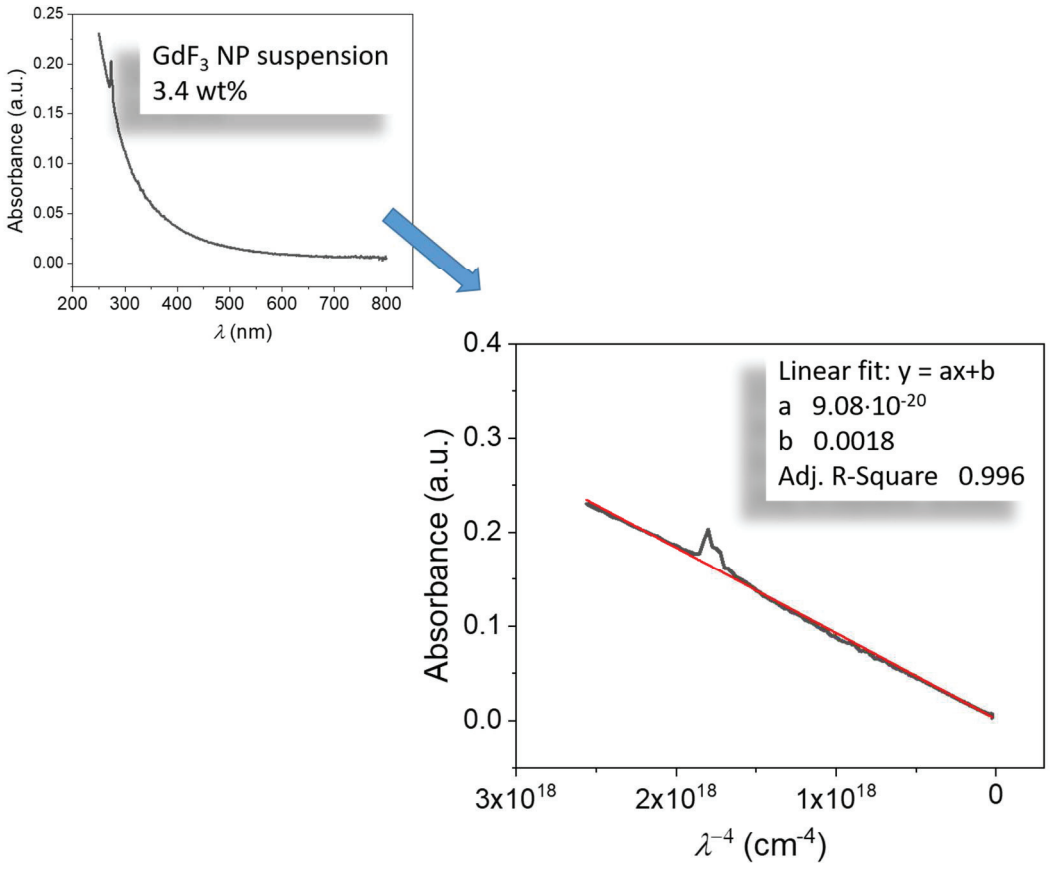

Figure 35 Linear fit of the plot absorbance vs. λ^{-4} for a GdF_3 suspension of 10.2 mg in 3 mL of water

The measured spectrum was obtained for a suspension containing 10.2 mg of NP in 3 mL of water, giving a concentration of 3400 µg/cm^3, cuvette length x is 1 cm, and refractive indices of the particles (GdF_3) and water are 1.59 and 1.33 respectively. The slope value obtained by a linear fit of data is $9.08 \cdot 10^{-20}$. The average radius (R) of a sphere having the same volume as the

particles is given by DLS measurements, and its value is approximatively 8 nm. Therefore, the estimated mass of one particle is $2.73 \cdot 10^{-18}$ g, and the corresponding number of GdF_3 molecules per particle is 7669. However, it has to be noted, that particle size and shape were coarsely approximated, and the strong dependence of our calculations on this parameter (R^6) induces high differences upon slight changes. A few examples are given in Table 2.

Table 2 Estimation of mass (m_p) of one NP and the number of GdF_3 molecules per particle for a given radius R

R (nm)	$m_p \times 10^{18}$ (g)	Nb of GdF_3 molecules per NP
6	0.49	1 365
7	1.22	3 442
8	2.73	7 669
9	5.53	15 547
10	10.40	29 255
20	666.12	1 872 341

From this calculation, the order of magnitude of the number of gadolinium ions is estimated to a few times 10^4, and the mass of one particle is ~ 10^{-18}–10^{-17} g.

GdF_3 NPs of approximately 16 nm, with reasonable polydispersity (0.14) obey the Rayleigh scattering law: $A\ (\lambda) = f(1/\lambda^4)$. This allowed us to calculate the following characteristic quantities for GdF_3 NPs:
Estimated GdF_3 NP mass: ~ 10^{-18}–10^{-17} g
Estimated number of Gd^{3+} ions per NP: ~ 10^4

III – Conclusions

In the present chapter, the synthesis of controlled size and morphology, crystalline GdF_3 nanoparticles by an original solvothermal method has been described. Full characterization of these particles showed that their surface is capped by solvent (pyrrolidinone) molecules and water. This organic and hydration layer represents approximately 8.5 % of the total weight of particles. XPS and zeta potential measurements revealed an excess of Gd^{3+} ions on the surface (ZP = + 45±10 mV). These surface characteristics make these particles highly stable in reasonably concentrated (20-50 wt%) aqueous suspension.

Microwave-assisted synthesis is a convenient and rapid method for particle synthesis; therefore, some important reaction parameters have been tested by using MW heating. First, the effect of MW was evaluated, compared to conventional heating, and we observed no significant

differences between particles obtained with these two methods. Same crystallinity and same size have been observed in both cases, however, MW-heating results in slightly higher monodispersity and globally less elongated particles. Growth of particles was followed as a function of MW treatment.

Increase of solvent viscosity resulted in the formation of less stable and more polydisperse particles by decreasing the solubility of the solid phase. Mean size increased in the first minute of heating; however, these big particles dissolved upon further heating. During the cooling, the increasing viscosity gave birth to a more polydisperse population of particles.

The concentration of precursors also significantly affected the morphology of particles. In a diluted medium, diffusion-controlled growth resulted in interesting dendritic morphology, but these particles were not stable, and after their dissolution at room temperature, small and monodispersed particles were observed. In a concentrated solution, spindle-like morphologies are spontaneously formed (without heating), and upon MW treatment, the coexistence of orthorhombic and hexagonal crystalline phases is observed.

Then, the effect of two organic additives, EDTA and copo-P, was studied. With EDTA nanospindle shaped mesocrystalline nanoparticles were observed. These objects are formed upon oriented attachment of small particles, which was tentatively explained by ionic interactions between particles, through EDTA bridges formed between particles.

Finally, scattering of GdF_3 NPs was measured by absorption spectroscopy, and analysis of the obtained spectrum showed, that the scattering of these particles obeys to Rayleigh scattering law. Therefore, Rayleigh formulas were applied to estimate the average mass of one NP and the number of GdF_3 molecules per particle.

Finally, we can conclude, that in view of the intended application of the GdF_3 nanoparticles, the optimal synthetic procedure has been found, which resulted in highly crystalline inorganic nanoparticles, with well-defined size and morphology, have been elaborated by a solvothermal method, with conventional heating. We showed, that it is possible to save time for the synthesis of these particles, by microwave heating. However, this technique is limited to small quantities.

In the next chapter, the attempted surface modification strategies of the inorganic GdF_3 nanoparticles are presented.

CHAPTER 3

Surface Modification of GdF_3 Nanoparticles

Content

I – Introduction to surface modification of nanoparticles

I.1 - Stabilization of colloids

Stability of aqueous colloidal suspensions is described by the so-called DLVO theory (named after Boris Derjaguin and Lev Landau, Evert Verwey and Theodoor Overbeek).[135] According to this theory, the net interaction energy between two particles is the combination of attractive van der Waals and repulsive electrostatic forces. The particles having kinetic energy (thermal energy) are subjected to Brownian motion; therefore, they collide continuously with each other. In the meantime, colloidal particles tend to associate in order to reduce their surface area, and without any restricting factors, they can approach each other so close, that the attractive van der Waals forces are capable to joint them irreversibly, leading to their aggregation and the destruction of the dispersion (the aggregates precipitate). Alternatively, if there is a source of interparticle repulsion capable of preventing particles from immediate contact, the dispersion will be stable.

Usually, we want to maximize the repulsive forces between the particles in order to prevent their gathering into fast settling aggregates. It is possible to prevent instability of particles by modifying their surface, for example, by adding a polymer coating layer. Three main coating strategies are used in aqueous medium: electrostatic, steric[136] and their combination, the electrosteric method.[137] In the following sections, these stabilization strategies are briefly described.

I.1.1 Electrostatic stabilization

Let us consider a particle characterized by an excess of positive charges on the surface, such as shown in ***Scheme 1***. In solution, this charged surface is surrounded by a compact and firmly attached layer of counter-ions, called the Stern layer. Out of this layer, in the vicinity of the particle, negative counter-ions are still attracted by the positively charged particle but are also repelled by negative ions forming the Stern layer. In the meantime, this layer attracts positive ions. This dynamic equilibrium creates a diffuse cloud of counter-ions, called the diffuse layer. Negative ion concentration in this layer decreases gradually until it reaches equilibrium concentration with the bulk phase of the solvent. Stern and diffuse layers together form the so-called electric double layer, which is a layer of liquid moving along with the particle. The

thickness of this layer depends on the counter-ion concentration and type: high electrolyte concentration (*e.g.,* the addition of salts) for example, compresses the double layer (***Scheme 1***).

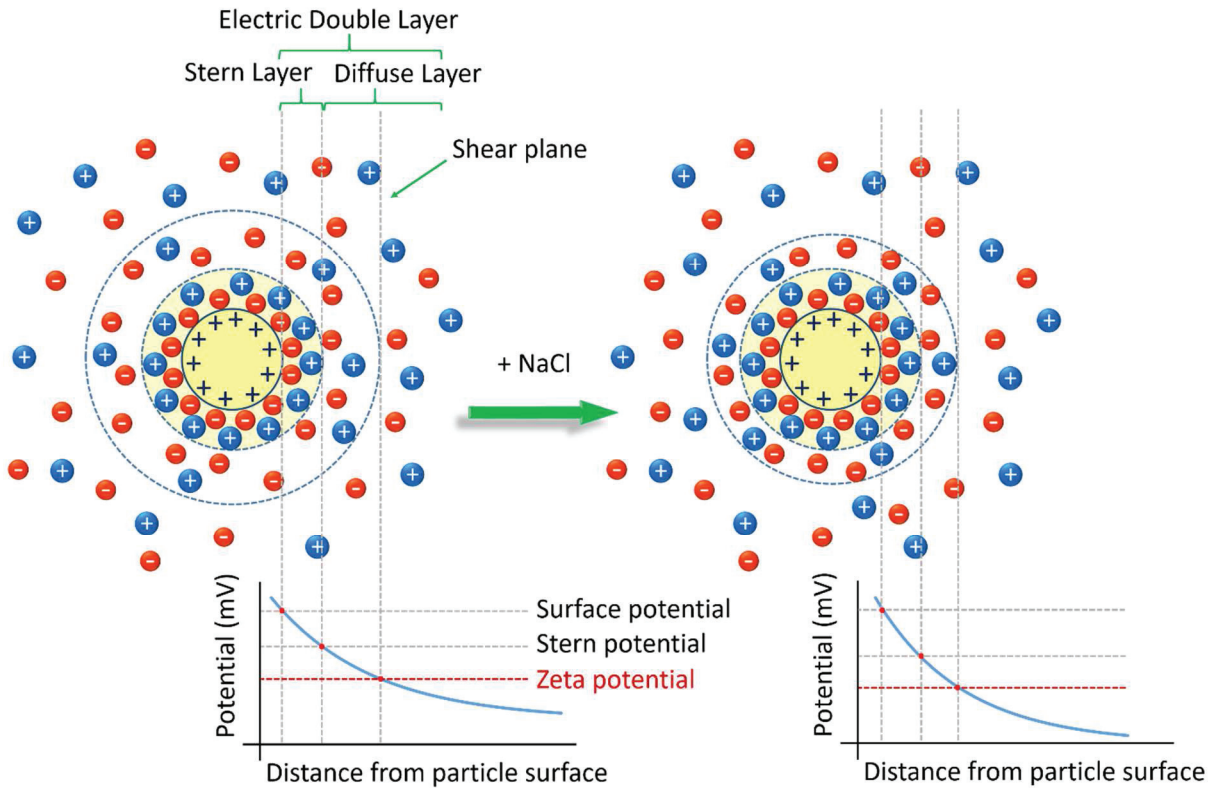

Scheme 1 The electric double layer formed around a positively charged particle is represented, with the corresponding energy potential curve. The double layer is compressed in the presence of high salt concentration.

When two particles approach each other, the existence of this double layer constitutes an energy barrier, preventing them from aggregation, provided that the double layer is thick enough. This is the principle of the so-called electrostatic stabilization, which can be quantified by electrophoretic light scattering measurements. The surface potential created by surface charges cannot be directly detected because of the thin layer of attached liquid with ions around the particles (electric double layer). However, it is possible to detect the potential at the boundary beyond which ions are not following the particle. This boundary is a surface of the hydrodynamic shear plane or slipping plane. The potential attributed to this plane is called zeta potential (ZP, units: mV) and is determined by applying an electric field to the nanoparticle dispersion and measuring its electrophoretic mobility. The absolute value of ZP provides information about the electrostatic repulsive forces, *i.e.,* the electrostatic stabilization of the particles. It is usually considered that colloids with ZP value of ±0 — 10 mV are unstable, ±10 — 20 mV is relatively stable, ±20 — 30 mV is moderately stable, and ≥ ±30 mV is highly stable.[138] This rule of thumb must be considered with care, because, as we will see in the next

paragraphs, other factors influence the stability. Therefore, a particle having a ZP absolute value close to zero can be stable indeed. Also, the effective ZP is influenced by the pH, concentration, and electrolyte concentration (ionic strength) in the liquid medium. At high salt concentrations (for example in the physiological medium $[Na^+] = [Cl^-] = 154$ mmol/L), the electrical double layer collapses (***Scheme 1***), which reduces the ZP, making it difficult to measure.

I.1.2 Steric stabilization

Steric stabilization consists of using nonionic macromolecules, which can be anchored or simply adsorbed on the particle surface and prevent particles surfaces coming into close contact. The basic idea behind this strategy is, when polymer-coated nanoparticles approach each other, the polymer chains in contact are confined to a smaller volume. This loss of freedom is entropically unfavorable; therefore, the interpenetration of polymer chains is limited, and this leads to an efficient repulsion preventing particle aggregation.[136] The efficiency of this repulsion is dependent on chain length, polymer solubility, and surface coverage as well. For example, if the chains are not long enough to keep particles at a distance, where van der Waals forces are weak, the colloid will not be stable. The solvent is also playing a key role in steric stabilization. For a maximum degree of freedom, the polymeric chain must be fully solvated by the medium, so that it can fully extend. If the chains are not sufficiently solvated, they collapse on the particle surface, allowing aggregation. Another case if the polymeric moieties have a higher affinity to each other than to the solvent, particles will tend to aggregate even with long chain polymers. On the other hand, when polymer chains intermingle, solvent molecules are excluded from the interaction volume, creating an osmotic pressure between this volume and the bulk solvent phase. The solvent is forced to flow back, hence favoring the separation between the particles.[136] Surface coverage density is also very important: if polymer concentration on the surface is low and the chain length is high compared to the particle dimensions, one chain can adsorb on more than one particle, creating a bridge between the particles and making them flocculate.

I.1.3 Electrosteric stabilization

There are cases when the electric double layer barrier is too low to stabilize the colloid, therefore another strategy of stabilization also involving steric stabilization has been developed. The combined effect of electrostatic and steric stabilization is typically achieved by polyelectrolyte or polyampholyte brushes, *i.e.,* polymers with one or several ionizable groups.[137] Typically, in biological media, the relatively high electrolyte concentration may destabilize the electric

double layer, and if there is no steric repulsion to maintain the particles separately, they form aggregates. Conversely, steric stabilization is not as sensitive to salt concentration.

I.1.4 Anchoring

The dispersing polymers are attached to the nanoparticles *via* different types of interactions, which are briefly summarized here.

- Physisorption. Polyelectrolytes, such as dextran, chitosan or alginate interact with charged nanoparticle surface (e.g., iron oxide) through Coulombic attraction. These polymers form a passivation layer around the particle and prevent aggregation. However, this type of adsorption is reversible. The adsorbed polymers are in equilibrium with free polymers in the solution, thus upon dilution or filtration, they desorb. This insufficient anchor is not acceptable for nanoparticles intended to biological applications, because *in vitro* or *in vivo* applications always involve high dilutions.
- Covalent linkages. Probably the most robust anchoring is achieved by covalent linkage to the nanoparticle surface, which can be done by two different approaches, referred to as "grafting from" and "grafting to" strategies. In the "grafting from" method, the polymer is directly grown from the initiator-functionalized surface. This method results usually in higher grafting density (polymer brushes). In this case, the entropy loss of the polymers due to their close packing is compensated by the strong driving force of covalent bonding.[139] Besides, in the "grafting to" strategy, the polymer is synthesized separately and equipped with a required functional group that can react with the functionalities on the nanoparticle surface. In this case, the interchain steric repulsion and competition with other molecules in solution (solvent for example) does not allow the growth of dense polymer brushes coating. A typical example of covalent attachment by "grafting to" method is the reaction of alkoxysilane functional group on the ligand and OH-group on iron oxide nanoparticle surface.
- Chemisorption. The end-functionalized polymer may be attached to the surface by coordinative bonds, such as metal-ligand interaction or by H-bonding. Here the anchoring functional group must have high affinity to surface functionalities, in order to obtain a robust coating. Carboxylic or phosphonic acid functions are often used for anchoring ligands to iron-oxide nanoparticles. Multivalent functional groups have increased ligand-metal interactions, resulting in stronger binding.[140] The advantage of this method is that polymer chains with the desired characteristics can be synthesized and purified before being grafted on the particle.

Once the dispersing polymer is adsorbed on the particle surface, it is highly undesirable that it desorbs easily. Therefore, the choice of anchoring is critical for coating robustness and must consider the nature of surface functionalities. Poor surface functionalization leads to aggregation of particles. Besides the strong anchoring, grafting density (*i.e.,* covered surface) is also of key importance for colloidal stability. Reversibly attached polymers are in equilibrium with the free polymer in solution, as a consequence, upon dilution, dialysis or filtration, induce important ligand desorption.[140] This process is of particular importance when the grafted particles are used *in vivo*. When the suspension is introduced in a living body, it always undergoes high dilution, causing insufficiently anchored ligand desorption and leading to agglomeration and protein adsorption on the particles.

I.1.5 Grafting density

The number of polymers per unit surface area (*i.e.,* grafting density) is a central parameter for the particle stability and hydrodynamic size. However, an accurate determination of such a number requires knowledge of the footprint, *i.e.,* the effective surface that occupies one ligand, which is a complex theoretical challenge. Therefore, instead of considering the surface density, it is common to compare surface coverage in terms of the number of ligands per particle.

In biological applications, the medium (blood for example) is characterized by high electrolyte concentration, which can destabilize poorly coated particles. Therefore, long circulation time and improved stealth properties are achieved with a high quality of surface coverage. The hydrodynamic size is also affected by polymer concentration on the particle surface, *via* chain lengths. Alexander[141] and de Gennes[142] first established a theoretical description of the density profile of polymers adsorbed on a flat surface, which was followed by several other theoretical works resulting in refined models, including highly curved surfaces, such as nanoparticles.[140] Nevertheless, due to the lack of experimental data on irreversibly adsorbed polymers on a highly curved surface, universally applicable grafting density profile is still a matter of debate. However, all these theories are based on the fundamental idea, that the grafting density and the nature of interactions between the polymer chains are closely related. For example, at very low polymer densities on the surface, the chains do not interact with each other, but if the chains are closely packed, the interchain interactions are important and determine the elongation of the chains, *i.e.,* the hydrodynamic size of the core-shell particle.

In a polymer solution, three types of interactions are competing: polymer-solvent, polymer-polymer, and solvent-solvent. These interactions determine the size of the polymer. The Flory-

Huggins theory[143] gives a thermodynamic model describing the energetic aspects of such a mixture. In this model, the polymer is characterized by its radius of gyration, R_G, which is approximated by a power law of the degree of polymerization, *i.e.,* the number of segments or monomers, *N*:

Equation 23

$$R_G \sim N^{\nu}$$

where ν is called the Flory-exponent. The value of ν for good solvents is 3/5 and for bad solvents is 1/3. The physical meaning behind that is in a good solvent, the polymer chain is swollen, expanded, and the solvent-chain contact is maximized; therefore, the chain is in a coil conformation with large size. The interactions between the chain segments (monomers) can be modeled in this case, by the so-called excluded volume interaction model introduced by Werner Kuhn, in 1934, which assumes, that two segments cannot occupy the same space at the same time. This model shows that the chain collapses resulting in a globular conformation, (hard sphere) when unfavorable polymer-solvent interactions (bad solvent) overcome the excluded volume effect. In the globular state polymer chains tend to aggregate and for a given temperature-polymer content, a microscopic phase separation happens, which is characterized by the so-called cloud point. At this point, the polymer solution becomes turbid. The coil state can be turned into the globule state in the same solvent, simply by changing the temperature. At the transition point (the so-called theta temperature) the polymer chain behaves as if it was an ideal chain and can be described by a random walk model (all bonds and torsion angles are equiprobable). The solvent is then called a theta solvent, and the corresponding Flory-exponent value is 1/2. At this point, the polymer is at the edge of solubility. The excluded volume expansion is canceled by the unfavorable interactions with the theta solvent, and the volume occupied by the chain is decreased compared to the coil state.

When polymers are attached to surfaces by endpoint grafting, the grafting density depends on the contribution of the resulting polymer-solvent, polymer-polymer, solvent-solvent interactions, but also on the polymer anchoring group affinity for the surface, which leads to three distinct grafting regimes,[139] schematically represented on ***Scheme 2***.

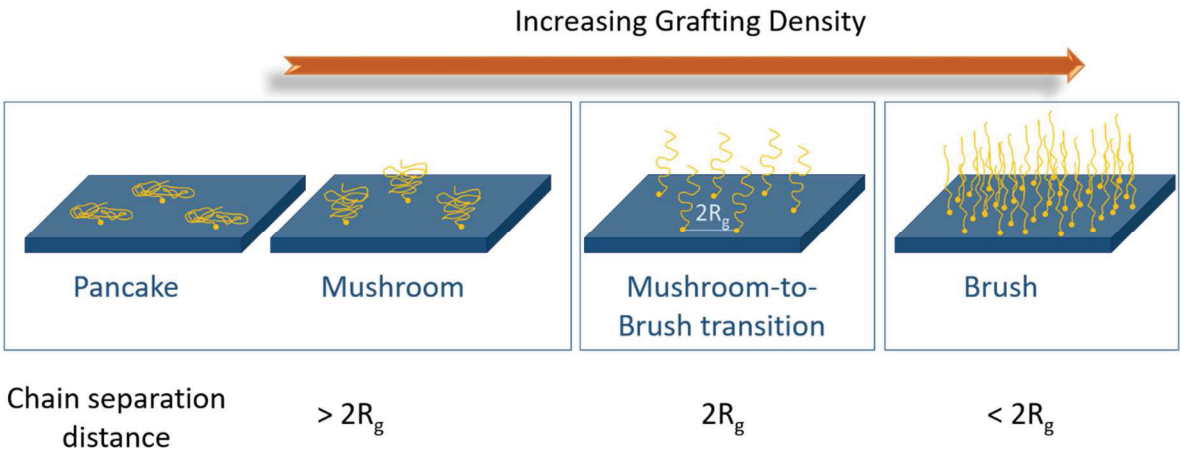

Scheme 2 Different conformations of tethered polymer coating on a solid surface. The conformation varies with the grafting density from mushroom (low density) to brush (high density).

At a critical value of density (low density), defined as the density corresponding to a chain separation distance on the surface equals to $2R_G$ of the chains, the chains start to interact with each other. Below this critical distance, the adsorbed chains are in the extended coil conformation, which is often referred to as "mushroom regime". If the polymer segments have high affinity to the surface or if the solvent is a "bad solvent" for the polymer, the chain is lying on the surface. This is called the "pancake regime". At high grafting density (above the critical value), in the "brush regime", the chains are forced to stretch away from the surface to avoid overlap between each other, forming a densely packed brush-like layer. As already mentioned, the latter regime is usually obtained by the "grafting from" instead of the "grafting to" method, because attachment of free polymers is not favored by the already tethered chains in the latter case. However, it is possible to generate a brush layer on the surface, with the "grafting to" method, by grafting brush-like copolymers. For linear chain polymers grafting density can be increased if the polymer volume is reduced when grafting it to the surface by generating theta solvent conditions[144] or even at the cloud point[145,146] of the polymer. In the experimental part, we will see that this effect is exploited in our grafting procedure.

Control of grafting density is important because it determines the polymer layer thickness: high density induces stretched polymer chains, hence increasing the layer thickness, which is observable on the increase of the hydrodynamic size of the core-shell nanoparticle.

I.2 - Surface Modification with phosphonate and bisphosphonate ligands

To obtain an electrosteric stabilization, head-tail architecture is a very efficient strategy. The head group anchors the ligand, and the tail is compatible with the solvent of application (*e.g.,* water for biology). Therefore, the choice of the anchoring moiety must be oriented towards chemical species presenting strong binding affinity to surface atoms/ions. For lanthanide-based inorganic nanoparticles carboxylic[147,148] or phosphonic acid[149] terminal groups are often used to ensure anchoring, but different surface modifications with multi-dentate chelating ligands are also reported.[117,150] In biological applications, highly biocompatible and sometimes bioactive ligands are required. Bisphosphonate compounds are one example reported for iron oxide[16] or gadolinium phosphate nanoparticles.[17] Phosphonate and bisphosphonate have a very strong affinity for lanthanide ions. Based on experimental results, Nash *et al.*[153] calculated the speciation for europium complexes with different chelating agents, such as oxalate, EDTA, citrate, PAA, etc. and found that bisphosphonate (called diphosphonate at that time) forms the most stable complexes. They ascertain, that compared to ligands terminated with one carboxylic acid group bisphosphonate complexes are 10^2 to 10^5 stronger. It is attributed to the presence of four oxygen donor atoms as opposed to two in carboxylates and the polar nature of the P=O bond. ***Scheme 3*** shows the possible binding modes of phosphonates on metal oxide surfaces. The possible coordination motifs via multiple bonds, include mono-, di- and tridentate coordination and H-boding as well.[154] Binding ability is even more versatile for bisphosphonates.

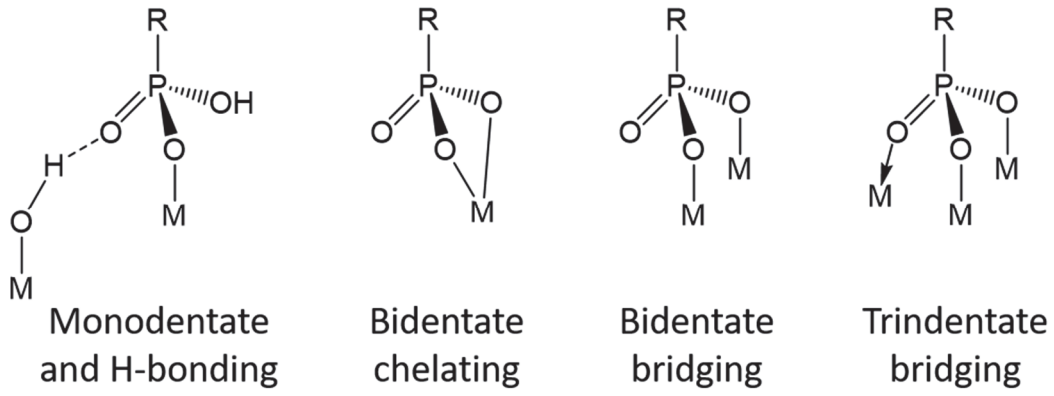

Scheme 3 Examples of the possible coordination modes of the phosphonate group on an inorganic surface. Adapted from ref. [154]

As Ca^{2+} ion (R^{ion} = 0.099 nm), Gd^{3+} ion (R^{ion} = 0.094 nm) is relatively small with a high charge density, which classifies it into the hard Lewis acid group of ions, therefore it shows a marked

preference for Lewis basic oxygen donor atoms.[155] Furthermore, it has been demonstrated that the thermodynamic stability of Gd^{3+} complexes increases linearly with ligand basicity, which is higher for phosphonates than for carboxylates.[156] Phosphonate molecules are characterized by two pKa values corresponding to the deprotonation of the two OH groups. For small molecules, pKa_1 is around 2.4, and pKa_2 is 7.5,[157], and these values may vary slightly with different substituent groups. Lamanna *et al.*[158] elaborated dendritic phosphonate ligands with pKa values of 3.1 and 5.4 for functionalization of iron oxide nanoparticles. The dendritic shell is strongly attached to the particles when grafted at a pH higher than the pKa values. The initially positively charged nanoparticles (ZP = + 38 mV) acquire a negative zeta potential (-16 mV) upon coating, due to the negatively charged phosphonate groups.

In the literature, several other studies are reported, which compare the anchoring strength of phosphonates and carboxylates on nanoparticles — for example, Illés *et al.*[159] studied the stability of biocompatible core-shell magnetite nanoparticles, PEGylated with three different anchoring, carboxylate (PEG-C), phosphonate (PEG-P) and a comb-like polymer with acrylic acid functionalities combined with PEG pendant groups (PEGA-AA). They observed that PEG-C coated particles have the same aggregation behavior than the naked particles even at high PEG-loading, while in the case of PEG-P and PEGA-AA, 0.5 mmol/g nanoparticle was enough to stabilize the hydrodynamic diameter and polydispersity. By examining surface charge changes at pH~6.5, they found that upon increasing the PEG-C polymer loading, the zeta potential of the particles was unchanged compared to the naked particles. As opposed, while increasing the two other polymer amount, the positive surface charges (ZP ~ +30 mV) of the particles are gradually neutralized (at approximatively 0.15 mmol/g particle), and subsequently overpassed to achieve a highly negative zeta potential (ZP ~ -35 mV) for a polymer loading of 0.5 mmol/g particle. This could be attributed to the difference in free dissociable groups providing extra charges for the electrostatic stabilization: PEG-C has no extra charges, whereas multiple carboxylic acid functions on the same backbone for PEGA-AA and multivalence of phosphonate both result in free negative charges. Therefore, PEG-P and PEGA-AA electrosterically stabilize the particles, which is proved by the constant hydrodynamic size of coated particles over a wide pH range (pH 4-10). The general conclusion of this work is that both nature and number of anchoring groups on one chain determine the stability of nanoparticles.

Qi *et al.*[160] reported phosphonate-terminated PEG (abbreviated as PPEG) oligomer grafting onto cerium oxide nanoparticles and grafting efficiency as a function of pH. At pH = 1.5, CeO_2

is cationically charged (Ce-OH_2^+), and PPEG is only slightly anionic ($pK_1 = 2.7$), but the 270 PPEG chains per NP providing a 1.6 nm thick shell (bare NP diameter is 9.2 and coated NP is 12.3 nm) provided very good stability. At pH 6.5, particles are less charged, and approximately 50% of PPEG ligands are anionically charged ($pK_2 = 7.8$), which resulted in a lower number of adsorbed ligands. The authors explain it by the electrostatic repulsion between the charged ligands while grafting onto the surface. However, the coated NPs were again stable during weak-long dialysis, suggesting, that the particles' surface is protected by less, but more flat (smaller hydrodynamic size) oligomers and it confirms, that phosphonate groups are strongly anchored to CeO_2 NP surface.

Bisphosphonates, with two phosphonate functions, constitute an even more effective attachment with multidentate chelating of one single anchoring group. It was observed in the late sixties, that bisphosphonates, chemically stable analogs of inorganic pyrophosphates naturally present in living bodies, can retard the growth and also the dissolution of hydroxyapatite crystals.[161] Following these first observations, their clinical use was rapidly developed, and today, BPs are the treatment of choice for metabolic bone diseases. Their medical application is related to a strong binding to Ca^{2+} ions. BP molecules are built up on a P-C-P skeletal, which prevents their enzymatic hydrolysis, unlike its naturally occurring pyrophosphate analog (ATP hydrolysis) and confers on them high chemical resistance. Their high binding affinity for calcium and other di- and trivalent minerals (*e.g.,* Mg^{2+}, Fe^{3+}, Al^{3+}) *via* the two phosphonates is enhanced by a hydroxyl group on the geminal carbon atom, creating a multi-dentate chelating bond.[162] The specific role of this -OH group was demonstrated by comparison of BP-metal complex stabilities obtained with other substituents (like Cl or H) on the (P-)C(-P) carbon in the molecule.[155] Gumienna-Kontecka *et al*.[163] studied complexation pattern of R-BP molecules (R = methyl, phenyl, and benzyl) with Al^{3+} and Fe^{3+} ions, as a function of pH and determined the stability constants, which were higher than for the clinically used, iron-chelating agent, deferiprone. Based on potentiometric titration, only three protonation constants could be accurately determined for these BP-ligands, because pKa_4 is much below 2 and the hydroxyl group on the carbon atom is very weakly acidic and does not deprotonate below pH = 13. The authors concluded, that below pH = 4 bis-complexes are formed, while above this pH, the equimolar (monomeric for Al^{3+} and dimeric for Fe^{3+}) complexes are the dominant species. This shows that besides steric hindrance high electric charge of the deprotonated ligands also influences the complex stoichiometry. Iron oxide nanoparticle coating with a clinically used bisphosphonate, zolendronate was found to be more

efficient at pH 7.4, than at acidic pH (~3).[164] The pKa values for the phosphonate part of this compound are 0.8, 2.89, 6.63 and 10.99, therefore, between pH = 3 and 6.6, only two oxygen atoms of bisphosphonate are deprotonated, while above pH = 6.6, three negative charges are present on the ligand, resulting in the electrostatic stabilization of the particles.

Given these numerous examples mentioned, one can easily conclude, that phosphonates and bisphosphonates are highly suitable as anchors for gadolinium-based nanoparticle functionalization. In the following paragraphs, we will strive to further strengthen this assumption and demonstrate that in the case of GdF_3 NPs specific BP-PEG ligands provide high stability.

II – Results and discussion

II.1 Phosphonate and bisphosphonate coating

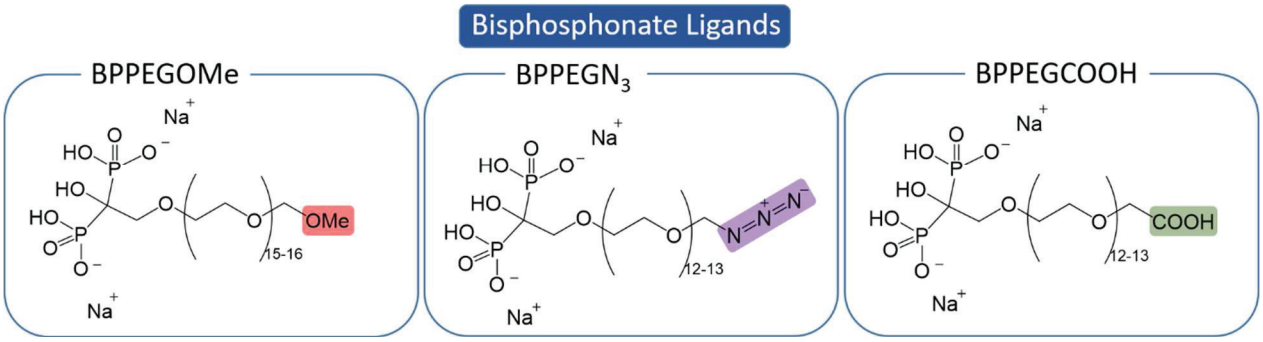

Scheme 4 Bisphosphonate-PEG ligands used for coating GdF_3 nanoparticles in this work.

Bifunctional bisphosphonate-PEG ligands synthesis was developed by Professor Marc Lecouvey's team (Université Paris 13, CSPBAT CNRS UMR 7244).[165] As partners in the NanoBrain ANR project, this team provided the ligands shown in ***Scheme 4***. These ligands are constituted by a PEG chain of approximately the same size (BPPEGOMe is slightly longer) which is functionalized on one end by a bisphosphonate group, providing the anchoring part of the ligand. The other end group is varying. BPPEGOMe is functionalized by the neutral methoxy group. Therefore, this ligand does not participate in any further surface modification of the particle. In contrast, $BPPEGN_3$ and BPPEGCOOH are functionalized by a reactive group, allowing to attach additional molecules to the nanoparticle.

These ligands were grafted onto two lanthanide fluoride nanoparticle cores, in different proportions. Composition and nomenclature of the obtained hybrid nanoobjects are summarized in ***Table 3***.

Table 3 Surface modified nanoparticles: BPPEG ligand grafted on lanthanide fluoride inorganic cores in different proportions.

Functionalized NP*	Core	BPPEGOMe (mol%)	$BPPEGN_3$ (mol%)	BPPEGCOOH (mol%)
Lu-100/0/0	LuF_3	100	0	0
Lu-95/0/5		95	0	5
Lu-0/0/100		0	0	100
Lu-50/50/0		50	50	0
Gd-95/5/0	GdF_3	95	5	0
Gd-90/10/0		90	10	0
Gd-90/5/5		90	5	5
Gd-50/50/0		50	50	0
Gd-10/90/0		10	90	0

*Letters refer to the lanthanide composing the inorganic core (Gd for GdF_3 and Lu for LuF_3), and the numbers give the relative ligand proportions. The first number gives the proportion of BPPEGOMe, the second gives $BPPEGN_3$ proportion, and the last number indicates BPPEGCOOH content.

Lutetium has very similar chemistry to gadolinium but is much less paramagnetic; therefore, lutetium-based nanoparticles were prepared as model compounds for NMR-studies.

II.1.1 Experimental conditions

The previously prepared inorganic nanoparticles (cores) were stored in a concentrated (20 – 50 wt%) aqueous suspension or as a powder obtained after freeze-drying process. For suspensions, the solid content was determined before the surface modification step, and the volume containing the required quantity of GdF_3 was withdrawn. Typically, to get 600 mg of GdF_3 ($n_{GdF3} = 2.80 \cdot 10^{-3}$ mol) from a solution with a solid content of 24 wt%, 2500 mg (approximately 2.4 mL) of the solution must be taken. For powders, the required quantity of solid was suspended in water (typically,100 mg of solid suspended in 500 µL of water).

The nanoparticle suspension was then added to a solution of the ligand, with a molar ratio of 1 ligand for 3 Gd^{3+}. This ratio was previously optimized during the thesis work of Francis Mpambani.[166] For example, in the case of the composition Gd-95/5/0, the amount of GdF_3 was 1200 mg in approximately 4.4 mL of water. This suspension was added to a solution containing 82 mg ($0.05*n_{GdF3}/3$) of $BPPEGN_3$ and 1930 mg ($0.95*n_{GdF3}/3$) of BPPEGOMe, dissolved in 16 mL of water. The mixture was vigorously stirred and heated to 80°C during 1 to 2 hours. The surface modified particle suspension was then transferred to a dialysis membrane (12-14 kDa molecular weight cutoff) for unreacted ligand removal. The typical dialysis time was five days. After purification, the sample was freeze-dried, and the white powder was stored in the solid state to improve the shelf life expectancy.

Example of the synthetic procedure for GdF_3 NP surface modification: **Gd-95/5/0**

- NP suspension: 2.584 g (approx. 2.4 mL) of GdF3 suspension of 24 wt%, corresponding to 0.620 mg of solid
- Ligand solution: 47 mg of $BPPEGN_3$ and 900 mg BPPEGOMe dissolved in 9 mL of water

After homogenization of each solution, the particle suspension was added under ultrasound mixing. The obtained mixture was heated to 80°C for 2h. After cooling the product was purified by dialysis (5 days) and the obtained solid was freeze-dried.

II.1.2 Characterization of surface modified particles

II.1.2.1 Surface modification with BPPEG- ligands

Grafting of BPPEG- ligands was verified by FTIR-ATR spectroscopy, thermogravimetric analysis (TGA), zeta-potential (ZP) and XPS measurements. Size modifications were followed by dynamic light scattering (DLS). Before analyzing ATR spectra of the particle, let us have a careful look at the free ligands spectra shown in ***Figure 36*** and the characteristic vibrations, we are interested in for the grafting.

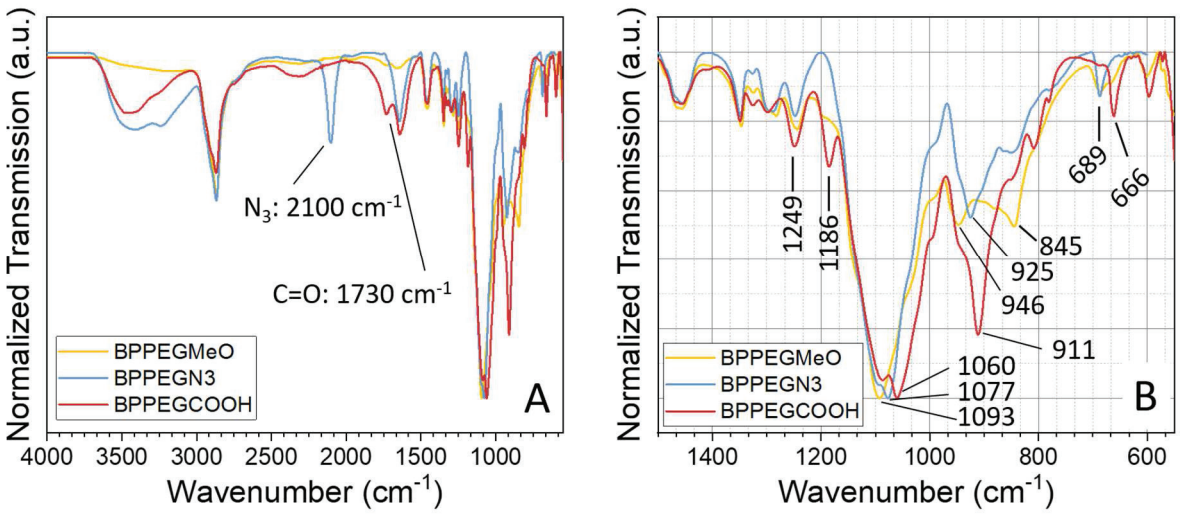

Figure 36 ATR spectra of free ligands from 550 to 4000 cm^{-1} (A) and the enlarged to the range 550 to 1500 cm^{-1} (B).

The characteristic bands of the terminal N_3 in $BPPEGN_3$ and C=O in BPPEGCOOH appears at 2100 cm^{-1} and 1730 cm^{-1} respectively. Despite a large overlap of bands attributed to ethylene glycol moieties, some differences appear in bisphosphonate vibrations in the fingerprint region (***Figure 36***B). However, we can distinguish four characteristic regions: bands at 1249 and 1186 cm^{-1} correspond to the P=O stretching vibrations, between 1050 and 1100 cm^{-1}, the overlapping P-O and C-O stretching vibrations are present, and the band between 911 and 845 cm^{-1} correspond to P-OH vibrations overlapping with methylene ($-CH_2-$) rocking

vibrations.[167,168] Finally, the P-O-H bending appears at 666 and 689 cm^{-1}. Varga *et al.*[169] studied the structure of PEG layer employing FTIR and identified the high-intensity doublet (not resolved) band at 1093 cm^{-1} as the ether C-O-C stretching vibration characteristic of gauche and trans conformations of PEG chain fragments.

The example of the composition NP@50%BPPEGOMe-50%$BPPEGN_3$ was selected (***Figure 37***A), to examine the general aspect of a grafted nanoparticle spectrum and the superimposition of the spectra of GdF_3 nanoparticles and their LuF_3 equivalents shows a perfect match between the two, supporting that the latter one can be used as a model compound in NMR studies. Importantly, it confirms the reproducibility of the grafting process.

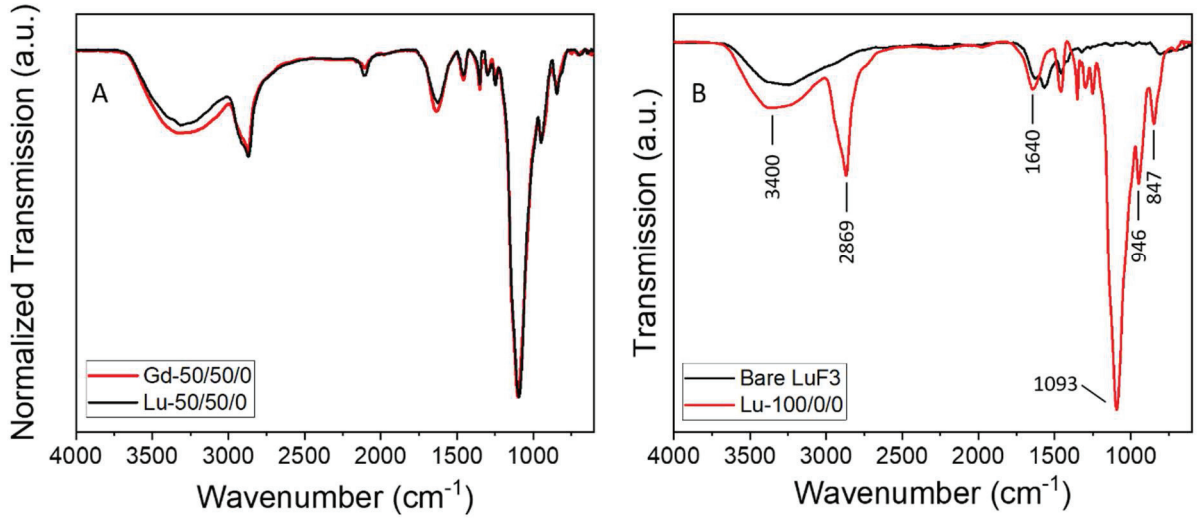

Figure 37 A) Comparison of ATR spectra of GdF_3 and LuF_3 particles coated with 50% BPPEGOMe and 50% $BPPEGN_3$ ligands. B) Bare and BPPEGOMe-coated LuF_3 nanoparticles ATR spectra.

Figure 37B compares LuF_3 nanoparticle spectrum before (bare NP) and after BPPEGOMe-coating. The characteristic vibrations of poly(ethylene) glycol and bisphosphonate moieties are clearly visible in the spectrum of the coated particle, evidencing the presence of BPPEG- ligands on the surface. A broad band centered at 3400 cm^{-1} (OH stretching) is due to the presence of adsorbed water molecules on the particles, despite their careful drying. Bending vibration of adsorbed water also appears as a sharp band at 1640 cm^{-1}.[170] The 2869 cm^{-1} band is attributed to C-H stretching of PEG moieties. These bands are observable on all grafted particles, evidencing BPPEG ligands on the surface.

In the fingerprint region (600-1500 cm^{-1}), comparison of the spectrum of Lu-100/0/0 to free BPPEGOMe ligand spectrum (***Figure 38***) shows some significant differences. Again, the characteristic bands of PEG and bisphosphonate moieties are highly overlapping; therefore, it is difficult to assign each vibration, but shape reorganization and intensity decrease of bands in

the range 900-1000 cm^{-1} corresponding to the P-O stretching vibrations[169,171–173] indicate coordination of bisphosphonate to the nanoparticle. This coordination is further supported by a significant decrease in intensity and a slight shift of P-O-H bending vibrations. The small intensity peak at 1250 cm^{-1} was assigned by several authors to ν(P=O).[171,172] This band does not change upon grafting reaction, indicating, that P=O does not participate in any coordination.

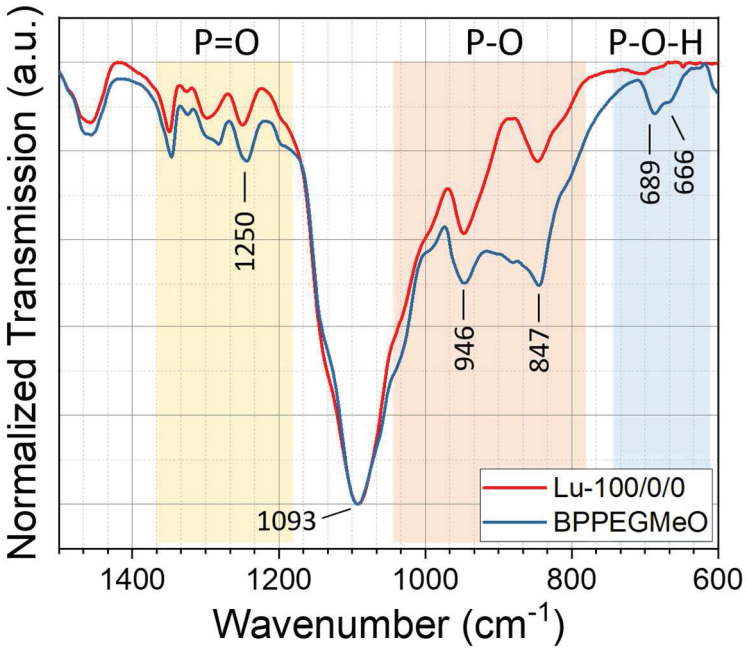

Figure 38 ATR spectra of free BPPEGOMe and LuF_3 nanoparticle coated with the same ligand.

Figure 39 shows the fingerprint region observed for GdF_3 particles coated with the three BPPEG- ligands in different proportions. Despite the slight differences in free ligand spectra, upon grafting, a very similar IR signature is obtained for blended PEG chains-modified nanoparticles (coated with a mixture of BPPEGOMe and $BPPEGN_3$) and for particles decorated with exclusively BPPEGOMe (see ***Figure 38***). This similarity is not unexpected, as the same coordination motif is assumed for all BPPEG- ligands.

In the region 1900-2300 cm^{-1}, the characteristic band of the azide group (N_3) appears at 2100 cm^{-1}, and as it is shown in ***Figure 40***, its relative intensity increases with the increasing $BPPEGN_3$ ligand proportion. Once again, the reproducibility of the grafting efficiency is observed when comparing Gd-95/5/0 and Gd-90/5/5, which are two batches of particles, both containing 5% of $BPPEGN_3$.

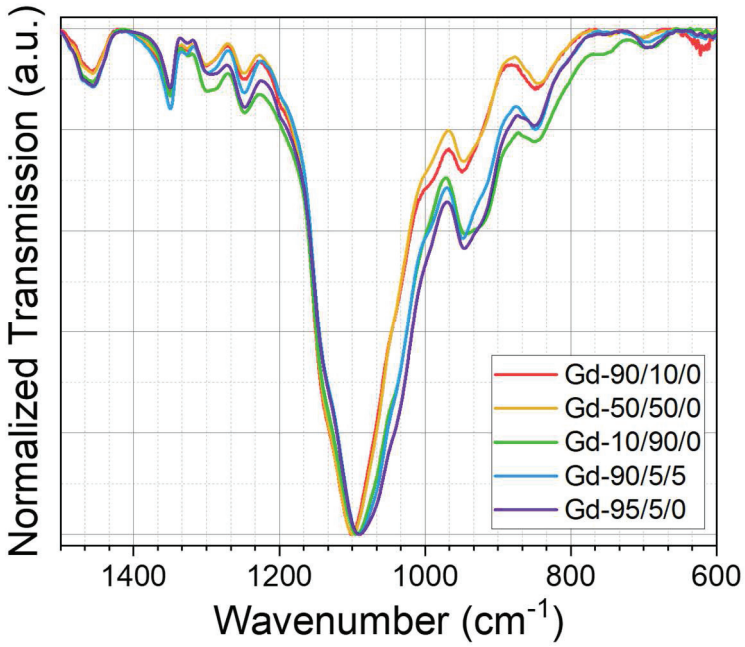

Figure 39 ATR spectra from 660 to 1500 cm^{-1}. Comparison of the GdF_3 particles coated with BPPEGOMe and $BPPEGN_3$ ligands in different proportions.

One exception is Gd-90/10/0, where the band is not observed, probably due to the low signal to noise ratio of this spectrum.

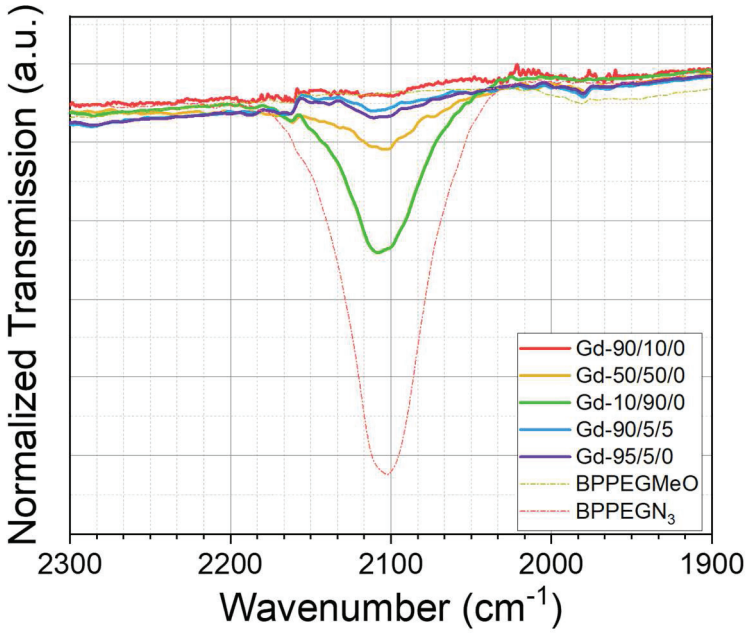

Figure 40 ATR spectra from 1900 to 2300 cm^{-1}. The relative intensity of the N_3 band increases with $BPPEGN_3$ ligand content.

Interestingly, the C=O band at 1730 cm^{-1} is not apparent in the spectrum of Lu-0/0/100 (***Figure 41***A), nanoparticles functionalized only with BPPEGCOOH. The deconvolution (***Figure 41***B) of the band peaking at 1632 cm^{-1} reveals three hidden peaks at 1726, 1646 and 1615 cm^{-1}. The

one at 1646 cm^{-1} corresponds to adsorbed water, and only a small intensity band is found at 1726 cm^{-1}, corresponding to the carbonyl stretching vibration, νC=O. However, the most intense band at 1615 cm^{-1} may be assigned to $\nu_{asym}(COO^{-})$, which suggests that the grafted BPPEGCOOH ligands are not only coordinated via the bisphosphonate terminal group but also by the carboxylate end.

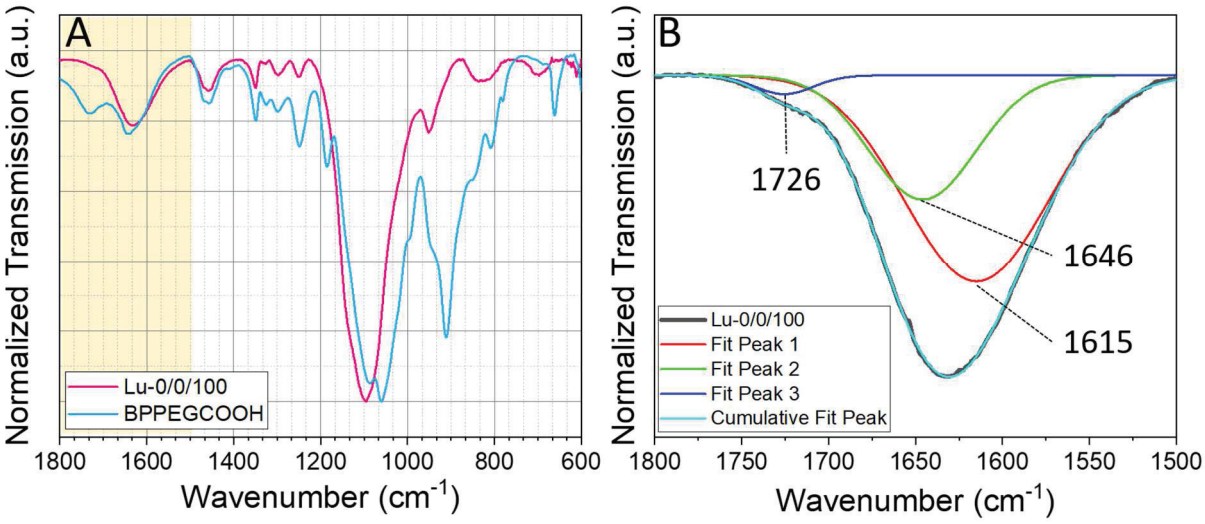

Figure 41 A) ATR spectra of LuF_3 particles coated with BPPEGCOOH and free BPPEGCOOH ligand. B) The peak corresponding to the carboxylate vibration is deconvoluted to three components, corresponding each to a different species.

Conclusions from ATR analysis

- The grafting process is reproducible
- Even after freeze-drying, adsorbed water is present on the particle surface
- The characteristic bands of PEG in the spectra support the successful grafting
- The bands of the functional group BP and PEG are overlaping, which makes it difficult to determine the exact coordination mode of BP anchoring group
- The P=O moiety in BP group does not seem to participate in coordination
- The characteristic band of N_3 appears in the spectra and the intensity evolution of the band seems to correlate the quantity of $BPPEGN_3$ ligand
- In the case of BPPEGCOOH, both BP and COOH groups are coordinated

Thermogravimetric analyses were performed on surface modified particles and compared to the bare nanoparticles to evaluate the mass of organic shell grafted. ***Figure 42*** shows the example of TGA analysis for Gd-95/5/0 nanoparticles. The weight loss for bare nanoparticles, due to the presence of small organic molecules was 8.5 %, while the coated particles lost 29.3 %. From 100 to 150°C water evaporation takes place. Then, the most important weight loss occurs

between 150 and 263°C (maximum of the first derivative peak is at 190°C), which is closely followed by a smaller peak around 292°C. These two losses correspond to PEG decomposition essentially and some trapped water evaporation. The small peak at 486°C may be attributed to phosphonate containing decomposition products.[174]

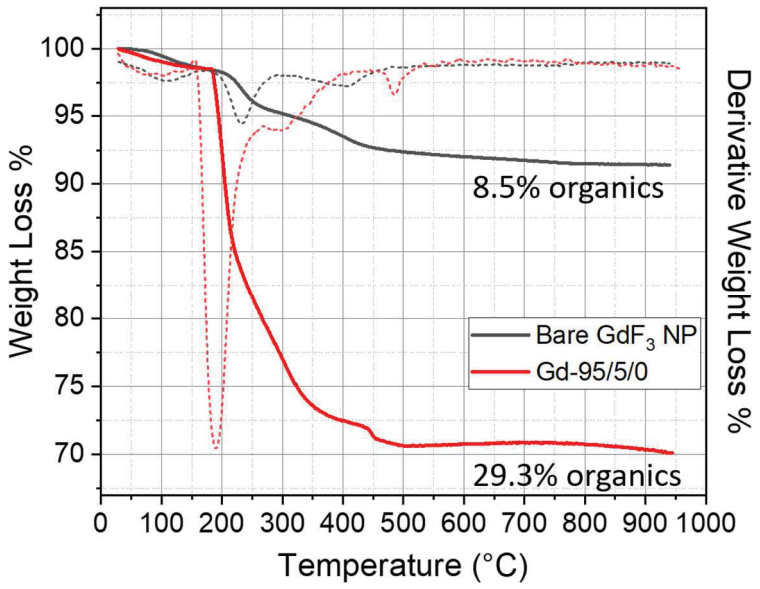

Figure 42 TGA curves (solid lines) for bare GdF_3 nanoparticles and coated with 95% of BPPEGOMe and 5% of $BPPEGN_3$ ligands. The heating rate was 10°C/min. Dashed lines represent the derivative curves.

Conclusions from TGA analysis

The measured organic content of Gd-95/5/0 nanoparticles was 29.3 wt%, which is significantly higher compared to the uncoated GdF_3 nanoparticles (8.5 wt%)

The size evolution of the particles with grafting was also followed by DLS measurements. The raw correlation data were reproducible (3 measurements), and a clear size difference appears when comparing the bare GdF_3 NPs and coated ones (***Figure 43***B). Consequently, the hydrodynamic diameter (mean number distribution) increased from 16 nm (GdF_3 particles) to 21 nm for Gd-95/5/0 (***Figure 43***A). Intensity distributions for both bare and coated particles suspensions were monomodal, with reasonable size distribution (PDI value is 0.16 for bare particles and 0.20 for coated particles). The fully extended PEG750 chain would result in a shell thickness of 6.4 nm approximatively; however, the value obtained here is only 2.5 nm, which is in accordance with a mushroom regime (for definition, please refer to paragraph ***I.1.5 Grafting density***) of the polymers.

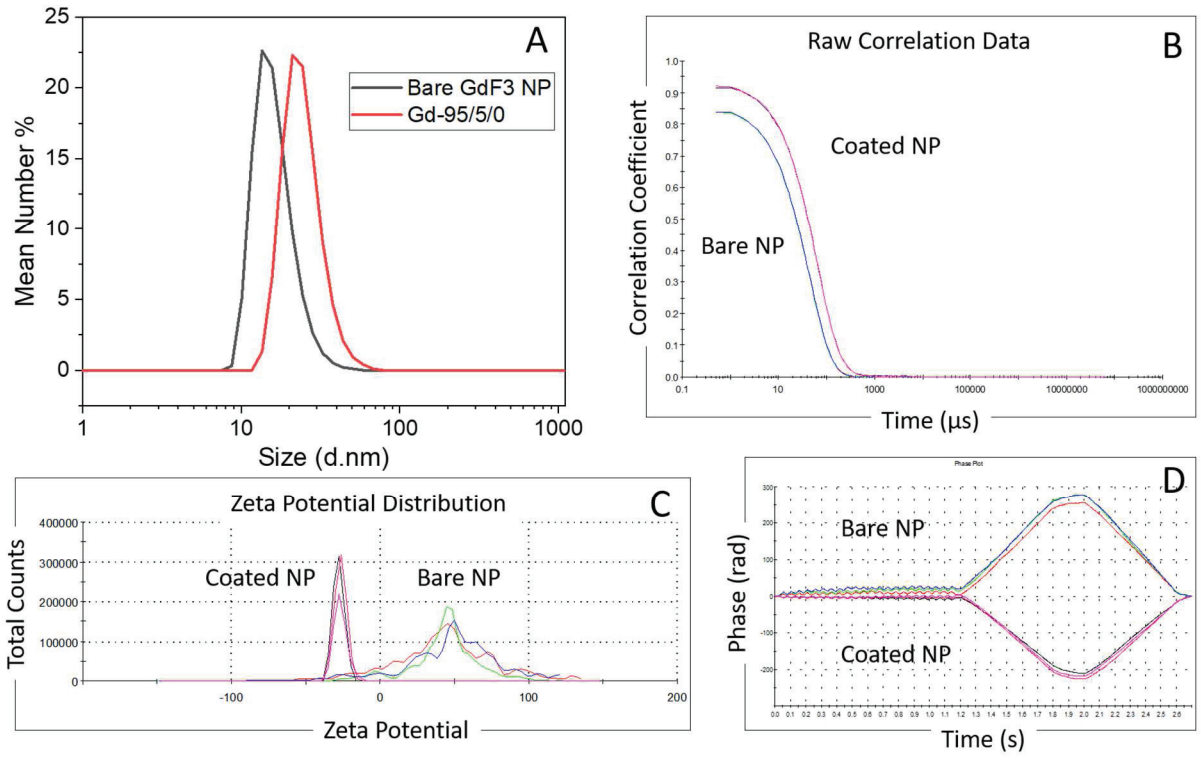

Figure 43 DLS and Zeta Potential measurements of bare GdF_3 and Gd-95/5/0 nanoparticles. A) Mean number size distribution. B) Raw correlation curves. C) Zeta Potential distributions. D) Phase plots.

The grafting was further supported by electrophoretic light scattering measurements. Bare particles were initially positively charged (***Figure 43*** C, D), with a wide zeta potential distribution, centered around +45±10 mV (pH ~ 4), while after surface modification, they acquire negative charges, inducing a zeta potential of -28±3 mV (at pH ~ 6.5) with a narrow distribution. This narrowing, as well as the charge inversion, were observed for all BPPEG- coated particles. As it was discussed in the introduction on bisphosphonates and phosphonates, excess negative charges are usually characteristic of surface modified particles with phosphonate anchoring and are explained by the negatively charged, deprotonated P-O moieties.[158,159]

Combination of the excess negative charges and polymer (PEG) coating constitute the highly desirable electrosteric stabilization, resulting in stable, non-aggregating particles. One exception was however observed: Lu-0/0/100 particles formed an unstable colloidal suspension leading to their precipitation. According to DLS measurements, this suspension was highly polydisperse (PDI > 0.5) and the determined sizes were about 500 nm. At the pH of the solution (~6.5 - 7), the carboxylic acid is also deprotonated and can form bridges between the particles. Through this cross-linking, large aggregates may form. The hydrodynamic properties and ATR

spectrum analysis seem to support this hypothesis. (Due to the low dispersibility of these particles, NMR analysis were not possible to perform.)

Conclusions from DLS analysis

- Upon grafting, the hydrodynamic diameter of the particles increases from 16nm (uncoated) to 21nm.
- This slight increase corresponds to the mushroom regime of the coating polymers.
- Polydispersity also increases (from 0.16 to 0.20), but remains in a reasonable range.
- Surface charge of the particles switches from a highly positive to a highly negative value (ZP: +45mV to −28mV), which evidences that deprotonated P-O moieties are present on the surface.
- Presence of charges and bulky polymers on the surface provide an electrosteric stabilization of the particles, which form a stable suspension.
- One exception was found in the case of BPPEGCOOH ligand, which seems to form bridges between the particles, making them aggregating and precipitating.

II.1.2.2 Surface modification with PEG-phosphonate (PPEG) ligand

Because of its commercial availability and known binding affinity to metal ions, the ligand phosphonate PEG (PPEG, ***Scheme 5***) was tested in grafting reactions. GdF_3 nanoparticles were grafted with a 50-50 mol% mixture of PPEG and $BPPEGN_3$. Comparison of its ATR spectrum (***Figure 44***) with one of the bisphosphonate equivalent, Gd-50/50/0 nanoparticles, reveals a significant difference in the relative intensity of the N_3 band (2100 cm^{-1}). The two spectra have been normalized to their maximum intensity at 1100 cm^{-1}, band arising from both PPEG/BPPEGOMe and $BPPEGN_3$ ligands. Therefore, the relative higher intensity N_3 band for PPEG containing sample suggests that the grafted PPEG:$BPPEGN_3$ ligand ratio is smaller than the ratio of BPPEGOMe:$BPPEGN_3$. This can be explained by a possible competitive binding between bisphosphonates and phosphonates: because of its higher denticity, bisphosphonates have higher binding affinity; hence, its attachment may adversely affect phosphonate ligand coordination.

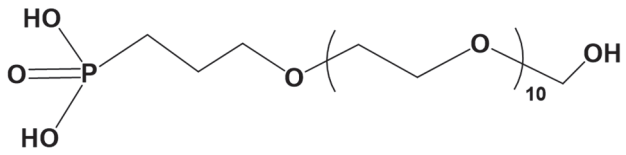

Scheme 5 Structure of PPEG ligand.

The same decrease in the amount of adsorbed phosphonates in the presence of bisphosphonates was observed by Rehor *et al.*[175] while they studied sorption and desorption of phosphonates and bisphosphonates on nanocrystalline TiO_2.

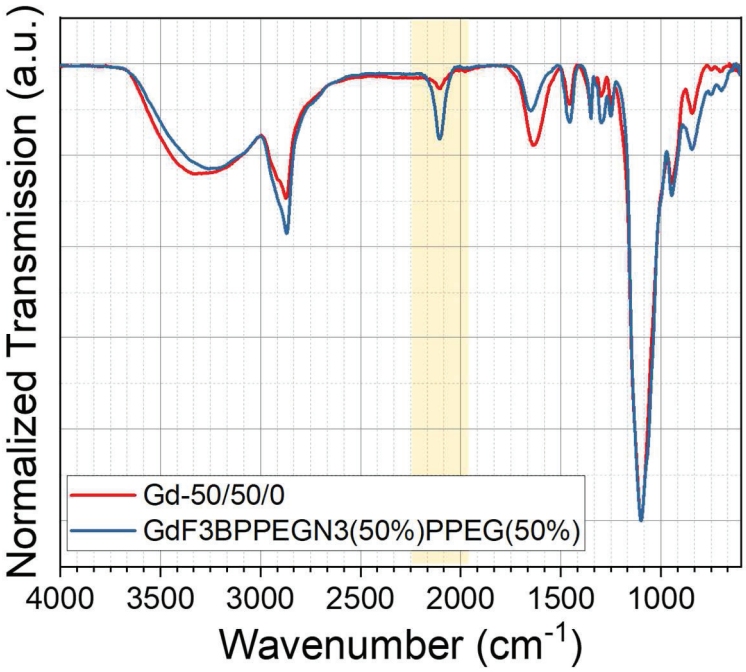

Figure 44 ATR spectra of Gd-50/50/0 and its phosphonate analog, Gd-50P/50/0.

The lower grafting density is confirmed by DLS measurements as well. In ***Table 4***, the measured hydrodynamic parameters are summarized for bare particles (GdF_3 and LuF_3), BPPEG- coated particles, and their analogs coated with a mixture of BPPEG and PPEG ligands.

Table 4 DLS measurement data measured for exclusively BPPEG- and mixed BPPEG-PPEG coated particles.

Only BPPEG coating				**Mixture of PPEG and BPPEGN_3coating**			
Particle	Z-average	PDI	Mean Number	Particle	Z-average	PDI	Mean Number
	d.nm		d.nm		d.nm		d.nm
LuF_3	**32**	**0.22**	**16**	–	–	–	–
Lu-100/0/0	58	0.23	25	Lu-100**P**/0/0	39	0.17	24
Lu-50/50/0	76	0.27	27	Lu-50**P**/50/0	130	0.43	17-49
GdF_3	**29**	**0.16**	**16**	–	–	–	–
Gd-50/50/0	98	0.22	24	Gd-50**P**/50/0	141	0.33	25
Gd-90/10/0	62	0.20	21	Gd-90**P**/10/0	112	0.43	29

First, we notice, that hydrodynamic parameters of the bare particles were independent of the nature of the rare earth metal. For the coated particles, in general, the mean number size averaged over a minimum of three measurements was quite similar for BPPEG coated and blended PEG-coated particles, except in the case of Lu-50P/50/0, where the value varied a lot in each measurement. However, the polydispersity index (PDI) value was systematically higher, when the particles were modified with a mixture of BPPEG and PPEG ligands, resulting in higher Z-average sizes. Higher polydispersity means higher tendency to aggregate, *i.e.,* lower stability of particles due to a less efficient surface coverage.

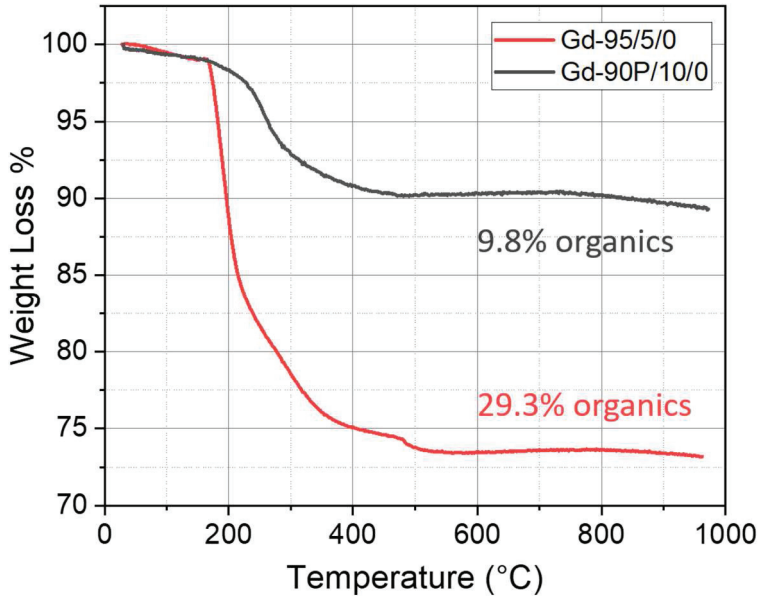

Figure 45 TGA curves for Gd-95/5/0 and Gd-90P/10/0 particles.

This hypothesis is further supported by TGA measurements. ***Figure 45*** compares the TGA curves of particle grafted with exclusively BPPEG ligands and blended PEG-coated particle. In the case of the first one, an organic shell of 29.3 % is detected, while for the second particle, only 9.8 % of organic loss is measured.

PPEG *vs.* BPPEG- ligands

- From ATR analysis: PPEG:$BPPEGN_3$ ligands ratio is significantly lower, than BPPEGOMe:$BPPEGN_3$ ratio, which supports that the higher denticity BPPEG- lignads have higher coordinating affinity to the nanoparticle surface.
- By DLS it was shown, that the particles coated with mixed BPPEG- and PPEG- ligands have the same size, than the exclusively BPPEG- ligands coated ones, however mixed coating is less efficient to prevent aggregation (higher PDI values)
- The less efficient surface coverage in the case of the mixed ligands is also reflected in the measured organic content, which is significantly lower for these particles, than for the BPPEG- coated ones.

II.1.2.3 Surface modification with Alendronic Acid ligand

Alendronic acid (AA, ***Scheme 6***) is an aminobisphosphonate used as a Ca^{2+} ion regulator drug, for bone density conservation. As a bisphosphonate compound, it is a potentially good anchoring molecule for GdF_3 nanoparticles. The idea behind the use of this molecule for surface modification was that it might help to elucidate how bisphosphonates coordinate to the surface and besides, with a terminal amine function, it opens the possibility to couple further molecules to the surface.

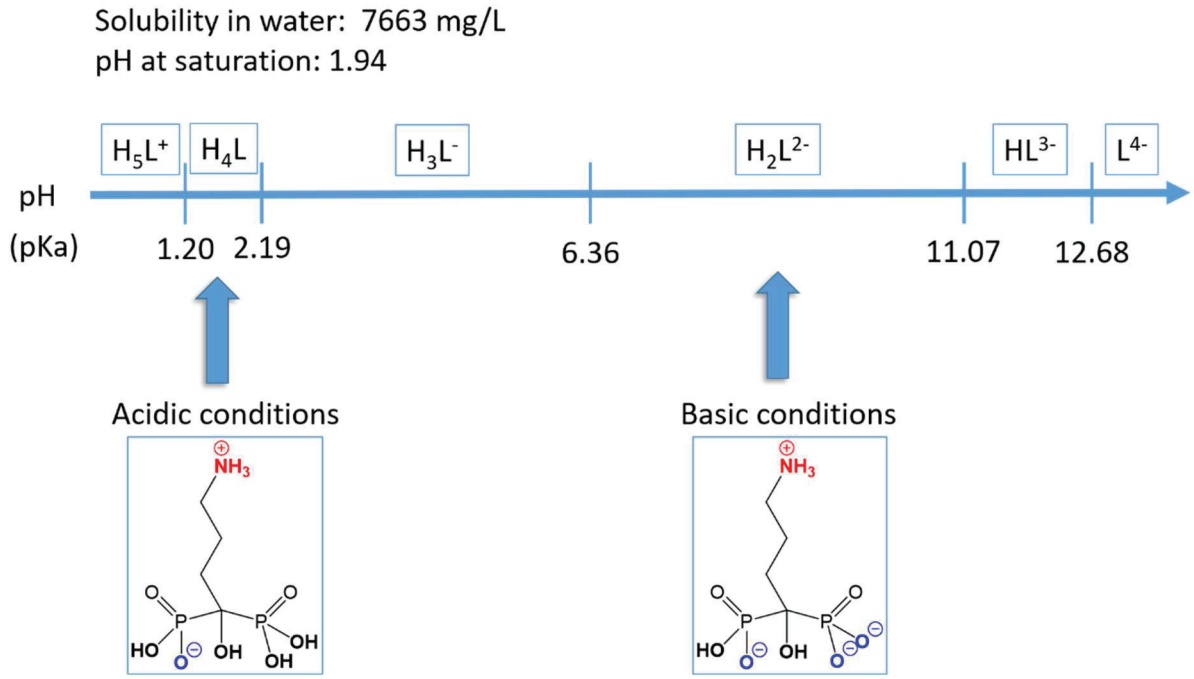

Scheme 6 Different dominant forms of alendronic acid (AA) in different pH ranges. The value indicated on the axis gives the pKa values corresponding to each deprotonation of AA.

As it is shown in ***Scheme 6***, alendronic acid is characterized by five pKa values within the whole pH range, which correspond to the progressive deprotonation of the four P-OH and the NH_3^+ groups.[176,177] Grafting reaction of AA to GdF_3 NPs, has been tested in two different pH conditions: acidic (pH ≈ 2) and basic (pH ≈ 8). In these two conditions, dominant species of AA has an overall charge of 0 and -2, respectively (***Scheme 6***). In both cases, the molar ratio Gd^{3+}:AA was fixed to 3:1.

Grafting in basic conditions: GdF_3@AA-b

First, 39 mg of AA was dissolved in 2 mL of aqueous solution, with a pH previously adjusted to 8 by addition NH_4OH. Then, 244 mg of GdF_3 dispersion (41 wt%) was added to this solution, which immediately became turbid. Under stirring, the mixture was heated up to 80°C during 1h and cooled down to room temperature. The solution was neutralized by a small amount of HCl, and the surface-modified nanoparticles were purified by centrifugation and freeze-dried.

Grafting in acidic conditions: GdF_3@AA-a

In the second tentative, the same procedure was followed, except, for the pH: no base was added; instead a saline solution (0.9 g NaCl in 100 mL of water) was the solvent. (In pure water, AA was not soluble at this concentration; therefore, the so-called salt effect was used to increase the solubility of this compound.) Upon addition of particle suspension, the mixture was again

turbid. The pH of the mixture was highly acidic, below pH = 2. When the pH was increased to neutrality by adding a solution of NH_4OH, the turbidity disappeared, resulting in a transparent solution.

Characterization

The ATR spectra (***Figure 46***) of both GdF_3@AA-a and GdF_3@AA-b show noticeable differences compared to the spectrum of free AA. The region attributed to P=O and P-O vibrations composed of several sharp peaks tightens into only a few, unresolved and large peaks, centered at about 1072 cm^{-1}, which is usually observed for chelating phosphorous species on metallic surfaces.[178] Bands of P-OH vibrations are also reorganized, and their relative intensities are decreased. In the meantime, -NH scissoring (1618 cm^{-1}) and -NH bending (1496 cm^{-1}) vibrations are also modified. Sharp scissoring doublet merges to one single large band centered at 1636 cm^{-1}, and bending peak is shifted to 1531 cm^{-1}.

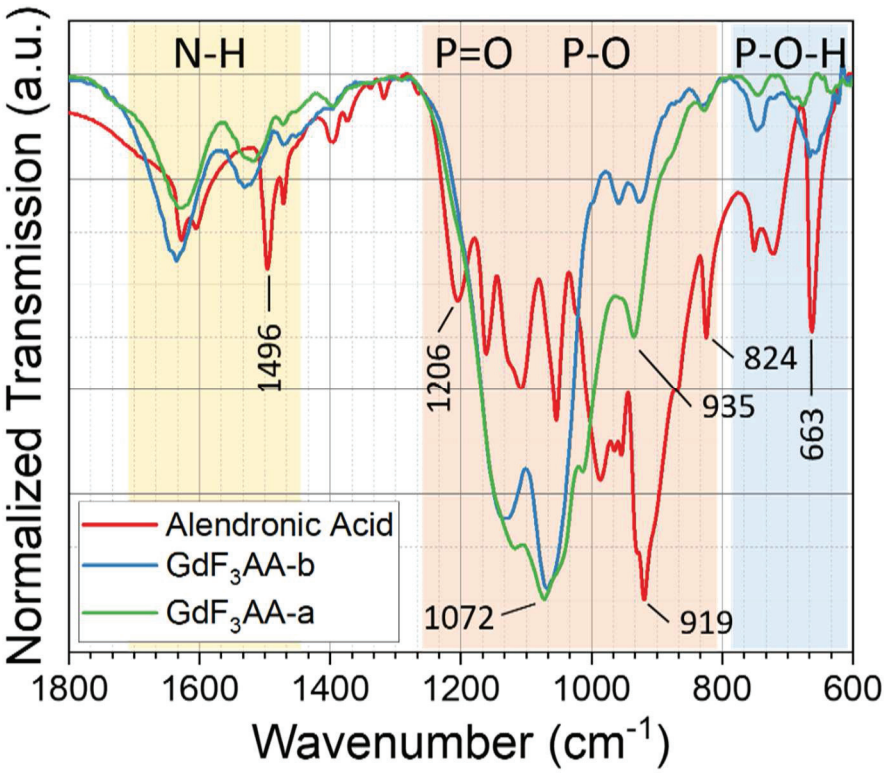

Figure 46 ATR spectra of free alendronic acid (red line) and the particles coated with AA in acidic (green line) and in basic (blue line) conditions.

Sangnier *et al.* attributed these latter changes to the involvement of the zwitterionic AA molecules in a multilayer formation on the nanoparticle surface, through anion/cation interactions between the negatively charged phosphonate and positively charged amino groups. However, differences in the P=O, P-O, and P-OH vibrations between the two particles

(GdF_3@AA-a and GdF_3@AA-b) suggest different coordination modes of AA on the surface. Benyettou *et al.*[171] performed theoretical modeling of FTIR spectra expected for AA coordinated through its bisphosphonate or its ammonium part to silver nanoparticle. They found a good agreement between their model and the experimental data and could conclude that AA is interacting with the particle through the phosphonate groups. Because of the complexity of the spectra, in our case, it is not possible to decide about the exact coordination mode of AA in the two different particles.

The freeze-dried functionalized particles were then resuspended in water, acidic (pH = 5) and basic (pH = 9) solutions for DLS and zeta potential measurements. The obtained data are summarized in ***Table 5***. GdF_3@AA-b in water is highly unstable, forming large size aggregates (mean number > 500 nm), with a high polydispersity index (0.56), and the measured zeta potential value is +6.6 mV. The positive zeta potential suggests that the particles are poorly covered because for alendronate coated nanoparticles zeta potential is usually negative at a pH close to the physiological value.[164,171,172] In a basic solution, the PDI decreases to 0.3, and the mean number size is about 190 nm. In acidic solution, however, the measured size and PDI are very close to the parameters obtained for the bare NPs.

In water, GdF_3@AA-a sample is less polydisperse (PDI 0.3) than the particles obtained with the basic conditions, but some aggregates are formed, resulting in a mean number size of 60 nm. In this case, the measured ZP is negative, but its absolute value is not high enough for electrostatic stability: -14 mV. Redispersed in acidic solution the size and PDI do not vary significantly, but in basic medium, the mean number size is 22 nm, and the low PDI of 0.16 shows a well dispersed colloidal suspension.

Table 5 DLS data measured for the two AA-coated nanoparticles (*a* refers to acidic and *b* to basic conditions).

	GdF_3AA-a				**GdF_3AA-b**			
Solvent medium	Z-average	PDI	Mean Number	Zeta Potential	Z-average	PDI	Mean Number	Zeta Potential
	d.nm		d.nm	mV	d.nm		d.nm	mV
H_2O	180	0.30	60	-14	> 1100	0.56	> 500	+6.6
Base (pH 9)	**38**	**0.16**	**22**	-	250	0.40	190	-
Acid (pH 5)	203	0.41	58	-	**33**	**0.21**	**19**	-

Differences in ATR spectra along with discrepancies in size and polydispersity evolutions suggest that different coordination of AA takes place when the grafting reaction occurs in acidic or basic conditions.

To further investigate AA coordination to the particle surface, an amine specific colorimetric test was performed. In solid phase supported peptide synthesis, the residual amino groups of amino acids may be tested with ninhydrin. The principle of the test presented on ***Scheme 7***, is based on the coupling of two colorless ninhydrin molecules, in the presence of a primary amine. A colorful complex, Ruhemann's Purple (or Blue) is formed, while the primary amine is converted to an aldehyde.

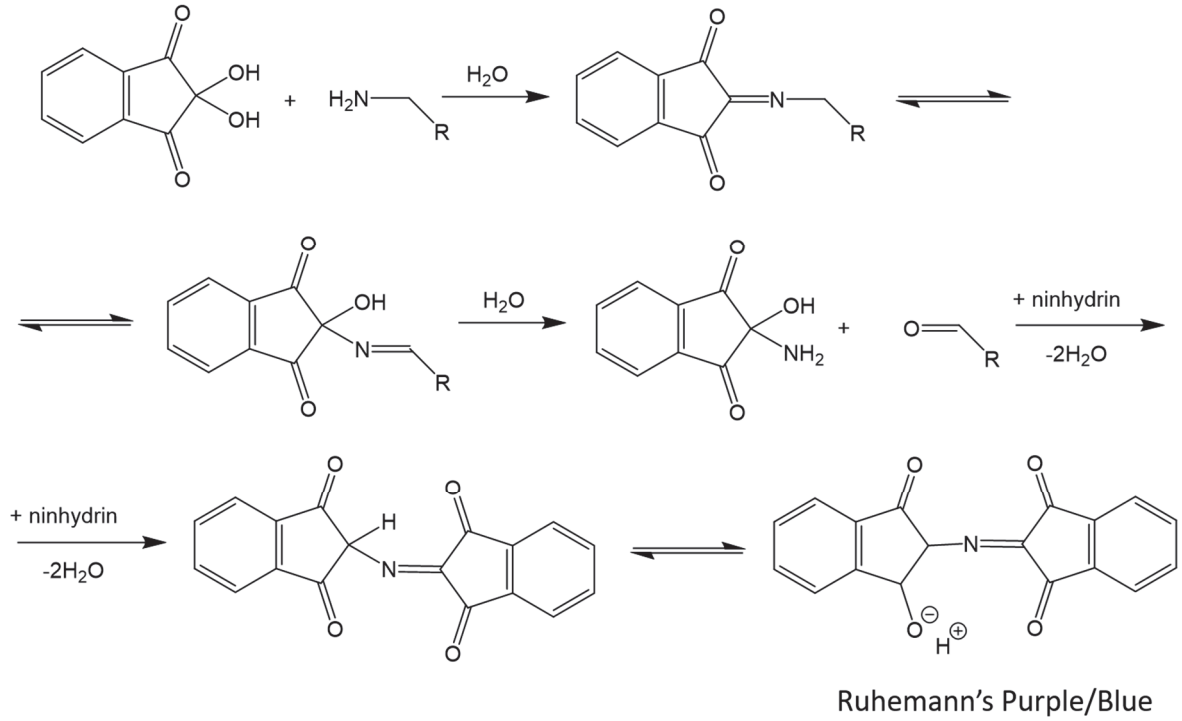

Scheme 7. Reaction mechanism corresponding to the detection of amines with ninhydrin. First, the primary amine reacts with a ninhydrin molecule through a condensation reaction. Then the imine (C=N bond) is cleaved by hydrolysis and a second ninhydrin molecule reacts with the intermediate to give the purple colored complex, Ruhemann's Purple or Blue.

For the detection of the free amino group on the particle surface, first, a ninhydrin reagent solution was prepared, according to a simple literature protocol.[179] As the reaction is highly sensitive to pH, ninhydrin (0.2 g) is dissolved in freshly prepared acetate buffer (2.5 mL, pH = 5). This solution was added to a small number of particles suspended in water, and the mixture was incubated in a 60°C water bath for a few minutes.

The ninhydrin test was positive for free alendronate and GdF_3@AA-a nanoparticles, but negative for GdF_3@AA-b, again showing a difference in the coordination of AA in the two cases. The results of this colorimetric test suggest that for GdF_3@AA-a, as expected, a free amino group is available on the surface (the bisphosphonate group is coordinated), while for GdF_3@AA-b, there is no free amino group at the particle surface.

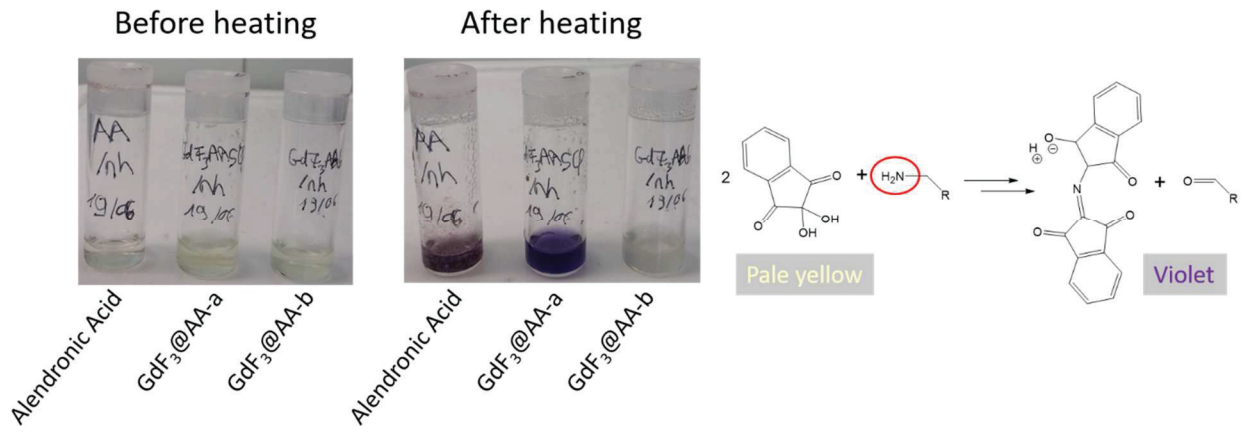

Figure 47 Results of ninhydrin test on the AA-coated particles and free AA for comparison. Before heating both solutions are pale yellow colored (unreacted ninhydrin), and upon heating, AA and GdF_3-AA-a solutions turn to violet (Ruhemann's purple), while the solution of GdF_3-AA-b remains yellow.

A more detailed study is needed to determine the exact reason for this different coordination, but one possible explanation would be that in the case of the grafting in basic conditions, the amino group is also participating in a coordinative bond with surface gadolinium ions or due to its zwitterionic nature, it interacts with the phosphonate group of another AA molecule, creating a multilayer on the surface. Both configurations have been invoked in the literature. Sangnier *et al.* grafted AA at pH 10 to gold nanoparticles and based on FTIR and ICP-AES measurements, concluded, that alendronate forms a multilayer.[178] In a review article, J. Galezowska reported theoretical and experimental works, that revealed the key role of the nitrogen atom in stereospecific recognition of aminobisphosphonates, such as alendronate, while binding to bone model hydroxyapatite surfaces.[155]

AA grafting

Both ATR and DLS measurments, along with ninhydrin colorimetric test reveal a different coordination mode of AA to the particles, when grafting in acidic or basic conditions. The ninhydrin test is positive, when free amino group is available: this is the case of free alendronate and AA-grafted particles in the acidic conditions (GdF_3@AA-a).

When the grafting is performed in basic conditions (GdF_3@AA-b), the colorimetric test is negative, showing that the amino group of AA is not available. One possible explanation is that AA is coordinating with both bisphosphonate and amino groups.

II.1.2.4 Surface modification with multiple attachments: copo-P

Copolymers are polymers synthesized from two or more type of repeating units and can be broadly classified into four categories: statistical, block, alternating, and graft copolymers. In this section, we are interested in a statistical copolymer (the sequential distribution of the repeat units obeys the statistical law), combining phosphonic acid functionalities and PEG side chains.

Scheme 8 describes the copolymer copo-P in detail. From the point of view of surface functionalization, one of the main advantages of this type of polymer is that it allows us to multiply the anchoring points and number of PEG chains within one single macromolecule.

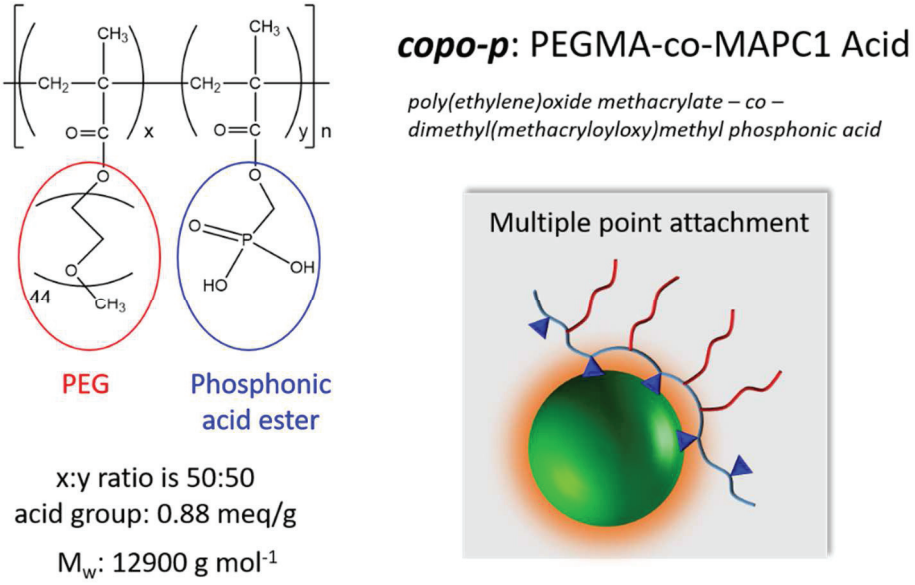

Scheme 8 Chemical structure of copo-P, the multiple point attachment copolymer purchased from *Specific Polymers*.

Hydrophilic PEG sidechains and phosphonates confer to the copolymer solubility in water, while the nonpolar backbone is hydrophobic. The combination of hydrophilic-hydrophobic properties within one molecule is the fundamental property of surfactants. In aqueous solution, when surfactant concentration at a given temperature reaches a critical value, called the critical micelle concentration (CMC), these molecules self-assemble into organized aggregates with different morphologies, the micelles. Micelle formation, *i.e.,* the appearance of larger size objects can be followed by different scattering techniques, such as DLS measurements. Hydrophilic polymers grafted on hydrophobic segments forming an amphiphilic copolymer are also able to self-assemble in an aqueous media. [180] For example, micelle formation of PEG-based random copolymers of poly(dodecyl methacrylate-co-polyethylene glycol methyl ether methacrylate), with different hydrophobic content has been studied in detail by Laskar *et al.*[181] They found that these copolymers have a very low CMC (*ca.* $7 \cdot 10^{-3}$ mg mL^{-1}) and DLS measurements revealed a mean hydrodynamic size in the range of 70–100 nm. Therefore, one can expect similar properties for the copolymer (copo-P), which is the subject of the present study.

A series of copo-P solutions of different concentration ranging from $4.05 \cdot 10^{-6}$ to $1.54 \cdot 10^{-2}$ mol L^{-1}, corresponding to 0.005-20 wt% of polymer in water, was prepared. After a careful

homogenization, the solutions were left to equilibrate during 24h. Then, each solution was measured by DLS, at 25°C, with an equilibration time of 5 minutes. The size evolution of polymer assemblies as a function of the concentration was followed, and the measured intensity was reported via the derived count rate (DCR, count rate without attenuation) for each colloidal solution. ***Figure 48*** shows DCR as a function of the logarithm of the polymer concentration.

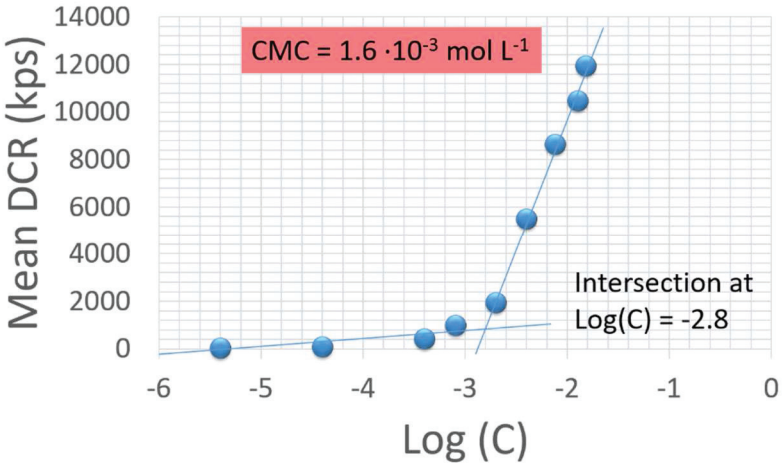

Concentration (wt%)	Concentration (mol/L)	Log(C)	DCR (kcps)
0.005	4.05E-06	-5.39	27
0.05	4.05E-05	-4.39	61
0.5	4.05E-04	-3.39	416
1	8.10E-04	-3.09	962
2.5	2.02E-03	-2.69	1931
5	4.05E-03	-2.39	5491
10	7.69E-03	-2.11	8615
16	1.28E-02	-1.89	10451
20	1.54E-02	-1.81	11919

Figure 48 CMC determination of copo-P. The curve shows the mean derived count rate (DCR) measured by DLS as a function of Log(C) (C denotes the concentration of copolymer in water). The intersection of the two straight lines gives CMC value. The table contains the corresponding data. (DCR is the measured count rate divided by the attenuation factor in kilo counts per seconds.)

The first linear relation of DCR *vs.* Log(C) changes abruptly to another linear function with a larger slope value. The intersection of the two straight lines at Log(C) = -2.8, corresponds to the critical micelle formation concentration. Therefore, the CMC of copo-P at 25°C has a value of $1.6 \cdot 10^{-3}$ mol L^{-1} (20.6 mg mL^{-1}).

Because of the dynamic nature of micelle formation, the temperature is also a key parameter in size evolution of the organized aggregates. The 10 wt% solution of copo-P was selected to observe the polymer assembly behavior as a function of temperature by DLS. The temperature in this experiment varied between 5 and 45°C and an equilibration time of 10 minutes was respected at each temperature change.

In ***Figure 49***, the temperature dependence of scattered intensity is represented. The data shows that first the aggregation of the copolymers is increasing, it reaches a maximum in the approximate range of 15-20°C, then the mean size decreases with temperature increase.

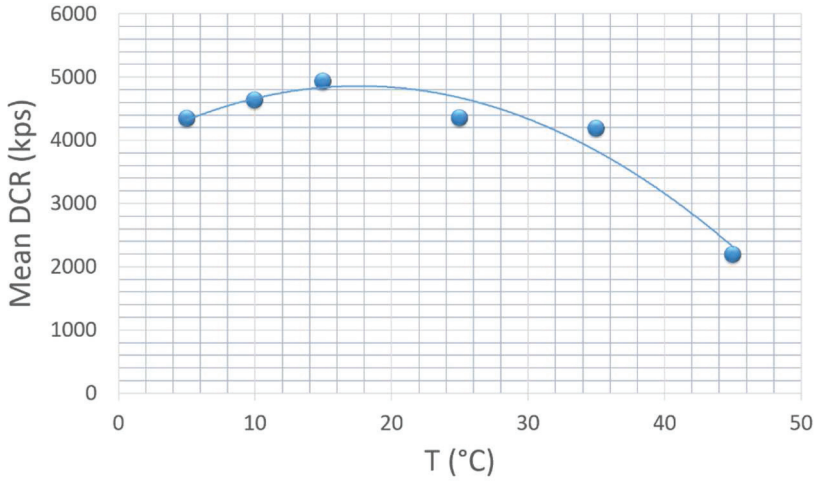

Figure 49 Mean derived count rate measured by DLS as a function of the temperature indicates an optimum temperature range for micelle formation.

After the characterization of its micelle formation, the copolymer was applied as a coating on GdF_3 nanoparticles. In the first grafting procedure, the usual 1:3 ligands to gadolinium ion ratio was respected, where "ligand" means phosphonic acid group (according to the supplier the phosphonic acid content is 0.88 meq/g of the copolymer). 1.32 mmol of GdF_3 in aqueous suspension (10 mL) was added to a solution (3 mL) of 0.5 g copo-P. The mixture was homogenized in an ultrasonic bath for 5 minutes and then heated to 80°C during 1h, under magnetic stirring. The grafted particle suspension was cooled to room temperature than dialyzed against water for five days and freeze-dried. A small amount was resuspended in water and analyzed by DLS.

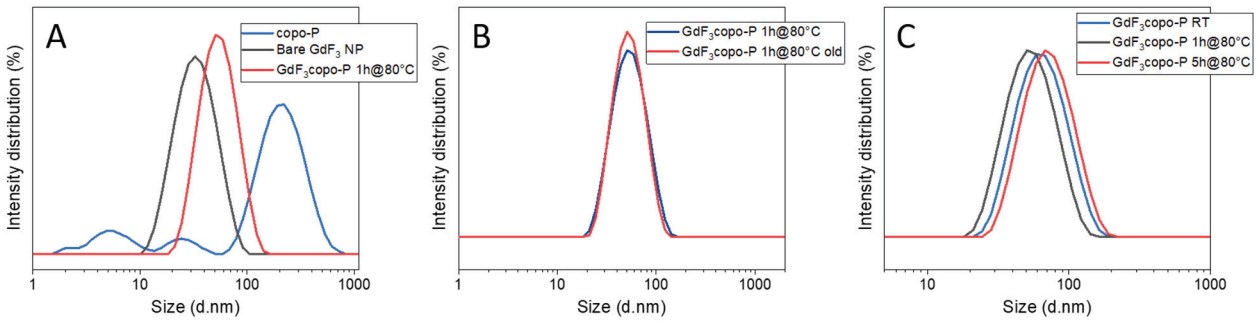

Figure 50 Intensity size distributions measured by DLS. A) comparison of free copolymer solution, bare GdF3 nanoparticle suspension and copo-P coated particles (ligands to Gd ratio of 1:3) after 1h of heating at 80°C. B) The copo-P coated particle suspension is compared with itself, 2.5 years later. C) Effect of heating time on coated particles.

Measured size and polydispersity data are summarized in ***Table 6***. Upon grafting, the Z-average and mean number sizes increased from 35 to 48 nm and from 20 to 30 nm, respectively, while the polydispersity index remained very low (0.15) and unchanged compared to the uncoated particles (0.15).

Grafting was further confirmed by zeta potential values: the bare particles are positively charged (+32 mV), and after grafting, ZP becomes negative (-22.5 mV). In ***Figure 50***A, the size distribution by the intensity of bare particles, free copolymer, and grafted particles are shown. The size distributions for particles are quite narrow. The copolymer at the concentration used here was above the CMC, therefore, micelles of a mean size of 110 nm are formed, along with some smaller aggregates. The particle suspension remained stable upon addition of acid (pH = 2) or base (pH = 9). During purification of different surface modified GdF_3 nanoparticles, acetone is used for precipitating the particles. In this case, even upon the addition of acetone, copo-P modified particles were not aggregating. The PEG chains of this copolymer are composed of 44 monomer units, and its extended length is around 15 nm. Considering the average naked particle size of 20 nm, a coating with fully extended chains would result in a size of 50 nm. However, we do not observe such a significant size increase; therefore, the chains are in a mushroom conformation, such as for the BP-PEG ligands.

The aqueous suspension characterized by DLS was kept at room temperature for 2.5 years without precipitating, and its DLS parameters were measured after this time lapse. An unexpected similarity (***Table 6***, ***Figure 50***B) of these parameters was observed by DLS, 2.5 years later.

Table 6 DLS and Zeta potential measurements of GdF_3 NPs, functionalized with copo-P

	Z-average (d.nm)	PDI	Mean Number (d.nm)	Zeta Potential (mV)
Free copo-P (c > CMC)	110	0.8	3	
Gd-copo-P(1:3) without heating	58	0.14	35	
Gd-copo-P(1:3) 1h heating	48	0.15	30	-22.5
Gd-copo-P(1:3) 5h heating	65	0.14	40	
Gd-copo-P(1:3) after 2.5 years	49	0.12	32	
Gd-copo-P(1:20) 1h heating	69	0.25	14	+9.0
Gd-copo-P(1:1) 1h heating	53	0.15	32	-25.0

In accordance with an efficient coating, TEM observations revealed highly dispersed particles as shown in ***Figure 51***, but the polymer layer was not observable by this technique. However, the shape of the particles seems to be more elongated after the grafting with copo-P.

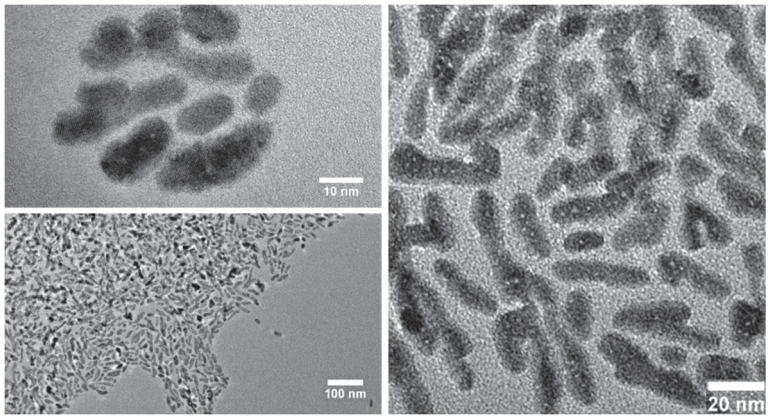

Figure 51 TEM picture of GdF_3 nanoparticles coated with copo-P (ratio of 1:3).

Comparison of free copolymer and copo-P grafted NPs ATR spectra (***Figure 52***) reveals several significant differences in the fingerprint region. Reorganization of the P-O vibrational region clearly indicates the coordination of phosphonate groups; in the meantime, the P=O vibrations are also shifted, indicating the participation of P=O bonds in a coordinative interaction.

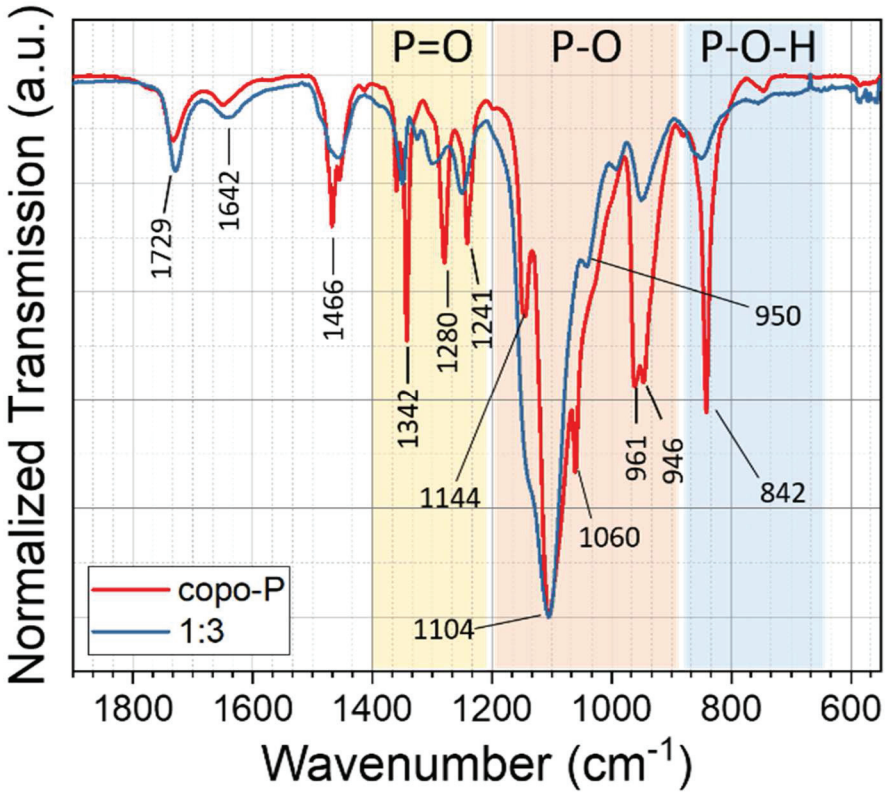

Figure 52 ATR spectra of free copo-P ligand and GdF_3 nanoparticles coated with this ligand (1:3 ratio)

Thermogravimetric analysis (***Figure 54***) revealed an organic content of 38,2 %, which corresponds to 308 chains and 954 phosphonate groups per NP.

The suspension of the same mixture of GdF_3 and copo-P was analyzed by DLS without any heating and after 5h of heating (80°C). The results were compared (***Figure 50***C) to the values obtained for the sample heated during 1h (80°C). In the first case, when the sample is not heated, just stirred at room temperature for one day, the mixture was characterized by slightly larger size, but the same PDI parameters, then the sample heated for 1h (***Table 6***). This is in accordance with the observations of J.F. Berret and coworkers,[182,183] who elaborated coated iron oxide nanoparticle whit the same copolymer and found, that a very efficient coating is induced at room temperature. When the sample is heated for 5h at 80°C, the low polydispersity is preserved, while the size increased from 48 to 65 nm, suggesting a thickening of the organic layer on the particle (***Table 6*** and ***Figure 50***) with longer heating.

The effect of ligand to gadolinium ion ratio on the size and grafting efficiency was tested by comparing the surface modified particles with a ratio of 1:3, 1:1, and 1:20. The 1:1 ratio represents a large excess of ligands compared to gadolinium ions on the surface, (*i.e.,* gadolinium accessible for the grafting), while with a 1:20 ratio there is a lack of ligand. The total gadolinium concentration was the same in all three cases, only the copolymer concentration varied. The grafting was performed at 80°C for 1h, and the particles were purified by dialysis.

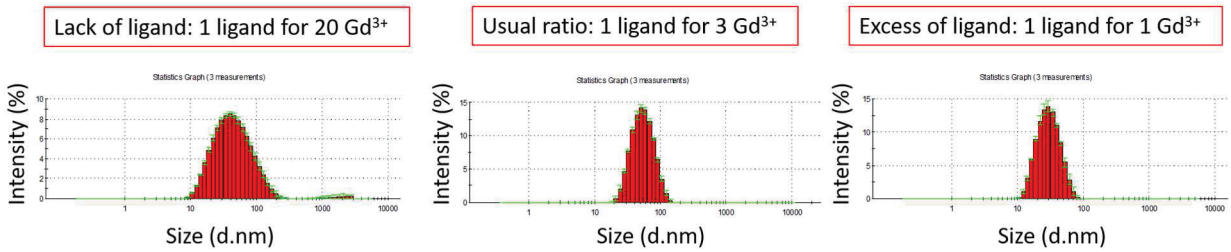

Figure 53 Intensity size distribution measured by DLS for the copo-P coated GdF_3 nanoparticles, with different gadolinium ions to ligands ratio.

Figure 53 shows the size distributions obtained in different ligand to gadolinium ratios and all size parameters and polydispersity values are listed in ***Table 6***. In the 1:3 and 1:1 case, PDI values are low, indicating, that no or only a few particle aggregates are present, due to an efficient coating, while the 1:20 ratio does not provide enough stabilization. The particles in the latter case form aggregates, which results in higher polydispersity (0.25) and higher z-average size (69 nm) values. Large excess of copolymer increases the size, suggesting a thicker organic layer. The surface charge is negative for the 1:3 and 1:1 case (-22.5 and -25 mV respectively), but a positive zeta potential (+9) for the 1:20 ratio indicates that the number of phosphonate

functionalities on the surface is insufficient to counterbalance the positive charges on the naked particle surface.

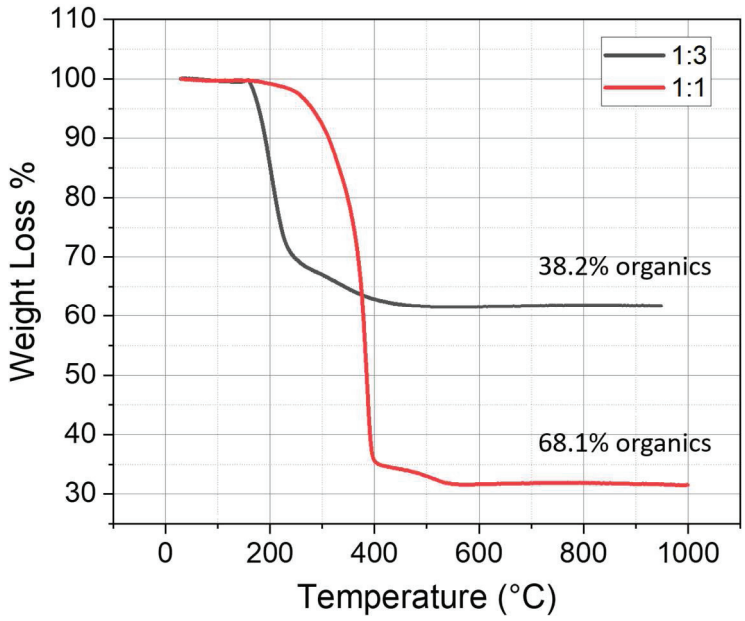

Figure 54 TGA curves for copo-P coated GdF_3 nanoparticles with Gd: ligands ratio of 1:3 (black curve) and 1:1 (red curve).

Thermogravimetric analysis results are also in accordance with these findings. Excess ligand (1:1 ratio) results in an organic mass loss of 68.1 % (***Figure 54***), which is much higher than the ones obtained for the 1:3 case (38.2 %).

Copo-P grafting

Upon grafting the multidentate copolymer (copo-P) on the particle, DLS showed a significant increase in size, but the polymers are still in the mushroom regime. Very low polydispersity is maintained and the ZP value switches from +32 mV to -22.5 mV, due to the negative charges of the ligand. As opposed to bisphosphonates, the P=O moiety also seems to take part in coordination.

Copo-P provides extremely high stability to the particles, which remain unchanged after more than two years. Copo-P also prevents particles from precipitation in acetone or even alkaline medium.

Increasing the heating time induces higher surface coverage. Excess ligand increased the organic content of the particles to 68.1 %.

II.2 Fluorescent labeling of BPPEG-coated GdF_3 nanoparticles

II.2.1 Introduction: Click chemistry

The analytical challenge of screening a large number of reactions in drug discovery initiated the development of effective conjugation techniques, inspired by nature (such as enzyme reactions). A new strategy for selective coupling reactions, giving a single product in high yield, without the formation of side-products and in mild, water-tolerant conditions was developed by Sharpless and coworkers,[184] who introduced the concept of click chemistry in 2001. This synthetic philosophy was quickly adopted by the scientific community and gained widespread use in biotechnology, material and polymer sciences, pharmaceutical and medicinal sciences, and so on.

One of the most popular click reactions is the conjugation reaction of two building blocks, one functionalized with azide and the other one with an alkyne group, which results in a five-membered triazole ring formation. R. Huisgen described this reaction in 1963 as a 1,3-dipolar cycloaddition and later was named after him as Huisgen cycloaddition.[185,186] Under physiological conditions, both alkyne and azide are unreactive because of a high activation barrier, however, at elevated temperature (>100°C), the cycloaddition takes place. The highly exothermic reaction results in a mixture of 1,4 and 1,5 regioisomers of 1,2,3-triazole. In 2002, Sharpless and his coworkers[187] and independently, Meldal *et al.*[188] reported the effective use of Cu(I) ion to catalyze the alkyne-azide cycloaddition. The catalyzed reaction occurs in mild conditions, 10^7 times faster than the classical thermally induced one and is highly regioselective. In 2013, Worrell *et al.*[189] brought the direct evidence of the intermediate complex formed with copper ion and explained the formation of only the 1,4-regioisomer. A variety of Cu(I) sources may be used, but usually, it is generated in situ from $CuSO_4$ with a reducing agent, such as sodium ascorbate.

Despite all the advantages of copper catalysis, it is not recommended for in vivo applications, due to the well-known cytotoxicity of Cu(I) ions. The copper catalyst was, for example, shown to cause mammalian cell death[190] and catalyzes reactive oxygen species (ROS) production.[191] The purification after the reaction is difficult, as the triazole moiety is nucleophilic. Therefore, it can bind Cu(I) ions, which makes copper removal arduous.

Rapidly after the publication of Sharpless *et al.*, azide-alkyne click reaction was applied for nanoparticle surface modification. For example, in 2006, Fleming *et al.*[192] reported their work on Au-nanoparticle functionalization by triazole cycloaddition. In parallel, different types of copper-free click reactions have been developed. Bertozzi's research group made a pioneering work by developing strain-promoted azide-alkyne cycloaddition (SPAAC) reactions.[193,194]

II.2.2. Fluorescent labeling of BPPEG-coated nanoparticle

In this section, the coupling of a fluorescent label on the BPPEG-coated GdF_3 nanoparticle is described. The coupling reaction takes place between the alkyne group of the chromophore and the azide function of $BPPEGN_3$ ligand *via* 1,3-dipolar cycloaddition.

The fluorophore LEM-A (***Scheme 9***; *LEM* for Lemke and *A* for alkyne), grafted on GdF_3 nanoparticle, has been synthesized in our laboratory by Yann Bretonnière and his coworkers.[195] Push-pull molecules composed of dicyanoisophorone electron acceptor and N-donor atom containing group was originally developed by Lemke[196] in 1974. Based on the same idea, Bretonnière *et al.* reported a series of compounds with different substituent groups on the nitrogen atom, and they showed that these compounds exhibit interesting optical properties. Upon excitation, they emit in the red and this emission is even more shifted towards NIR region in polar hydrogen-donor solvents. This red emission with positive solvatochromism displaying a large Stokes shift (*ca.* 5000 cm^{-1}) is very advantageous in biological applications, because fluorescence imaging of tissues requires fluorescent labels emitting in the optical transparency window of tissue components (700–1000 nm). However, the highly dipolar Lemke-type chromophores are inherently lipophilic due to their extended conjugated carbon backbone, which prevents their direct use as a dye for imaging in physiological media. Later, the same research group published the synthesis and full spectroscopic study of the first example of water-soluble Lemke chromophore.[197] The two oligomerized hydroxyethyl acrylate arms coupled to the fluorophore did not alter emission properties of the latter, but rather resulted in strong red-NIR fluorescence in water. The efficiency of this compound as a two-photon probe has been demonstrated by successful *in vivo* imaging of the cerebral vasculature of mice. Redon *et al.* associated different carbohydrate structures with LEM-A to attaining suitable hydrosolubility and studied optical properties of the LEM-A derivative.[195] This modification has been made for mimicking the structure of natural glycolipids and target membrane of mouse skeletal muscle cells.

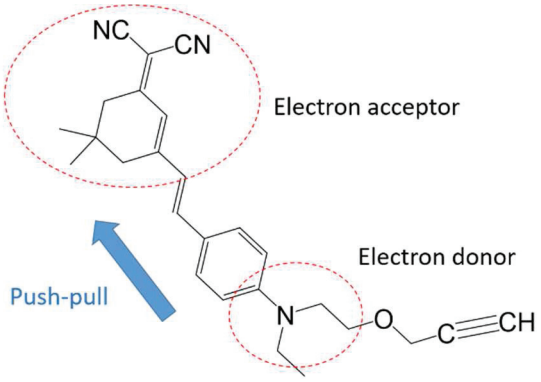

Scheme 9 Molecular structure of LEM-A fluorophore

In the light of the properties as mentioned above of Lemke-type chromophores, LEM-A clearly appeared as a promising candidate for the fluorescent labeling of our nanoparticles. In this case, hydrosolubility of the molecule is provided by their attachment to the BPPEG-coated GdF_3 nanoparticles, which form a stable suspension in water. The fluorescent nanoparticle thus obtained will be referred to as SKClick11.

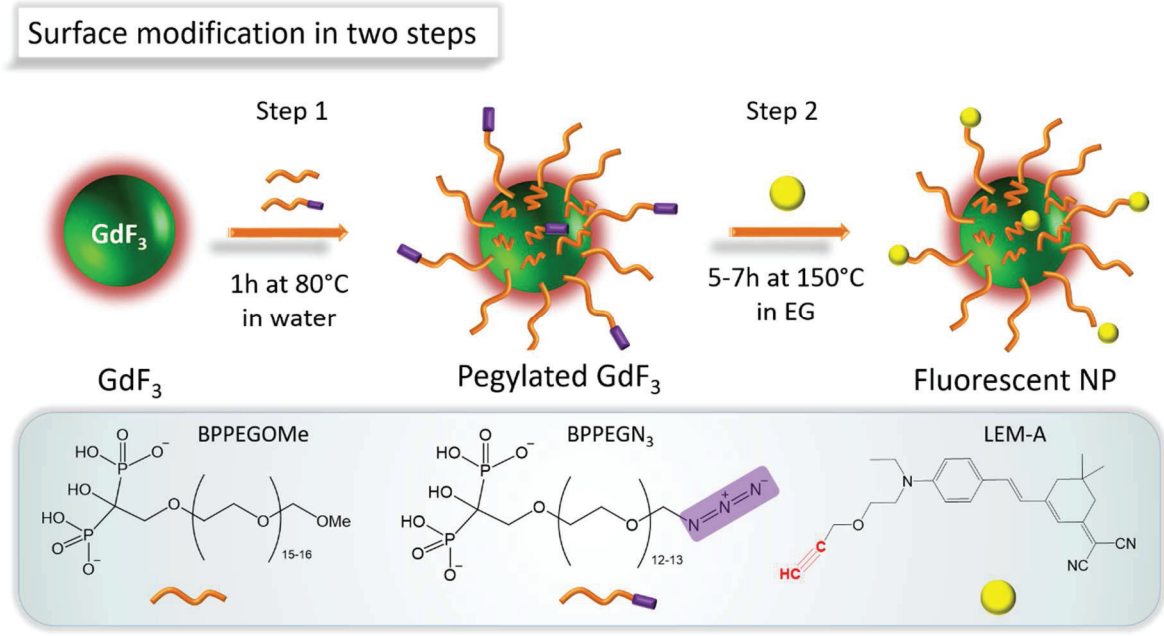

Scheme 10 Synthetic route of the fluorescent dye-labeled nanoparticles. The upper part shows the chemical structure of coating ligands and the chromophore (LEM-A).

Experimental conditions

As it was previously mentioned, Cu(I) catalysis is not recommended for *in vivo* applications. Therefore, the thermal activation of the 1,3-cycloaddition is adopted here. A relatively high-temperature treatment for several hours is needed for the activation. Before performing the click reaction on the particle surface, the stability of the free chromophore was tested in different

high boiling temperature solvents, such as N-methyl-2-pyrrolidone (NMP; T_{boil} = 202°C), dimethylformamide (DMF; T_{boil} = 153°C) and ethylene glycol (EG; T_{boil} = 197°C). Solutions with the same concentration of chromophore ($3 \cdot 10^{-3}$ mg mL^{-1}) were prepared in the different solvents and were heated to 125°C during 2h for DMF and NMP. After approximatively 1h, as it is shown in ***Figure 55***, the solution lost its pink color in both cases, indicating the degradation of the chromophore, while in the case of EG, the solution was only slightly discolored even after heating to 150°C for 7h.

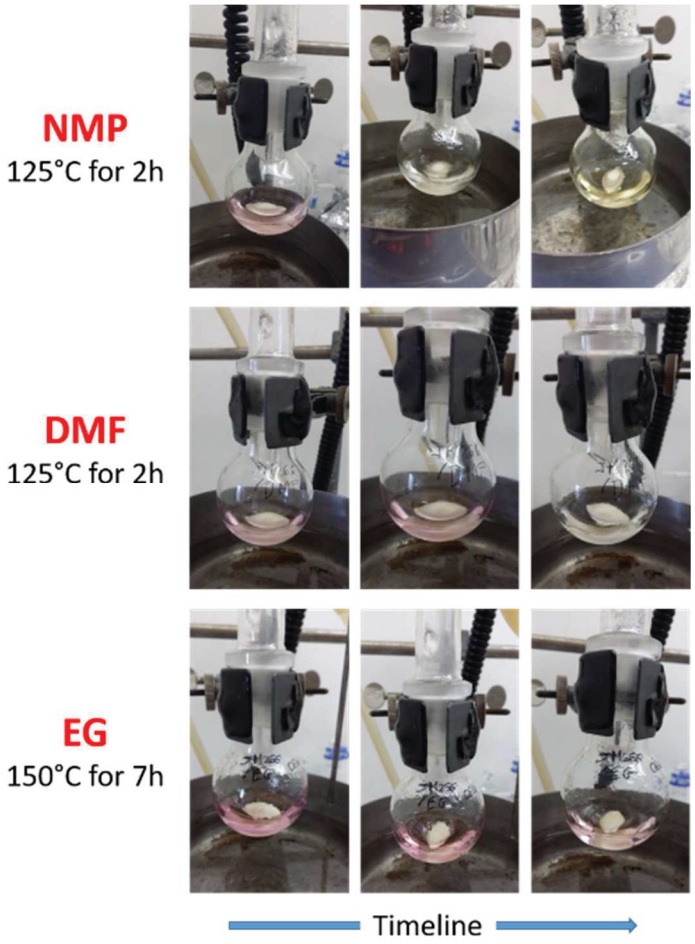

Figure 55 Stability tests of LEM-A, upon heating in different solvents. NMP: *N*-methyl-2-pyrrolidone; DMF: dimethylformamide; EG: ethylene glycol. Discoloration of the solution indicates the degradation of the chromophore.

This visual observation was confirmed by spectroscopic measurements. In ***Figure 56***A, the absorption spectra of the NMP solution was recorded before and after heating. The absence of an absorption band at 526 nm, accompanied by a significant increase in the intensity of the band at 326 nm clearly indicates a high structural reorganization (degradation) of the chromophore molecule. In EG, the 526 nm band is unchanged upon heating and the 326 nm one increased

only slightly, proving that the chromophore resists much better to heating in EG. Therefore, this solvent was adopted for the click reaction on the particle surface.

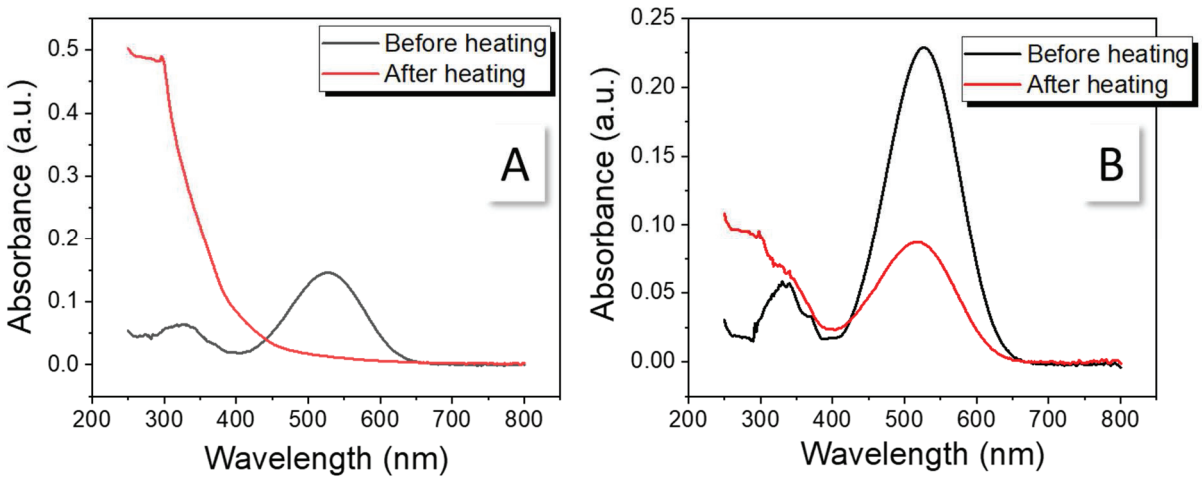

Figure 56 UV-Visible absorption spectra of the chromophore LEM-A before and after heating. A) In NMP; B) In EG.

For the chromophore coupling to the particle, several attempts (summarized in ***Table 7***) have been performed with slightly different conditions (concentration, heating temperature and heating time) and finally, the following procedure was adopted. An aqueous suspension of the BPPEG-coated NP, here Gd-95/5/0, was prepared from 800 mg of particles in 2 mL of water. In another vial, 9.2 mg ($2.31 \cdot 10^{-5}$ mol) of LEM-A was dissolved in 8 mL of EG. The required amount of chromophore was calculated to be equal (in moles) to the amount of N_3-functionalized BPPEG in the weighted NP. In this example, the quantity of $BPPEGN_3$ ligand theoretically present in 800 mg of Gd-90/5/0 particles, is 19.9 mg ($2.31 \cdot 10^{-5}$ mol). The two solutions were homogenized (ultrasonic bath) and the NP suspension was slowly added to the chromophore solution, under ultrasonic agitation. The mixture was transferred in a 25 mL round bottom flask equipped with a condenser and then heated to 150°C for 5h, under vigorous agitation. After that time, the mixture was let to cool down to room temperature, and the particles were precipitated in acetone (twice the volume of the mixture). The acetone solution was then centrifuged (14000 relative centrifugal force or RCF, 20 min) and the supernatant was centrifuged again to collect as many particles as possible. The pellet was resuspended in a small amount of ethanol (typically 2-3 mL) and centrifuged for 45 min (12000 RCF). The resuspension-centrifugation cycle was repeated until the supernatant became colorless (typically 5-6 times). The as purified particles were resuspended in water and subjected to freeze-drying, to produce a dry powder of the colored fluorescent NPs.

Characterization

Table 7 Reaction conditions of click reactions performed on different BPPEG-coated GdF_3 and LuF_3 nanoparticles

	BPPEG-coated NP	NP Mass (mg)	LEM-A Mass (mg)	V_{EG} (mL)	V_{H2O} (µL)	T (°C)	$t_{heating}$ (h)	Successful coupling
SKClick1	Gd-90P/10/0	100	3.2	2.4	600	150	7	Yes
SKClick2	Gd-50/50/0	100	13.0	3.5	500	150	7	Yes
SKClick3	Gd-90/10/0	50	12.0	22	300	150	7	No
SKClick4	Gd-90/10/0	50	12.2	3	250	150	7	No
SKClick5	Gd-50P/50/0	100	14.8	3	500	150	7	Yes
SKClick6	Lu-50/50/0	100	13.2	3	500	150	7	Yes
SKClick7	Lu-50P/50/0	100	14.9	3	500	150	7	Yes
SKClick8	Gd-90/10/0	50	1.5	1.8	100	120	16	Yes
SKClick9	Gd-90/10/0	42	1.3	2	200	120	20	No
SKClick10	Gd-95P/5P/0	300	5.2	3	1	120	20	Yes
SKClick11	Gd-95/5/0	800	9.2	8	2	150	5	Yes
SKClick12	Gd-90/5/5	300	4.2	1.5	500	150	6	Yes

The fluorescently labeled particles are named SKClick*n* (***Table 7***), where *n* denotes reaction number. All the particles have been characterized by DLS, ATR, and absorption spectroscopy. In three cases, these techniques did not reveal any trace of the chromophore, therefore based on this observation, we concluded, that the coupling reaction was not successful, or the total quantity of chromophore was under the detection limit of the measurements. In the sake of clarity and simplicity, only a few general aspects will be discussed through the examples of SKClick1, SKClick2, SKClick11, and SKClick12.

Nanoparticle SKClick1

The absorption spectra of the NP-LEM-A mixtures were recorded before and after heating. ***Figure 57***A shows the superimposition of these spectra in the case of SKClick1. No significant changes were observed, confirming that the chromophore was not degraded. ***Figure 57***B, C, and D illustrate the purification steps of SKClick1. The third supernatant is colored, while the fourth is not colored anymore, which is confirmed by their absorption spectra. The pellet of purified NPs shown on picture D in ***Figure 57*** was resuspended in water, and its absorption spectrum revealed the absorption band characteristic of the chromophore, which is superimposed to the continuous scattering background caused by the particles. This band supports the presence of the chromophore on the particle.

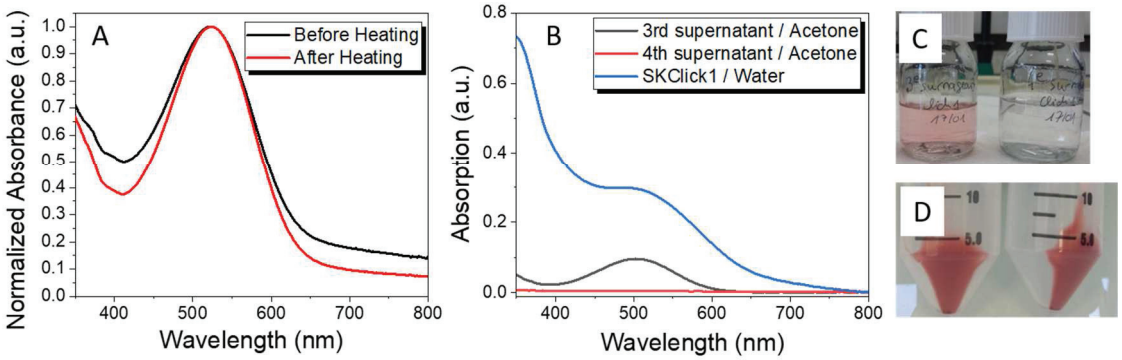

Figure 57 SKClick1 particles. A) Absorption spectra before and after heating the particle suspension with LEM-A. B) Purification steps of SKClick1 followed by absorption spectroscopy. C) Picture of the 3rd (pink) and 4th (colorless) supernatants. D) Picture of the pellets of SKClick1 after purification.

Nanoparticle SKClick2

The scattering of Gd-50/50/0 NPs measured by absorption spectroscopy is shown in ***Figure 58***B. After reaction with the chromophore (SKClick2 particles), the absorption band is even more pronounced than for SKClick1, which is in accordance with the higher chromophore content. The apparent maximum appears at 507 nm.

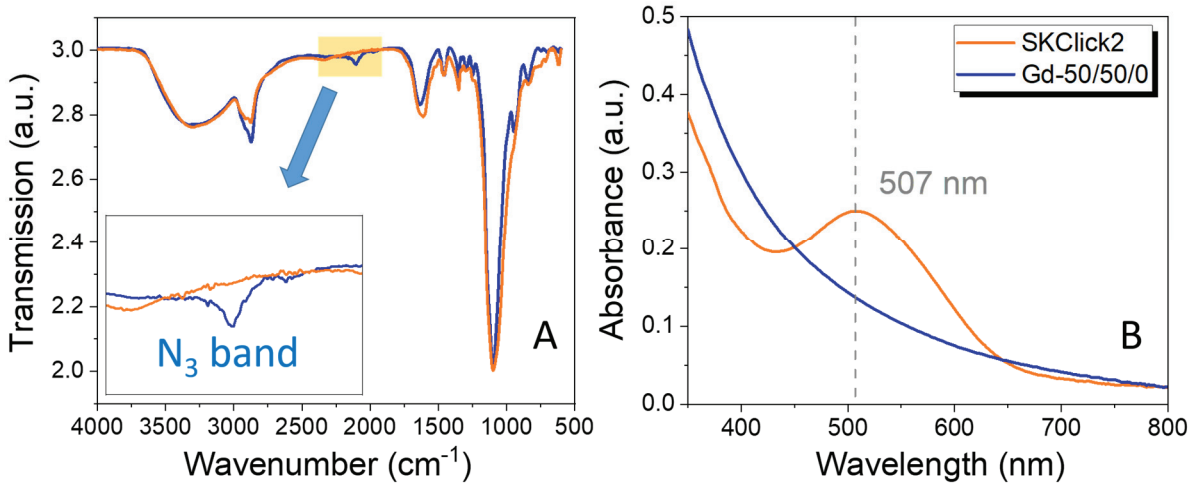

Figure 58 ATR (A) and absorption (B) spectra of Gd-50/50/0 particles before (blue line) and after (orange line) click reaction. The N_3 vibration band disappears, and an absorption band appears upon reaction with the chromophore.

However, the real (without the scattering) absorption band maximum is probably at higher wavelengths. In the ATR spectrum of Gd-50/50/0, the characteristic band of N_3 group is clearly visible, and upon the coupling reaction, it disappears, which is additional evidence for the successful click reaction. However, the quantity of chromophore on the surface is probably not

enough to be detected by ATR; thus, no trace of the bands corresponding to the chromophore could be observed.

Nanoparticle SKClick11

In ***Table 8***, size and PDI values obtained by DLS measurements of SKClick11 are compared to the values of the particle before click reaction, Gd-95/5/0. Both z-average and mean number sizes are slightly larger after the coupling, but this increase is more likely due to the presence of a few aggregates, which is suggested by the slight increase of PDI. Interestingly, zeta potential decreases from -26 mV to -40 mV, which would suggest higher stability of SKClick11, compared to Gd-95/5/0, but the more negative value may also indicate a difference in the coordination mode of bisphosphonate anchoring groups.

Table 8 DLS data measured for Gd-95/5/0 and SKClick11 particles. (Before and after click reaction)

Sample	Z-average (d.nm)	PDI	Mean number (d.nm)	Zeta Potential (mV)
Gd-95/5/0	44	0.20	25	-26
SKClick11	57	0.25	29	-40

Thermogravimetric measurements (***Figure 59***) reveal that the organic content of the particle after click reaction (14.4%) is significantly smaller than for Gd-95/5/0 (29.3%). Decrease of the organic content indicates ligand desorption at the NP surface, which is probably due to the temperature treatment and/or high-speed centrifuging. Indeed, high temperature is needed to activate the Huisgen cycloaddition, and high centrifugal forces are required to precipitate stable SKClick11 particles, particularly from the initial, highly viscous EG solvent. It is worth noting that despite the decreased coating layer aqueous suspension of SKClick11 particles were stable at least for three weeks, which proves their efficient electrosteric stabilization.

Assumptions concerning ligand desorption and coordination modification are further supported by XPS measurements. ***Figure 60*** shows the range O1s binding energy range of high-resolution XPS spectra observed for the particles before click reaction (Gd-90/5/5) and the corresponding fluorescent particles, SKClick12, besides the spectrum of SKClick11. In the three cases, the deconvoluted signal is composed of two peaks.

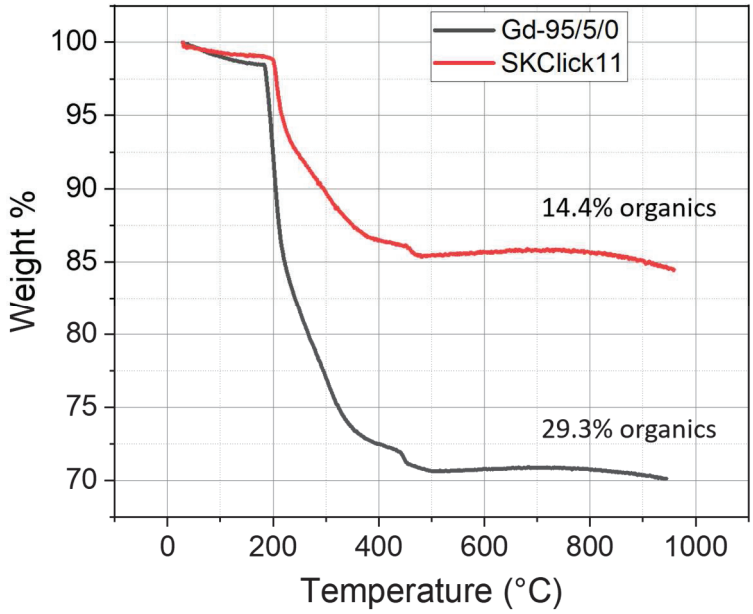

Figure 59 TGA curves obtained for Gd-95/5/0 particles before (black line) and after (red line) click reaction. Ligand desorption is observed.

According to reference databases, the peak at 530 eV corresponds to a metal-oxygen bond binding energy, here Gd-O, and the other observable peak at 532 eV is indicative of P-O(H) bond. Before reaction with the chromophore, the relative peak area of Gd-O (81.2 eV) is dominant compared to the peak area of P-O(H) bond (18.8 eV), while after click reaction, the ratio of the relative peak areas is changed: the Gd-O peak area decreases compared to P-O(H) peak area. This evolution can be interpreted by the change of phosphonate coordination mode, for example, from bidentate it switches to monodentate coordination.[198] This is accompanied by the increase of free P-O(H) bonds and decrease of Gd-O bonds on the surface. In addition, this assumption explains the higher negative surface charge after the click reaction, observed in the zeta potential measurements (***Table 8***).

XPS is a powerful analytical method for elemental analysis: the relative concentration of the observed elements may be expressed as a number fraction, *i.e.,* atomic percentage (at%, denoted as % in the following discussion). Elemental compositions at the surface of naked GdF_3 particle, the BPPEG-coated Gd-90/5/5 particle, the same particle after reaction with the chromophore (SKClick12) and SKClick11 are shown in ***Figure 61***.

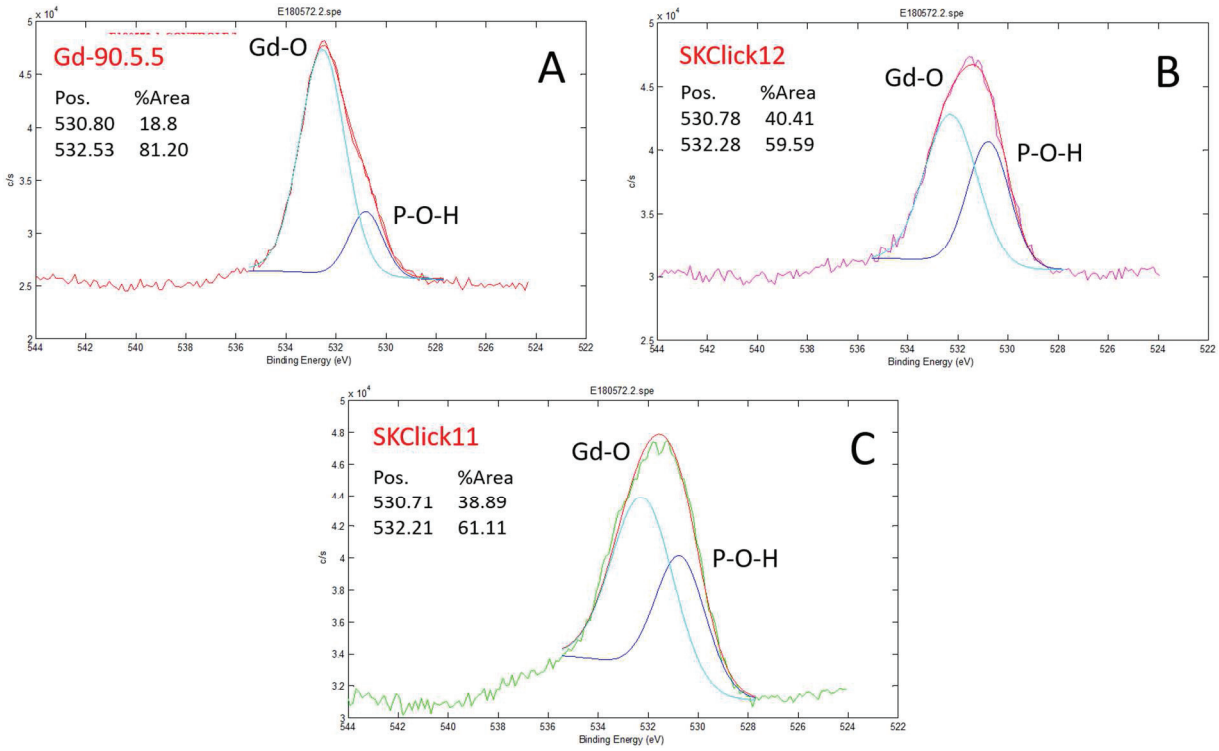

Figure 60 High-resolution XPS spectra of O1s peaks and their deconvolution, for A) Gd-90/5/5 B) SKClick12 and C) SKClick11 nanoparticles.

The sample composed of naked GdF_3 nanoparticles was pyrolyzed at 700°C (5h), in order to remove any organic compounds on the surface, but this temperature was low enough to do not alter the GdF_3 crystal structure (melting temperature of the solid-solid transition of GdF_3 is > 1300 K)[199]. XPS measurement indicated that the gadolinium concentration (67.6 %) at the surface is more important than the fluoride concentration (26.3 %). Upon surface coating, the observable gadolinium content drops to 22.6 %, which is comparable to the fluoride (19.0 %) composition. Decrease in the relative gadolinium content is accompanied by a large organic content due to the coating: 29.1 % C and 24.0 % O. The same batch of particles were subjected to click reaction with the chromophore and after the reaction, a decrease in the organic content (11.4 % C and 14.3 % O) is observed, and at the same time, the relative apparent gadolinium content is increased to 44.4 %. This tendency is also observed for the SKClick11 nanoparticles (12.2 % C and 13.7 % O). This definitely confirms ligand desorption following click reaction and purification steps.

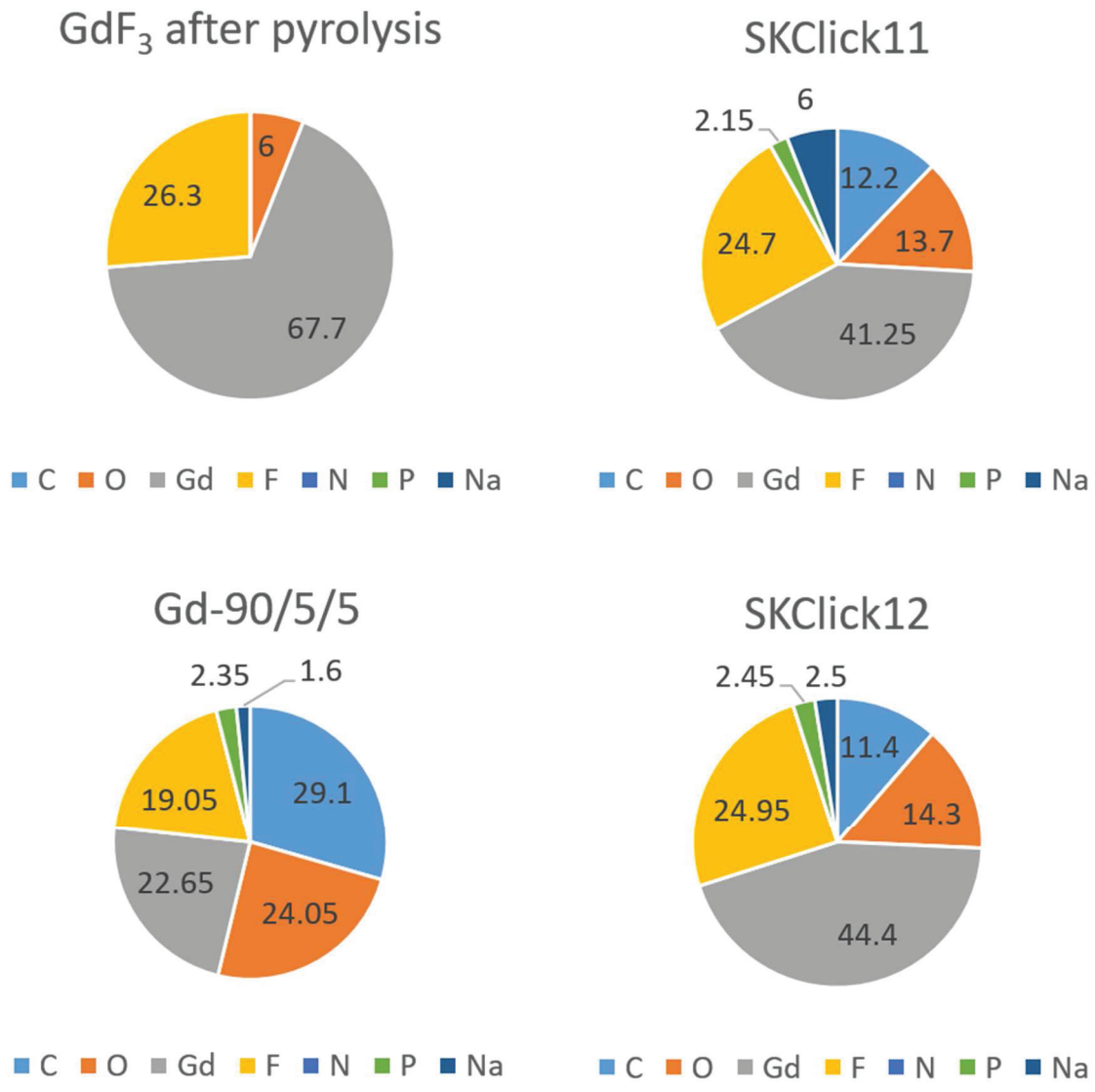

Figure 61 Elemental composition determined by XPS of the surface of particles.

II.2.3 Control test for chromophore attachment

A control experiment has been performed to prove, that the chromophore content in the fluorescent nanoparticles is effectively attached to the particle surface and is not only trapped in the PEG layer. In the experimental control protocol, every parameter was strictly identical to those of the chromophore coupling reaction, except the heating. The same amount from the same batch of functionalized NP Gd-95/5/0 was incubated with the chromophore solution in EG, with the same concentration as for SKClick11. After the homogenization in an ultrasonic bath, the mixture was magnetically stirred during 20h at room temperature.

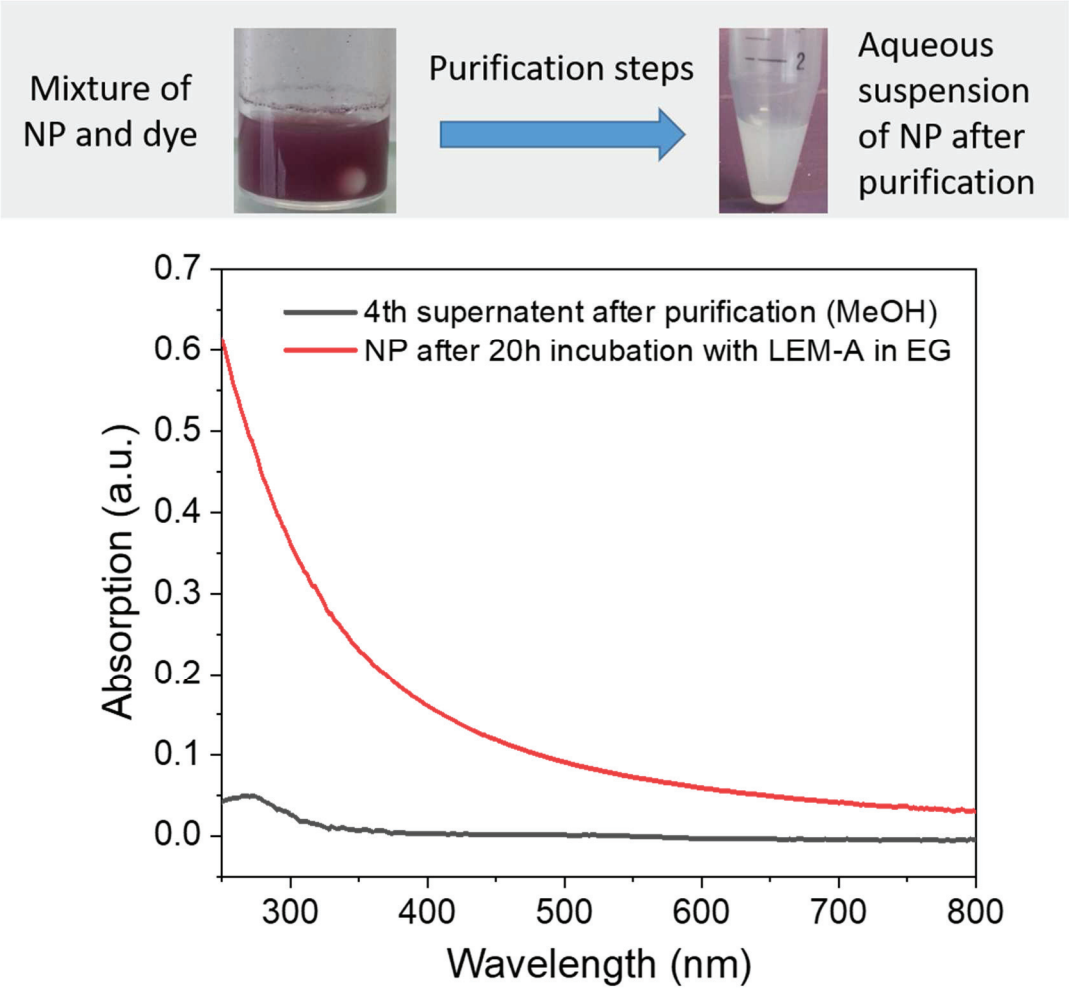

Figure 62 Click reaction test without heating: upon purification, the suspension loses its purple color, and the initial particles (without chromophore) are recovered. This is confirmed by absorption spectroscopy: the last supernatant after purification and the purified particles do not contain the chromophore.

The particles were then subjected to the same purification procedure (precipitation in acetone and centrifugation-redispersion cycles). When the supernatant became colorless, the purified white colored particles were redispersed in water, and their absorption spectra (***Figure 62***) were recorded. Neither the supernatant nor the suspension spectra showed absorption band of the chromophore. Results of this test support the fact that the chromophore is chemically attached to the pink colored particles obtained after the coupling reaction.

Click reaction

- Thermally induced click reaction strategy was preferentially applied for chromophore coupling to the nanoparticles.
- The thermal stability of LEM-A chromophore was tested in different solvents and EG was adopted, because it has a high boiling temperature, in which both particles and the chromophore are soluble and it does not degrade LEM-A.
- The presence of the chromophore on the particle was confirmed by ATR (N_3 band disappears) and absorption spectroscopy (emergence of the absorption band characteristic of LEM-A)
- High temperature (150°C) heating for several hours and/or high speed centrifugation during purification induce a ligand loss confirmed by TGA and XPS analysis.
- XPS: excess Gd^{3+} ion on the surface of the uncoated particle is partially hidden in the coated ones and upon click reaction the organic content decreases.
- XPS analysis also revealed modification in the coordination mode of BPPEG- ligands: after click reaction, the relative ratio of Gd-O bonds decrases in favor of the P-O(H) bonds.
- Release of some P-O bonds of BP moieties is also confirmed by a higher negative zeta potential value.
- Inspite of ligand loss, SKClick11 nanoparticles remained stable in aqueous suspension.
- Finally, successful chromophore coupling was also confirmed by a control exeriment, which allowed to prove that LEM-A is chemically attached and is not only embeded inside the PEG chains.

II.2.4 Estimation of the number of ligands per nanoparticle

In the introduction of this chapter, it was mentioned, that in the case of "grafting to" method with linear chain polymers the grafting density can be increased, when theta solvent conditions are achieved or when the cloud point of the polymer is reached, *i.e.,* when the polymer chains shrink. Visually, when clouding occurs, the polymer solution becomes turbid. That is what we could observe for BPPEG ligands (***Figure 63***) between 60 and 70°C. Therefore, the purpose of heating to 80°C of the mixture BPPEG-nanoparticle in our procedure was to maintain this clouding conditions and increase grafting efficiency.

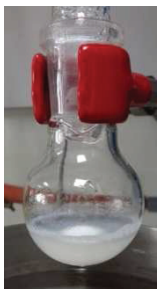

Figure 63 The initially transparent nanoparticle-BPPEG mixture becomes turbid at the cloud point of BPPEG.

Thermogravimetric results were used to estimate the number of ligands per nanoparticle in order to compare the grafting efficiency. The particles are assumed to be prolate ellipsoid

(***Figure 64***) as it seems to best approximate their shape according to TEM observations. Based on TEM and DLS measurements, the following average dimensions are taken for volume calculation: a = 6 nm; b = 10 nm, then the volume found for one nanoparticle is 1508 nm^3. Taking the density of bulk GdF_3, which is 7.1 g cm^{-3}, the estimated mass of one particle is $1.07 \cdot 10^{-17}$ g. With this result and considering that the residual mass obtained in TGA measurement is the inorganic core of the particles, for a known mass of sample it is possible to estimate the number of NPs in the sample.

Prolate ellipsoid volume:

$$V_{NP} = \frac{4}{3} \cdot \pi \cdot a^2 \cdot b$$

Figure 64 GdF_3 nanoparticles are assumed to of prolate ellipsoid shape, their volume is calculated with the formula given in this figure.

In the same way, by assuming that the mass loss is due to the organic layer decomposition (here, water content is neglected), the number of ligands in the known mass of sample can be evaluated. (Calculation details are presented in Appendix 1.) However, it must be stressed that this estimation involves several coarse approximations; therefore, the obtained ligands per nanoparticle ratios are only significant in terms of comparison between each other and cannot be considered as real absolute quantities.

Table 9 Data of TGA measurements of bare and coated GdF_3 nanoparticles, with the calculated numbers of ligands and nanoparticles in the sample.

	Bare GdF_3	Gd-90P/10/0	Gd-95/5/0	SKClick11	Gd-copo-P(1:3)	Gd-copo-P(1:1)
Sample weight (mg)	35.292	6.200	11.524	5.838	11.132	8.642
Residual mass (%)	91.5	90.2	70.7	85.6	61.8	31.9
Residual mass (mg)	32.292	5.592	8.147	4.997	6.880	2.757
Mass loss (%)	8.5	9.8	29.3	14.4	38.2	68.1
Mass loss (mg)	3.000	0.608	3.377	0.841	4.252	5.885
Total number of ligands	2.10E+18	3.78E+17	2.10E+18	5.24E+17	1.98E+17	2.74E+17
Total number of NPs	7.61E+14	5.22E+14	7.61E+14	4.67E+14	6.43E+14	2.57E+14
Ligands/NPs ratio	**7037**	**724**	**2763**	**1122**	**308**	**1063**
Anchoring groups/NPs	**7037**	**724**	**2763**	**1122**	**954**	**3295**

The bare nanoparticle surface is covered by small solvent molecules (2-pyrrolidone) from the synthetic procedure. The estimated value of their number on one particle is about 7000. The previously discussed lower stability of Gd-90P/10/0 particles due to poor surface coverage is confirmed here, with a ligands-per-NPs ratio of only 724. The exclusively BPPEG

functionalized Gd-95/5/0 particles are functionalized with a much higher number of ligands: 2763. Following our assumption on ligand desorption upon click reaction (or purification), the ligands per NPs ratio drops to 1122, which is less than the half of the ratio obtained for the particle before chromophore addition but is still higher than for the phosphonate functionalized one. When considering the particles coated with the copo-P polymer, the estimation of the number of ligands per NPs ratio gives small numbers (308 for the 1:3 and 1063 for the 1:1 particle). However, one must keep in mind, that this ligand contains in average three phosphonate functionalities per polymer chain; therefore, the number of anchors is multiplied by 3. Then, if we compare the number of anchors per nanoparticles for the BPPEG coated particles (where this ratio is the same than the ligands/NPs ratio) to the particles functionalized with copo-P, the remarkably high stability of Gd-copo-P(1:1) is comprehensive, with the highest number of anchors, 3295. With 954 anchors per NPs, Gd-copo-P(1:3) is more stabilized, than Gd-90P/10/0, but less than SKClick11.

II.3 Targeting moiety addition: Lovastatin

Statins are fungal origins compounds used as cholesterol-lowering medications, contributing to reducing the risk of mortality and illness of cardiovascular diseases. They affect endogenous cholesterol synthesis by inhibiting the hydroxymethyl glutaryl coenzyme A reductase (HMG CoA), the enzyme responsible for a key step in the cholesterol biosynthetic pathway. Structural similarity of statins with the natural substrate of the HMG-CoA enzyme is the reason why statins can efficiently bind to the active site of HMG CoA.[200] This structural moiety is the modified 3,5-dihydroxyglutaric acid, the pharmacophore common to all statins, which confers them hydrophilicity. This part of the molecule is completed with a hydrophobic hydrocarbon ring. Amphiphilic drugs are known to diffuse easily in biological fluids and through lipid membranes, including the BBB.[201]

The statin of interest here is lovastatin (also called mevinolin or monacolin K), which was first isolated in 1979 by Endo from filamentous fungus Monascus ruber.[202] In its prodrug form, the backbone of the molecule is composed of a 5-membered lactone moiety attached to a hexahydro naphthalene ring (***Figure 65***). After oral administration, it is hydrolyzed to the active mevinolinic acid (pharmacophore) form.

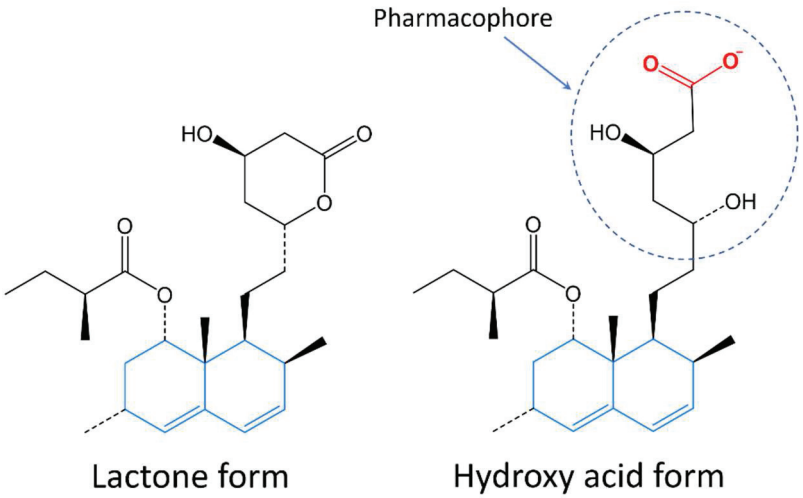

Figure 65 Molecular structures of the two forms (lactone and hydroxy acid) of lovastatin.

Later, other statins have been isolated, such as simvastatin, which is a structural modification of lovastatin: it has an additional methyl group on the α-carbon of the ester side chain. In 1986, Hoffman and his coworkers investigated the potency of a series of ester derivatives of simvastatin (*i.e.,* lovastatin) and found that addition of an aliphatic group in the side chain increases the efficiency of the statin.[203] This observation initiated the development of new derivatives. The chemical procedure leading to the replacement of the ester side-chain by another one has been developed by Willard and Smith, in 1982.[204] First, the side chain is cleaved, to give a secondary alcohol function, then the other hydroxy group on the lactone ring is protected by a silyl function (***Scheme 11***). The new side chain is coupled by the esterification reaction between the appropriate acid chloride and the non-protected hydroxy function in the presence of 4-dimethylaminopyridine. In the last step, the alcohol function is deprotected with tetra-*n*-butylammonium fluoride (TBAF). The overall process is composed of 6 steps. This general procedure was adapted by Hoffman *et al.*, who noticed, that according to the steric demand of the acid chloride derivative, more vigorous conditions are required. However, due to the very hindered nature of the axial hydroxy group, the yield of these reactions was low (about 48 %). An alternative solution was proposed by Askin *et al.*: their procedure involves the protection of the lactone carbonyl as an amide, and instead of hydrolyzing the side chain, it is methylated with excess methyl iodide.[205] They reported an exceptionally high yield of 91 %. Both chemical procedures require several steps and difficult separation from side products. Need for the simple and selective production of statins at the industrial scale guided researchers to the enzymatic substitution of the α-methylbutyrate side chain with α-dimethylbutyrate or

other derivatives, with acyltransferase[206], lovastatine esterase[207] or with a mutant fungus[208] (Aspergillus terreus).

Besides their cholesterol-lowering effect, statins have also been reported to have an anti-inflammatory effect[209]; however, the mechanism of action in inflammation is still a matter of debate. Vorup-Jensen and coworkers studied the interaction of simvastatin with complement receptor 3 (CR3) and proposed a novel explanation for the anti-inflammatory effect of this molecule.[78] CR3 is a complement receptor expressed on the surface of many immune cells, such as monocytes and macrophages and it was shown, that in pro-inflammatory environments, it is present in its ligand-binding ("open") conformation. Moreover, a high correlation was observed between the level of CR3 expressed on monocytes and the severity of acute ischemic stroke. It was also demonstrated on animal models of Alzheimer disease, that the inhibition of CR3 expressed on microglial cells has a neuroprotective effect. All these observations lead to the conclusion, that this receptor is a good potential target in anti-inflammatory therapy. Jensen *et al.*, showed that simvastatin is able to antagonize the complement fragments of CR3. They evidenced that simvastatin in its carboxylate form complexes the Mg^{2+} ions in the metal ion-dependent adhesion site (MIDAS) of CR3. The strong affinity of $Mg^{2+}$to carboxylates constitute the basis of anti-inflammatory effect of simvastatin.

Here we aimed to take advantage of the statin pharmacophore to induce specific interaction with the CR3 receptor and thus target the activated immune cells to label them with the nanoparticles. For that reason, the statin molecule, more specifically lovastatin, must be attached to the nanoparticle surface without altering its structural features required for recognition and binding. ***Scheme 11*** shows the basic idea of our strategy, which consists of hydrolyzing the side chain of lovastatin in order to keep an alcohol function at this site. In the meantime, the other alcohol function must be protected by a silyl group. The obtained lovastatin derivative has been elaborated by our collaborators, Prof. Marc Lecouvey's research group. Lovastatin derivative, from now referred to as "lovastatin", is then reacted with the carboxylic acid function of BP-PEG-COOH ligand tethered on the particle surface *via* esterification and in the last step, the lactone ring of lovastatin is deprotected (***Scheme 12***).

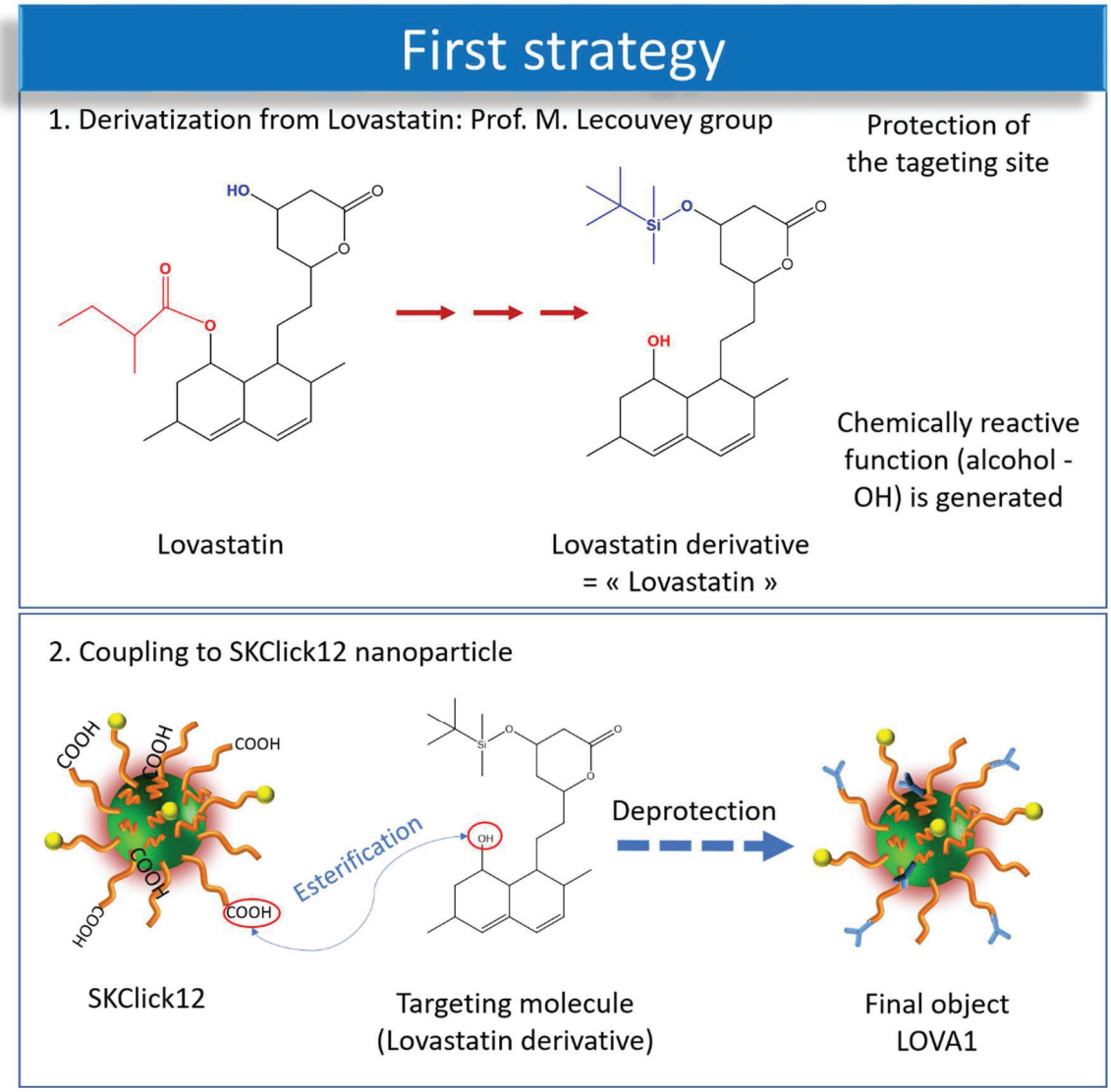

Scheme 11 First strategy for lovastatin coupling to SKClick 12 nanoparticle.

II.3.1 Steglich esterification

One of the most commonly used esterification procedure is the so-called Steglich esterification, developed by Steglich and Neises in 1978.[210] According to the authors, this protocol is adapted for sterically demanding esters, and its principle can be summarized as follows (for the detailed mechanism, please refer to ref. [211]_). Dicyclohexyl carbodiimide (DCC) activates the carboxylic acid by forming an O-acylisourea, which in turn reacts with N,N-dimethylaminopyridine (DMAP). This acyl transfer results in the formation of the amide (active ester) intermediate, reacting with the alcohol to give the ester and the stable dicyclohexylurea (DHU) byproduct. As proposed by Steglich, in practice, the carboxylic acid is mixed with DMAP (3-10 mol%) and the alcohol, in a dry solvent, then the solution is cooled to 0°C, and

DCC is added dropwise. The reaction mixture is stirred at 0°C for 5 minutes and 3h at room temperature.

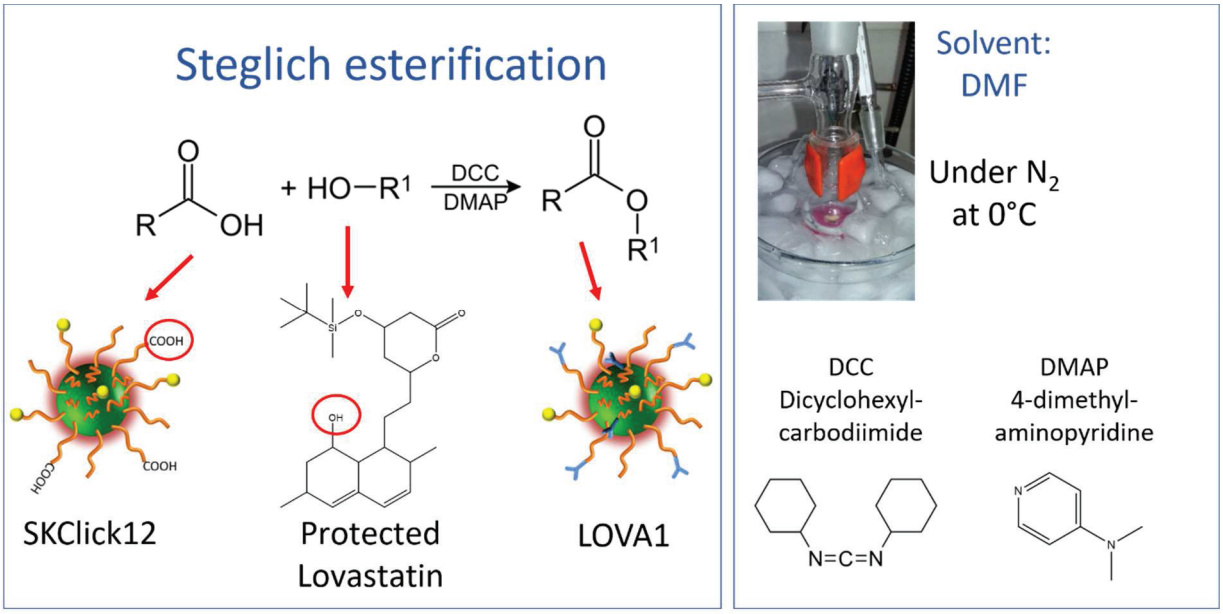

Scheme 12 Principle of Steglich esterification.

Experimental details

In SKClick12, only 5% of the total ligand content is BPPEG-COOH. Therefore, the required quantities of DCC, DMAP, and lovastatin are small and cannot be precisely weighted. Hence, stock solutions of these compounds were first prepared:

- Stock DMAP ($7.10 \cdot 10^{-3}$ mol L^{-1}): 13.0 mg in 15 mL of anhydrous DMF
- Stock DCC ($1.77 \cdot 10^{-2}$ mol L^{-1}): 18.3 mg in 5 mL of anhydrous DMF
- Stock DMAP ($3.55 \cdot 10^{-3}$ mol L^{-1}): 15.4 mg in 10 mL of anhydrous DMF

100 mg of SKClick12 NP were introduced in a three-necked round-bottom flask (dry), and 3 mL of anhydrous DMF was added. The suspension was sonicated and magnetically stirred under nitrogen, until homogenization. Then 50 µL of DMAP ($3.55 \cdot 10^{-7}$ mol) stock solution and 1mL of lovastatin ($3.55 \cdot 10^{-6}$ mol) stock solution were added. The mixture was then cooled to 0°C and 200 µL of DCC ($3.55 \cdot 10^{-6}$ mol) stock solution was added dropwise. After 10 minutes stirring at 0°C, the mixture was let heat up to room temperature and stirred for an additional 24h. Visually no change was observed.

As the product DHU and reagents (DCC, DMAP, and lovastatin) are all soluble in acetone, the usual purification steps were followed for the particles: precipitation in acetone and washing-centrifuging cycles. The obtained solid was then freeze-dried and analyzed.

No difference could be observed in ATR spectra of the particles before and after reaction with lovastatin. Lovastatin was not either detectable by XPS and MALDI-TOF analysis, confirming, that the reaction did not take place.

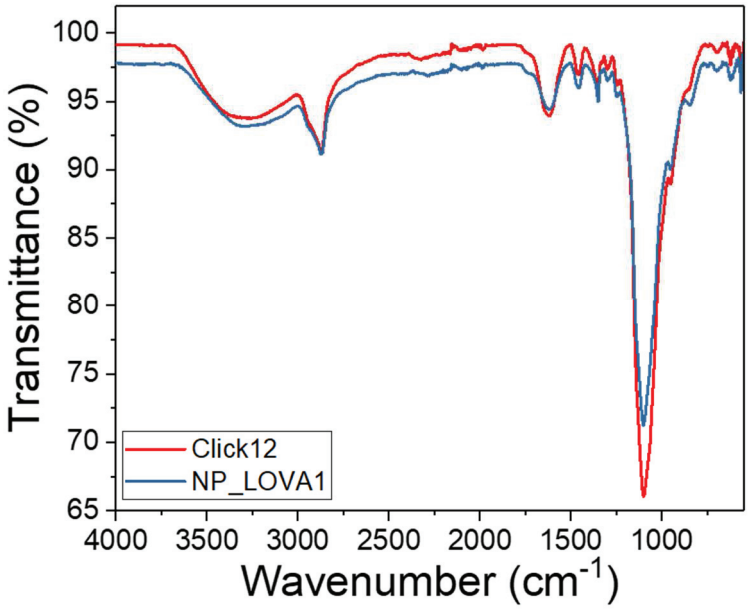

Figure 66 ATR spectra of SKClick12 NP before (red line) and after (blue line) reaction with lovastatin.

In order to study the reactivity of the alcohol function of lovastatin and try to optimize the reaction conditions, model reactions have been performed.

First, the coupling with a commercially available di-carboxylic acid terminated PEG ($PEG(COOH)_2$) was tested, instead of the particle (***Scheme 13***). The reaction was followed by thin layer chromatography (TLC), which again showed no difference between the reagents and the product mixture.

No reaction could be observed even by varying reaction parameters, such as increasing the stirring time at 0°C or different concentrations.

Another commonly used carbodiimide for esterification is 1-(3-dimethylaminopropyl)-3-ethylcarbodiimide (EDC). As a second strategy, this compound was used for the acid activation, along with DMAP catalysis and the solvent was dry dichloromethane. Again, several attempts have been performed for the coupling of lovastatin to $PEG(COOH)_2$, without success.

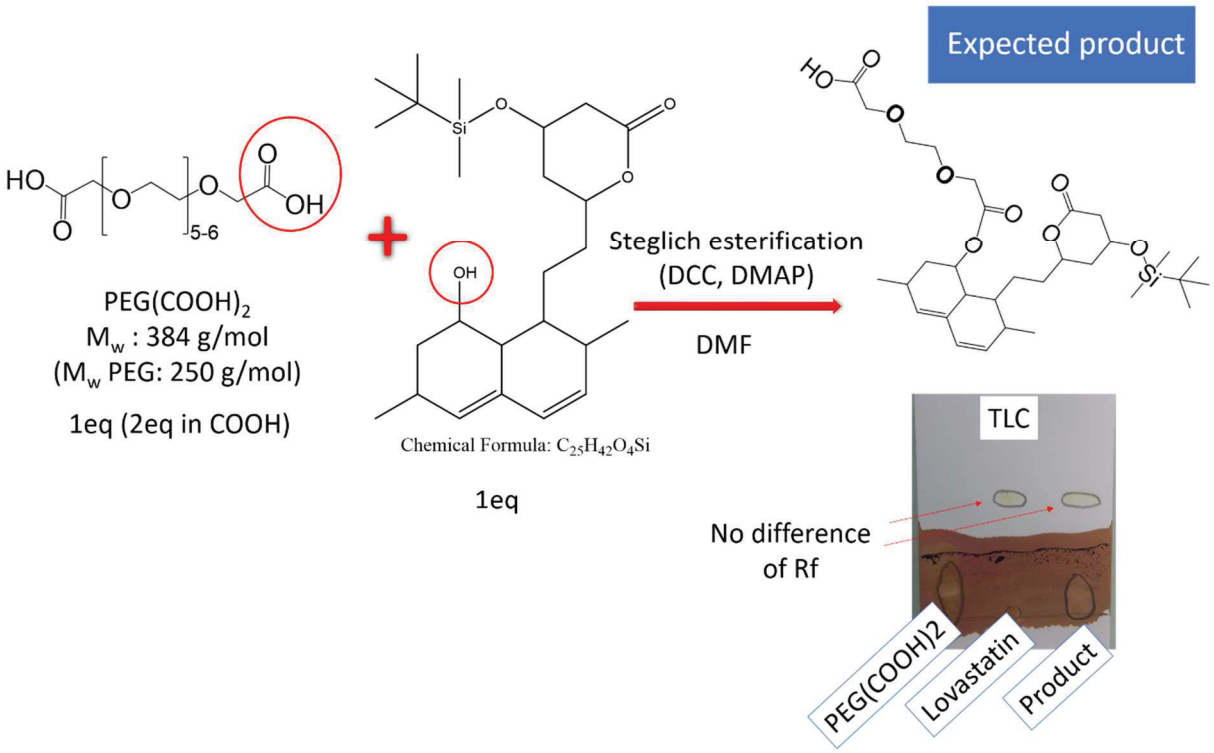

Scheme 13 Steglich esterification procedure between lovastatin and $PEG(COOH)_2$. The product was analyzed by thin layer chromatography (TLC) (mobile phase Et_2O; revelator: I_2 and a solution of $KMnO_4$). The product is a mixture of the two initial compounds.

II.3.2 Other classical esterification methods

Maleic anhydride in the presence of the base triethylamine was tentatively reacted with lovastatin, but the TLC test showed no trace of the product. Another classical esterification method involving triethylamine catalysis is the coupling of acetyl chloride with alcohol, but this method again gave the same negative result.

In the next attempt to react the sterically hindered secondary alcohol function of lovastatin with a carboxylic acid, $PEG(COO)_2$ was first transformed by oxalyl to the more reactive acid chloride derivative and the as obtained $PEG(COCl)_2$ was then reacted with lovastatin, in the presence of DMAP.

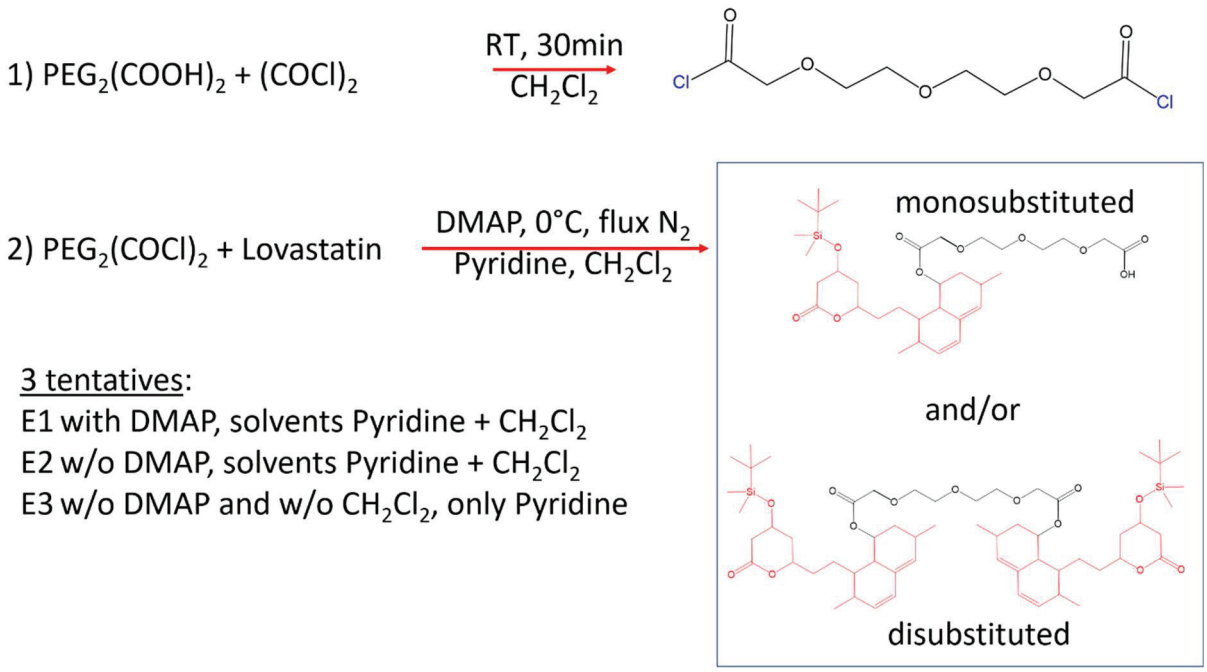

Scheme 14 Reaction scheme for the esterification of lovastatin with $PEG(COOH)_2$ through $PEG(COCl)_2$.

Reaction conditions

Three slightly different conditions have been tested, as described in ***Scheme 14***. Here the third protocol (E3, ***Scheme 12***) is described in detail. In a three-necked round-bottom flask, 311 mg of $PEG(COOH)_2$ was dissolved in 2 mL of dry dichloromethane (DCM). A large excess (500 µL) of oxalyl chloride [$(COCl)_2$] was added, and the mixture was stirred under an inert atmosphere, at room temperature for 2h. Solvent and excess oxalyl chloride were evaporated, and the product was dissolved in dry DCM (500 µL). Lovastatin (40 mg) was dissolved in 1 mL of anhydrous pyridine, under N_2 flux. Both solutions were cooled to 0°C, and lovastatin solution was added dropwise (in 10 min, under N_2 atmosphere) to the acid chloride solution. The mixture was maintained at 0°C for 1h and then let to warm up to room temperature. After stirring of 20h, the solvent was evaporated, and the obtained semi-solid product was analyzed by TLC, NMR, and LC-MS (Liquid chromatography coupled to Mass spectrometry).

TLC analysis of the crude product revealed three spots of successive retardation factor (Rf). The first one was aligned with free lovastatin, showing that the reaction was not total, but two other intensive spots clearly indicated that some reaction occurred. In order to identify these two products, first, the ^{1}H-NMR spectrum (***Figure 67***) of the crude product was analyzed and compared to the spectra of free lovastatin and $PEG(COOH)_2$.

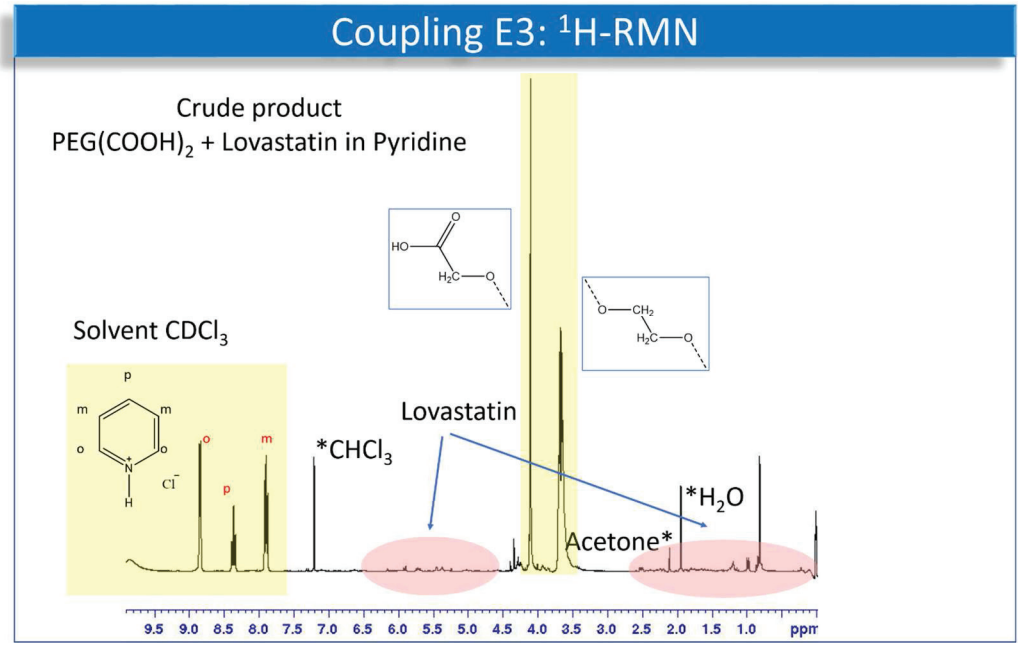

Figure 67 ^{1}H-NMR spectrum of the crude product of lovastatin esterification with PEG(COOH)$_2$

Proton signals of pyridinium chloride are present in the region from 7.5 to 9.5 ppm, which is a byproduct of the reaction. As PEG(COOH)$_2$ was in large excess, the signals of this molecule are very intense compared to lovastatin.

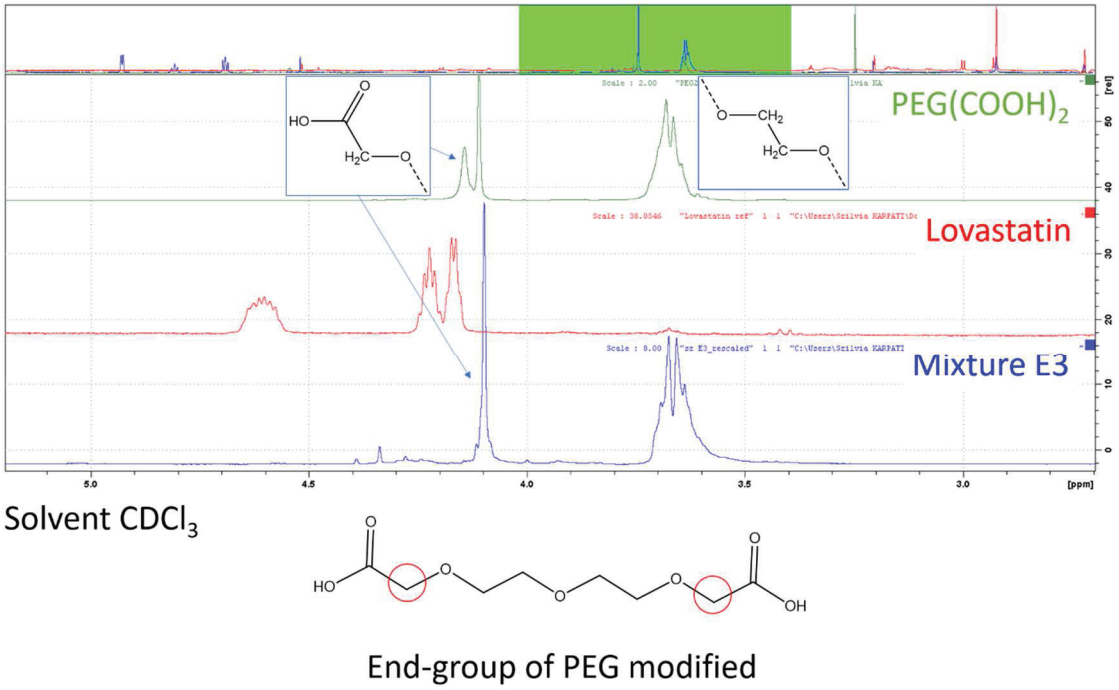

Figure 68 ^{1}H-NMR spectra of lovastatin, PEG(COOH)$_2$ and their reaction product: comparison of the range containing the chemical shifts of PEG.

A closer examination of PEG signals (***Figure 68***) reveals that the initial doublet corresponding to the protons at both ends of PEG(COOH)$_2$ is converted to a singlet, indicating a transformation

of the end groups. A zoom in on the spectrum between 4 and 6 ppm (***Figure 69***), allows seeing the signals of lovastatin. The free lovastatin spectrum is in perfect agreement with literature data[212,213], and comparison with the signals of the product reveals a new peak at 5.37 ppm, besides the signal of H-C4. According to the interpretation by several authors[208,212,214] of ester derivatives of lovastatin, this new signal may be attributed the H-C1-ester.

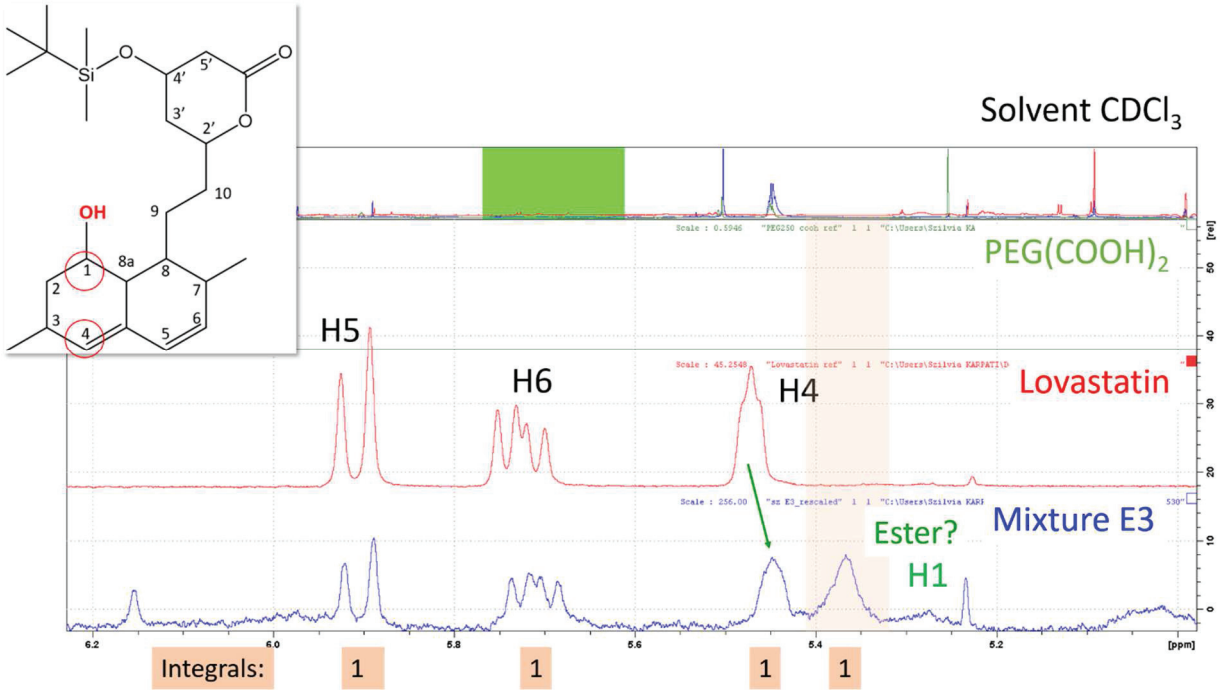

Figure 69 ^{1}H-NMR spectra of lovastatin, PEG(COOH)$_2$ and their reaction product: comparison of the range containing the signals of H-C5, H-C6, and H-C4 protons of lovastatin.

To further investigate the product, an LC-MS analysis has been performed, after separation on a C18 column, with a gradient of solvent from 100% water to 100% acetonitrile. The signal collected on the UV detector (254 nm) as a function of retention time, shows different peaks. The first peak corresponds to the unreacted PEG(COOH)$_2$, and there is no peak corresponding to free lovastatin, which is expected at approximately 7 minutes. The peaks in between are not present in the signals of PEG(COOH)$_2$ and lovastatin; therefore, they can arise from the products of the reaction. When examining the MS spectrum, the characteristic ions of the mono- and disubstituted PEG(COOH)$_2$ with lovastatin are identified. The adduct ions are listed in ***Table 10***.

Table 10 Ionic fragments (mono- and disubstituted PEG(COOH)$_2$ with lovastatin) identified in the reaction product of reaction E3.

Monosubstituted
Exact mass: 638.35

m/z experimental	m/z calculated	Corresponding Ion
661.5	661.3	$[M+Na]^+$
656.6	656.3	$[M+NH_4]^+$
1319.8	1318.7	$[2M+ACN+H]^+$
671.6	671.3	$[M+MeOH+H]^+$
683.3	683.3	$[M+2Na-H]^+$

Disubstituted
Exact mass: 1054.62

m/z experimental	m/z calculated	Corresponding Ion
1076.1	1077.5	$[M+Na]^+$
1071.8	1072.6	$[M+NH_4]^+$

The presence of these esters (mono- and disubstituted PEG(COOH)$_2$) provided evidence that the sterically hindered alcohol function on C4 of lovastatin can be esterified by a relatively large molecule, such as PEG(COOH)$_2$. However, when the same procedure was applied to the free BPPEG-COOH ligand, the esterification reaction failed.

II.3.3 New strategy: addition of a linker (Fmoc-NH-PEG-COOH) on Lovastatin

As the OH-function of lovastatin is hindered as well as the carboxylic acid on the nanoparticle surface, it is possible, that these steric constraints prevent the expected esterification reaction.

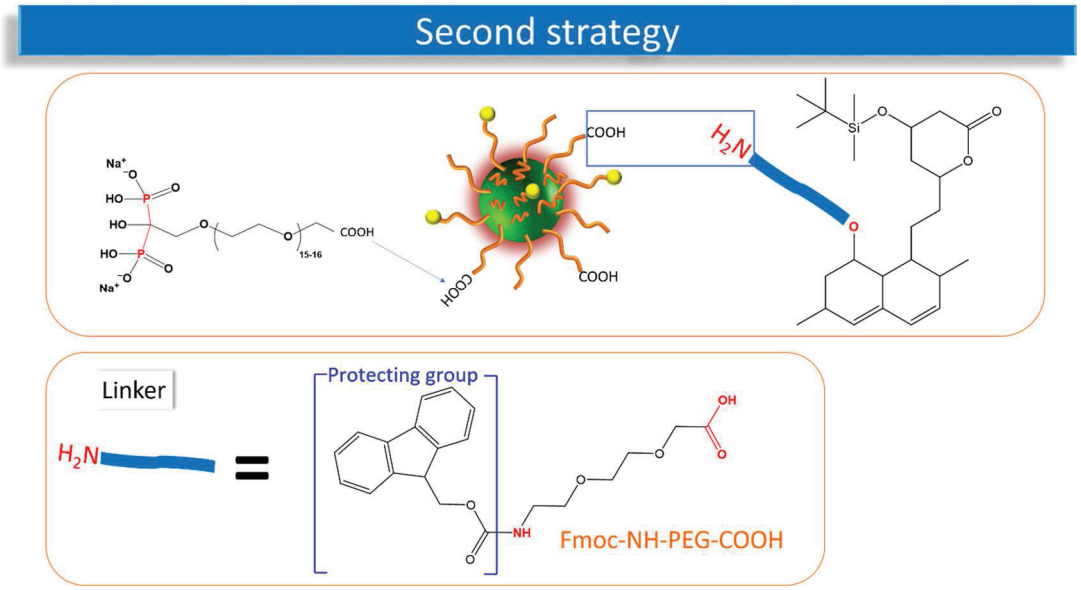

Figure 70 Second strategy for lovastatin coupling to SKClick12 nanoparticles.

Therefore, a new strategy has been proposed by Prof. Marc Lecouvey, which involves a linker attachment to lovastatin, bringing a more accessible functional group (***Figure 70***). The linker

of choice is a bifunctional diethylene glycol (H_2N-PEG-COOH), with a carboxylic acid on one end, able to react with the alcohol and an amine function on the other end, expected to react with the COOH of the particle. To avoid side reactions, the amine function is protected with the base-labile protecting group, fluorenylmethyloxycarbonyl (Fmoc), often used in organic synthesis.

This second strategy consisted of five main steps summarized in ***Scheme 15***. In the first step, the linker COOH function is transformed into an acid chloride, such as previously in the case of $PEG(COOH)_2$. The second step also follows the procedure, which led to the successful esterification reaction between $PEG(COOH)_2$ and lovastatin, *i.e.,* esterification in the presence of pyridine. After that, the Fmoc protecting group is cleaved, in order to proceed to the coupling reaction between the amino group of the linker and the particles, by the classical EDC-NHS coupling reaction. In the last step, the lovastatin lactone ring must be deprotected to give the targeting nanoparticle.

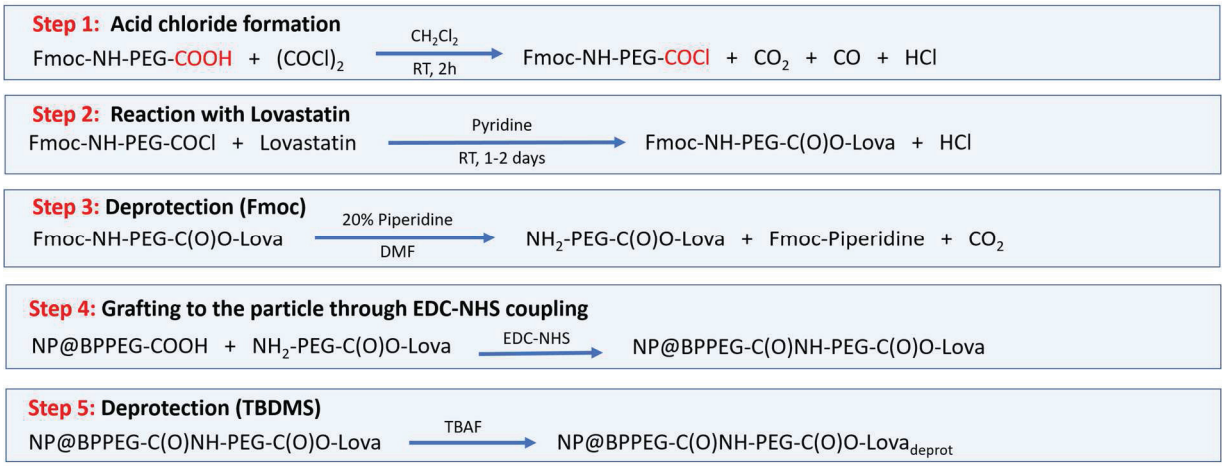

Scheme 15 Five steps of the second strategy for lovastatin coupling to SKClick12 nanoparticles.

Three slightly different attempts have been made for step 2, but the LC-MS and TLC analysis showed that the esterification reaction did not occur, and ^{1}H-NMR confirmed, that the purified product is a mixture of the initial compounds.

In light of this failure, a series of further model reactions have been performed for a better understanding of lovastatin reactivity.

II.3.4 Model reactions

As steric hindrance was suspected to prevent lovastatin from esterification with PEG derivatives, a small molecule, acetyl chloride was used as a source of acid chloride, and

different combinations of pyridine/DMAP/TEA were tested as bases, without success (reactions LovAc 1, LovAc 2, LovAc 3 and LovAc 4).

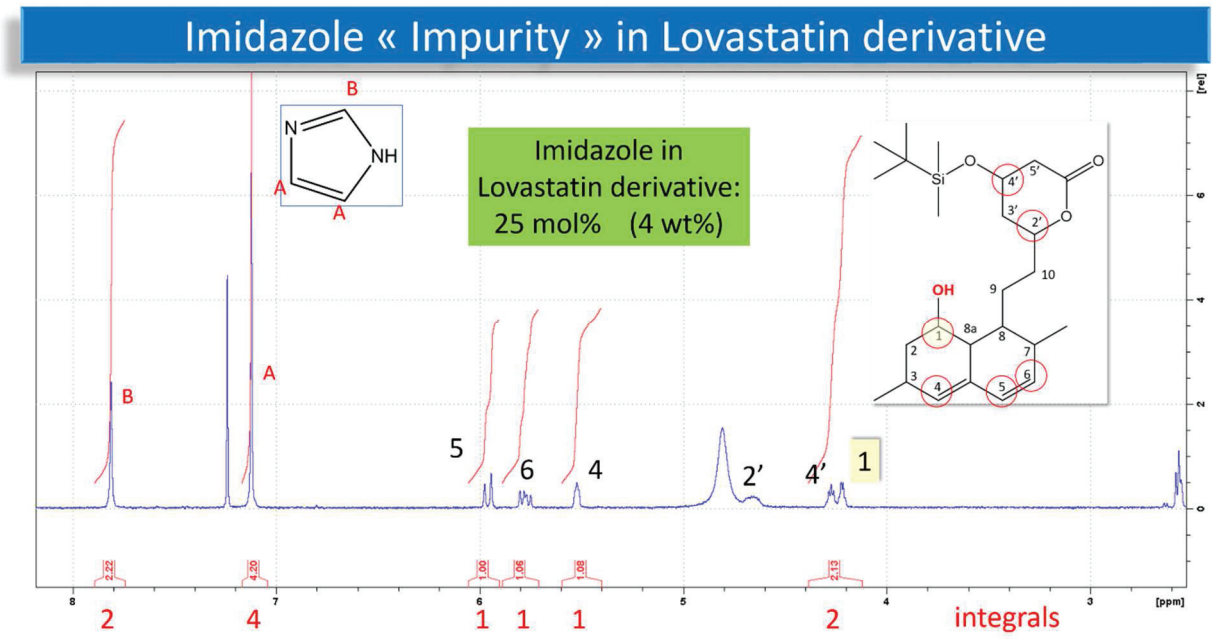

Figure 71 ^{1}H-NMR spectrum of lovastatin, with imidazole impurity.

During the derivatization of lovastatin and more specifically in the silyl protection step, imidazole is used, and according to the ^{1}H-NMR analysis (***Figure 71***), this molecule is present in the lovastatin batch (4 wt%, 25 mol%). In the literature, imidazole is described by several authors, as an ester hydrolysis catalyst,[215,216,216,217] therefore we considered the possibility, that this molecule is responsible for the failure of esterification and purified it by extraction (organic solvents: petrol ether and chloroform) and washing with 0.5M HCl. The purified lovastatin sample was analyzed by ^{1}H-NMR, which confirmed its purity as compared to the original batch (***Figure 72***).

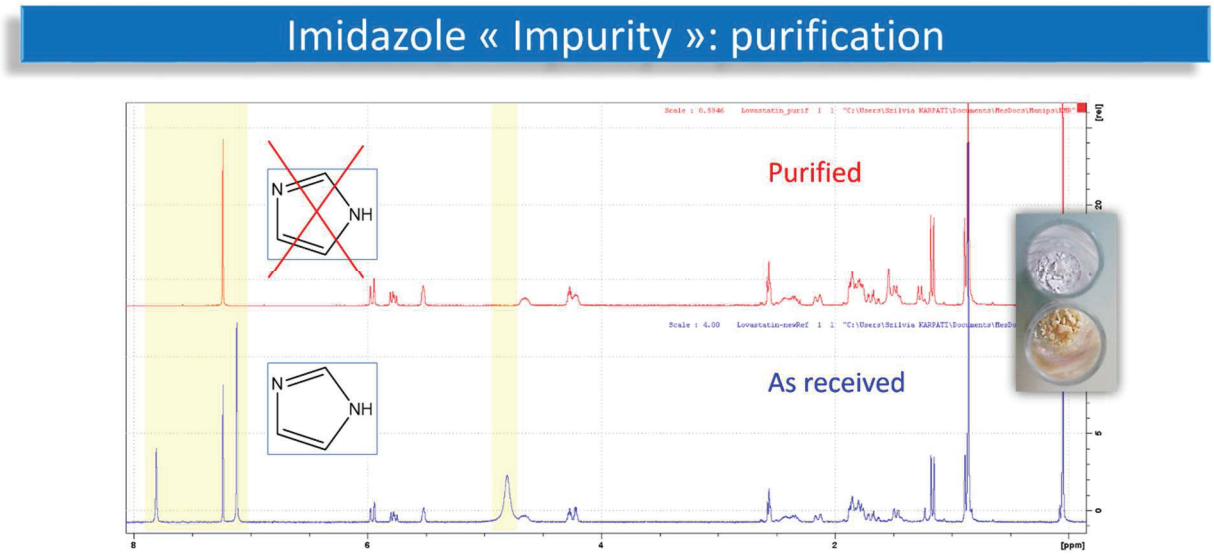

Figure 72 ^{1}H-NMR spectra: after purification of lovastatin, there is no more imidazole impurity.

For further reactions summarized in ***Table 11***, the purified sample was used. Lovastatin to acetyl chloride ratio, the presence or not of DMAP, nature of base and solvent have been varied, and the product was analyzed by NMR.

Table 11 Summary of reaction conditions for esterifications LovAc 5 to LovAc 8.

Reaction Ref.	Lovastatin : Acetyl Chloride ratio	Catalyst	Base	Solvent
LovAc 5	Large excess of Acetyl chloride	-	Pyridine (excess)	$CDCl_3$
LovAc 6	1 : 1.5	-	TEA (4eq)	CH_2Cl_2
LovAc 6 excess	Large excess of Acetyl chloride	-	Large excess of TEA	CH_2Cl_2
LovAc 7	1 : 1	DMAP (<1eq)	TEA (1.5eq)	$CHCl_3$
LovAc 8	1 : 1.5	DMAP (<1eq)	Pyridine (2eq)	CDCl3

Examination of these NMR spectra revealed that the expected ester is formed only if the acetyl chloride is in very large excess (30-40 equivalent), *i.e.,* for reactions "LovAc 5" and "LovAc 6 excess". ***Figure 73*** shows, for example, the NMR spectrum of the product "LovAc 6 excess" and its comparison with LovAc 6 and free lovastatin.

When only a slight excess (1.5 equivalent) of acetyl chloride is added (LovAc 6), no reaction occurs, the measured NMR spectrum is the same as free lovastatin. However, with a very large excess of reagent (LovAc 6 excess), the signal corresponding to H-C1 is shifted from 4.2 to 5.4 ppm, which is the isomer shift expected for ether derivatives of lovastatin. The other new peaks correspond to some side products due to the large excess of acetyl chloride; therefore, the reaction conditions still needed to be optimized.

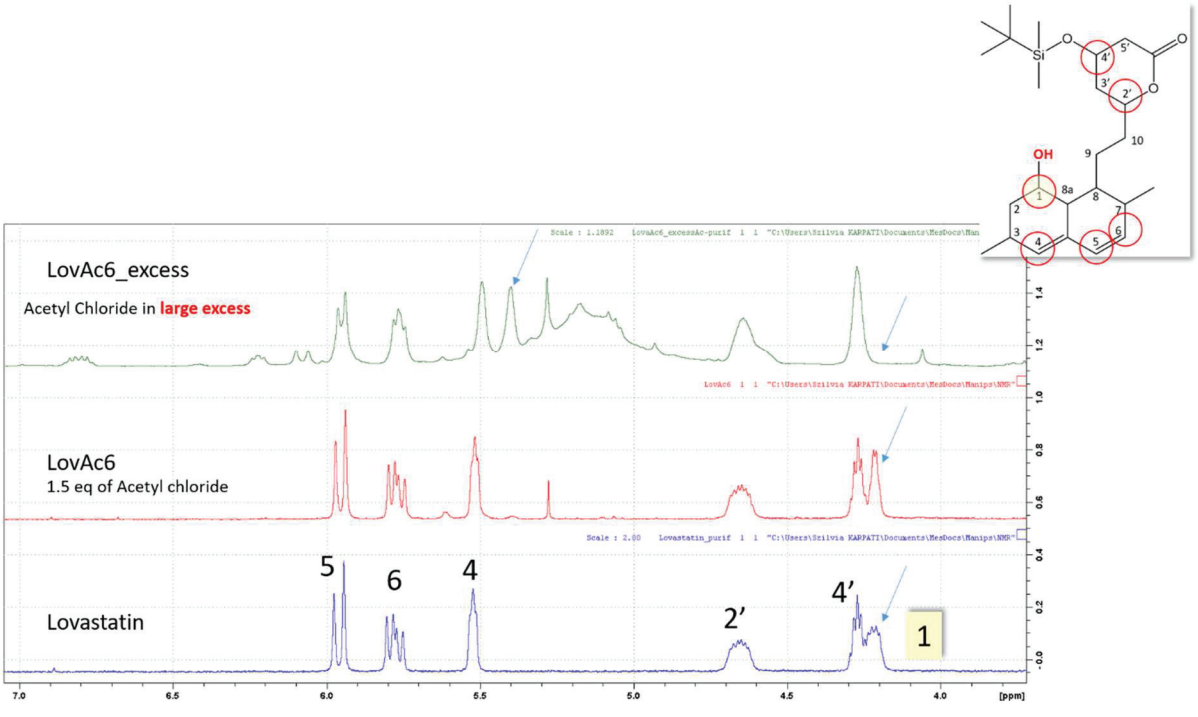

Figure 73 ^{1}H-NMR spectra of reaction product LovAc 6 and LovAc 6-excess, compared to lovastatin.

Sorensen *et al.*[208] reported a 72 % reaction yield, when acylating the dihydro analog of our lovastatin derivative. Their procedure consisted in the addition of a 100-fold excess of (S)-2-methylbutyric anhydride in the presence of DMAP (1 equivalent) and pyridine. Therefore, in comparison, our results are not surprising.

Table 12 Summary of reaction conditions for esterifications LovAc 9 and LovAc 10.

Reaction Ref.	Lovastatin : Acetyl Chloride ratio	Catalyst	Base	Solvent
LovAc 9	1 : 100	DMAP (1eq)	Pyridine	Pyridine
LovAc 10	Same as LovAc9 but heated at 50°C for 2h			

Based on Sorensen's work, we performed attempt LovAc 9, with a 100-fold excess of acetyl chloride, in the presence of DMAP (1 eq) and pyridine as solvent (***Table 12***). The mixture was stirred at room temperature for 72h and then purified by extraction with dichloromethane, washed with 0.5M HCl, dried with sodium sulfate. The mixture was filtered, and the solvent was evaporated.

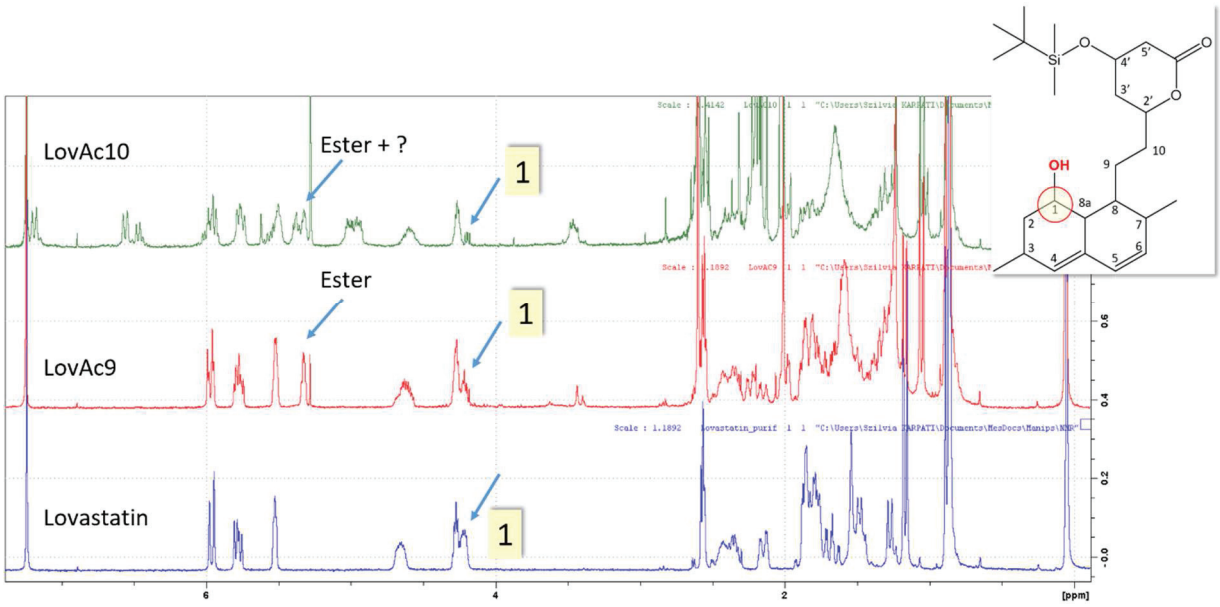

Figure 74 ^{1}H-NMR spectra of reaction product LovAc 9 and LovAc 10, compared to lovastatin.

Besides unreacted lovastatin, TLC analysis showed a second spot, suggesting that some reaction occurred. NMR spectrum revealed that the esterification occurred partially (***Figure 74***). A new signal, corresponding to the ester appears, besides the unchanged lovastatin signals. The formation of the expected ester derivative was further confirmed by LC-MS analysis (***Figure 75***). The parent ion m/z 476.6 corresponds to the protonated ester derivative and is accompanied with the ions resulting from its successive fragmentations.[218,219]

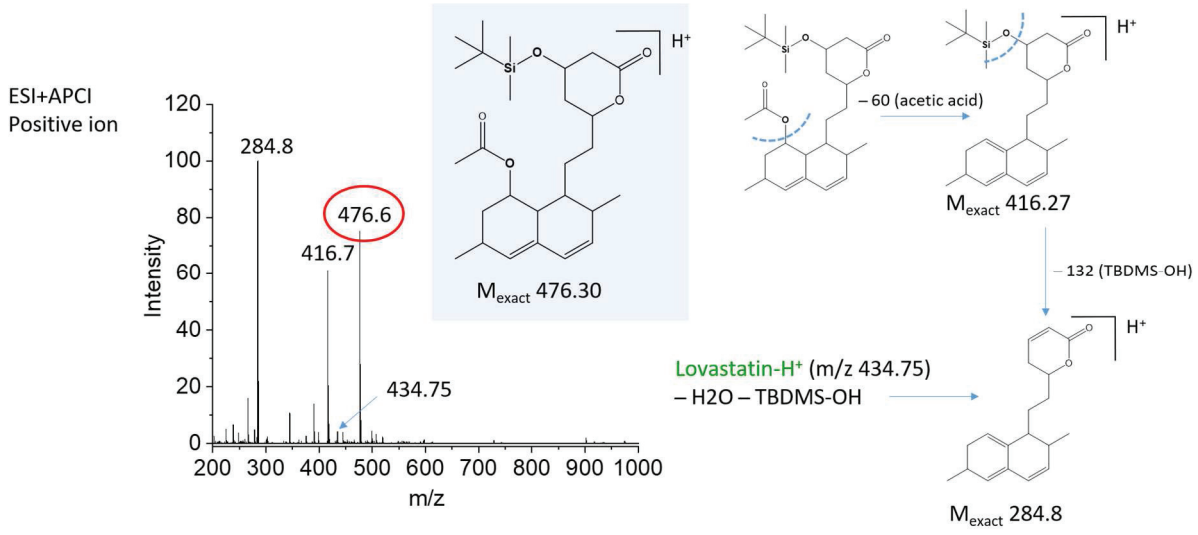

Figure 75 Fragment ions of acylated lovastatin obtained by LC-MS measurement and the assumed fragmentation path.

In order to increase the efficiency of esterification, the same conditions were reproduced in LovAc 10 reaction, but the mixture was heated to 50°C, during 2h. Unfortunately heating, even

at relatively low temperature, seems to induce side reactions: the NMR spectrum of this product shown in ***Figure 74***, shows a mixture of unreacted lovastatin, its ester derivative, and some other unidentified peaks.

As the best results have been obtained with procedure LovAc 9, the same procedure was applied to the reaction between lovastatin and Fmoc-NH-PEG-COCl. However, the NMR analysis of the mixture after one week of stirring revealed no trace of any reaction between the two compounds.

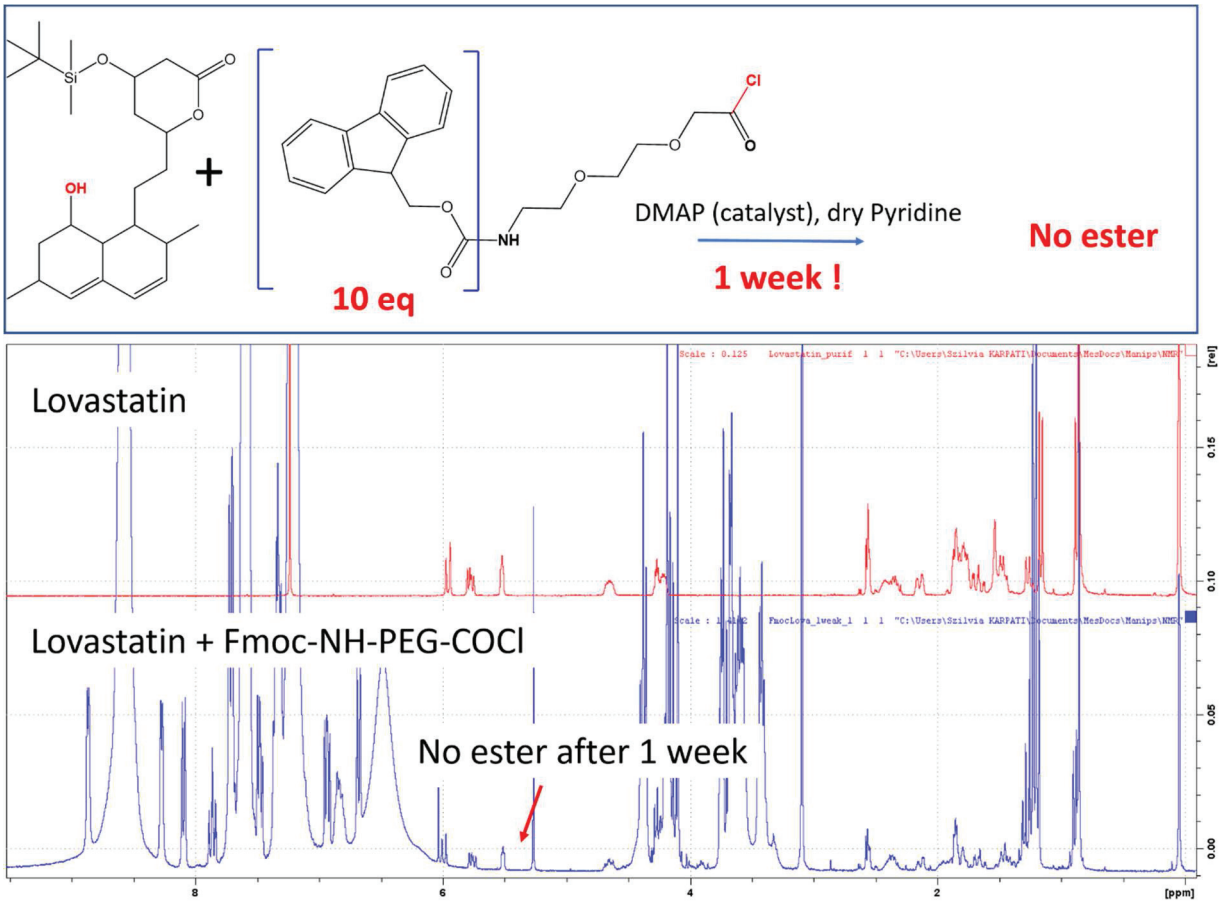

Figure 76 ^{1}H-NMR spectra of reaction product lovastatin with Fmoc-NH-PEG-COOH.

After this last attempt, this strategy was also abandoned. It was concluded, that the steric hindrance is still too important with Fmoc-NH-PEG-COOH and lovastatin can react only with small molecules, such as acetyl chloride.

Targeting molecule coupling

- Lovastatin was selected as targeting molecule for CR3 complement receptor expressed on monocytes and microglia
- Steglich esterification was attempted as coupling reaction between Lovastatin and BPPEGCOOH functionalized nanoparticles, but the initial strategy failed
- Reaction conditions have been optimized with the model compound $PEG(COOH)_2$, however the successful protocol failed again, when it was applied to the ligand BPPEGCOOH
- The next strategy consisted in coupling a linker (Fmoc-NH-PEG-COOH) on Lovastatin and subsequently reacting the linker with the particle. This strategy also failed.
- Several model reactions have been attempted with acetyl chloride, to probe the reactivity of Lovastatin. One protocol involving the presence of a large excess of acetyl chloride seemed promising, however when applied to Fmoc-NH-PEG-COCl, no reaction occured.

III – Conclusions

Synthesis and characterization of hybrid GdF_3 nanoparticles are reported, with an organic layer consisting of PEG chains. Strong anchoring is obtained through bisphosphonate coordination to surface gadolinium ions. In the case of a mixture of two or three different end-functionalized BPPEGs, the initial mixing ratio (*e.g.*, BPPEGOMe and $BPPEGN_3$) seems to be retained on the surface of the particles, corresponding to a statistical grafting process. Particles exclusively grafted with BPPEGCOOH ligands are precipitating. The examination of the vibrational bands in the ATR spectrum shows the coordination of the carboxylate part along with the BP part. Therefore, we concluded that BPPEGCOOH ligand tends to form bridges between the particles, forming large aggregates. The exact coordination mode of BP moiety could not be determined; however, ATR spectra suggest, that the P=O oxygen does not participate to the coordination and the excess negative surface charge on coated particles correspond to free $P–O^-$ groups. The excess negative charges combined with steric repulsion of PEG chains result in highly stable particles, stabilized by electrosteric process. The coating layer thickness suggests mushroom conformation of PEG chains.

Compared to its BP analog, phosphonate PEG is a less efficient coating ligand, due to its weaker anchoring (coordinating) affinity. TGA analysis of the unstable PPEG-coated particles revealed significantly lower organic content (10 %) compared to its BPPEG analog (30 %). When mixed to BPPEG ligands, the binding competition results in higher BPPEG to PPEG ratio, than expected from the initial mixing ratio.

The alendronic acid coating was realized at two different pH-conditions: acidic and basic. DLS measurements suggested higher colloidal stability for the particles prepared in acidic

conditions. According to ATR spectra, the coordination mode of alendronic acid is different in the two synthetic procedures (acidic and basic conditions), which was confirmed by a colorimetric test with ninhydrin. Based on our analysis results, we proposed that for the particles prepared in basic conditions, both BP and NH^{3+} groups are participating in coordinative bonds.

Coating efficiency and particle stability were studied with a multiple point attachment ligand, copo-P, with long PEG side chains. This ligand was shown to form micelles (CMC = $1.6 \cdot 10^{-3}$ mol L^{-1}) and it readily coordinates to the particles already at room temperature, but we observed, that longer heating time (5h *vs.* 1h at 80°C) favors the attachment (increased layer thickness). Different ligands to gadolinium ion ratios were tested: lack of ligand (1:20), usually applied 1:3 ratio and excess of ligand (1:1). The ratio 1:20 was clearly not enough to stabilize the particles, which precipitated after aggregation. In contrary, 1:3 and 1:1 ratio resulted in stable suspensions. The particles grafted with 1:3 ratio, were remarkably stable: their suspension, kept at room temperature for 2.5 years were characterized by the same hydrodynamic parameters (size and PDI) as freshly prepared. With a 1:1 ratio the highest organic content (68 %) and grafting density (anchoring groups/NPs ratio 3295) is achieved, among all the particles in the present work.

Fluorescent labeling of the nanoparticles is obtained by attachment of the chromophore LEM-A, *via* thermally induced Huisgen cycloaddition. The reaction takes place between the alkyne function of LEM-A and the azide function on the particle surface. The successful coupling was demonstrated by absorption spectroscopic measurement and indirectly by ATR spectra (disappearance of the N_3 band). The chemical attachment was further confirmed by a control test, realized in the same conditions, but without heating. No trace of the chromophore was detected in the suspension of the control particles, after their purification. However, significant ligand desorption is observed upon heat treatment (5-7 h at 150°C) and/or high-speed centrifugation. TGA measurements show a decrease of organic content from 30 to 14% and the number of ligands to nanoparticles shifts from 2763 to 1122, which is still enough to procure high stability to the fluorescent particles (SKClick11) In addition, XPS analysis revealed a different coordination mode of the bisphosphonates before and after chromophore coupling. The ligands initially bidentate seems to coordinate by essentially monodentate mode after the reaction, which is supported by a more negative zeta potential value. As ligand desorption occurs, one would expect to measure a more positive ZP value, because of more free gadolinium ions on the surface, instead, here the more negative value could be attributed to a higher number of free $P–O^-$ groups in the monodentate coordination mode.

In the last step of the final multimodal nanoobject preparation, the targeting molecule, lovastatin was tentatively attached to the particle. In the first strategy, a direct esterification reaction between the carboxylic acid groups on the particle and the hydroxyl group of lovastatin was attempted without success. A series of model reactions involving esterification of $PEG(COOH)_2$ with lovastatin have been performed. Partial reaction occurred in pyridine (without DMAP) when $PEG(COOH)_2$ was first transformed to its more reactive $PEG(COCl)_2$ derivative. The mono- and disubstituted products were identified by ^{1}H-NMR and LC-MS. However, the same conditions did not lead to a reaction with the acid chloride derivative of BPPEG(COOH) ligand, forcing us to find another strategy. In the second strategy, we devised to attach a linker (Fmoc-NH-PEG-COOH) to lovastatin, which in turn could react with the particles, but our attempts failed. In order to find the optimal conditions, we used acetyl chloride to esterify lovastatin, and we found that reaction occurs only if the reagent is in very large excess. This observation is in accordance with literature method using 100-fold excess of reagent compared to lovastatin derivative.[208] Heating the reaction mixture did not increase yield, but induced side reactions, therefore in the last attempt, we used a large excess of Fmoc-NH-PEG-COOH, in the presence of 1 eq of DMAP and stirred the reaction mixture at room temperature during one week. Analysis of crude product revealed that no reaction occurred. We concluded then that the secondary alcohol of lovastatin presents an important steric hindrance. Therefore, it reacts only with small molecules, such as acetyl chloride, in very large excess and a completely new approach must be imagined for attachment of this molecule to the surface.

CHAPTER 4

Multimodal contrast agent

Content

I – The multimodal nanoplatform

I.1 Spectroscopic study

Previously, in section ***II.2 Fluorescent labeling of BPPEG-coated GdF3 nanoparticles (Chapter 3)***, the fluorophore LEM-A and its coupling to the pegylated GdF_3 nanoparticle have been described. Two photon absorption properties of this fluorophore were mentioned. The present section describes characterization of the whole fluorescent core-shell nanoparticle as a multimodal contrast agent. First, the optical properties required for two photon microscopy are presented, then the measure of r_1 and r_2 relaxivities of the particles is featured.

I.1.1 Absorption and fluorescence properties of the fluorescent GdF_3 nanoparticles

I.1.1.1 Determination of the molar extinction coefficient of LEM-A in different solvents

Molar extinction coefficient (ε) of a chromophore indicates the probability of photon absorption by the compound. Therefore, it is an important property of a fluorescent label. LEM-A UV-visible absorption spectra (***Figure 77***) have been recorded, in three different polarity solvents: methanol (MeOH) polarity index 5.1; acetonitrile (ACN) polarity index 5.8 and dichloromethane (DCM) polarity index 3.1. Spectra present in all three cases a strong and structureless band between 400 and 650 nm, accompanied by a smaller intensity band at lower wavelengths (from 250 to 400 nm). Peak maxima are undergoing a slight shift due to solvatochromic effect (***Table 13***).

The molar extinction coefficient (ε), of the fluorophore LEM-A was determined from these spectra, by the following procedure. Precise amount (3.9 mg for MeOH and ACN solutions and 4.4 mg for DCM solution) of the compound LEM-A was weighted and 10 mL of solvent (10 mL volumetric flask) was added to make a concentrated solution. Serial dilutions (dilution factor range 100-2000) were then prepared so that the corresponding optical densities (OD) fall in the range of approximately 0.015 – 0.30 and absorption spectra were recorded.

According to the Beer-Lambert law (***Equation 10***), a linear fit of the OD(λ_{max}) *vs.* c plots were performed to obtain the molar extinction coefficients. ***Figure 77*** A, C, E shows the absorbance spectra recorded for each solution at different dye concentrations. OD *vs.* concentration data and their linear fits are shown in ***Figure 77*** B, D, F. Calculated ε values are summarized in

Figure 77 (table). The determined molar extinction coefficient values are in agreement with the values found by Massin *et al.* for similar compounds.[197]

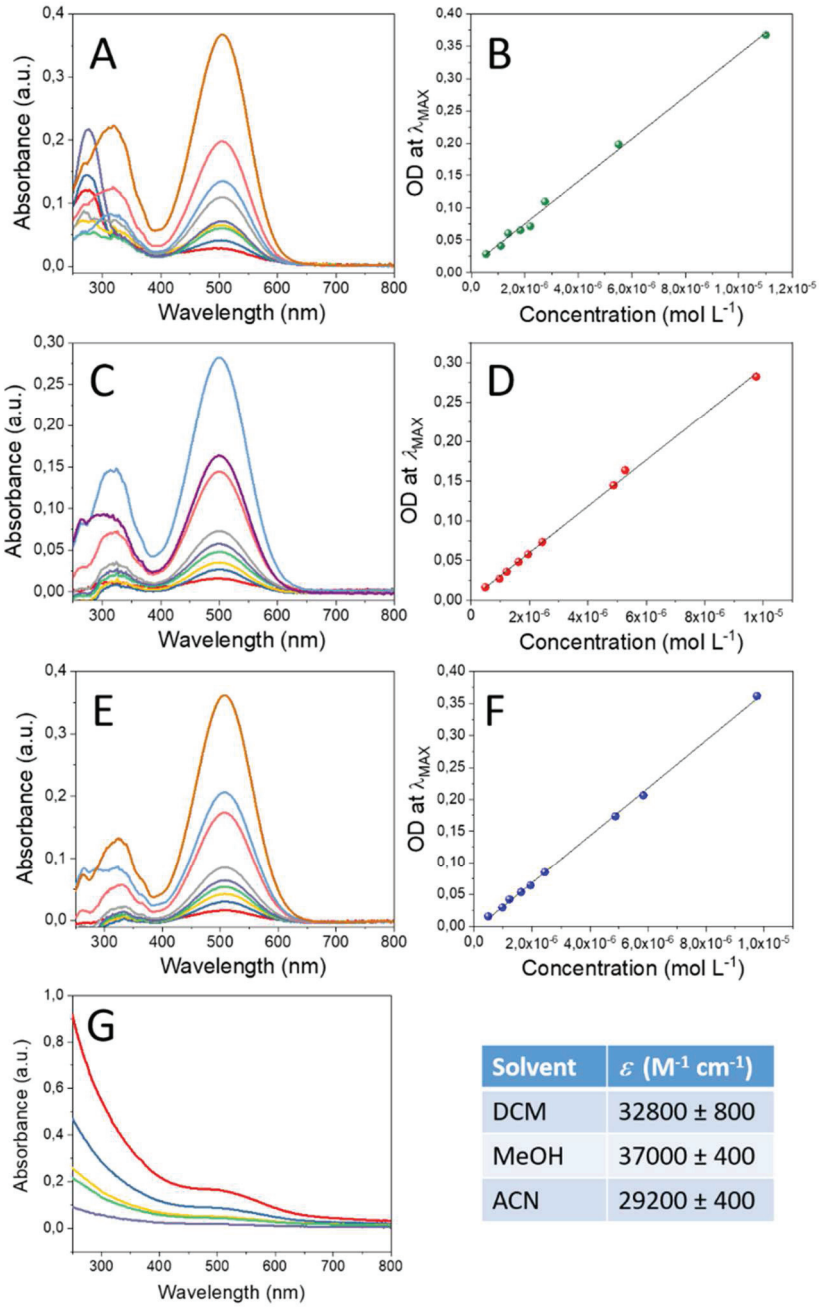

Solvent	ε (M^{-1} cm^{-1})
DCM	32800 ± 800
MeOH	37000 ± 400
ACN	29200 ± 400

Figure 77 Absorption spectra of free dye LEM-A in different solvents and of SKClick11 NP in water. Absorption spectra of LEM-A at different concentrations in dichloromethane (A), in acetonitrile (C) and in methanol (E). Peak maxima are at 505 nm, 500 nm and 507 nm respectively. Graphs B, D and F show the linear relation of OD *vs* concentration used for ε determination in different solvents. The table summarizes the ε values found for the chromophore LEM-A in the different solvents (dichloromethane, methanol and acetonitrile).

I.1.1.2 Absorption properties of LEM-A labeled nanoparticle SKClick11

Absorption spectra of aqueous SKClick11 nanoparticle suspensions were recorded at different concentrations (***Figure 77***G). Careful examination of this spectrum evidences an absorption

band above the continuous scattering background created by the particles. (This band is less pronounced than for SKClick2 particles, showed in Chapter 2, due to the lower fluorophore content. When subtracting the spectrum (***Figure 78***) of the particles without fluorescent probe (Gd-95/5/0) from the one equipped with the probe (SKClick11), a similar absorption profile appears than for the free dye in EG, with a strong (maximum 526 nm) and a weaker (around 326 nm) band. Peak maximum value of 526 nm is highly red-shifted compared to the maxima measured in other solvents (***Table 13***) showing that the dye molecule on the surface of the particle is in a highly polar medium. Since this molecule is insoluble in water, it is more likely, that the probe, covalently attached is embedded in the high polarity PEG chains.

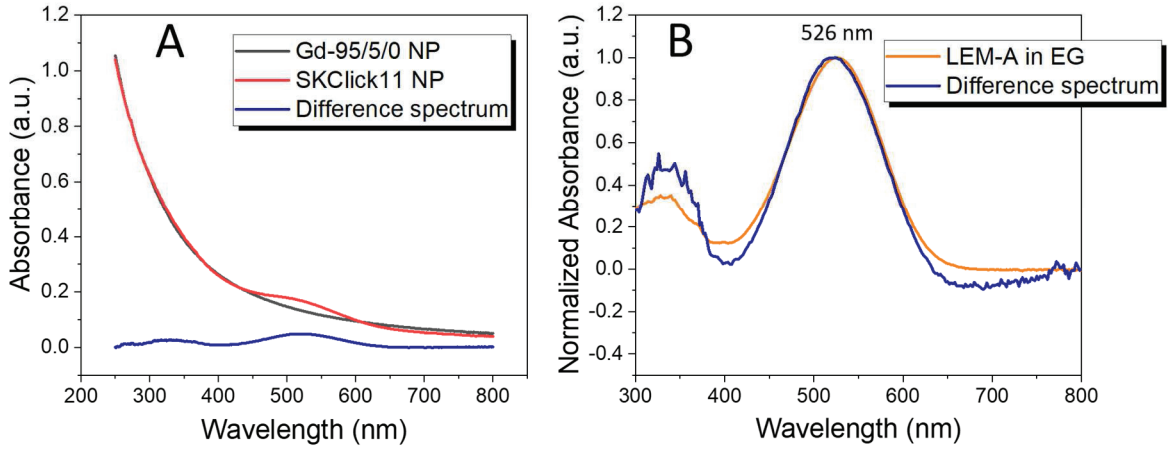

Figure 78 A) Absorption spectra of BP-PEG coated NP (Gd-95/5/0) (black line), fluorescent BP-PEG coated NP (SKClick11) (red line)and their difference (blue line). B) Normalized absorptions spectra of free probe (LEM-A) in EG (orange line) and the difference spectrum represented on graph A.

I.1.1.3 Fluorescent properties of LEM-A labeled nanoparticle SKClick11

Fluorescence emission spectra were recorded for the free probe in different solvents and for the probe-nanoparticle system in water (***Figure 79***). Concentrations and the corresponding absorption data are listed in Appendix 2.

Massin *et al.*[220] studied the spectroscopic properties of similar Lemke chromophore derivatives and found that these compounds undergo a positive solvatochromism (red-shifted maxima) by increasing solvent polarity. Herein we observe the same behavior: broad and structureless fluorescence emission profiles of free dye are very similar in shape, but the maximum emission is undergoing a significant positive solvatochromism (***Figure 80***):

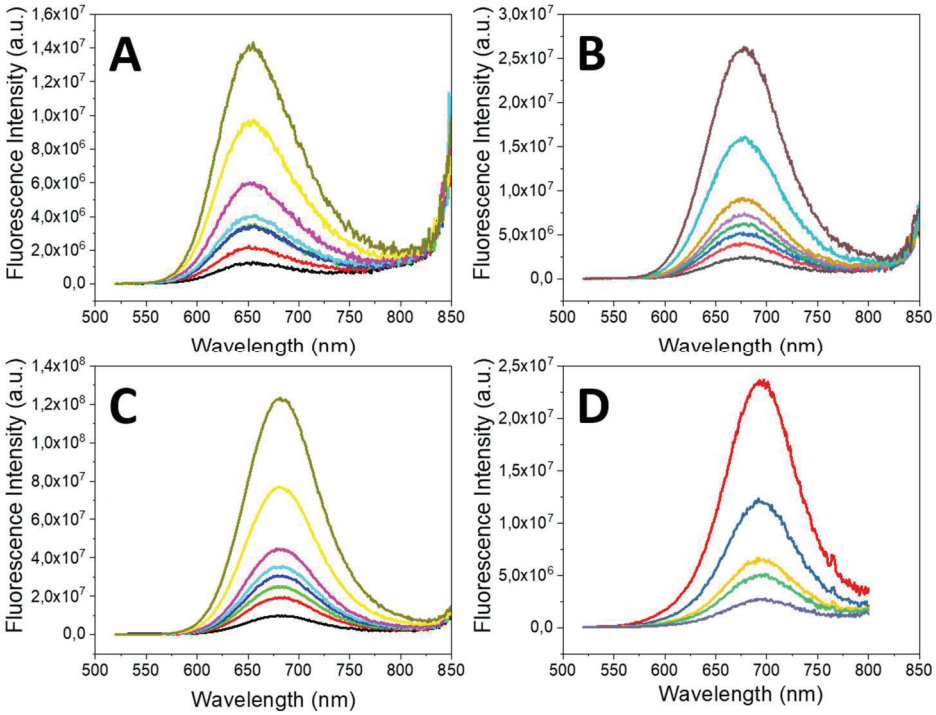

Figure 79 Fluorescence emission spectra of LEM-A and SKClick11 in different solvents. Excitation wavelength was 510 nm in each case. Emission maxima are observed at 634 nm in dichloromethane (A), 653 nm in acetonitrile (B) and 658 nm in methanol (C). Emission maximum for the particles (D) is at 682 nm.

the values are shifted from 634 nm in dichloromethane, to 653 nm in acetonitrile and 658 nm in methanol. The maximum emission for SKClick11 is also in perfect alignment with the solvent polarity dependence of the free dye series. Indeed, water (or PEG medium), the most polar solvent, induces a maximum emission shifted to 682 nm.

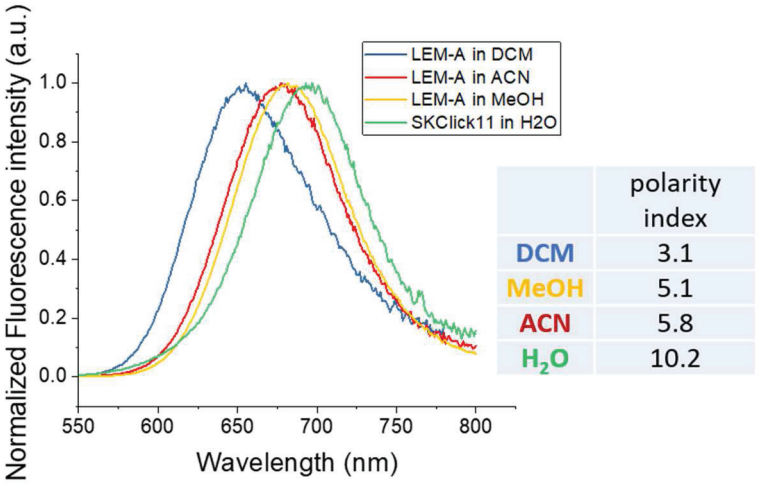

Figure 80 Solvatochromism in the fluorescence emission of LEM-A. Normalized fluorescence emission spectra of free chromophore in dichloromethane (blue line), in acetonitrile (red line) and in methanol (yellow line). Most important red shift is observed for the chromophore grafted (green line) on the NPs, suspended in water. The maximum shifts from 634 nm in dichloromethane, to 653 nm in acetonitrile and 658 nm in methanol. For the chromophore grafted on the particle SKClick11, the maximum emission is at 682 nm.

I.1.1.4 Fluorescence quantum yield determination

Fluorescence quantum yield is a key parameter for a fluorophore, as it is defined as the ratio of photons absorbed to photons emitted and indicates the probability of fluorescence emission, compared to non-radiative effects. In other words, quantum yield of a fluorophore characterizes efficiency of the compound as a fluorescent label. Moreover, brightness, *i.e.,* the perceived intensity of fluorescence, is given by the product of the quantum yield of a fluorophore and its molar extinction coefficient at the excitation wavelength.[221]

Two different approaches to QY determination are possible: absolute and relative measurements. For absolute QY determination a calibrated integrating sphere setup is required, while for relative QY, the fluorophore is compared to a fluorescent standard of known quantum yield and characterized by similar optical properties as the investigated compound and conventional spectrometers can be used for this measurement.

Here, the second method, relative determination was chosen, with Erythrosin B as reference, which absorbs in the similar wavelength range than LEM-A and is soluble in both water and methanol.[222] Relative quantum yields (QY) were measured according to the procedure described in *A Guide to Recording Fluorescence Quantum Yields*.[223]

Table 13 - Relevant spectroscopic data of free probe LEM-A and the fluorescent SKClick11 NP.

	λ_{max} (nm)	$\varepsilon(\lambda_{max})$ ($mM^{-1}cm^{-1}$)	λ_{em} (nm)	$\Delta\bar{\nu}$ (cm^{-1})	QY	σ_{TPA} (GM)
LEM-A						
in DCM	505	32800	634	4029	0.01	
in ACN	500	29200	653	4686	0.03	
in MeOH	507	37000	658	4527	0.13	15 (ex@840 nm)
SKClick11						
in H_2O[a]	526	–	682	4568	0.03	4-5 (ex@840 nm)
Scattering-corrected [b]					0.13	

[a] Fluorescence lifetime measurements revealed two characteristic times for the suspension of SKClick11 nanoparticles in water.
[b] λ_{max} obtained after subtraction of scattering and the corresponding quantum yield value are reported.

If the integrated fluorescence intensity (emission spectrum area) is represented versus the OD(λ_{exc}), the result is usually a straight line and the slope of this line is used to calculate the absolute QY values by using the following equation:

Equation 24

$$\varphi_S = \varphi_R \frac{slope_S}{slope_R} \frac{n_S^2}{n_R^2}$$

where the subscripts S and R denote the sample and the reference respectively; φ is the fluorescence quantum yield and n is the solvent refractive index at the excitation wavelength (here 510 nm).

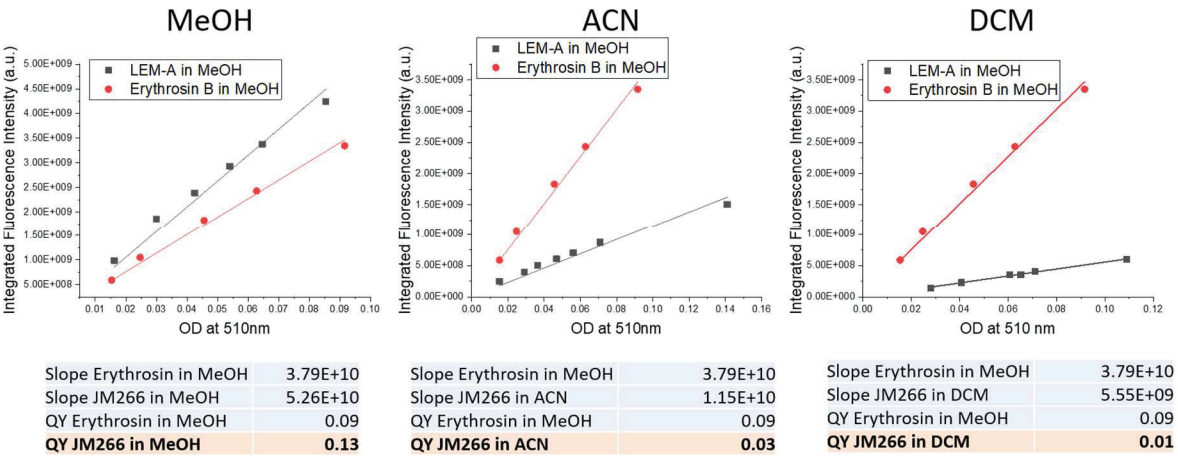

Slope Erythrosin in MeOH	3.79E+10
Slope JM266 in MeOH	5.26E+10
QY Erythrosin in MeOH	0.09
QY JM266 in MeOH	**0.13**

Slope Erythrosin in MeOH	3.79E+10
Slope JM266 in ACN	1.15E+10
QY Erythrosin in MeOH	0.09
QY JM266 in ACN	**0.03**

Slope Erythrosin in MeOH	3.79E+10
Slope JM266 in DCM	5.55E+09
QY Erythrosin in MeOH	0.09
QY JM266 in DCM	**0.01**

Figure 81 Quantum yield determination of LEM-A in different solvents. Red plots correspond to the reference compound, Erythrosin B and black ones correspond to the fluorophore LEM-A.

In the next step, the quantum yield of the fluorescent nanoparticle SKClick11 was determined, relative to Erythrosin B. Fluorescence emission spectra were recorded for the reference (Erythrosin B) and the nanoparticle in water.

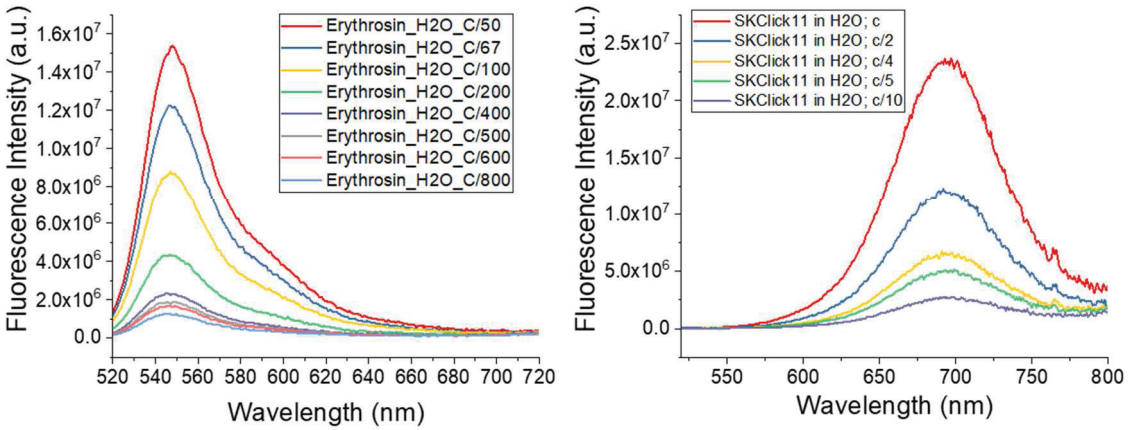

Figure 82 Fluorescence emission spectra at different concentrations of Erythrosin and SKClick NP, in water. The excitation wavelength is 510 nm.

The apparent quantum yield for the fluorophore-nanoparticle system is 0.03, but the OD must be corrected, because as already mentioned, scattering due to the particles dominates the absorption spectra.

Massin *et al.*[220] observed that a heteroatom on the β position of the ethylene group borne by the *N*-donor atom results in a decrease of the quantum yield to a few percent (4-7 %). They explained this decrease by the lowering of electron donating ability of nitrogen atom. In this work the measured relative quantum yield of free dye in dichloromethane and acetonitrile is low (~ 1 and 3 % respectively), but in methanol this value increases to 13 % (***Table 13***).

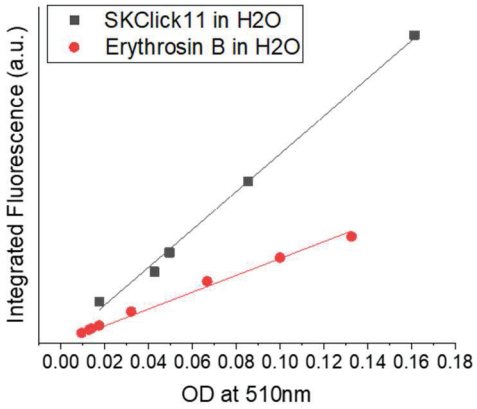

Slope Erythrosin	6.29E+09
Slope SKClick11d	1.41E+10
QY Erythrosin in H2O	0.012
QY SKClick11d in H2O	**0.03**

Figure 83 Linear plots used for the relative quantum yield determination of SKClick11 nanoparticles. Red dots correspond to the integrated fluorescence values plotted against the corresponding OD values, measured at the excitation wavelength of 510 nm.

The low quantum yield value found in dichloromethane may be explained by two additional effects: the presence of heteroatom (oxygen) on the β position of the ethylene group and low solvent polarity. However, polarities of acetonitrile and methanol are quite similar, so the difference in quantum yield values obtained for these two solvents cannot be simply explained by polarity effects, but hydrogen-bond donor abilities are also playing an important role. As mentioned before absorbance of the probe-NP system is highly dominated by scattering, so the measured OD (510 nm) values used for relative quantum yield determination, results in an apparent quantum yield of only 3 %. By subtracting the scattering (***Figure 78***) from the absorption spectrum, it is possible to obtain an estimated value of the real OD (510 nm), that comes from the fluorophore alone. Quantum yield calculation with this estimated OD results in 13 %, which is similar to the value found for methanol solution of free dye. It is very unlikely that the highly lipophilic chromophore is surrounded by water molecules, instead, polar PEG chains on the particle surface may offer a more favorable environment.

I.1.2 Two-photon absorption properties

Once the linear spectroscopic properties determined, LEM-A and SKClick11 nanoparticle were tentatively characterized by two-photon absorption spectroscopy. These measurements have been performed by Professor Mikael Lindgren (Department of Physics, Faculty of Natural Sciences of the Norwegian University of Science and Technology).

A solution of LEM-A in methanol (25 µM) has been characterized by two-photon absorption spectroscopy, at different excitation wavelengths ranging from 800 to 880 nm, with a 400 µL cell. As reference, alkaline (NaOH, pH=13) solution of fluorescein was used. Typical example of spectra is shown in ***Figure 84*** and the other spectra are reported in Appendix 4.

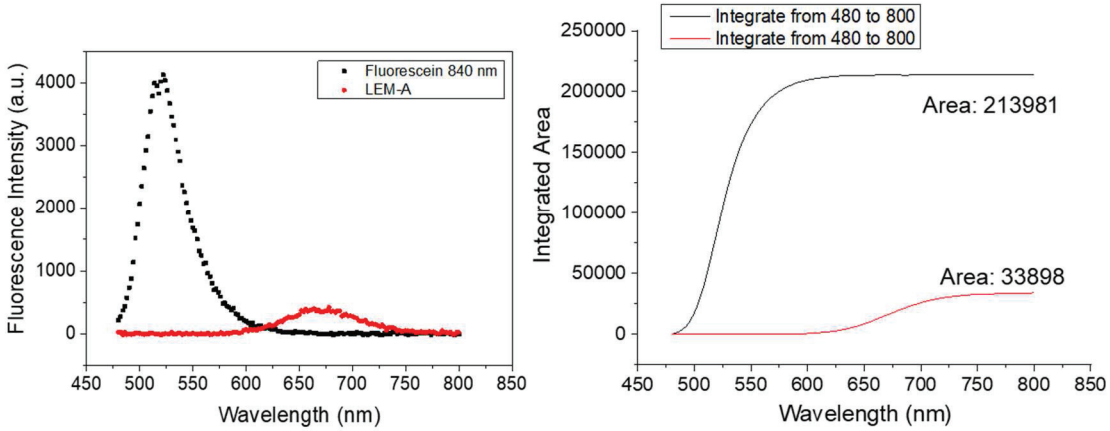

Figure 84 Two-photon induced fluorescence spectra of LEM-A in MeOH and Fluorescein in NaOH solution (pH=13). Excitation wavelength used was 840 nm (left graph). The corresponding integrated spectral area are represented on the right graph.

Two-photon absorption coefficients (σ_{TPA}, quoted in the units of Goeppert-Mayer, GM) have been determined from these spectra, by using the following formula:[224]

Equation 25

$$\sigma_{sample} = \frac{A_{sample}\phi_{Ref}}{A_{Ref}\phi_{sample}}\sigma_{Ref}$$

where A stands for the integrated spectral area of sample/reference and ϕ is the fluorescence quantum yield (0.92 for Fluorescein and 0.13 for LEM-A).

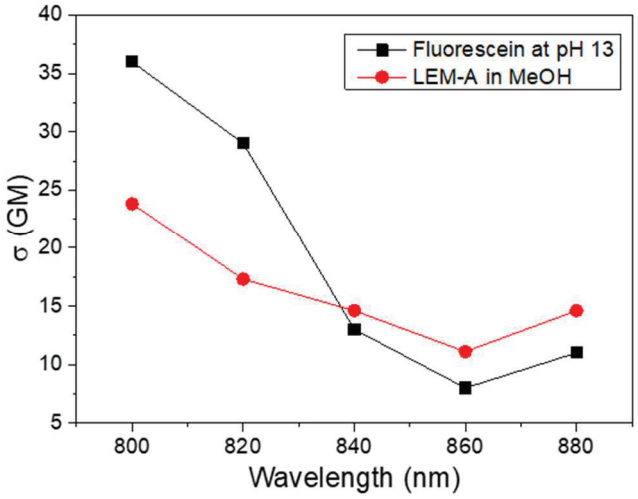

Figure 85 Two-photon absorption cross section values (σ) as a function of the excitation wavelength.

A suspension of SKClick11 (14.8 mg in 500 µL water) was tentatively characterized by two-photon absorption spectroscopy, however, the scattering due to the particles decreases significantly both excitation and emission efficiency. The baseline corrected spectrum of SKClick11 particles obtained by excitation at 840 nm is shown in ***Figure 86***.

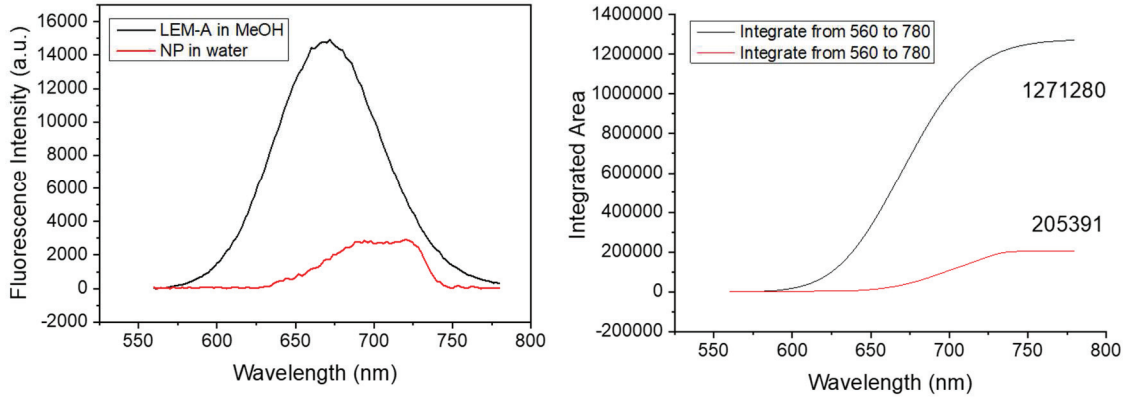

Figure 86 Two-photon induced fluorescence spectra of SKClick11 NP in water and LEM-A in MeOH. Excitation wavelength used was 840 nm (left graph). The corresponding integrated spectral area are represented on the right graph.

According to the absorption spectrum corrected for scattering, the estimated concentration of fluorophore in the nanoparticle suspension was approximately 20 µM, which is comparable to the concentration of fluorophore in the free dye solution (LEM-A in MeOH). Besides the decreased fluorescence intensity compared to free probe, nanoparticle spectrum is red-shifted, just as observed in fluorescence spectroscopy (see ***Figure 80***). The two-photon absorption cross section at 840 nm excitation has been evaluated to be approximately 4-5 GM, which is three

times lower than the value found for free probe (15 GM). This low value is probably due to the loss of light due to scattering. A more extensive study would be required to obtain more precise two-photon absorption characteristics. Particle scattering induces signal loss and in addition there is a lack of reliable references for two-photon absorption measurements, therefore it was not possible to determine the cross section in the wavelength range of our interest, *i.e.,* around 960 nm.

I.2 MRI phantom measurements

Relaxivities r_1 and r_2 of the inorganic GdF_3 core and the fluorescent SKClick2 and SKClick11 nanoparticles have been determined by phantom measurements. For comparison, relaxivity values of Dotarem, a clinically used Gd-complex CA were also measured in the same conditions. Phantoms (***Figure 87***) were prepared in water with a range of gadolinium concentration from 0 to 5 mM.

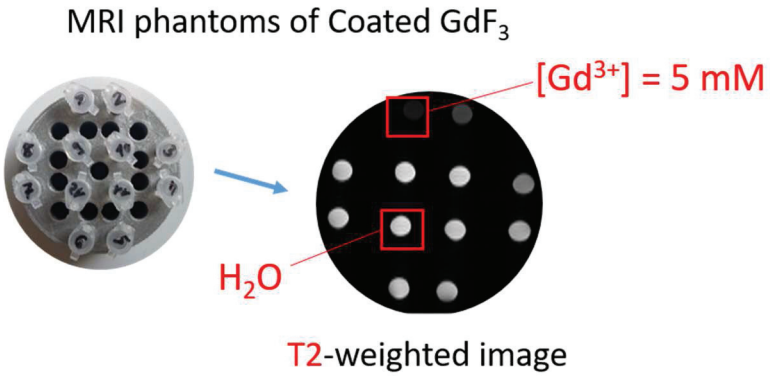

Figure 87 MRI phantoms prepared with SKClick11 nanoparticles at different Gd-concentrations and the corresponding T2-weighted image.

According to *Equation 2* and *Equation 3* in the introduction (***II.1.3.1 T1 relaxation mechanism in Chapter 1***), the slope of the plot $1/T_i$ as a function of $[Gd^{3+}]$ concentration gives the relaxivity r_i. ***Figure 88*** shows this plot for GdF_3 nanoparticles and Dotarem.

Linear regression of these plots resulted in the relaxivities summarized in ***Table 14***. Relaxivities r_1 and r_2 of Dotarem are almost equal, giving an r_2/r_1 ratio of 1.3. By comparison GdF_3 nanoparticles have lower r_1 and higher r_2 relaxivities, resulting in higher r_2/r_1 ratios, which is expected for nanoparticles, because of a higher local concentration of gadolinium ion than in the case of Gd-chelates and the decreased tumbling rate. It is worth noting, that as opposed to Gd-chelates, Gd-based NPs are more adapted as T2 CAs.

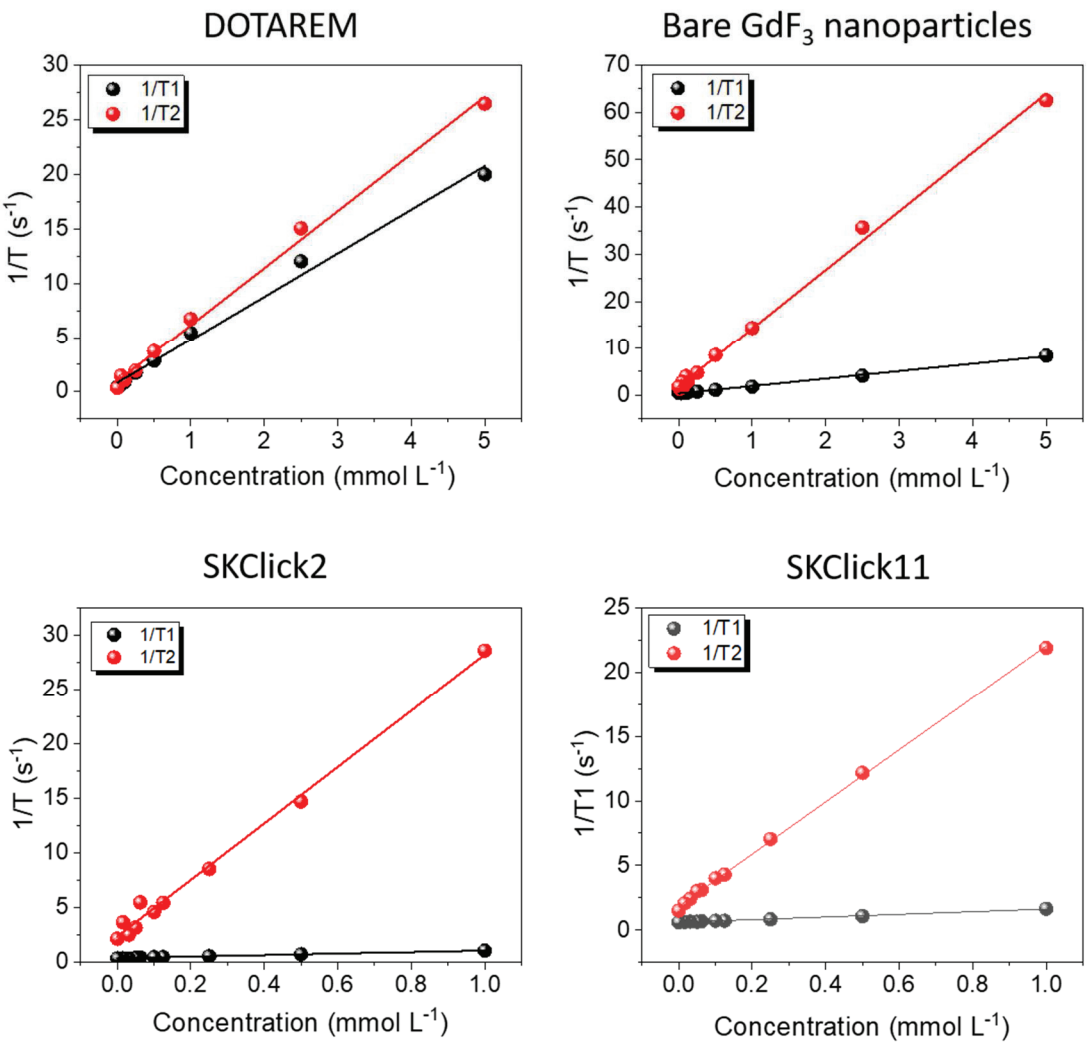

Figure 88 Plots of 1/T values (s^{-1}) vs. gadolinium concentration (mmol L^{-1}) measured at 7T.

When the inorganic core (GdF_3 NP) is coated with a PEG layer (SKClick2 and SKClick11), r_2 relaxivity increases. As it was explained in the introduction (***II.1.3.2 T2 relaxation mechanism***), a hydrophilic coating increases water residency time in the particle surrounding (second sphere), which favors relaxation.

Table 14 Relaxivities r1 and r2 determined by phantom measurements

	r_1 (mM^{-1} s^{-1})	r_2 (mM^{-1} s^{-1})	r_2/r_1
Dotarem®	4.0	5.2	1.3
Bare GdF_3 NP	1.6	12.4	7.8
SKClick2 NP	0.7	25.8	36.0
SKClick11 NP	1.0	20.2	20.2
Feraheme® [225]	3.1	68.0	21.9

Measurements were performed at 25°C, using a 7T MRI magnet.

However, reasons for the different r_2/r_1 ratios of SKClick2 and SKClick11 are not obvious. In Chapter 3 (***II.2.2. Fluorescent labeling of BPPEG-coated nanoparticle***), it was demonstrated, that upon prolonged heating at 150°C, for the fluorescent coupling reaction, PEG loss happens. SKClick2 particles were subjected to longer heating time, therefore the PEG density on their surface is lower, than for SKClick11, which is also evidenced by their lower stability in colloidal suspension. Therefore, particle aggregation of SKClick2 increases the CA size, which increases r_2 relaxivity. In addition, water molecules can easily approach the less crowded surface in SKClick2, which may favor relaxation processes. SKClick11 particles are characterized by an r_2/r_1 ratio of 20.2, which is similar to the value measured for the commercially used USPIO nanoparticles, Feraheme® (r_2/r_1 = 22).[225] SKClick11 nanoparticle is therefore a promising candidate for T2 contrast enhancement in MRI.

I.3 Toxicological assessment

As mentioned in the introduction, free gadolinium ions may present health risks. In addition, exposure to nanoparticles may also induce adverse effects, therefore it seems obvious, that before any *in vivo* application, toxicity of the contrast agent preparation has to be assessed. Toxicological assessment in the present study has been performed by Clémence Gaudin, under the supervision of Patrice Marche and Marion Ressejac (Institute for Advanced Biosciences, Grenoble)

Effect of SKClick2 and SKClick11 nanoparticles on cell lines THP-1 (human macrophages) A549 (epithelial-like cells from human lung), HepG2 (human hepatocytes) and HEK 293T (human kidney) has been studied. Evaluation of potential cytotoxicity of the particles was assessed by two complementary standard methods: LDH and MTT.

Lactate dehydrogenase (LDH) is an enzyme released into the extracellular space, when cells are damaged, therefore increased LDH level in the cell culture medium indicates compromised cell membranes. Therefore, by quantifying LDH activity level, cell death may be evaluated. Quantification is performed by fluorescence measurement of a molecule (Resazurin), converted to a fluorescent product (Resorufin), upon LDH enzyme activation. The fluorescent product is proportional to the number of non-viable cells.

Cell metabolic activity and viability may be assessed by a colorimetric assay, based on the enzymatic (mitochondrial reductase) reduction of the yellow compound, MTT (3-(4,5-dimethylthiazol-2-yl)-2,5-diphenyltetrazolium bromide) to its purple formazan form, which

accumulates in healthy cells. The water-insoluble formazan is then extracted from cells and the concentration is determined by absorption measurement.

In both LDH and MTT tests, the cells were incubated with nanoparticle suspensions of different concentrations ranging from 0 nM to 5000 nM of Gd. Cells were examined at 48 h and 72 h of contact with the particles.

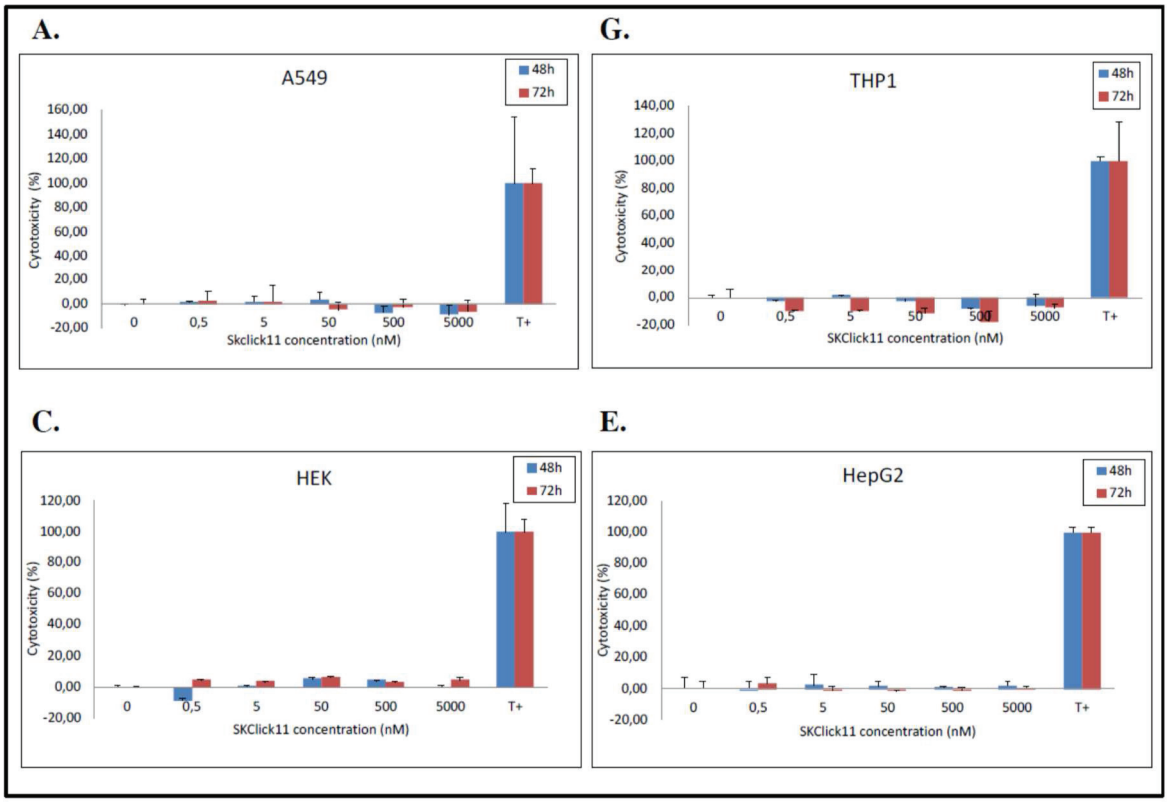

Figure 89 LDH assay results: effect of SKClick11 nanoparticles on four cell types (A549, THP-1, HEK, HepG2), after 48 h and 72 h of exposition. T+ corresponds to the positive control, with 100% cell death. (Negative values are due to the positive control.) Figure courtesy of Clémence Gaudin.

At both contact times (48 and 72 h), cytotoxicity percentage varied between 0 and 9 %, independently of the cell type, which allows to conclude, that SKClick11 nanoparticles have no cytotoxic effect.

Results obtained with MTT assay are shown in ***Figure 90***. There are no significant differences observed within the different cell lines and over exposure time: 85 to 100 % of cells survive in contact with the nanoparticles. Survival rates exceeding 100 % are explained by increased absorbance due to cell proliferation. Unmodified cell metabolic activity shows, that the particles do not have cytotoxic effect.

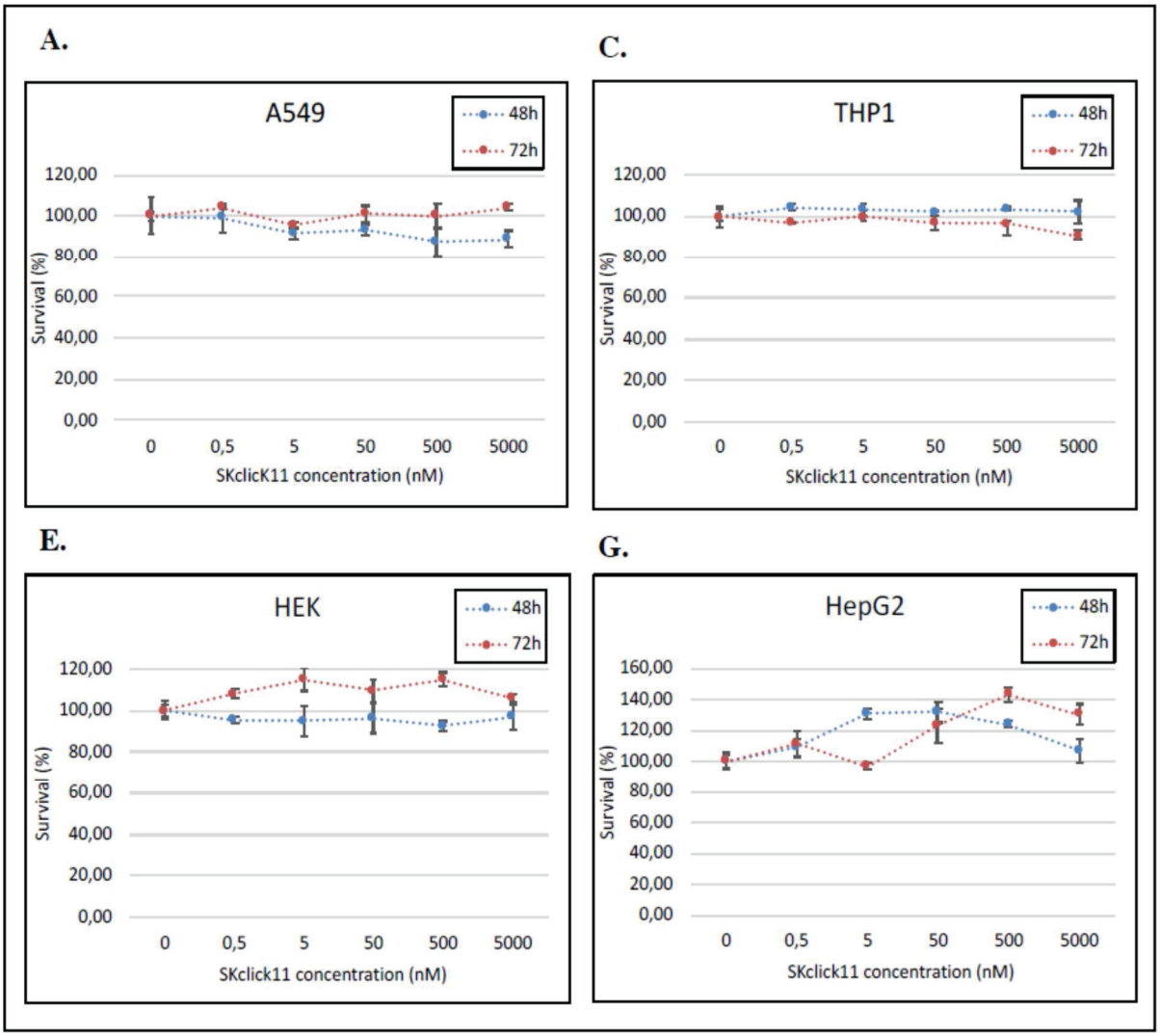

Figure 90 MTT assay results: effect of SKClick11 nanoparticles on four cell types (A549, THP-1, HEK, HepG2), after 48 h and 72 h of exposition. Figure courtesy of Clémence Gaudin.

Results of the two complementary tests, evaluating cell death (LDH) and cell survival (MTT) do not show potential cytotoxic effect of pegylated GdF_3 nanoparticles.

II – In vivo biological application

Preclinical *in vivo* experiments have been performed by our collaborators. The animal model of ischemia has been prepared (both surgery and clot formation in the brain) by Violaine Hubert, under the supervision of Marlène Wiart (CarMeN Laboratory, University of Lyon 1, INSERM, INRA, CNRS). MR imaging was performed by the same persons and Radu Bolbos (MRI platform of CERMEP – imagerie du vivant). Cranial window positioning and two-photon microscopy observations have been realized by Inès Hristovska, under the supervision of Olivier Pascual (Lyon Neuroscience Research Center, INSERM, CNRS, University of Lyon 1).

As I was curious and wanted to see how these experiments were performed, I was present during all the imaging sessions. This made me more aware of understand the precise goal of each experimental step. This also allowed me to communicate more easily with our neurobiologist collaborators, because as a chemist, I became more familiar with the specific vocabulary and the basic biological concepts that are involved in the project.

II.1 – MRI imaging of post-stroke neuroinflammation with USPIO nanoparticles

Following the pioneering work of Weissleder *et al.*[67] and Rauch *et al.*[68] on the observation of macrophages by USPIO-enhanced MRI, Nighoghossian's and simultaneously Jander's group first, introduced iron oxide nanoparticles as MRI contrast agent in human patients to image inflammation after ischemic stroke.[226–228] From ex vivo, human brain autopsy studies, Jander's group evidenced, that there is an accumulation of USPIO-labeled macrophages in the periphery of the ischemic lesion.[227] In vivo MRI imaging performed in 2007 by the same group, showed, that USPIO-laden macrophages infiltrated the infarcted parenchyma and USPIO signal was not due to nanoparticle extravasation through deficient BBB.[226] They demonstrated, that larger nanoparticles, such as SPIO (ferumoxide, Resovist; 60-150 nm) are rapidly cleared from the blood through the reticuloendothelial system and accumulate in the liver and the spleen, allowing efficient liver imaging. Oppositely, smaller nanoparticles, USPIO (Ferumoxtran-10, Sinerem; 20-50 nm) have longer circulation time, with a blood half-life of 24-36 h, favoring their accumulation in macrophages, allowing particularly efficient imaging of lymph node.[2]

Independently, Nighoghossian *et al.* imaged ten patients, in the subacute phase of ischemic stroke and reported similar conclusions on the USPIO labelling of macrophages in the peripheral area. They showed, that it is due to an active nanoparticle uptake by the cells and by comparing patients presenting severe and mild BBB disruption, observed, that USPIO-related enhancement in the parenchyma is not correlated to BBB disfunction. They also demonstrated, that the volume of damage in the subacute phase is related to the intensity of inflammatory process.[228]

The same group used USPIO nanoparticles as contrast agents for imaging acute phase (in the first 36 hours, post-injury) of ischemic stroke in small animal model. The small size of murine brain represents a challenge both from surgical point of view and MR-imaging. Wiart *et al.* created the proof of concept that USPIO-enhanced MR imaging of phagocytic cells is possible in mouse models of ischemia.[229]

Based on these experiences, we hypothesized, that our Gd-based nanoparticles, which have similar dimensions, will get phagocytosed by infiltrating macrophages and this labeling will allow to image inflammation.[230]

II.2 – Animal model of ischemic stroke

Since a large majority of ischemic stroke cases concern the middle cerebral artery (MCA), most of the animal models developed to mimic human ischemia are based on transient (tMCAO) or permanent (pMCAO) occlusion of this artery.[231] A large number of models requiring or not craniectomy, have been developed and are described in a comprehensive review.[232] In the present studies after a complex surgical intervention, including skull thinning procedure and craniectomy to expose the artery, has been performed on carefully selected mice (swiss type, 6-8 weaks male) and the permanent occlusion (the clot) of the MCA has been induced by either electrocoagulation[229] or by direct application of ferric chloride (30 %) solution-soaked tissue,[233] according to the protocols described previously.

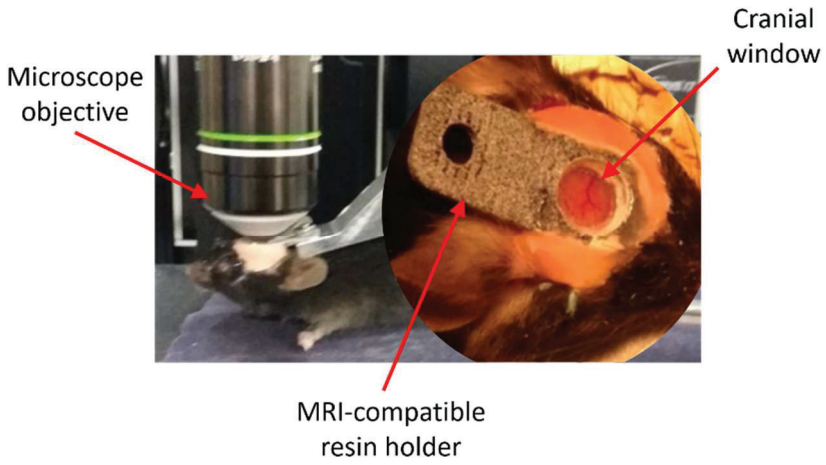

Figure 91 Cranial window implanted on the model animal head and positioning of the mouse under two photon microscopy objective.

For two-photon imaging purposes a cranial window was then implanted at the periphery of the lesion (***Figure 91***), equipped with an MRI-compatible (not metal) resin holder to fix the head of the anesthetized animal, during the observation.

Transgenic, CX3CR1-eGFP mice[234] were used as animal model. Microglia of these mutant mice express green fluorescent protein, which make these cells easily detectable by fluorescence two-photon microscopy (***Figure 100***).

II.3 – Multimodal application of SKClick11 nanoparticles: the proof-of-concept

II.3.1. MRI modality

To testify MRI enhancement properties of the surface modified GdF_3 particles and optimize the MRI sequences to apply, SKClick8 (10 % of $BPPEGN_3$ and 90 % of BPPEGOMe ligands) particles were injected intravenously into the right retro-orbital sinus [235] of the mouse, which was subjected to the surgery protocol to induce a permanent middle cerebral artery occlusion by electrocoagulation (***Figure 92***).

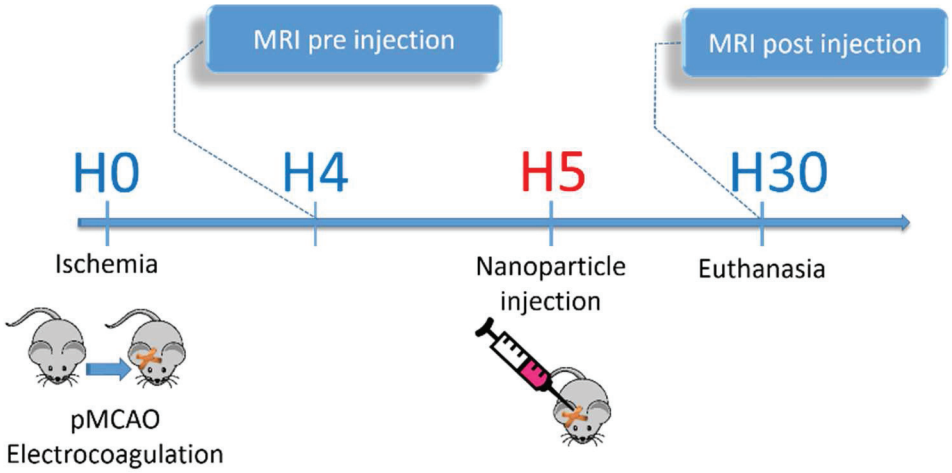

Figure 92 Overview of the in vivo study timeline.

Four hours after pMCAO, a basal MRI was performed on the anesthetized animal, to visualize the lesion in the brain. Then, the contrast agent was injected intravenously (2.25 mmol of Gd/kg; $[Gd^{3+}]$ = 246 mmol L^{-1} in physiological saline solution, [NaCl] = 0.1 M in water). One day after the injury (at H30), a post-injection MRI observation confirmed the presence of the particles inside the lesion.

Figure 93 shows three MRI slices of the mouse brain, before and after contrast agent administration. T2-weighted image confirms the presence of an infarcted area, appearing in white. After one-day post injection, this area contains a multitude of hypointense details (black signals), corresponding to the local signal reduction by the nanoparticles. As expected, the lesional area is hypointense in T1-images, due to the presence of excess water (edema).

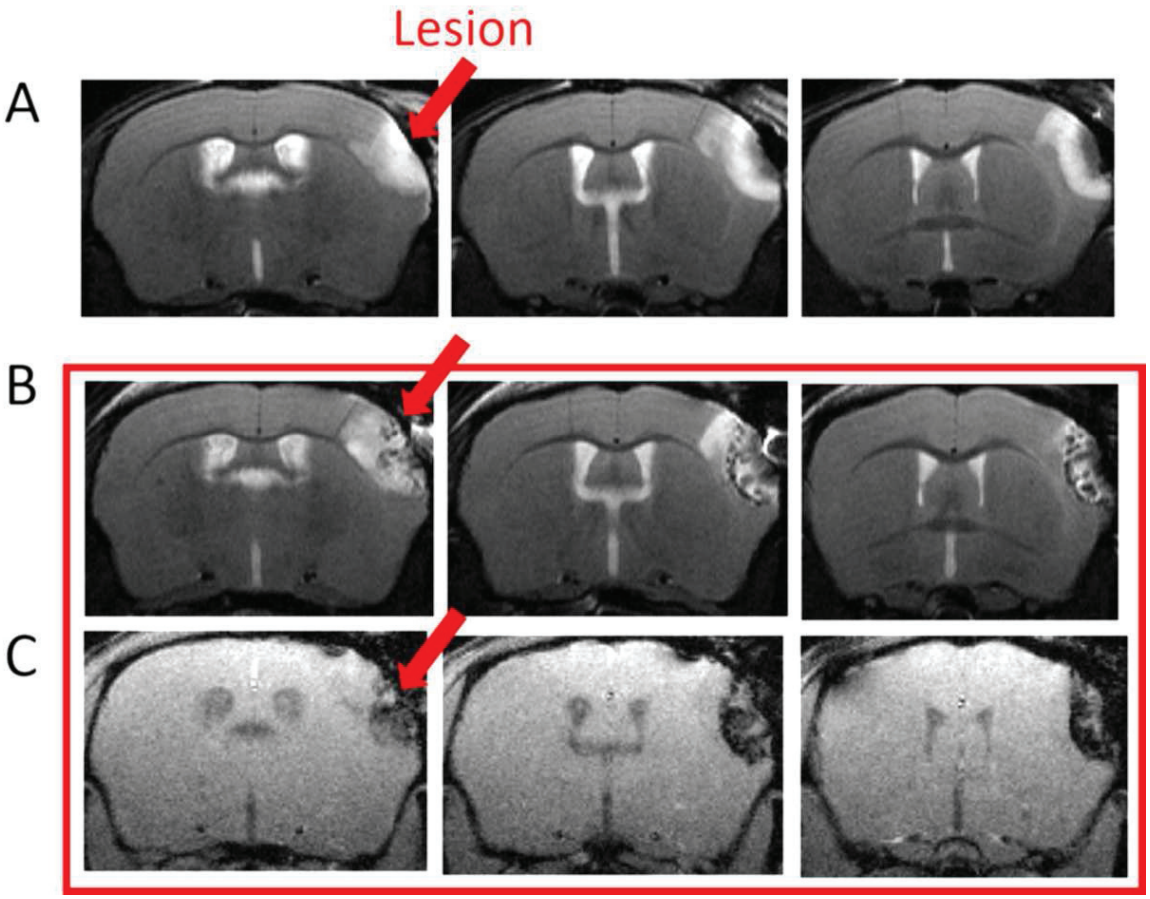

Figure 93 Post ischemia in vivo MR imaging of mouse brain, before (A) and after (B,C) injection of SKClick8 nanoparticles. A and B snapshots are T2 weighted images and C is T1 weighted. (Animal model preparation and imaging performed by Marlène Wiart, Violaine Hubert and Radu Bolbos)

II.3.2. Two-photon imaging modality

Once the MRI modality of the particles confirmed, a second *in vivo* experimental protocol has been established for the pilot experiment of visualization of the nanoparticles by two photon microscopy.

In this protocol pMCAO in the animal model (CX3CR1-eGFP mice) was induced by the method using $FeCl_3$ solution. One day after the injury, the cranial window was installed and nine days post-injury, the mouse brain was imaged by intravital microscopy (***Figure 94***). Upon excitation at 920 nm, eGFP expressed on microglia of the transgenic mouse emits as expected, at 508 nm, in the green region.[51]

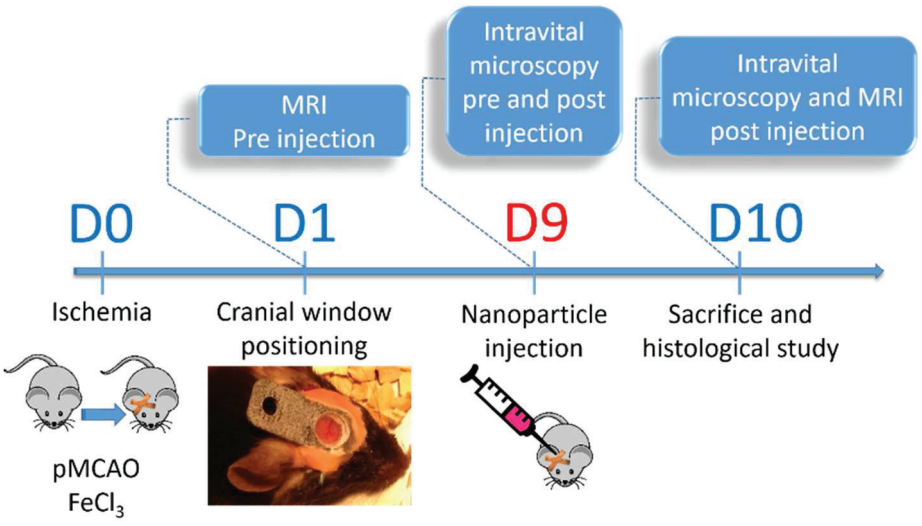

Figure 94 Overview of the in vivo study timeline.

With typical observation parameters, 1.5 µm thick slices of brain tissue are imaged at several z-heights, which after reconstruction results in an imaging depth of approximately 30 µm.

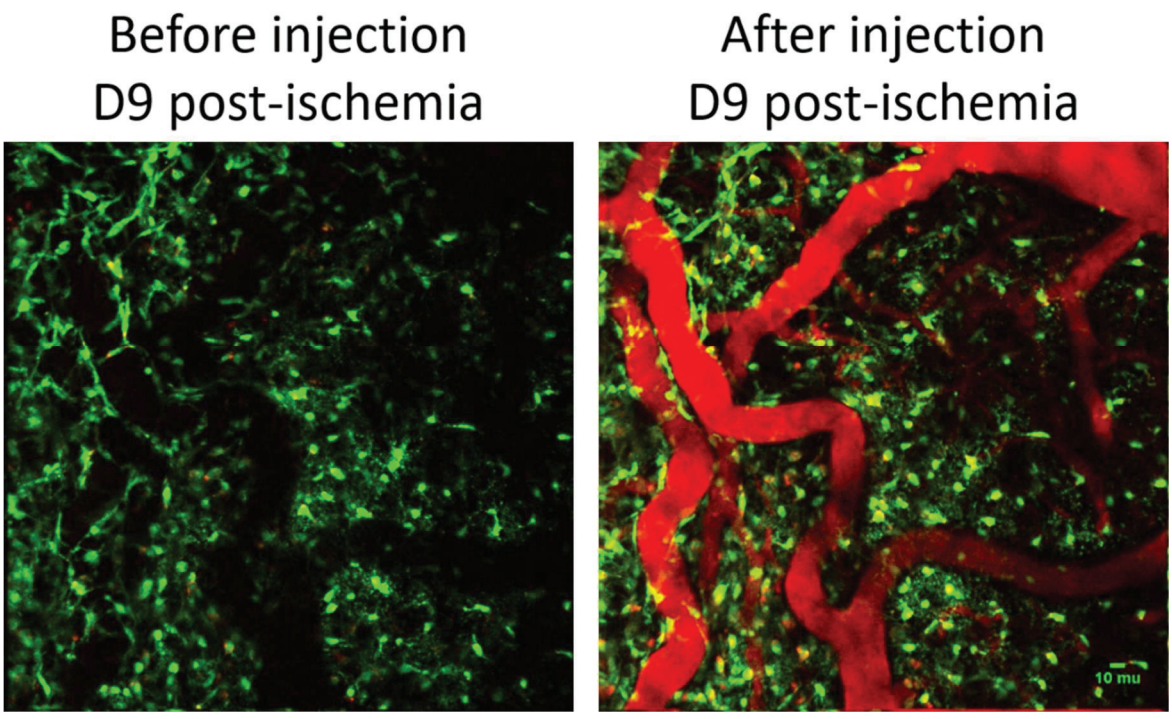

Figure 95 In vivo two-photon images before and after injection of SKClick11 nanoparticles. In vivo experiments and images performed by Inès Hristovska, Violaine Hubert and Olivier Pascual.

Then, a suspension of SKClick11 nanoparticle (2 mmol of Gd/kg; $[Gd^{3+}] = 554$ mmol L^{-1} in physiological saline solution) is injected intravenously, without moving the animal, to image the same tissue area. This time, two excitation wavelengths are applied, one at 920 nm for

eGFP, detected in a canal < 560 nm and the other one at 980 nm, which excites the chromophore coupled to the particles. Emission of this label (630 nm) is detected in the canal > 560 nm. A bright and intense red signal lights up the blood vessels in the brain, which confirms that our fluorescent nanoparticles are also suitable for two-photon imaging modality.

II.3.3. CT modality

During the time of this thesis project, pre-clinical SPCCT brain imaging with SKClick particles was not possible, because the first SPCCT prototype (Philips Healthcare, Haifa, Israel) was uninstalled and the installation of the new, clinical prototype, which was intended to replace the first one, has been delayed.

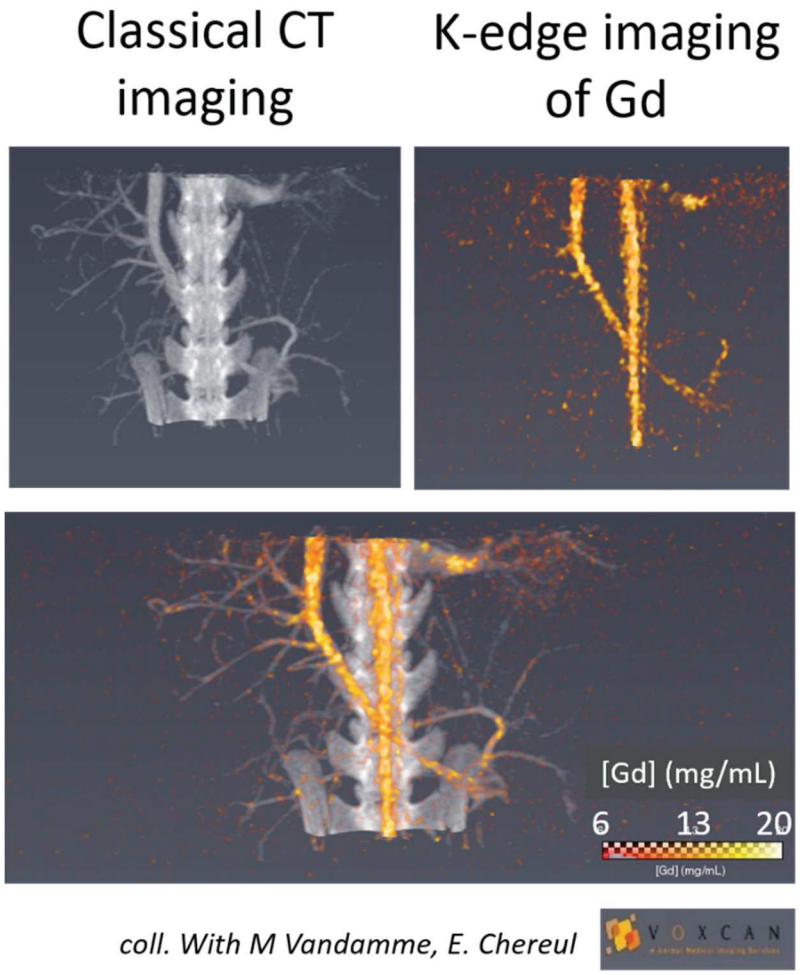

Figure 96 Rat abdomen images 5 minutes post-injection of GdF_3-nanoparticles. Classical CT image, SPCCT gadolinium k-edge and overlay of the images; (Courtesy of the authors from publication [57])

Nevertheless, the feasibility of using GdF_3 nanoparticles as contrast agents for CT imaging was demonstrated in the frame of a parallel project (SPCCT European project in the H2020-PHC-2015 call, project ID 668142), in which our team is involved for the SPCCT specific CA design.

The GdF_3 inorganic core was functionalized with commercially available phosphonate PEG ligands, and a suspension of this nanoparticle was injected into mice and rats as blood pool contrast agent for SPCCT imaging.[57] The animals were imaged both with conventional CT and SPCCT.

Figure 96 shows *in vivo* imaging of a rat abdomen with the two techniques and their overlay. In the classical CT, blood vessels are not clearly distinguishable from bones, however gadolinium k-edge shows exclusively the blood network containing Gd. It is interesting to note, that the precise local concentration of Gd can be obtained from this technique and is indicated on the figure by the color scale.

This series of experiments evidenced the efficiency of GdF_3 nanoparticles as contrast agent for the new generation scanner, spectral photon counting CT.

Another evidence for X-ray imaging contrast enhancement properties of GdF_3 nanoparticles, was brought in the frame of the present project (Nanobrain), by X-ray phase-contrast computed tomography, performed at the European Synchrotron Radiation Facility (ESRF, Beamline ID19). This imaging method for metallic NPs was recently developed by Wiart and co-workers, as a virtual histology tool, with 6.5-µm spatial resolution.[71]

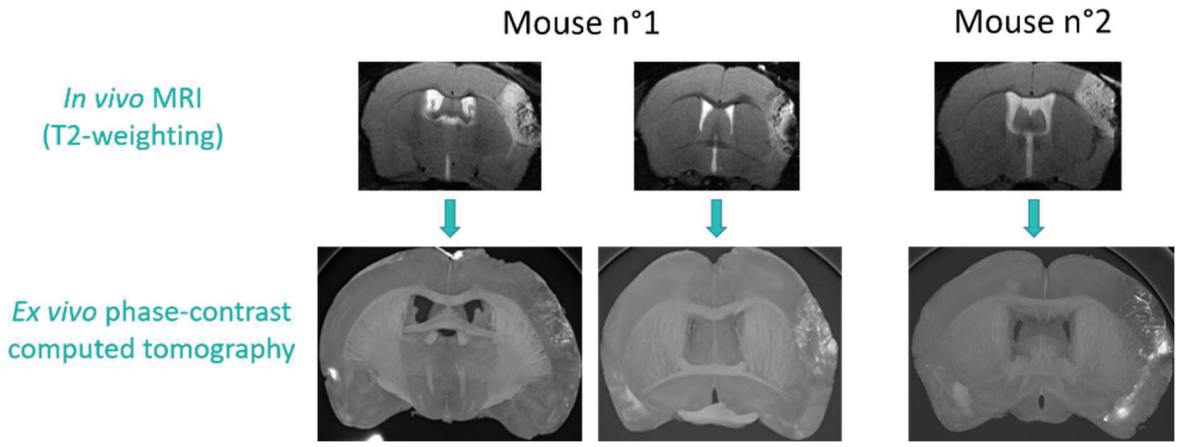

Figure 97 In vivo MRI and ex vivo phase-contrast computed tomography images of mice brains, after pMCAO and injection of SKClick11 nanoparticles. These experiences and the presented images were performed by Marlène Wiart and Violaine Hubert.

A subgroup of 8 animals, injected with SKClick11 nanoparticles were imaged post-mortem by this technique. After in vivo MR imaging, the mice were euthanized, and their brains were prepared for post-mortem imaging, the vascular bed was washed with phosphate buffer (0.1 N), in order to remove blood. ***Figure 97*** shows the phase-contrast images of the brains, with the corresponding MR-images, for two mice. In the phase-contrast images, nanoparticles give a

very bright hyperintense signal. Comparison of *in vivo* MR images with the *ex vivo* histological analysis demonstrates that the hypointense signals seen on MRI are due to the presence of gadolinium in the brain.

II.4 – Biodistribution and pharmacokinetic study

In two-photon microscopy observations, it was evidenced that SKClick11 nanoparticles have a long circulation time in the blood. ***Figure 98*** shows images of the same brain area before and after CA injection. The red signal is still significantly detected 24 hours after nanoparticle injection.

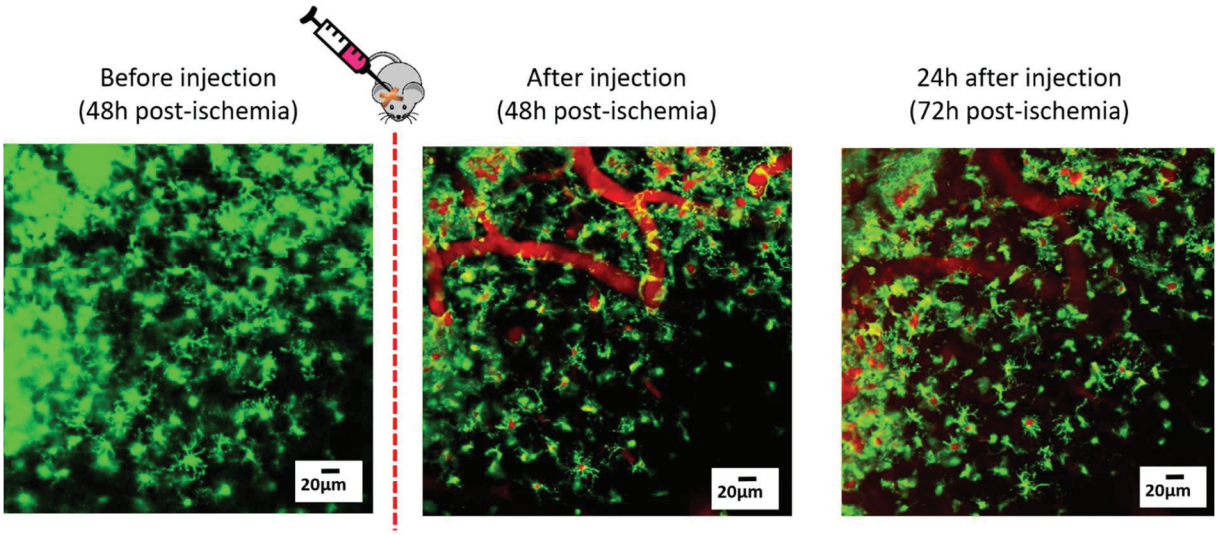

Figure 98 Two photon images of mouse brain after pMCAO, pre and post-injection of SKClick11 nanoparticle suspension. Microglia appear in green and the SKClick11 nanoparticles are in red. (In vivo experiments and images performed by Inès Hristovska, Violaine Hubert, Marlène Wiart and Olivier Pascual.)

Five healthy mice received intravenous injection of SKClick11 nanoparticle suspension (2 mmol of Gd/kg) and particle-accumulation in different organs involved in the clearance process was followed by MRI. As expected, nanoparticles are accumulating in liver and spleen with a long vascular remanence of more than 7 hours of blood half-life (***Figure 99***).

This half-life value is intermediate between the circulation time of USPIO nanoparticles (12-14 h),[236,237] and Gd-complexes (1.6 h),[237] therefore it is optimal for accumulation in the brain and longitudinal imaging, with a reasonable clearance time from blood.

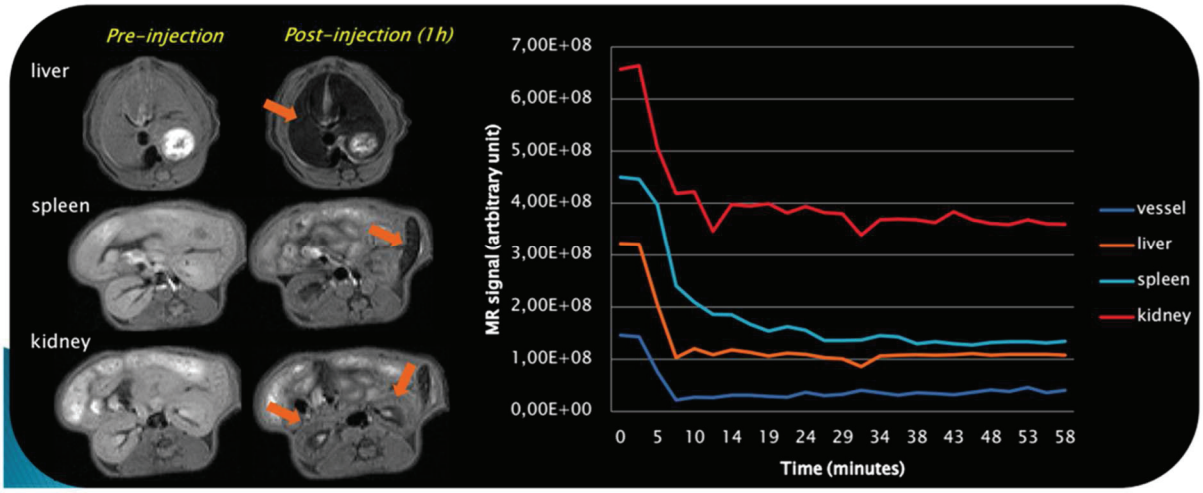

Figure 99 In vivo biodistribution and pharmacokinetic of SkClick11 nanoparticles in mice. Dynamic abdominal MRI has been performed every 2-3 minutes before, during and up to one-hour post-injection, every 2-3 minutes. (Figure courtesy of Violaine Hubert.)

II.5 – Dual modality *in vivo* imaging of neuroinflammation biomarkers

As it was briefly mentioned in the introduction, microglia are the primary immune cells of the central nervous system. In healthy brain tissue, this cell is in a so-called "resting" state, which is slightly misleading, because this cell has many roles in normal condition, such as sculpting developing neuronal circuits (participating in memory and learning) and constantly surveilling neuronal activity. Microglia form a 3-dimentional lattice within brain tissue and each cell has its own territory to scan.[13] They are also waste-scavengers: they engulf death neurons and debris. They detect, transduce and integrate extracellular signals, such as ATP-loss of apoptotic cells and are able to react accordingly.

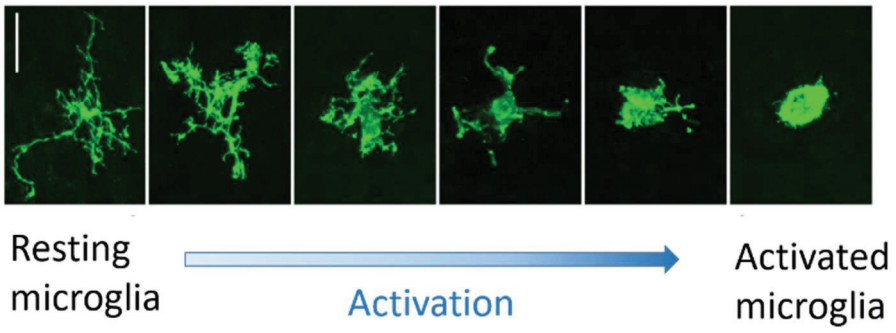

Figure 100 Different morphologies of microglia, depending on their activation state. Figure adapted from ref. [238] with permission. (Scale bar is 20 µm)

When microglia detect a modification in homeostasis, they are able to modify their phenotype to become activated and change their function. Upon activation, they change their morphology

(***Figure 100***) from a highly ramified to an amoeboid, compact form. Initially, two different phenotypes of activated microglia were described, M1 and M2. M1 corresponds to the classically activated microglia, which secrets pro-inflammatory mediators and tends to induce neuronal death. The alternatively activated M2 form, is considered as anti-inflammatory, secreting cytokines that prevent inflammation and contributes to tissue repair and recovery. To date, it became clear that this traditional M1-M2 dichotomy does not accurately describe the complexity of microglial status. M1 and M2 states are only two extreme phenotypes and actually microglia status may include several subtypes.[239]

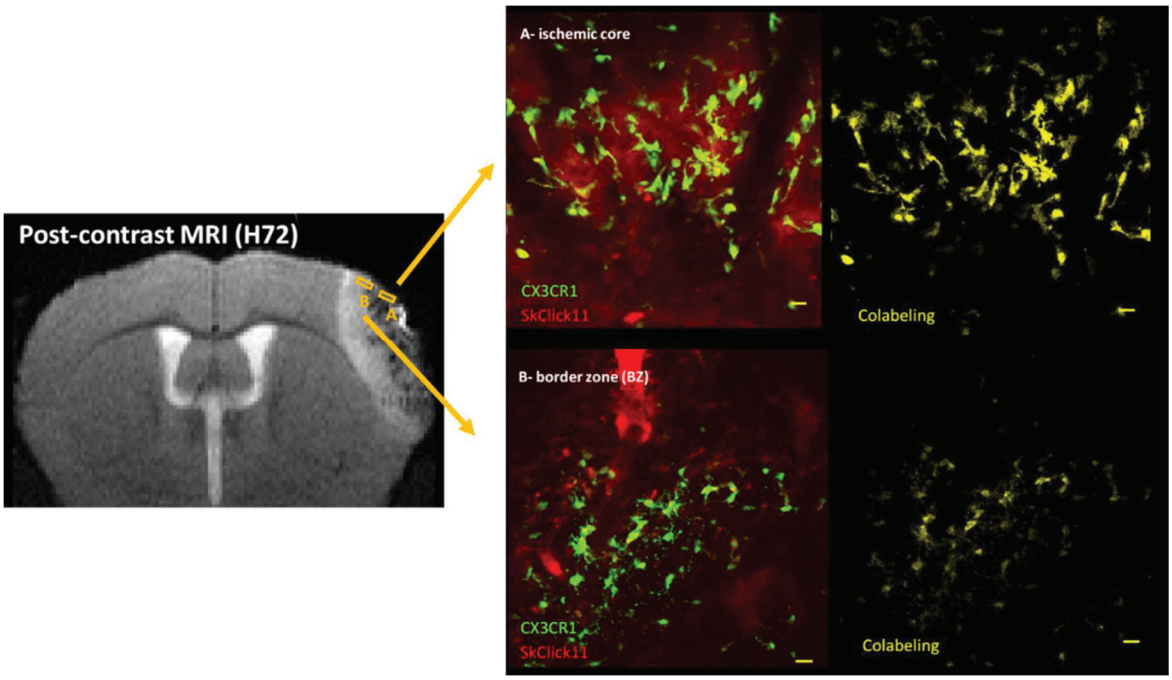

Figure 101 Identification of the lesion and its periphery with MRI observation on the same mouse guided two photon observations of these two areas. SKClick11 nanoparticles and microglia/macrophages colocalize, suggesting phagocytosis of the particles. Adapted from figure realized by Violaine Hubert and Inès Hristovska.

A back-to-back MRI and intravital two photon microscopy observations of CX3CR1-GFP mouse, 72 h after pMCAO shown in ***Figure 101*** evidences colocalization of microglia/macrophages and the particles, in particular in the activated cells, which suggests phagocytosis of the particles by the infiltrating macrophages and microglia.

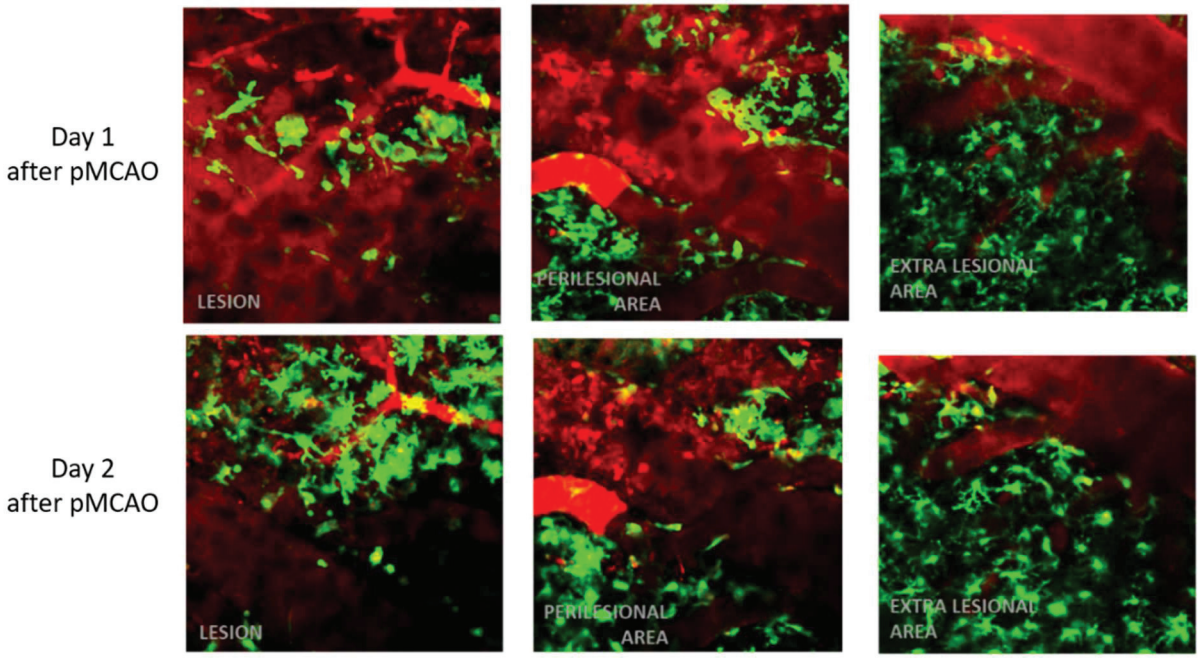

Figure 102 Two photon images of the three areas of the brain: inside the lesion, at the perilesional area and outside of the lesion. The same areas are compared one and two days after pMCAO. Green signal corresponds to microglial cells expressing GFP, and the particles in the blood flow or in the parenchyma appear in red. (Adapted from figure realized by Inès Hristovska and Olivier Pascual)

In a next series of experiments, based on MRI coordinates, as well as microglia cells morphology, three distinct areas were successfully identified by two photon imaging. One image of each region, observed at one day and two days post-pMCAO, is shown in ***Figure 102***. Unramified, amoeboid morphology of microglia (green signal), corresponding to an activated form, are visible in the infarct core. Two days after the injury, a significant recruitment of microglia is observed in the same area. Due to leakage through compromised BBB, SKClick11 nanoparticles induce a diffuse signal in the parenchyma, within this region. On day 1, no significant nanoparticle internalization was observed, however on day 2, nanoparticles signal in the microglia is increased in the lesioned and the peri-lesional area, due to phagocytosis. Oppositely, the highly ramified microglia in the extralesional area do not colocalize with the particles, which are only visible inside the intact blood vessels.

Combined *in vivo* MRI and two photon microscopy observations showed that SKClick11 nanoparticle is a good contrast agent for these two techniques. Furthermore, this particle is biocompatible and stealth enough to circulate in the blood stream for several days and is small enough to be delivered in the parenchyma, through the compromised BBB.

III - Conclusions

Results presented in this chapter are the outcome of a successful multidisciplinary and collaborative work. The elaborated and fully characterized nanoparticle contrast agent has been shown to be effective in the three targeted modalities: MRI, CT and two-photon intravital microscopy. Toxicological assessment showed no cytotoxicity effects.

The *in vivo* experiments aiming at imaging inflammation after ischemic stroke were successfully performed. Biocompatibility and stealth of the particles were demonstrated. With a long circulation time in blood, their optimal size and surface properties led to their phagocytose by activated macrophages (resident or infiltrating) in the lesion core. The uptake of the particles by the mononuclear phagocytic system and the multimodality of the nanoparticle labels allowed to follow efficiently the cells of interest in space and time, by the combined imaging techniques.

GENERAL CONCLUSIONS

The ambitious objective of the collaborative project NanoBrain was to promote a new approach leading to a deeper understanding of neuroinflammation in ischemic stroke, by sharing expertise and competencies in neuroscience, nanotechnology, and biochemistry. This thesis contributed to the project with the development of a multimodal nanoprobe, which allowed the imaging of inflammation in the brain. The nanoprobe is a hybrid nanoparticle, specially designed for MRI, (SPC)CT and two-photon intravital microscopy.

In the first part of the work, we discussed the elaboration and characterization of the inorganic core, comprised of gadolinium trifluoride. The GdF_3 nanoparticles were synthesized by an original solvothermal route, which involves the complexation of both fluoride and gadolinium sources. Complexation is believed to slow down the release of F^- and Gd^{3+} ions, leading to better control of nanoparticle nucleation and growth. This synthetic method resulted in highly crystalline and water-dispersible particles with well-controlled size and morphology. We pointed out that the measured scattering in the absorption spectrum of GdF_3 nanoparticles obeys to the Rayleigh scattering law, which enabled us to evaluate the average mass of one nanoparticle and the number of GdF_3 entities per particle.

Microwave-assisted synthesis has been examined as an alternative heating method. We found that the heating (conventional and microwave) technique does not have a significant effect on the size of the particles, which are slightly less elongated and more monodisperse. Compared to conventional heating (autoclave), microwave heating presents some advantages, like decreased reaction time and convenient reaction vessel; however, the up-scaling is not possible, because the volume of the sample is limited in this technique. To have an insight into the mechanism of nucleation and growth of these nanoparticles, we examined the effect of MW-heating time, solvent viscosity, concentration, and the presence of organic additives in the reaction medium. Both in the usual and high viscosity mixture, we observed after one minute of heating the formation of large nanoobjects, which dissolve upon further heating, followed by new nucleation and growth. The completely different growing process is observed in a high viscosity medium. During the cooling, the viscosity of EG increases rapidly; therefore, we think that it induces a decrease in the critical cluster size, leading to less stable and more irregularly shaped nanocrystals. The critical role of the concentration was also observed. In a highly diluted medium (at constant Gd^{3+}:F^- ratio), dendrite-like nanoparticles were obtained, due to the diffusion-limited conditions. These objects were unstable and dissolved spontaneously. Their coarsening resulted in very small and spherical particles. Oppositely, in the high concentration medium, large-size elongated nano-assemblies formed before any heat treatment. These objects

seem to dissolve, and finally, a mixture of hexagonal and orthorhombic nanoparticles is obtained, which was often reported in the literature for gadolinium-based nanoparticles. The mixed crystalline phase gives rise to heterogeneous morphologies.

Finally, the effect of two organic additives, EDTA, and a multidentate polymer (copo-P), was compared. We observed that the presence of the multidentate ligand prevents particle aggregation, while EDTA favors the assembly of the small particles into a spindle-like superstructure. Based on the coordination mode of EDTA and literature review, we suggested, that EDTA forms bridges between the small particles and induces their oriented attachment.

In the second part, we reported different surface-modification processes for the optimized inorganic core. A series of hybrid nanoparticles were synthesized by using three bisphosphonate-PEG ligands (BPPEGOMe, BPPEGN$_3$, and BPPEGCOOH). We found that the ligand BPPEGCOOH tends to aggregate the particles, through the interparticle bridging. The BPPEGN$_3$ ligand was included in order to subsequently react with the fluorophore LEM-A, *via* alkyne-azide click reaction. Except for the particles functionalized with exclusively BPPEGCOOH, all the other particles were stable in aqueous solution. This is explained by the combined electric and steric stabilization effects of BPPEG- ligands.

The commercial phosphonate-PEG ligand (PPEG) revealed to be a less efficient coating ligand because phosphonate group has less denticity than bisphosphonate; therefore, PPEG anchoring on the particle is less stable.

A well-known small molecule bisphosphonate, alendronic acid (AA) was also examined as surface modifying ligand. The lack of steric stabilization resulted in less stable particles, supporting the importance of the combined electrosteric effect of functionalized PEG-containing ligands. We observed, that when alendronic acid reacts with the particles in basic medium, the molecule is attached by a different coordination mode, then in the case of the acidic medium. Based on analytical results, we suggested, that in the basic conditions, AA coordinates with both its bisphosphonate and amino groups.

Exceptionally stable colloidal suspensions were obtained by using copo-P as surface modifying ligand. This multidentate polymer offers very efficient surface protection, preventing any aggregation phenomena, even after more than two years.

Combination of results from different analytical techniques allowed us to conclude, that the unmodified (bare) NP have an excess of positive charges due to Gd^{3+} ions, which is also

observed for incompletely covered particles. Oppositely, the efficiently stabilized particles benefit from stabilization effect of the excess negative charges of bisphosphonates, as well as the steric stabilization of PEG-chains. Despite its demonstrated efficiency of anchoring, BPPEG- ligands may detach from the particle in extreme conditions, such as heating at 150°C for several hours and/or long-lasting high-speed centrifugation. Nevertheless, the fluorescent SKClick11 particles, which were subjected to this treatment, are still stable enough for *in vivo* applications.

Lovastatin was initially planned to be coupled to the nanoparticles, for targeting the CR3 receptors expressed on the activated immune cells. Unfortunately, after a large number of attempts, this molecule revealed to be extremely difficult to react, and we did not succeed in its attachment on the particles.

The fluorescent hybrid nanoparticle SKClick11 has been extensively characterized from a chemical point of view, but also as a contrast agent. The successful attachment of LEM-A has been demonstrated by several analytical and experimental techniques, and two-photon absorption properties were measured. Relaxivities of the particle have been measured, and we found, that SKClick11 is an efficient T2-contrast agent. Its relaxation properties at 7T are very similar to Feraheme®, a commercial iron oxide nanoparticle-based CA. Toxicity of the SKClick11 particles has been evaluated on four human-derived cells, with two different methods. In all cases, it was found that the nanoparticles have no cytotoxic effect.

Several series of *in vivo* experiments have been performed with injection of the particle suspension. The conclusions drawn from these experiments were that SKClick11 NP is an efficient CA for MRI, SPCCT, and two-photon microscopy. Furthermore, the optimized size and surface properties make the particles stealth enough to have a long blood half-life. Long-circulating time in the blood favors accumulation across a dysfunctional BBB. Finally, the uptake of the nanoobjects by phagocytic immune cells was observed. Nanoparticle labeling of these cells allowed to follow them by two-photon microscopy and MRI. Therefore, we demonstrated that our multimodal nanoprobe is suitable for imaging inflammation processes in the brain. We believe that this nanoprobe can contribute to the better understanding of this complex biological process and hopefully, someday an efficient treatment for neuroinflammation will be developed.

If I had one extra year (or two) ...

If I had more time for this exciting multidisciplinary research work, I would certainly try to do the following experiments:

Trying to elucidate or at least better understand nanoparticle nucleation and growth is an interesting hot topic. As I tried to show, the scientific community has collected a large amount of information about the different parameters, which determine crystallinity, size, and morphology of nanoparticles, but the exact mechanisms are not understood. In the case of our GdF_3 nanoparticles, we demonstrated, that crystallinity, size, and morphology are influenced by the temperature, reaction time, viscosity of the solvent, and the presence of organic additives. The significant difference found in the case of the synthesis with EDTA and copo-P should be further explored. For example, by increasing the amount of these ligands until their quantity equals the number of Gd^{3+} ions. I would expect, in this case, a more pronounced effect of the ligands, which could result in highly monodisperse individual NPs for copo-P.

The spindle-like assemblies need to be studied more in detail. One could, for example, try to repeat the same synthesis without EDTA, in water. This would show if the small particles are bridged only by EDTA or the electrostatic forces due to the presence of different ions on the surface of the particle are the driving force of assembly. The unknown crystalline phase detected in the sample with EDTA should also be elucidated.

Other chelates could also be used in the same conditions, to compare their effects. In particular, comparison of nanoparticles formed from mononuclear complexes of gadolinium ions with the ones formed from bi- or trinuclear complexes could be interesting. The initial form of the gadolinium complex may have an impact on the nucleation phase.

Surface modification of the nanoparticles is also a rapidly developing research area, and the quality of the coating is very important, particularly in biological applications. In our case, I evidenced, that the BPPEG- coated NPs lose some ligand content after the click reaction. I suggested that it may be attributed to long-lasting heating and/or high-speed centrifuging. This could be elucidated by subjecting the BPPEG- coated particles to the same heating procedure and purifying them with relatively slow centrifuging. Oppositely, the same particles could be centrifuged at high speed, without any heating.

One could also find the lowest temperature, which is high enough to activate the alkyne-azide cycloaddition. The reaction could also be catalyzed by Cu(I), to compare the yield and see what the maximum quantity of chromophore is, that can be attached to the particle.

The multidentate polymeric ligand, copo-P, results in extremely high stability particles. This is a very interesting property for biological applications. However, this polymer cannot be coupled with the chromophore. It would be interesting to find or synthesize a similar ligand (multidentate, with strong anchoring points and PEG-chains), functionalized with azide functions, for example. I believe that the GdF_3 nanoplatform coated with such a ligand would be extremely stable and stealth contrast agent. However, the relaxivity properties have to be determined. It would also be interesting to see if it resists to high temperatures and high-speed centrifuging.

Relaxivity measurements on phantoms of both SKClick2 and SKClick11 have been performed. We found that r_2/r_1 relaxivity ratio of SKClick2 ($r_2/r_1 = 36.0$) is significantly higher than the ratio for SKClick11 ($r_2/r_1 = 20.2$). This could be explained by two effects, which are not completely independent. SKClick2 has fewer ligands on the surface; therefore, water molecules can approach Gd^{3+} ions on the surface more easily, which favors the relaxation process. The other possible explanation is that, because SKClick2 is less coated, it is prone to aggregate. Size increase due to aggregation increases the relaxivity effects of the particles. A systematic relaxivity measurement of a series of BPPEG- coated nanoparticles would be necessary to establish the relation between surface coating density and relaxation efficiency of the particles.

From the biological point of view, the long-term effects and biodistribution of the nanoparticles would be important to follow. This could also contribute to the knowledge-base of *in vivo* nanoparticle effects in general.

This short list of ideas is far from exhaustive, and lots of other questions could be asked in the field of nanoparticle growth, surface modification, biological effects of nanoparticles and stroke imaging.

APPENDICES

Appendix 1

To calculate the ligands per nanoparticle ratios in Chapter 3, the following relations have been used:

$$V_{NP} = \frac{4}{3} \cdot \pi \cdot a^2 \cdot b$$

$$m_{NP} = V_{NP} \cdot \rho$$

$$m_{inorg} = \frac{Residual\ mass\ (\%)}{Sample\ weight\ (mg) \cdot 100}$$

$$N_{NP} = \frac{m_{inorg}}{m_{NP}}$$

$$m_{org} = \frac{Mass\ loss\ (\%)}{Sample\ weight\ (mg) \cdot 100}$$

$$n_{org} = \frac{m_{org}}{M_{w,ligand}}$$

$$N_{ligands} = n_{org} \cdot \mathcal{N}_A$$

$$\frac{N_{ligands}}{N_{NP}}$$

where the different letters and symbols refer to:

V_{NP}	volume of one nanoparticle
a, b	two diameters of the elliptic nanoparticle (a < b)
m_{NP}	mass of one nanoparticle
ρ	density of GdF_3 bulk phase (7.1 g cm^{-3})
m_{inorg}	mass of the inorganics in the sample
N_{NP}	total number of nanoparticles in the sample
m_{org}	mass of the organics in the sample
n_{org}	number of moles of the organics in the sample
$M_{w,ligand}$	molar mass of the ligand
$N_{ligands}$	total number of ligands in the sample
N_A	Avogadro number

Appendix 2

Details of the absorption measurements for the determination of the molar extinction coefficients of the chromophore LEM-A in different solvents.

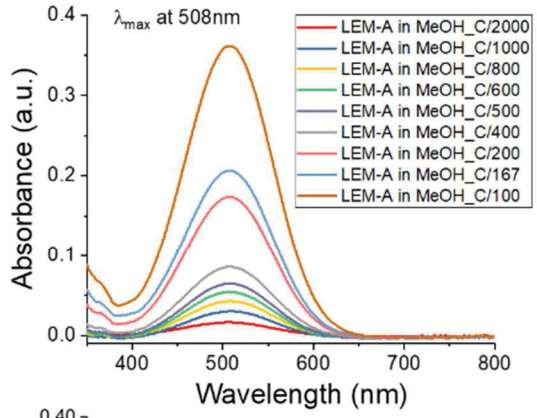

Dilution	C (mol L^{-1})	OD at λ_{max}
C/100	9.76E-06	0.3613
C/167	5.85E-06	0.2063
C/200	4.88E-06	0.1736
C/400	2.44E-06	0.0854
C/500	1.95E-06	0.0647
C/600	1.63E-06	0.0541
C/800	1.22E-06	0.0426
C/1000	9.76E-07	0.03
C/2000	4.88E-07	0.0162

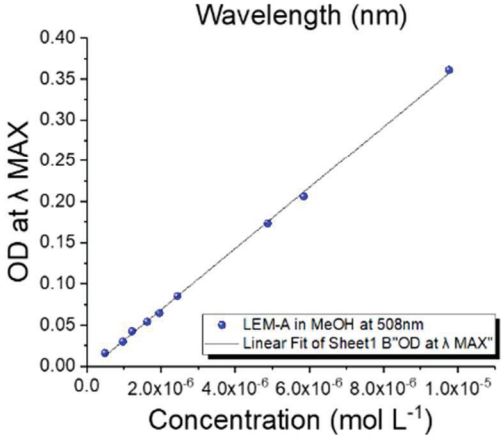

Equation	y = a + b*x
Plot	OD at λ MAX
Weight	No Weighting
Intercept	-0.006 ± 0.001
Slope	37151 ± 389
Residual Sum of Squares	7.79585E-5
Pearson's r	0.99962
R-Square (COD)	0.99923
Adj. R-Square	0.99912

Figure A2.1 Absorption spectra of LEM-A in methanol (MeOH), at different concentrations. C designs the initial concentration corresponding to the 3.9 mg of solid dissolved in 10 mL of solvent. The exact concentrations and the corresponding OD values are reported in the upper table. In the other table, the fitting parameters are shown, which correspond to the OD vs. concentration plot.

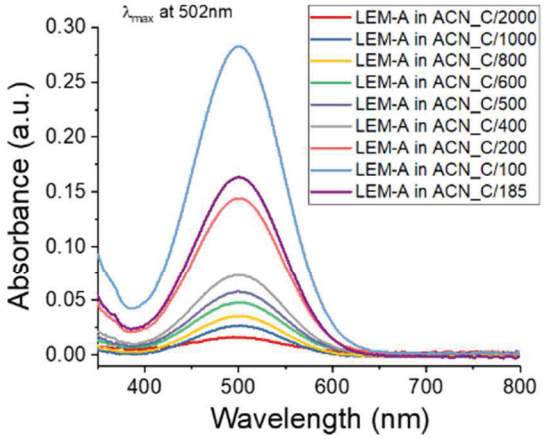

Dilution	C (mol L^{-1})	OD at I_{max}
C/100	9.76E-06	0.2823
C/185	5.28E-06	0.1633
C/200	4.88E-06	0.1444
C/400	2.44E-06	0.0731
C/500	1.95E-06	0.0576
C/600	1.63E-06	0.0481
C/800	1.22E-06	0.0354
C/1000	9.76E-07	0.0269
C/2000	4.88E-07	0.0163

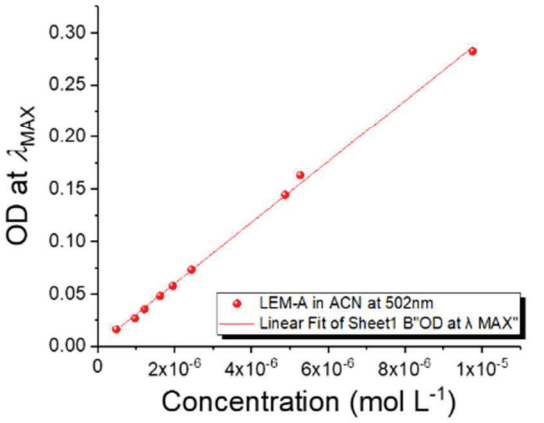

Equation	y = a + b*x
Plot	OD at λ MAX
Weight	No Weighting
Intercept	0.001 ± 0.001
Slope	29201 ± 430
Residual Sum of Squares	9.20777E-5
Pearson's r	0.99924
R-Square (COD)	0.99848
Adj. R-Square	0.99826

Figure A2.2 Absorption spectra of LEM-A in acetonitrile (ACN), at different concentrations. C designs the initial concentration corresponding to the 3.9 mg of solid dissolved in 10 mL of solvent. The exact concentrations and the corresponding OD values are reported in the upper table. In the other table, the fitting parameters are shown, which correspond to the OD vs. concentration plot.

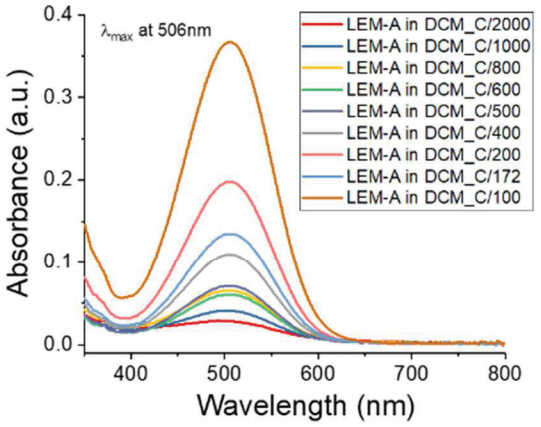

Dilution	C (mol L^{-1})	OD at l_{max}
C/100	1.10E-05	0.3672
C/172	6.40E-06	0.1349
C/200	5.51E-06	0.198
C/400	2.75E-06	0.1097
C/500	2.20E-06	0.0715
C/600	1.84E-06	0.0655
C/800	1.38E-06	0.0608
C/1000	1.10E-06	0.0412
C/2000	5.51E-07	0.0286

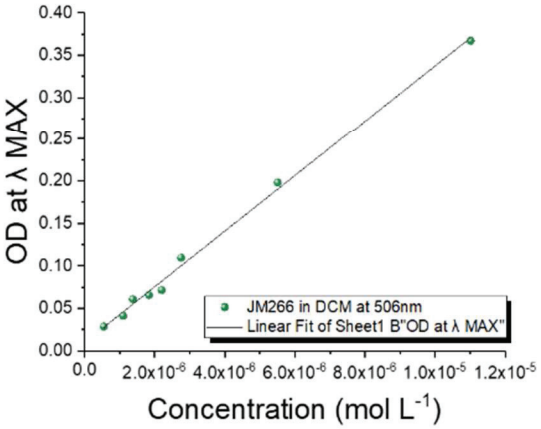

Equation	y = a + b*x
Plot	OD at λ_{MAX}
Weight	No Weighting
Intercept	0.01 ± 0.004
Slope	32768 ± 836
Residual Sum of Squares	3.52667E-4
Pearson's r	0.99805
R-Square (COD)	0.99611
Adj. R-Square	0.99546

Figure A2.3 Absorption spectra of LEM-A in dichloromethane (DCM), at different concentrations. C designs the initial concentration corresponding to the 4.4 mg of solid dissolved in 10 mL of solvent. The exact concentrations and the corresponding OD values are reported in the upper table. In the other table, the fitting parameters are shown, which correspond to the OD vs. concentration plot.

Appendix 3

Protons (or hydrogen nuclei) are characterized by a quantum mechanical property, called nuclear spin (denoted as I), which causes them to act like a small magnet (magnetic dipole). According to quantum mechanics, a spin I, has $(2I+1)$ possible orientation, having the same energy. This degeneracy of states disappears, when an external field, $\boldsymbol{B_0}$ is applied to the nucleus (this is the so-called nuclear Zeeman effect). In the case of protons ($I = 1/2$) two orientations are possible: parallel and anti-parallel to the direction of $\mathbf{B_0}$. The parallel orientation (also called as spin-up state) is energetically more favorable (lower energy), than the anti-parallel (spin-down) state. Due to the interaction between the magnetic moment of the nucleus and the magnetic field, the former one will precess (Larmor precessing) around the magnetic field in these two directions, with an angular frequency ω_0, proportional to the magnitude of the external field.

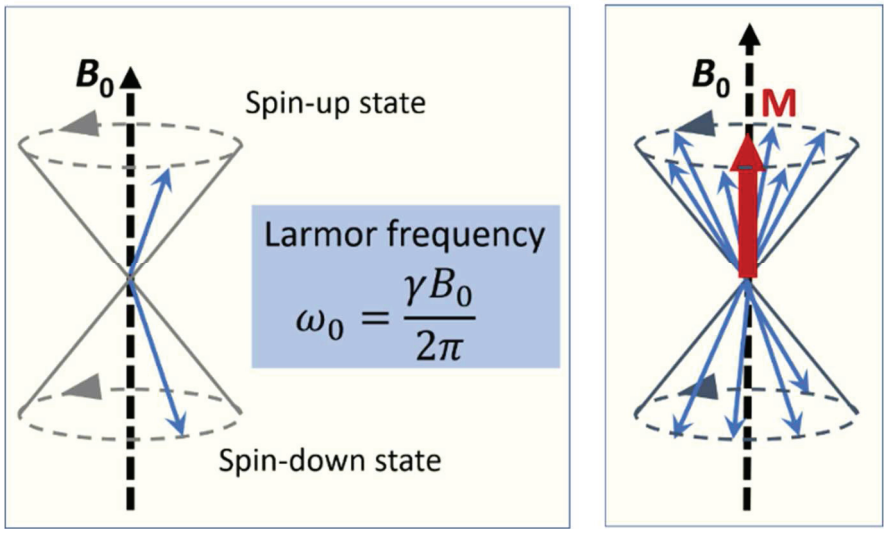

Figure A3.1 Schematic representation of spin states and the resulting magnetic moment M of the spin-system

Let us consider a system composed of a set of protons (*e.g.* a certain amount of water) put in a static and homogeneous magnetic field ($\mathbf{B_0}$). When all spins reached the thermal equilibrium under the external constraint, then the probability to observe spin-up and spin-down states is described by the Boltzmann equation, which predicts, that the spin population in parallel state is slightly larger than the anti-parallel one. This slight excess state creates a macroscopic magnetic moment **M**, of the set of nuclei under consideration. The magnetic moment **M** is

aligned with $\mathbf{B_0}$ and has a magnitude M_0, which is the thermal equilibrium magnetization of the system. Magnetization along the external field cannot be measured, therefore, a second magnetic field is applied, $\mathbf{B_1}$, in order to flip **M** into the xy-plane (transverse), perpendicular to $\mathbf{B_0}$ (which defines the z-axis). This can be achieved by applying an oscillating radio-frequency pulse, which induces an electromagnetic field rotating in the xy-plane, with the same angular frequency as the protons (Larmor frequency). The oscillating pulse excite spins, *i.e.* by absorption of energy some of the protons in the system switches from up- to down-state, so that the populations "spin-up" and "spin-down" are equal. Consequently, the net magnetization **M** is in the xy-plane (Figure A3.2), *i.e.* $M_z = 0$. In addition, this RF-pulse forces spins to precess in phase.

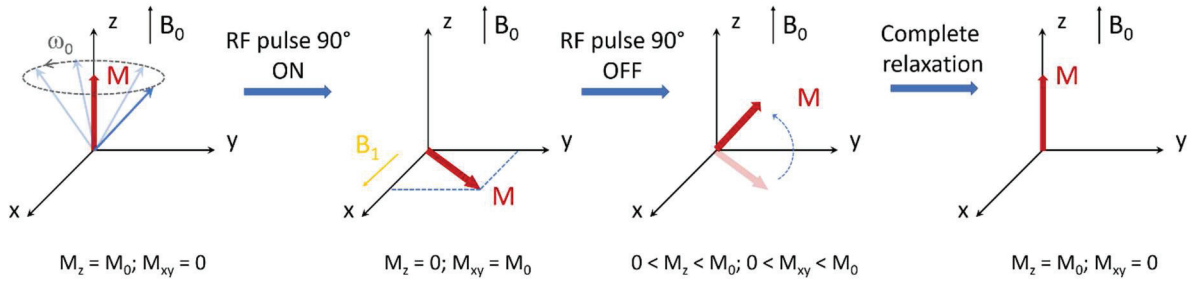

Figure A3.2 Illustration of different orientations of the magnetic moment M after a RF pulse of 90°and its relaxation, in presence of a B_0 external field.

Once $\mathbf{B_1}$ field is switched off, the nuclei start to gradually come back to their equilibrium state, *i.e.* **M** realigns with $\mathbf{B_0}$. The processes through which spin system relaxes towards its equilibrium state involve energy exchange with its environment (spin-lattice relaxation) as well as between the spins (spin-spin relaxation). Longitudinal magnetization component (M_z) of **M** corresponds to spin-lattice relaxation, while transversal component (M_{xy}) describes spin-spin relaxation. Spin-spin interactions cause their dephasing, therefore the individual contributions to M_{xy} of protons progressively cancel each other, resulting in magnetization decay. In the meantime, as the equilibrium spin population distribution reaches progressively its equilibrium sate, the overall M_z recovers its initial value, M_0. Equations of motion governing these two components are given by the so-called Bloch equations:

$$\frac{dM_z}{dt} = -\left(\frac{M_z - M_0}{T_1}\right)$$

$$\frac{dM_{xy}}{dt} = -\frac{M_{xy}}{T_2}$$

where T_1 and T_2 are characteristic times of longitudinal and transversal relaxations respectively. The solution of these equations for a 90° pulse are:

$$M_z(t) = M_0\left(1 - e^{-t/T_1}\right)$$

$$M_{xy}(t) = M_0 e^{-t/T_2}$$

Figure A3.3 shows the plot of these relaxion functions. Because of their exponential nature, it is difficult to determine, when these functions (magnetization) reach their maximum, therefore T_1 is defined by convention, as the time required for protons to recover approximately 63% (1-1/exp(1)) of the initial longitudinal magnetization (M_0) and T_2, the time needed for the transverse magnetization (M_{xy}) to fall to approximately 37% (1/exp(1)) of its initial value.

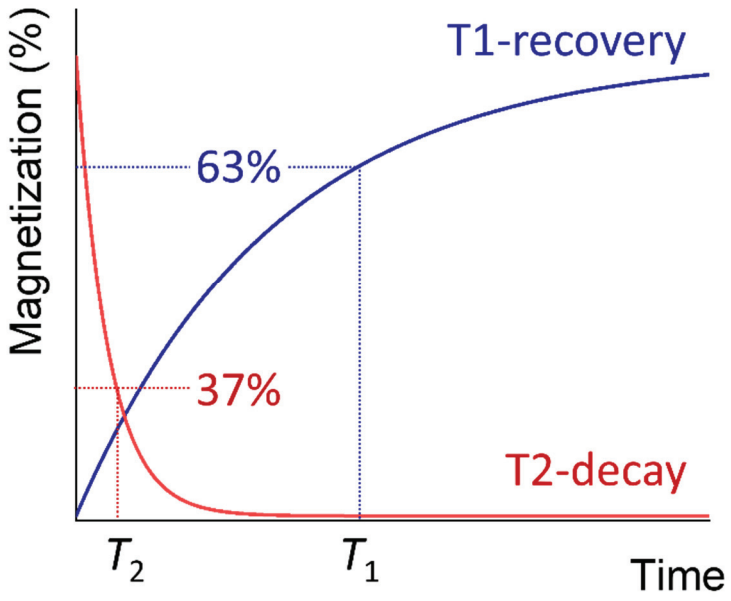

Figure A3.3 T1-recovery and T2-decay during relaxation processes.

The recorded signal called FID (Free Induction Decay), contains both intensity and phase information in the time-domain and is mathematically treated via Fourier-transformation, to obtain frequency-domain data (NMR spectrum). For imaging purposes, a complex 3D reconstruction of a large number of data must be performed to obtain the required visualization of anatomical details.

In a living body water is the most abundant compound, therefore a huge number of protons are present. During MR imaging the above-mentioned proton signals are recorded. The acquired image of magnetized tissue/body reflects the signal produced by the local magnetization density

of protons. As the density of protons (*i.e.,* the number of relaxing protons per unit of volume) varies slightly in different types of tissues, the signal intensity varies. However, these small density variations only allow to obtain a poor contrast anatomical image, which is of little interest from a clinical point of view. To distinguish for example anatomically normal, healthy tissues from pathologies the contrast between these tissues with similar proton densities must be enhanced.

A basic MRI experiment consists in the following steps: 1. subject is placed in the external magnetic field (protons are in equilibrium), 2. RF pulse excitation of protons (out-of-equilibrium state), 3. T_2 (faster) and T_1 (slower) relaxations occur and are recorded. In practice, these steps are repeated several times to obtain a stronger signal. The subsequent steps constitute an MR sequence (Figure A3.4). Repetition time of pulses (TR), flip angle (*e.g.* 90°), and the time laps between the pulse and the acquisition, called echo time (TE) are operator-selectable parameters, which influence image contrast.

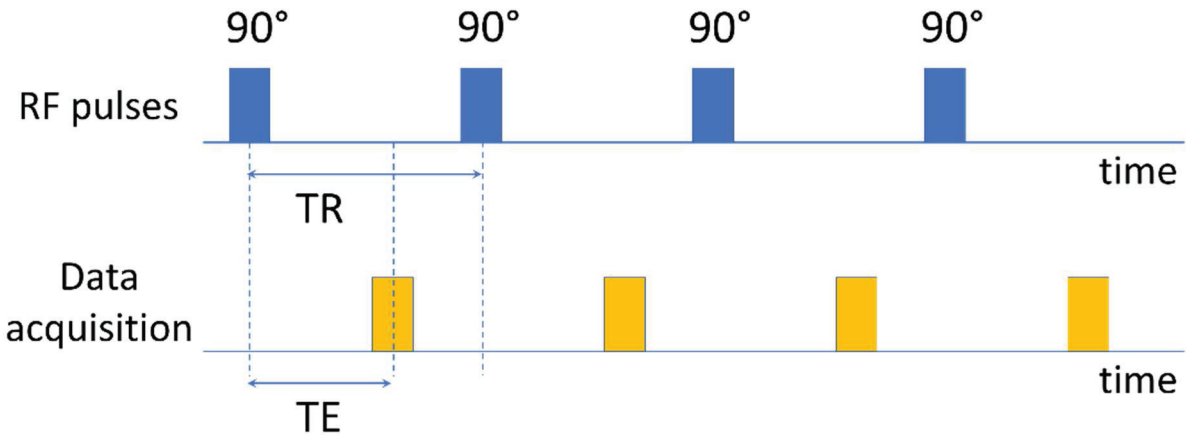

Figure A3.4 Scematic representation of a simple MR sequence as a function of time. The repetition time(TR) is the time laps between two RF pulses of 90°. Echo time is the time between the pulse and the data acquisition.

TR mainly controls T_1 and TE mainly controls T_2. Now, let us compare signals obtained for two tissues or fluids A and B, with relaxation times T_{1A}, T_{2A} and T_{1B}, T_{2B} respectively (*A* is fat, and *B* is cerebrospinal fluid for example), and let's see how contrast evolves with these parameters. Figure A3.5 shows relaxation curves for A and B. When a short TR is applied, T1-signal is very small for both tissues/fluids, therefore both appear in dark on the image. However, if the repetition time value is on a timescale, where the signal difference is maximum for A and B, the contrast will be high. In the case of T2-signal, the maximum contrast is obtained for an echo time comparable to the time, when difference in signals A and B is maximum.

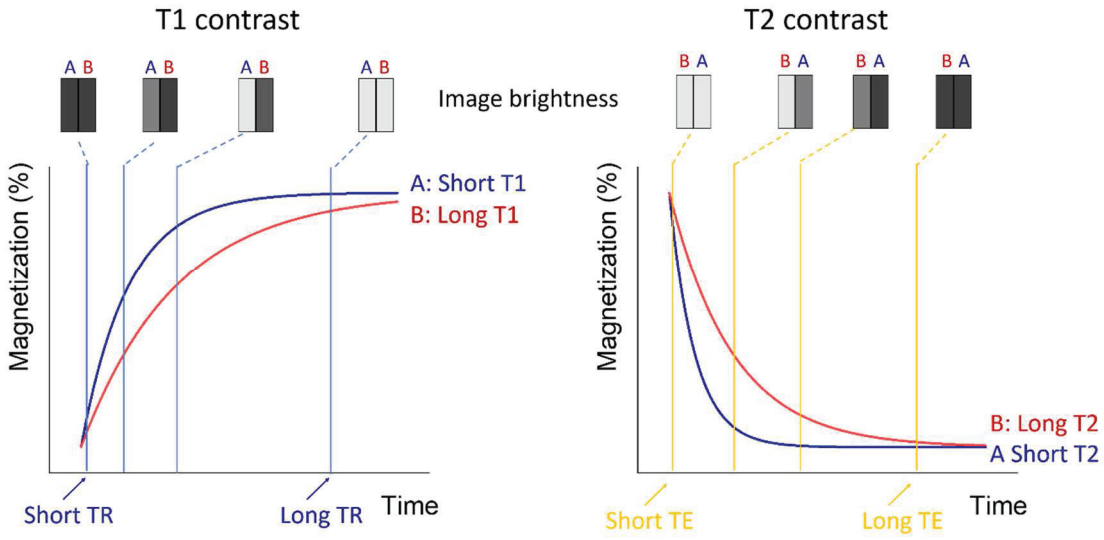

Figure A3.5 Schematic diagram illustrating T1 and T2 contrast with different TR and TE times.

T1-contrast: for short TR, if T_1 is shorter (rapid recovery), the image is brighter. T2-contrast: for long TE, if T_2 is shorter (rapid recovery), the image is darker.

Appendix 4

Two-photon induced fluorescence emission spectra of the fluorophore LEM-A and the reference compound, fluorescein. Fluorescein is dissolved in NaOH, at pH = 13 and LEM-A is in methanol.

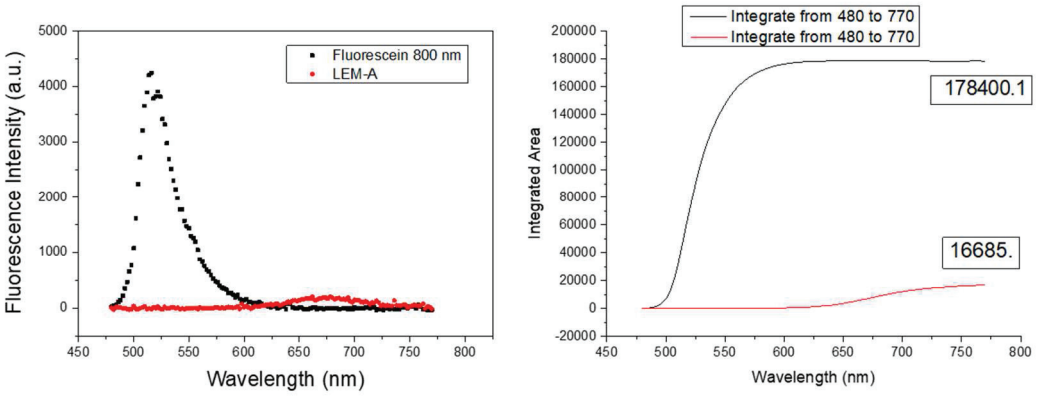

Figure A4.1 Two-photon induced emission spectra measured upon excitation at 800 nm. The corresponding integrated area are shown on the right graph. (Integration range: 480-770 nm)

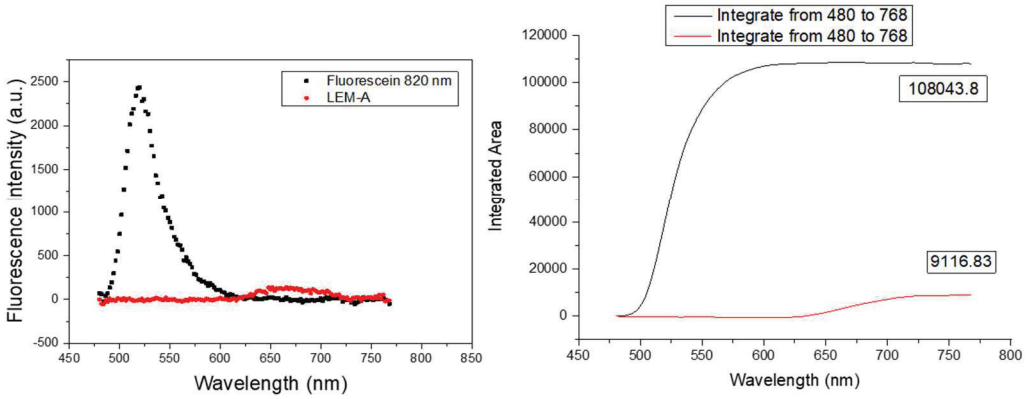

Figure A4.2 Two-photon induced emission spectra measured upon excitation at 820 nm. The corresponding integrated area are shown on the right graph. (Integration range: 480-768 nm)

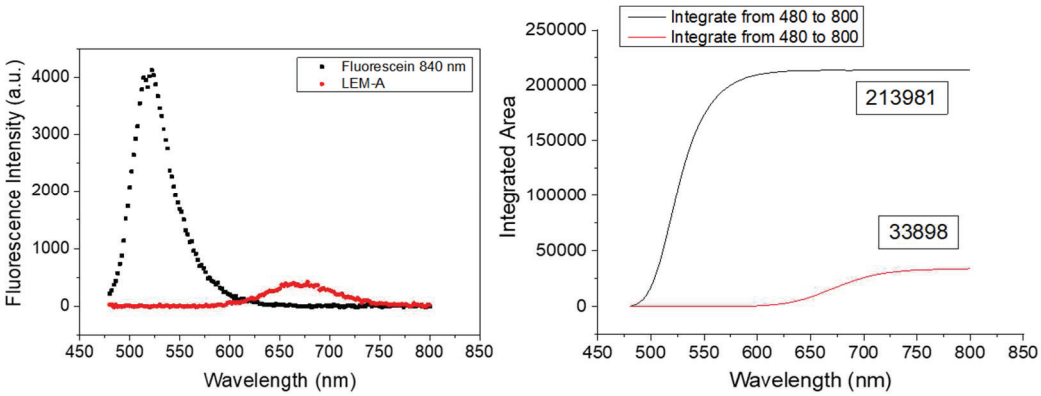

Figure A4.3 Two-photon induced emission spectra measured upon excitation at 840 nm. The corresponding integrated area are shown on the right graph. (Integration range: 480-800 nm)

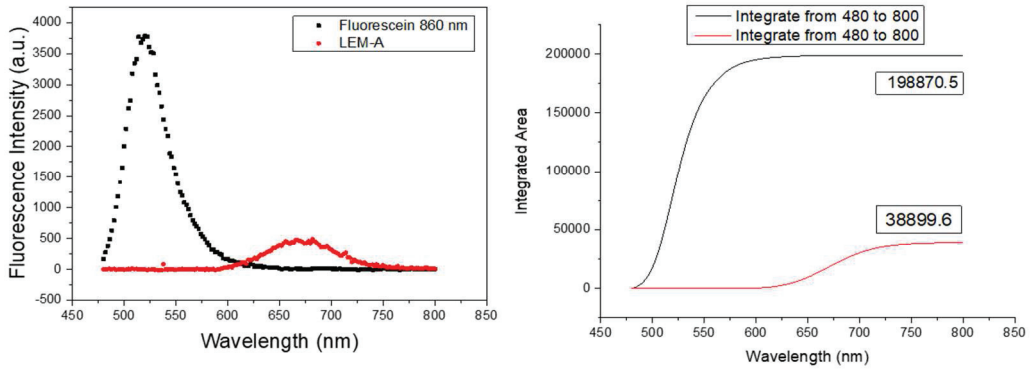

Figure A4.4 Two-photon induced emission spectra measured upon excitation at 860 nm. The corresponding integrated area are shown on the right graph. (Integration range: 480-800 nm)

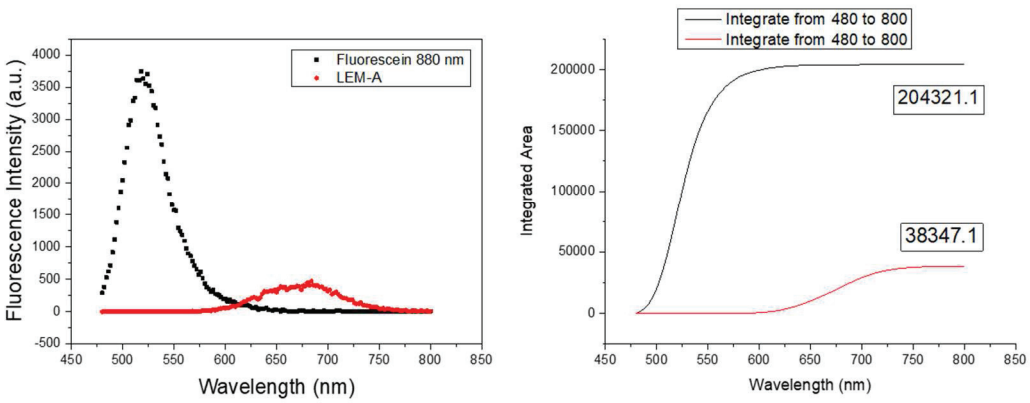

Figure A4.5 Two-photon induced emission spectra measured upon excitation at 880 nm. The corresponding integrated area are shown on the right graph. (Integration range: 480-800 nm)

List of References

[1] W. Johnson, O. Onuma, M. Owalabi, S. Sachdev, Stroke: a global response is needed. *Bull. World Health Organ.* **2016**.
[2] S. Jander, M. Schroeter, A. Saleh, *Stroke* **2007**, *38*, 642.
[3] S. Panagiotou, S. Saha, *Front. Neurosci.* **2015**, *9*, 182.
[4] A. Srinivasan, M. Goyal, F. A. Azri, C. Lum, *RadioGraphics* **2006**, *26*, S75.
[5] Saver Jeffrey L., *Stroke* **2006**, *37*, 263.
[6] C. R. Gomez, *J. Stroke Cerebrovasc. Dis.* **1993**, *3*, 1.
[7] M. Gauberti, S. M. De Lizarrondo, D. Vivien, *Eur. Stroke J.* **2016**, *1*, 20.
[8] A. Da Silva-Candal, B. Argibay, R. Iglesias-Rey, Z. Vargas, A. Vieites-Prado, E. López-Arias, E. Rodríguez-Castro, I. López-Dequidt, M. Rodríguez-Yáñez, Y. Piñeiro, T. Sobrino, F. Campos, J. Rivas, J. Castillo, *J. Nanobiotechnology* **2017**, *15*, 30.
[9] del Zoppo Gregory J., Saver Jeffrey L., Jauch Edward C., Adams Harold P., *Stroke* **2009**, *40*, 2945.
[10] X. Liu, *Interv. Neurol.* **2012**, *1*, 3.
[11] A.-G. Ceulemans, T. Zgavc, R. Kooijman, S. Hachimi-Idrissi, S. Sarre, Y. Michotte, *J. Neuroinflammation* **2010**, *7*, 74.
[12] E. P. Thelin, T. Tajsic, F. A. Zeiler, D. K. Menon, P. J. A. Hutchinson, K. L. H. Carpenter, M. C. Morganti-Kossmann, A. Helmy, *Front. Neurol.* **2017**, *8*, 351.
[13] M. W. Salter, B. Stevens, *Nat. Med.* **2017**, *23*, 1018.
[14] S. Fumagalli, C. Perego, F. Pischiutta, E. R. Zanier, M.-G. De Simoni, *Front. Neurol.* **2015**, *6*, 81.
[15] J. Leary, J. Key, *Int. J. Nanomedicine* **2014**, 711.
[16] L. Zhang, R. Liu, H. Peng, P. Li, Z. Xu, A. K. Whittaker, *Nanoscale* **2016**, *8*, 10491.
[17] A. Merbach, L. Helm, E. Toth, *J. Am. Chem. Soc.* **2002**, *124*, 884.
[18] S. Yamada, T. Matsuzawa, K. Yamada, S. Yoshioka, S. Ono, T. Hishinuma, *Tohoku J. Exp. Med.* **1989**, *158*, 203.
[19] D. C. Preston, Magnetic Resonance Imaging (MRI) of the Brain and Spine: Basics. *https://casemed.case.edu/clerkships/neurology/Web%20Neurorad/MRI%20Basics.htm* **2006**.
[20] M. E. Hayden, P.-J. Nacher, In *Magnetic Resonance Imaging Handbook*; SABA, L., Ed.; CRC press, 2016; Vol. 1.
[21] R. B. Lauffer, *Chem. Rev.* **1987**, *87*, 901.
[22] C. de Haën, *Top. Magn. Reson. Imaging* **2001**, *12*, 221.
[23] I. R. Young, G. J. Clarke, D. R. Bailes, J. M. Pennock, F. H. Doyle, G. M. Bydder, *J. Comput. Tomogr.* **1981**, *5*, 543.
[24] M. Laniado, H. J. Weinmann, W. Schörner, R. Felix, U. Speck, *Physiol. Chem. Phys. Med. NMR* **1984**, *16*, 157.
[25] H. S. Thomsen, S. K. Morcos, T. Almén, M.-F. Bellin, M. Bertolotto, G. Bongartz, O. Clement, P. Leander, G. Heinz-Peer, P. Reimer, F. Stacul, A. van der Molen, J. A. Webb, *Eur. Radiol.* **2013**, *23*, 307.
[26] T. Grobner, *Nephrol. Dial. Transplant.* **2006**, *21*, 1104.
[27] C. Cabella, S. G. Crich, D. Corpillo, A. Barge, C. Ghirelli, E. Bruno, V. Lorusso, F. Uggeri, S. Aime, *Contrast Media Mol. Imaging* **2006**, *1*, 23.
[28] T. Kanda, K. Ishii, H. Kawaguchi, K. Kitajima, D. Takenaka, *Radiology* **2013**, *270*, 834.
[29] J. W. Choi, W.-J. Moon, *Korean J. Radiol.* **2019**, *20*, 134.
[30] M. Botta, L. Tei, *Eur. J. Inorg. Chem.* **2012**, *2012*, 1945.

[31] É. Tóth, R. D. Bolskar, A. Borel, G. González, L. Helm, A. E. Merbach, B. Sitharaman, L. J. Wilson, *J. Am. Chem. Soc.* **2005**, *127*, 799.
[32] B. Drahoš, I. Lukeš, É. Tóth, *Eur. J. Inorg. Chem.* **2012**, *2012*, 1975.
[33] E. Terreno, D. D. Castelli, A. Viale, S. Aime, *Chem. Rev.* **2010**, *110*, 3019.
[34] M. Bietenbeck, A. Florian, C. Faber, U. Sechtem, A. Yilmaz, *Int. J. Nanomedicine* **2016**, *11*, 3191.
[35] J. Estelrich, M. J. Sánchez-Martín, M. A. Busquets, *Int. J. Nanomedicine* **2015**, *10*, 1727.
[36] N. Bloembergen, *J. Chem. Phys.* **1957**, *27*, 572.
[37] I. Solomon, *Phys. Rev.* **1955**, *99*, 559.
[38] L. Helm, A. E. Merbach, *Chem. Rev.* **2005**, *105*, 1923.
[39] Z. Jászberényi, A. Sour, É. Tóth, M. Benmelouka, A. E. Merbach, *Dalton Trans.* **2005**, 2713.
[40] S. Laus, R. Ruloff, E. Toth, A. E. Merbach, *Chem. – Eur. J.* **2003**, *9*, 3555.
[41] E. J. Werner, A. Datta, C. J. Jocher, K. N. Raymond, *Angew. Chem. Int. Ed.* **2008**, *47*, 8568.
[42] L. M. De León-Rodríguez, A. F. Martins, M. C. Pinho, N. M. Rofsky, A. D. Sherry, *J. Magn. Reson. Imaging* **2015**, *42*, 545.
[43] W. Zhang, L. Liu, H. Chen, K. Hu, I. Delahunty, S. Gao, J. Xie, *Theranostics* **2018**, *8*, 2521.
[44] R. Weigert, N. Porat-Shliom, P. Amornphimoltham, *J. Cell Biol.* **2013**, *201*, 969.
[45] A. M. Smith, M. C. Mancini, S. Nie, *Nat. Nanotechnol.* **2009**, *4*, 710.
[46] R. Weissleder, *Nat. Biotechnol.* **2001**, *19*, 316.
[47] J. Liu, *Front. Optoelectron.* **2015**, *8*, 141.
[48] G. Yang, F. Pan, C. N. Parkhurst, J. Grutzendler, W.-B. Gan, *Nat. Protoc.* **2010**, *5*, 201.
[49] J. Herz, B. H. Zinselmeyer, D. B. McGavern, *Microsc. Microanal.* **2012**, *18*, 730.
[50] J. Zhao, J. Chen, S. Ma, Q. Liu, L. Huang, X. Chen, K. Lou, W. Wang, *Acta Pharm. Sin. B* **2018**, *8*, 320.
[51] E. Spiess, F. Bestvater, A. Heckel-Pompey, K. Toth, M. Hacker, G. Stobrawa, T. Feurer, C. Wotzlaw, U. Berchner-Pfannschmidt, T. Porwol, H. Acker, *J. Microsc.* **2005**, *217*, 200.
[52] T. G. Phan, A. Bullen, *Immunol. Cell Biol.* **2010**, *88*, 438.
[53] H. Lusic, M. W. Grinstaff, *Chem. Rev.* **2013**, *113*, 1641.
[54] I. Danad, Z. A. Fayad, M. J. Willemink, J. K. Min, *JACC Cardiovasc. Imaging* **2015**, *8*, 710.
[55] S. Si-Mohamed, D. Bar-Ness, M. Sigovan, D. P. Cormode, P. Coulon, E. Coche, A. Vlassenbroek, G. Normand, L. Boussel, P. Douek, *Nucl. Instrum. Methods Phys. Res. Sect. Accel. Spectrometers Detect. Assoc. Equip.* **2017**, *873*, 27.
[56] J. Kim, D. Bar-Ness, S. Si-Mohamed, P. Coulon, I. Blevis, P. Douek, D. P. Cormode, *Sci. Rep.* **2018**, *8*, 1.
[57] N. Halttunen, F. Lerouge, F. Chaput, M. Vandamme, S. Karpati, S. Si-Mohamed, M. Sigovan, L. Boussel, P. Chereul, P. Douek, S. Parola, Hybrid Nano-GdF3 contrast media allows pre-clinical in vivo element-specific K-edge imaging and quantification. *Sci. Rep.* **2019**, Under revision.
[58] M. Cui, Y. Zhou, B. Wei, X.-H. Zhu, W. Zhu, M. A. Sanders, K. Ugurbil, W. Chen, *Sci. Rep.* **2017**, *7*, 2733.
[59] E. Duguet, S. Vasseur, S. Mornet, J.-M. Devoisselle, *Nanomed.* **2006**, *1*, 157.
[60] R. F. Minchin, D. J. Martin, *Endocrinology* **2010**, *151*, 474.
[61] Y. Cao, L. Xu, Y. Kuang, D. Xiong, R. Pei, *J. Mater. Chem. B* **2017**, *5*, 3431.
[62] A. C. Anselmo, S. Mitragotri, *Bioeng. Transl. Med.* **2016**, *1*, 10.

[63] H. S. Choi, J. V. Frangioni, *Mol. Imaging* **2010**, *9*, 7290.2010.00031.
[64] D. S. Albrecht, C. Granziera, J. M. Hooker, M. L. Loggia, *ACS Chem. Neurosci.* **2016**, *7*, 470.
[65] B. Zinnhardt, T. Viel, L. Wachsmuth, A. Vrachimis, S. Wagner, H.-J. Breyholz, A. Faust, S. Hermann, K. Kopka, C. Faber, F. Dollé, S. Pappata, A. M. Planas, B. Tavitian, M. Schäfers, L. M. Sorokin, M. T. Kuhlmann, A. H. Jacobs, *J. Cereb. Blood Flow Metab.* **2015**, *35*, 1711.
[66] R. Veksler, I. Shelef, A. Friedman, *Arch. Med. Res.* **2014**, *45*, 646.
[67] R. Weissleder, G. Elizondo, J. Wittenberg, C. A. Rabito, H. H. Bengele, L. Josephson, *Radiology* **1990**, *175*, 489.
[68] M. Rausch, A. Sauter, J. Fröhlich, U. Neubacher, E. W. Radü, M. Rudin, *Magn. Reson. Med.* **2001**, *46*, 1018.
[69] J. Dulińska-Litewka, A. Łazarczyk, P. Hałubiec, O. Szafrański, K. Karnas, A. Karewicz, *Materials* **2019**, *12*, 617.
[70] L. H. Deddens, G. A. F. Van Tilborg, W. J. M. Mulder, H. E. De Vries, R. M. Dijkhuizen, *Cerebrovasc. Dis.* **2012**, *33*, 392.
[71] M. Marinescu, M. Langer, A. Durand, C. Olivier, A. Chabrol, H. Rositi, F. Chauveau, T. H. Cho, N. Nighoghossian, Y. Berthezène, F. Peyrin, M. Wiart, *Mol. Imaging Biol.* **2013**, *15*, 552.
[72] S. Bok, T. Wang, C.-J. Lee, S.-U. Jeon, Y.-E. Kim, J. Kim, B.-J. Hong, C. J. Yoon, S. Kim, S.-H. Lee, H. J. Kim, I. H. Kim, K. H. Kim, G.-O. Ahn, *Biomed. Opt. Express* **2015**, *6*, 3303.
[73] J. Neumann, S. Henneberg, S. von Kenne, N. Nolte, A. J. Müller, B. Schraven, M. W. Görtler, K. G. Reymann, M. Gunzer, M. Riek-Burchardt, *PLOS ONE* **2018**, *13*, e0193970.
[74] T. Li, S. Pang, Y. Yu, X. Wu, J. Guo, S. Zhang, *Brain* **2013**, *136*, 3578.
[75] A. Scheller, D. Vivien, F. Kirchhoff, C. Orset, R. E. Sandu, A. Popa-Wagner, *Scanning Microsc.* 9.
[76] T. A. Springer, *Nature* **1990**, *346*, 425.
[77] R. Yokel, E. Grulke, R. MacPhail, *Wiley Interdiscip. Rev. Nanomed. Nanobiotechnol.* **2013**, *5*, 346.
[78] M. R. Jensen, G. Bajic, X. Zhang, A. K. Laustsen, H. Koldsø, K. K. Skeby, B. Schiøtt, G. R. Andersen, T. Vorup-Jensen, *J. Biol. Chem.* **2016**, *291*, 16963.
[79] R. P. Feynman, *Eng. Sci.* **1960**, *23*, 22.
[80] J. Polte, *CrystEngComm* **2015**, *17*, 6809.
[81] R. Becker, W. Döring, *Ann. Phys.* **1935**, *416*, 719.
[82] V. K. L. Mer, *Ind. Eng. Chem.* **1952**, *44*, 1270.
[83] V. K. LaMer, R. H. Dinegar, *J. Am. Chem. Soc.* **1950**, *72*, 4847.
[84] A. R. Pascoe, Q. Gu, M. U. Rothmann, W. Li, Y. Zhang, A. D. Scully, X. Lin, L. Spiccia, U. Bach, Y.-B. Cheng, *Sci. China Mater.* **2017**, *60*, 617.
[85] P. Mahon, The Solution to Dissolution: Solubility and Stable Formulations. *IFormulate Ltd* **2014**.
[86] N. T. K. Thanh, N. Maclean, S. Mahiddine, *Chem. Rev.* **2014**, *114*, 7610.
[87] T. A. Witten, L. M. Sander, *Phys. Rev. B* **1983**, *27*, 5686.
[88] H. Imai, In *Biomineralization I: Crystallization and Self-Organization Process*; Naka, K., Ed.; Topics in Current Chemistry; Springer Berlin Heidelberg: Berlin, Heidelberg, 2007; pp. 43–72.
[89] W. Ostwald, *Z. Für Phys. Chem.* **1900**, *34U*, 495.
[90] I. M. Lifshitz, V. V. Slyozov, *J. Phys. Chem. Solids* **1961**, *19*, 35.
[91] C. Wagner, *Z. Für Elektrochem. Berichte Bunsenges. Für Phys. Chem.* **1961**, *65*, 581.

[92] D.-K. Lee, S.-I. Park, J. K. Lee, N.-M. Hwang, *Acta Mater.* **2007**, *55*, 5281.
[93] R. L. Penn, *J. Phys. Chem. B* **2004**, *108*, 12707.
[94] R. L. Penn, J. F. Banfield, *Science* **1998**, *281*, 969.
[95] Q. Zhang, S.-J. Liu, S.-H. Yu, *J. Mater. Chem.* **2008**, *19*, 191.
[96] C. Dhand, N. Dwivedi, X. J. Loh, A. N. J. Ying, N. K. Verma, R. W. Beuerman, R. Lakshminarayanan, S. Ramakrishna, *RSC Adv.* **2015**, *5*, 105003.
[97] A. Jabłoński, *Nature* **1993**, *131*, 839.
[98] Dynamic Light Scattering Spectrophotometer DLS-8000 | Otsuka Electronics. *http://www.otsukael.com/product/detail/productid/23/category1id/2/category2id/2/category3id/32*.
[99] D. E. Koppel, *J. Chem. Phys.* **1972**, *57*, 4814.
[100] S. W. Provencher, *Comput. Phys. Commun.* **1982**, *27*, 213.
[101] J.-M. Rabanel, P. Hildgen, X. Banquy, *J. Control. Release Off. J. Control. Release Soc.* **2014**, *185*, 71.
[102] M. Kasha, *Discuss. Faraday Soc.* **1950**, *9*, 14.
[103] X. Ma, H. Tian, *Angew. Chem. Int. Ed.* **2014**, *53*, 8817.
[104] J. R. Lakowicz, B. R. Masters, *J. Biomed. Opt.* **2008**, *13*, 029901.
[105] B. Valeur, M. N. Berberan-Santos, *Molecular Fluorescence: Principles and Applications*; Wiley-VCH Verlag GmbH & Co. KGaA: Weinheim, Germany, 2012.
[106] P. Rahman, M. Green, *Nanoscale* **2009**, *1*, 214.
[107] A. Escudero, A. I. Becerro, C. Carrillo-Carrión, N. O. Núñez, M. V. Zyuzin, M. Laguna, D. González-Mancebo, M. Ocaña, W. J. Parak, *Nanophotonics* **2017**, *6*, 881.
[108] Mansmann, *Z. Für Krist.* **1965**, *122*, 375.
[109] J. Xie, Z. Gao, E. Zhou, X. Cheng, Y. Wang, X. Xie, L. Huang, W. Huang, *Nanoscale* **2017**, *9*, 15974.
[110] S. Rodriguez-Liviano, N. O. Nuñez, S. Rivera-Fernández, J. M. de la Fuente, M. Ocaña, *Langmuir* **2013**, *29*, 3411.
[111] F. Chaput, F. Lerouge, S. Tusseau-Nenez, P.-E. Coulon, C. Dujardin, S. Denis-Quanquin, F. Mpambani, S. Parola, *Langmuir* **2011**, *27*, 5555.
[112] F. Chaput, C. Desroches, S. Parola, Method for preparing rare earth fluoride nanoparticles **2016**.
[113] T. Samanta, C. Hazra, A. E. Praveen, S. Ganguli, V. Mahalingam, *Eur. J. Inorg. Chem.* **2016**, *2016*, 802.
[114] C. Dong, M. Raudsepp, F. C. J. M. van Veggel, *J. Phys. Chem. C* **2009**, *113*, 472.
[115] T. Passuello, M. Pedroni, F. Piccinelli, S. Polizzi, P. Marzola, S. Tambalo, G. Conti, D. Benati, F. Vetrone, M. Bettinelli, A. Speghini, *Nanoscale* **2012**, *4*, 7682.
[116] C. Li, J. Yang, P. Yang, H. Lian, J. Lin, *Chem. Mater.* **2008**, *20*, 4317.
[117] Y. Li, Y. Wang, Y. Song, X. Zhou, K. Zheng, Y. Sheng, H. Zou, *CrystEngComm* **2017**, *19*, 1517.
[118] Y.-C. Guo, C. Cai, Y.-H. Zhang, *AIP Adv.* **2018**, *8*, 055308.
[119] K.-H. Park, S.-J. Oh, *Phys. Rev. B* **1993**, *48*, 14833.
[120] I. Bilecka, M. Niederberger, *Nanoscale* **2010**, *2*, 1358.
[121] L. Ma, W.-X. Chen, Y.-F. Zheng, J. Zhao, Z. Xu, *Mater. Lett.* **2007**, *61*, 2765.
[122] L. Ma, W.-X. Chen, X.-Y. Xu, L.-M. Xu, X.-M. Ning, *Mater. Lett.* **2010**, *64*, 1559.
[123] H. Wang, T. Nann, *Nanoscale Res. Lett.* **2011**, *6*.
[124] S. Eiden-Assmann, G. Maret, *Mater. Res. Bull.* **2004**, *39*, 21.
[125] S. Sturm, B. Ambrozic, M. Bele, N. Kostevsek, K. Z. Rozman, In *European Microscopy Congress 2016: Proceedings*; American Cancer Society, 2016; pp. 149–150.
[126] A. Noculak, A. Podhorodecki, *Nanotechnology* **2017**, *28*, 175706.
[127] X. Wang, J. Zhuang, Q. Peng, Y. Li, *Inorg. Chem.* **2006**, *45*, 6661.

[128] X. Zhang, T. Hayakawa, M. Nogami, Y. Ishikawa, *J. Nanomater.* **2010**, *2010*, 1.
[129] Y.-J. Xu, J. Lin, Y. Lu, S.-L. Zhong, L. Wang, L. Dong, Y.-D. Wu, J. Peng, L. Zhang, X.-F. Pan, W. Zhou, Y. Zhao, L.-P. Wen, S.-H. Yu, *Nanoscale* **2016**, *8*, 13399.
[130] Z. Xu, C. Li, P. Yang, Z. Hou, C. Zhang, J. Lin, *Cryst. Growth Des.* **2009**, *9*, 4127.
[131] J. Li, H. Cai, S. Dong, T. Zhang, C. Peng, X. Shi, M. Shen, *New J. Chem.* **2017**, *41*, 15136.
[132] J. Martínez-Esaín, J. Ros, J. Faraudo, S. Ricart, R. Yáñez, *Langmuir* **2018**, *34*, 6443.
[133] J. Martínez-Esaín, J. Faraudo, T. Puig, X. Obradors, J. Ros, S. Ricart, R. Yáñez, *J. Am. Chem. Soc.* **2018**, *140*, 2127.
[134] I. N. Evdokimov, A. A. Fesan, A. P. Losev, *Energy Fuels* **2017**, *31*, 3878.
[135] H. Ohshima, In *Colloid and Interface Science in Pharmaceutical Research and Development*; Elsevier, 2014; pp. 1–28.
[136] D. H. Napper, *J. Colloid Interface Sci.* **1977**, *58*, 390.
[137] G. Fritz, V. Schädler, N. Willenbacher, N. J. Wagner, *Langmuir* **2002**, *18*, 6381.
[138] S. Bhattacharjee, *J. Controlled Release* **2016**, *235*, 337.
[139] S. Das, M. Banik, G. Chen, S. Sinha, R. Mukherjee, *Soft Matter* **2015**, *11*, 8550.
[140] E. Amstad, M. Textor, E. Reimhult, *Nanoscale* **2011**, *3*, 2819.
[141] S. Alexander, *J. Phys.* **1977**, *38*, 983.
[142] P. G. de Gennes, *Macromolecules* **1980**, *13*, 1069.
[143] P. J. Flory, *J. Chem. Phys.* **1942**, *10*, 51.
[144] M. Kim, S. K. Schmitt, J. W. Choi, J. D. Krutty, P. Gopalan, *Polymers* **2015**, *7*, 1346.
[145] A. Al-Ani, H. Pingle, N. P Reynolds, P.-Y. Wang, P. Kingshott, *Polymers* **2017**, *9*, 343.
[146] P. Kingshott, H. Thissen, H. J. Griesser, *Biomaterials* **2002**, *23*, 2043.
[147] F. Carniato, K. Thangavel, L. Tei, M. Botta, *J. Mater. Chem. B* **2013**, *1*, 2442.
[148] F. N. Sayed, V. Grover, V. Sudarsan, B. N. Pandey, A. Asthana, R. K. Vatsa, A. K. Tyagi, *J. Colloid Interface Sci.* **2012**, *367*, 161.
[149] A.-A. Guay-Bégin, P. Chevallier, L. Faucher, S. Turgeon, M.-A. Fortin, *Langmuir* **2012**, *28*, 774.
[150] P. R. Diamente, R. D. Burke, F. C. J. M. van Veggel, *Langmuir* **2006**, *22*, 1782.
[151] R. Torres Martin de Rosales, R. Tavaré, A. Glaria, G. Varma, A. Protti, P. J. Blower, *Bioconjug. Chem.* **2011**, *22*, 455.
[152] B. Abécassis, F. Lerouge, F. Bouquet, S. Kachbi, M. Monteil, P. Davidson, *J. Phys. Chem. B* **2012**, *116*, 7590.
[153] K. L. Nash, *J. Alloys Compd.* **1997**, *249*, 33.
[154] C. Queffélec, M. Petit, P. Janvier, D. A. Knight, B. Bujoli, *Chem. Rev.* **2012**, *112*, 3777.
[155] J. Gałęzowska, *ChemMedChem* **2018**, *13*, 289.
[156] T. J. Clough, L. Jiang, K.-L. Wong, N. J. Long, *Nat. Commun.* **2019**, *10*, 1420.
[157] T. S. Elliott, A. Slowey, Y. Ye, S. J. Conway, *MedChemComm* **2012**, *3*, 735.
[158] G. Lamanna, M. Kueny-Stotz, H. Mamlouk-Chaouachi, C. Ghobril, B. Basly, A. Bertin, I. Miladi, C. Billotey, G. Pourroy, S. Begin-Colin, D. Felder-Flesch, *Biomaterials* **2011**, *32*, 8562.
[159] E. Illés, E. Tombácz, M. Szekeres, I. Y. Tóth, Á. Szabó, B. Iván, *J. Magn. Magn. Mater.* **2015**, *380*, 132.
[160] L. Qi, A. Sehgal, J.-C. Castaing, J.-P. Chapel, J. Fresnais, J.-F. Berret, F. Cousin, *ACS Nano* **2008**, *2*, 879.
[161] R. G. G. Russell, *Bone* **2011**, *49*, 2.
[162] E. Puljula, P. Turhanen, J. Vepsäläinen, M. Monteil, M. Lecouvey, J. Weisell, *ACS Med. Chem. Lett.* **2015**, *6*, 397.

[163] E. Gumienna-Kontecka, R. Silvagni, R. Lipinski, M. Lecouvey, F. Cesare Marincola, G. Crisponi, V. M. Nurchi, Y. Leroux, H. Kozlowski, *Inorganica Chim. Acta* **2002**, *339*, 111.
[164] F. Benyettou, Y. Lalatonne, O. Sainte-Catherine, M. Monteil, L. Motte, *Int. J. Pharm.* **2009**, *379*, 324.
[165] S. Kachbi-Khelfallah, M. Monteil, M. Cortes-Clerget, E. Migianu-Griffoni, J.-L. Pirat, O. Gager, J. Deschamp, M. Lecouvey, *Beilstein J. Org. Chem.* **2016**, *12*, 1366.
[166] F. Mpambani, Multifunctional magnetic and fluorescent nanoparticles for beta-amyloid targeting in neurodegenerative disease diagnosis. (PhD dissertaion), Université Claude Bernard Lyon 1, 2013.
[167] K. Shameli, M. Bin Ahmad, S. D. Jazayeri, S. Sedaghat, P. Shabanzadeh, H. Jahangirian, M. Mahdavi, Y. Abdollahi, *Int. J. Mol. Sci.* **2012**, *13*, 6639.
[168] L. Sandiford, A. Phinikaridou, A. Protti, L. K. Meszaros, X. Cui, Y. Yan, G. Frodsham, P. A. Williamson, N. Gaddum, R. M. Botnar, P. J. Blower, M. A. Green, R. T. M. de Rosales, *ACS Nano* **2013**, *7*, 500.
[169] Z. Varga, J. Mihály, S. Berényi, A. Bóta, *Eur. Polym. J.* **2013**, *49*, 2415.
[170] H. Belhadj, A. Hakki, P. K. J. Robertson, D. W. Bahnemann, *Phys. Chem. Chem. Phys.* **2015**, *17*, 22940.
[171] F. Benyettou, R. Rezgui, F. Ravaux, T. Jaber, K. Blumer, M. Jouiad, L. Motte, J.-C. Olsen, C. Platas-Iglesias, M. Magzoub, A. Trabolsi, *J. Mater. Chem. B* **2015**, *3*, 7237.
[172] B. F. Hardouin J, *J. Bioanal. Biomed.* **2012**, *04*.
[173] G. Thomas, F. Demoisson, J. Boudon, N. Millot, *Dalton Trans.* **2016**, *45*, 10821.
[174] T. F. Parangi, U. V. Chudasama, *ACS Omega* **2019**, *4*, 3716.
[175] I. Řehoř, V. Kubíček, J. Kotek, P. Hermann, J. Száková, I. Lukeš, *Eur. J. Inorg. Chem.* **2011**, *2011*, 1981.
[176] V. Kubíček, J. Kotek, P. Hermann, I. Lukeš, *Eur. J. Inorg. Chem.* **2007**, *2007*, 333.
[177] J. Ke, H. Dou, X. Zhang, D. S. Uhagaze, X. Ding, Y. Dong, *J. Pharm. Anal.* **2016**, *6*, 404.
[178] A. P. Sangnier, R. Aufaure, L. Motte, C. Wilhelm, E. Guenin, Y. Lalatonne, *Beilstein J. Nanotechnol.* **2018**, *9*, 2947.
[179] B. C. Koops, A. J. Slotboom, H. M. Verheij, In *Progress in Biotechnology*; Ballesteros, A.; Plou, F. J.; Iborra, J. L.; Halling, P. J., Eds.; Stability and Stabilization of Biocatalysts; Elsevier, 1998; Vol. 15, pp. 127–134.
[180] L. Li, K. Raghupathi, C. Song, P. Prasad, S. Thayumanavan, *Chem Commun* **2014**, *50*, 13417.
[181] P. Laskar, B. Saha, S. K. Ghosh, J. Dey, *RSC Adv.* **2015**, *5*, 16265.
[182] V. Torrisi, A. Graillot, L. Vitorazi, Q. Crouzet, G. Marletta, C. Loubat, J.-F. Berret, *Biomacromolecules* **2014**, *15*, 3171.
[183] G. Ramniceanu, B.-T. Doan, C. Vezignol, A. Graillot, C. Loubat, N. Mignet, J.-F. Berret, *RSC Adv.* **2016**, *6*, 63788.
[184] H. C. Kolb, M. G. Finn, K. B. Sharpless, *Angew. Chem. Int. Ed.* **2001**, *40*, 2004.
[185] R. Huisgen, *Angew. Chem. Int. Ed. Engl.* **1963**, *2*, 565.
[186] R. Huisgen, *Angew. Chem. Int. Ed. Engl.* **1963**, *2*, 633.
[187] V. V. Rostovtsev, L. G. Green, V. V. Fokin, K. B. Sharpless, *Angew. Chem. Int. Ed.* **2002**, *41*, 2596.
[188] C. W. Tornøe, C. Christensen, M. Meldal, *J. Org. Chem.* **2002**, *67*, 3057.
[189] B. T. Worrell, J. A. Malik, V. V. Fokin, *Science* **2013**, *340*, 457.
[190] E. M. Sletten, C. R. Bertozzi, *Angew. Chem. Int. Ed.* **2009**, *48*, 6974.
[191] V. Hong, N. F. Steinmetz, M. Manchester, M. G. Finn, *Bioconjug. Chem.* **2010**, *21*, 1912.

[192] D. A. Fleming, C. J. Thode, M. E. Williams, *Chem. Mater.* **2006**, *18*, 2327.
[193] N. J. Agard, J. A. Prescher, C. R. Bertozzi, *J. Am. Chem. Soc.* **2004**, *126*, 15046.
[194] J. M. Baskin, J. A. Prescher, S. T. Laughlin, N. J. Agard, P. V. Chang, I. A. Miller, A. Lo, J. A. Codelli, C. R. Bertozzi, *Proc. Natl. Acad. Sci. U. S. A.* **2007**, *104*, 16793.
[195] S. Redon, J. Massin, S. Pouvreau, E. De Meulenaere, K. Clays, Y. Queneau, C. Andraud, A. Girard-Egrot, Y. Bretonnière, S. Chambert, *Bioconjug. Chem.* **2014**, *25*, 773.
[196] R. Lemke, *Synthesis* **1974**, *1974*, 359.
[197] J. Massin, A. Charaf-Eddin, F. Appaix, Y. Bretonnière, D. Jacquemin, B. van der Sanden, C. Monnereau, C. Andraud, *Chem. Sci.* **2013**, *4*, 2833.
[198] R. Quiñones, S. Garretson, G. Behnke, J. W. Fagan, K. T. Mueller, S. Agarwal, R. K. Gupta, *Thin Solid Films* **2017**, *642*, 195.
[199] S. . Stankus, R. . Khairulin, K. . Lyapunov, *J. Alloys Compd.* **1999**, *290*, 30.
[200] C. R. Sirtori, *Pharmacol. Res.* **2014**, *88*, 3.
[201] C. W. Fong, *Eur. J. Med. Chem.* **2014**, *85*, 661.
[202] A. Endo, *J. Antibiot. (Tokyo)* **1979**, *32*, 852.
[203] W. F. Hoffman, A. W. Alberts, P. S. Anderson, J. S. Chen, R. L. Smith, A. K. Willard, *J. Med. Chem.* **1986**, *29*, 849.
[204] A. K. Willard, R. L. Smith, *J. Label. Compd. Radiopharm.* **1982**, *19*, 337.
[205] D. Askin, T. R. Verhoeven, T. M. H. Liu, I. Shinkai, *J. Org. Chem.* **1991**, *56*, 4929.
[206] X. Xie, Y. Tang, *Appl. Environ. Microbiol.* **2007**, *73*, 2054.
[207] L.-C. Chen, Y.-K. Lai, S.-C. Wu, C.-C. Lin, J.-H. Guo, *Enzyme Microb. Technol.* **2006**, *39*, 1051.
[208] J. L. Sorensen, K. Auclair, J. Kennedy, C. Richard Hutchinson, J. C. Vederas, *Org. Biomol. Chem.* **2003**, *1*, 50.
[209] S. Campoy, S. Sierra, B. Suarez, M. C. Ramos, J. Velasco, J. S. Burgos, J. L. Adrio, *J. Antibiot. (Tokyo)* **2010**, *63*, 499.
[210] B. Neises, W. Steglich, *Angew. Chem. Int. Ed. Engl.* **1978**, *17*, 522.
[211] H. A. Shahid, S. Jahangir, M. Hanif, T. Xiong, H. Muhammad, S. Wahid, S. Yousuf, N. Qureshi, *J. Mol. Struct.* **2017**, *1149*, 792.
[212] U. Holzgrabe, B. W. K. Diehl, I. Wawer, *J. Pharm. Biomed. Anal.* **1998**, *17*, 557.
[213] G. S. Brenner, D. K. Ellison, M. J. Kaufman, In *Analytical Profiles of Drug Substances and Excipients*; Brittain, H. G., Ed.; Academic Press, 1992; Vol. 21, pp. 277–305.
[214] A. A. Al-Badr, G. A. E. Mostafa, In *Profiles of Drug Substances, Excipients and Related Methodology*; Elsevier, 2014; Vol. 39, pp. 433–513.
[215] T. C. Bruice, T. H. Fife, J. J. Bruno, P. Benkovic, *J. Am. Chem. Soc.* **1962**, *84*, 3012.
[216] J. F. Kirsch, W. P. Jencks, *J. Am. Chem. Soc.* **1964**, *86*, 833.
[217] A. Lombardo, *J. Chem. Educ.* **1982**, *59*, 887.
[218] F. Song, A. El-Demerdash, S.-J. S. H. Lee, R. E. Smith, *J. Pharm. Biomed. Anal.* **2012**, *57*, 76.
[219] M.-N. Li, C.-R. Li, W. Gao, P. Li, H. Yang, *Anal. Chim. Acta* **2017**, *982*, 156.
[220] J. Massin, W. Dayoub, J.-C. Mulatier, C. Aronica, Y. Bretonnière, C. Andraud, *Chem. Mater.* **2011**, *23*, 862.
[221] C. Würth, M. Grabolle, J. Pauli, M. Spieles, U. Resch-Genger, *Nat. Protoc.* **2013**, *8*, 1535.
[222] N. Boens, W. Qin, N. Basarić, J. Hofkens, M. Ameloot, J. Pouget, J.-P. Lefèvre, B. Valeur, E. Gratton, M. vandeVen, N. D. Silva, Y. Engelborghs, K. Willaert, A. Sillen, G. Rumbles, D. Phillips, A. J. W. G. Visser, A. van Hoek, J. R. Lakowicz, H. Malak, I. Gryczynski, A. G. Szabo, D. T. Krajcarski, N. Tamai, A. Miura, *Anal. Chem.* **2007**, *79*, 2137.

[223] J. Y. HORIBA, A Guide to Recording Fluorescence Quantum Yields **2012**.
[224] M. A. Albota, C. Xu, W. W. Webb, *Appl. Opt.* **1998**, *37*, 7352.
[225] H. Wei, O. T. Bruns, M. G. Kaul, E. C. Hansen, M. Barch, A. Wiśniowska, O. Chen, Y. Chen, N. Li, S. Okada, J. M. Cordero, M. Heine, C. T. Farrar, D. M. Montana, G. Adam, H. Ittrich, A. Jasanoff, P. Nielsen, M. G. Bawendi, *Proc. Natl. Acad. Sci.* **2017**, *114*, 2325.
[226] A. Saleh, M. Schroeter, C. Jonkmanns, H.-P. Hartung, U. Modder, S. Jander, *Brain* **2004**, *127*, 1670.
[227] G. Stoll, M. Bendszus, *Neuroscience* **2009**, *158*, 1151.
[228] N. Nighoghossian, M. Wiart, S. Cakmak, Y. Berthezène, L. Derex, T.-H. Cho, C. Nemoz, F. Chapuis, G.-L. Tisserand, J.-B. Pialat, P. Trouillas, J.-C. Froment, M. Hermier, *Stroke* **2007**, *38*, 303.
[229] M. Wiart, N. Davoust, J.-B. Pialat, V. Desestret, S. Moucharrafie, T.-H. Cho, M. Mutin, J.-B. Langlois, O. Beuf, J. Honnorat, N. Nighoghossian, Y. Berthezène, *Stroke* **2007**, *38*, 131.
[230] F. Chauveau, T. H. Cho, Y. Berthezène, N. Nighoghossian, M. Wiart, *Int J. Clin. Pharmacol. Ther.* **2010**, *48*, 718.
[231] F. Fluri, M. K. Schuhmann, C. Kleinschnitz, *Drug Des. Devel. Ther.* **2015**, *9*, 3445.
[232] A. Durukan, T. Tatlisumak, *Pharmacol. Biochem. Behav.* **2007**, *87*, 179.
[233] H. Karatas, S. E. Erdener, Y. Gursoy-Ozdemir, G. Gurer, F. Soylemezoglu, A. K. Dunn, T. Dalkara, *J. Cereb. Blood Flow Metab.* **2011**, *31*, 1452.
[234] S. Jung, J. Aliberti, P. Graemmel, M. J. Sunshine, G. W. Kreutzberg, A. Sher, D. R. Littman, *Mol. Cell. Biol.* **2000**, *20*, 4106.
[235] T. Yardeni, M. Eckhaus, H. D. Morris, M. Huizing, S. Hoogstraten-Miller, *Lab Anim.* **2011**, *40*, 155.
[236] M. Gkagkanasiou, A. Ploussi, M. Gazouli, E. P. Efstathopoulos, *J. Neuroimaging* **2016**, *26*, 161.
[237] K. P. Doyle, L. N. Quach, H. E. D. Arceuil, M. S. Buckwalter, *Neurosci. Lett.* **2015**, *584*, 236.
[238] C. L. Cunningham, V. Martinez-Cerdeno, S. C. Noctor, *J. Neurosci.* **2013**, *33*, 4216.
[239] X. Hu, R. K. Leak, Y. Shi, J. Suenaga, Y. Gao, P. Zheng, J. Chen, *Nat. Rev. Neurol.* **2015**, *11*, 56.